DOC.20040219.0001

OCRWM	**ERRATA 001**	3. QA: QA 4. Page 1 of 3

1. Condition Report No. CR-1100

2. DC Tracking Number 38364

5. Product DI MDL-NBS-HS-000016

6. Title Drift-Scale Radionuclide Transport

7. Revision 00

8. Description of Error	9. Clarification/Restriction
A search of DIRS indicates you are currently using DIRS Reference 161530 *Drift-Scale Coupled Processes (DST and TH Seepage) Models*, MDL-NBS-HS-000015 REV 00, which has been assigned URN 1087. This document has never been approved and the URN is invalid. The DIRS reference has been marked as bad and cannot be used.	The model report, *Drift-Scale Radionuclide Transport* (DI: MDL-NBS-HS-000016 REV00) and associated DIRS have been corrected to reference DIRS 166512 [BSC (Bechtel SAIC Company) 2003. *Drift-Scale Coupled Processes (DST and TH Seepage) Models*. MDL-NBS-HS-000015 REV 00C. Las Vegas, Nevada: Bechtel SAIC Company. ACC: MOL.20030910.0160. TBV-5666.] (See attached, corrected report page 98 and corrected DIRS page 5.)

10. Responsible Manager (Print Name) Paul R. Dixon   Initials PRD   Date 2/17/04

160828 BSC (Bechtel SAIC Company) 2001. *Unsaturated Zone and Saturated Zone Transport Properties (U0100).* ANL-NBS-HS-000019 REV 00 ICN 02. Las Vegas, Nevada: Bechtel SAIC Company. ACC: MOL.20020311.0017.

158726 BSC (Bechtel SAIC Company) 2001. *UZ Flow Models and Submodels.* MDL-NBS-HS-000006 REV 00 ICN 01. Las Vegas, Nevada: Bechtel SAIC Company. ACC: MOL.20020417.0382.

161619 BSC (Bechtel SAIC Company) 2002. *Advection Versus Diffusion in the Invert.* ANL-EBS-MD-000063 REV 00F. Las Vegas, Nevada: Bechtel SAIC Company. ACC: MOL.20030812.0379. TBV-5400

160247 BSC (Bechtel SAIC Company) 2002. *Analysis of Geochemical Data for the Unsaturated Zone.* ANL-NBS-HS-000017 REV 00 ICN 02. Las Vegas, Nevada: Bechtel SAIC Company. ACC: MOL.20020314.0051.

160819 BSC (Bechtel SAIC Company) 2002. *Technical Work Plan for: Performance Assessment Unsaturated Zone.* TWP-NBS-HS-000003 REV 02. Las Vegas, Nevada: Bechtel SAIC Company. ACC: MOL.20030102.0108.

160146 BSC (Bechtel SAIC Company) 2002. *Total System Performance Assessment-License Application Methods and Approach.* TDR-WIS-PA-000006 REV 00. Las Vegas, Nevada: Bechtel SAIC Company. ACC: MOL.20020923.0175.

161773 BSC (Bechtel SAIC Company) 2003. *Analysis of Hydrologic Properties Data.* MDL-NBS-HS-000014 REV 00. Las Vegas, Nevada: Bechtel SAIC Company. ACC: DOC.20030404.0004.

160240 BSC (Bechtel SAIC Company) 2003. *Calibrated Properties Model.* MDL-NBS-HS-000003 REV 01. Las Vegas, Nevada: Bechtel SAIC Company. ACC: DOC.20030219.0001.

162318 BSC (Bechtel SAIC Company) 2003. *Drift Scale THM Model.* MDL-NBS-HS-000017 REV 00. Las Vegas, Nevada: Bechtel SAIC Company. ACC: DOC.20030818.0003.

166512 BSC (Bechtel SAIC Company) 2003. *Drift-Scale Coupled Processes (DST and TH Seepage) Models.* MDL-NBS-HS-000015 REV 00C. Las Vegas, Nevada: Bechtel SAIC Company. ACC: MOL.20030910.0160. TBV-5666.

162050 BSC (Bechtel SAIC Company) 2003. *Drift-Scale Coupled Processes (DST and THC Seepage) Models.* MDL-NBS-HS-000001 REV 02. Las Vegas, Nevada: Bechtel SAIC Company. ACC: DOC.20030804.0004.

164101 BSC (Bechtel SAIC Company) 2003. *Repository Design Project, Repository/PA IED Emplacement Drift Committed Materials (2).* 800-IED-WIS0-00302-000-00A. Las Vegas, Nevada: Bechtel SAIC Company. ACC: ENG.20030627.0004.

17	BSC (Bechtel SAIC Company) 2003. *Analysis of Hydrologic Properties Data.* MDL-NBS-HS-000014 REV 00. Las Vegas, Nevada: Bechtel SAIC Company. ACC: DOC.20030404.0004. 161773	Entire	Reference Only	4.1.1, 6.4.5; Tables 4.1-2a, 4.1-2b, 4.1-2d	Fracture and matrix hydrogeologic properties	N/A
18	BSC (Bechtel SAIC Company) 2003. *Calibrated Properties Model.* MDL-NBS-HS-000003 REV 01. Las Vegas, Nevada: Bechtel SAIC Company. ACC: DOC.20030219.0001. 160240	Entire	Reference Only	4.1.3	Uncertainty in calibrated hydrogeologic properties	N/A
		6	Reference Only	6.3.3.1	Information on drift-scale calibrated properties	N/A
19	BSC (Bechtel SAIC Company) 2003. *Drift Scale THM Model.* MDL-NBS-HS-000017 REV 00. Las Vegas, Nevada: Bechtel SAIC Company. ACC: DOC.20030818.0003. 162318	Entire	Reference Only	7.1	Support for drift-scale radionuclide transport conceptual and mathematical models	N/A
20	BSC (Bechtel SAIC Company) 2003. *Drift-Scale Coupled Processes (DST and TH Seepage) Models.* MDL-NBS-HS-000015 REV 00C. Las Vegas, Nevada: Bechtel SAIC Company. ACC: MOL.20030910.0160. TBV-5666 166512	Entire	Reference Only	7.1	Support for drift-scale radionuclide transport conceptual and mathematical models	N/A
21	BSC (Bechtel SAIC Company) 2003. *Drift-Scale Coupled Processes (DST and THC Seepage) Models.* MDL-NBS-HS-000001 REV 02. Las Vegas, Nevada: Bechtel SAIC Company. ACC: DOC.20030804.0004. 162050	Entire	Reference Only	7.1	Support for drift-scale radionuclide transport conceptual and mathematical models	N/A
22	BSC (Bechtel SAIC Company) 2003. *Repository Design Project, Repository/PA IED Emplacement Drift Committed Materials (2).* 800-IED-WIS0-00302-000-00A. Las Vegas, Nevada: Bechtel SAIC Company. ACC: ENG.20030627.0004. 164101	Entire	Product Output	4.1.7; Figures 4.1-1, 6.4-1; Tables 4.1-1, 6.4-5	Drift invert geometry	N/A
	BSC (Bechtel SAIC Company) 2003.	Entire	Product	4.1.6;	Information on invert materials	N/A

OCRWM	**MODEL COVER SHEET**	1. QA: QA Page 1 of 104

DOC.20030902.0009

2. Type of Mathematical Model

☒ Process Model ☒ Abstraction Model ☐ System Model

Describe Intended Use of Model

The purpose of this Model Report is to document two models for drift-scale radionuclide transport. The reason for a separate assessment of drift-scale transport is that the effects of waste emplacement drifts on flow are not captured in the flow fields used for radionuclide transport at the mountain scale. The results of this model report are planned to be used in TSPA.

3. Title

Drift-Scale Radionuclide Transport

4. DI (including Rev. No. and Change No., if applicable):

MDL-NBS-HS-000016 REV00

5. Total Attachments 12	6. Attachment Numbers – No. of Pages in Each I-4, II-2, III-2, IV-6, V-6, VI-4, VII-10, VIII-4, IX-8, X-18, XI-4, XII-16

	Printed Name	Signature	Date
7. Originator	J.H. Houseworth	SIGNATURE ON FILE	8/22/03
8. CSO	B. Kirstein	SIGNATURE ON FILE	8/25/03
9. Checker	P. Persoff	SIGNATURE ON FILE	8/25/03
10. QER	S. Harris	SIGNATURE ON FILE	8/25/03
11. Responsible Manager/Lead	J.S.Y. Wang	SIGNATURE ON FILE	8/25/03
12. Responsible Manager	P. Dixon	SIGNATURE ON FILE	8/25/03

13. Remarks

Block 9. Additional Checker is L. Pan

OFFICE OF CIVILIAN RADIOACTIVE WASTE MANAGEMENT
MODEL REVISION RECORD

1. Page: 2 of: 104

2. Model Title:
Drift-Scale Radionuclide Transport

3. DI (including Rev. No. and Change No., if applicable):
MDL-NBS-HS-000016 REV00

4. Revision/Change No.	5. Description of Revision/Change
REV00	Initial Issue

TABLE OF CONTENTS

TABLE OF CONTENTS (Continued)

LIST OF FIGURES

LIST OF FIGURES (Continued)

LIST OF TABLES

LIST OF TABLES (Continued)

ACRONYMS

3-D	three-dimensional, three dimensions
ACC	Accession Number
AP	Administrative Procedure (DOE)
BSC	Bechtel SAIC Company, LLC
CFR	Code of Federal Regulations
CRWMS	Civilian Radioactive Waste Management System
DIRS	Document Input Reference System
DOE	Department of Energy
DTN	Data Tracking Number
FEPs	features, events, and processes
FY	Fiscal Year
IED	Interface Exchange Drawing
LA	License Application
LBNL	Lawrence Berkeley National Laboratory
NRC	Nuclear Regulatory Commission
OCRWM	Office of Civilian Radioactive Waste Management
PA	Performance Assessment
QA	Quality Assurance
SCM	Software Configuration Management
SN	Scientific Notebook
TBV	To Be Verified
TSPA	Total System Performance Assessment
TSw	Topopah Spring welded units

ACRONYMS (Continued)

U.S.	United States
UZ	Unsaturated Zone
YMP	Yucca Mountain Project
YMRP	*Yucca Mountain Review Plan, Information Only*

1. PURPOSE

The purpose of this Model Report is to document two models for drift-scale radionuclide transport. This has been developed in accordance with *Technical Work Plan for: Performance Assessment Unsaturated Zone* (Bechtel SAIC Company, LLC (BSC) 2002 [160819]), which includes planning documents for the technical work scope, content, and management of this Model Report in Section 1.15, Work Package AUZM11, "Drift-Scale Radionuclide Transport." The technical work scope for this Model Report calls for development of a process-level model and an abstraction model representing diffusive release from the invert to the rocks, partitioned between fracture and matrix, as compared to the fracture-release approach used in the Site Recommendation. The invert is the structure constructed in a drift to provide the floor of that drift. The plan for validation of the models documented in this Model Report is given in Section I-5 of Attachment I in BSC (2002 [160819]). Note that the model validation presented in Section 7 deviates from the technical work plan (BSC 2002 [160819], Section I-5) in that an independent technical review specifically for model validation has not been conducted, nor publication in a peer-reviewed journal. Model validation presented in Section 7 is based on corroboration with alternative mathematical models, which is also called out by the technical work plan (BSC 2002 [160819], Section I-5), and is sufficient based on the requirements of AP-SIII.10Q for model validation. See Section 7 for additional discussion.

The phenomenon of flow and transport in the vicinity of the waste emplacement drift are evaluated in this model report under ambient thermal, chemical, and mechanical conditions. This includes the effects of water diversion around an emplacement drift and the flow and transport behavior expected in a fractured rock below the drift. The reason for a separate assessment of drift-scale transport is that the effects of waste emplacement drifts on flow are not captured in the flow fields used for radionuclide transport at the mountain scale (*UZ Flow Models and Submodels,* BSC 2003 [163045]).

The effects of variations in the flow field and fracture-matrix interaction in the vicinity of a waste emplacement drift are investigated through sensitivity studies using a dual-continuum flow and transport model, called the drift shadow model (Houseworth et al. 2003 [164394]). In the drift shadow model, the flow is significantly perturbed (reduced) beneath the waste emplacement drifts. However, comparisons of transport in this perturbed flow field with transport in an unperturbed flow field show similar results if the transport is initiated in the rock matrix. This has led to a fracture-matrix partitioning model that focuses on the partitioning of radionuclide transport between the fractures and matrix upon exiting the waste emplacement drift. The fracture-matrix partitioning model computes diffusive transport from the invert (for drifts without seepage) into the rock water in the fractures and matrix. The reason for introducing the fracture-matrix partitioning model is to broaden the conceptual model for flow beneath waste emplacement drifts in a way that does not rely on the specific flow behavior predicted by a dual continuum model and to ensure that radionuclide transport is not underestimated. The intended use of the model is to partition the releases from waste emplacement drifts between fractures and matrix in the underlying rock for subsequent transport calculation in Total System Performance Assessment (TSPA). The TSPA transport calculations are conducted using mountain-scale flow and transport models that do not account for the presence of waste emplacement drifts or drift-shadow flow phenomena.

The principal output of the fracture-matrix partitioning model is the distribution of radionuclide releases between the fractures and rock matrix from drifts with diffusive-dominated transport into the rock. Uncertainty in the fracture-matrix partitioning model is evaluated through the development of results over a suitable range of parameters that affect release fractions to the rock matrix and fractures. The distribution of radionuclide releases between fractures and matrix from drifts with advective-dominated transport into the rock is also provided.

Model limitations for the fracture-matrix partitioning model include the following approximations:

1. Fracture flow occurs beneath a waste emplacement drift within a distance less than the fracture spacing. Given fracture spacings that are, on average, less than one meter, the zone of reduced flow in the fracture-matrix partitioning model is greatly reduced in comparison with the drift shadow model.

2. The model is restricted to steady-state conditions (see Section 6.4). Therefore, the initial transient period is not treated, which is initially dominated by diffusive transfer into the rock. This initial radionuclide partitioning ratio will be approximately equal to the water content ratio of the fractures and matrix and will only asymptotically approach the partitioning ratio predicted by the fracture-matrix partitioning model.

3. The effects of dryout during the boiling and re-wetting periods are ignored, during which fracture water saturations are disproportionately reduced in comparison with the matrix (e.g., see Figure 6.3-2). This will lead to preferential entry of radionuclides to the matrix during the thermally-perturbed period.

4. All fractures are flowing in the fracture-matrix partitioning model as opposed to the active fracture model, where only a subset of the fractures are flowing. This leads to greater contact between the invert and flowing fractures and, therefore, greater releases from the invert to the rock fractures.

All of these limitations lead to a conservative prediction for fracture-matrix partitioning of radionuclide releases from drifts without seepage.

2. QUALITY ASSURANCE

Development of this model report and the supporting modeling activities have been determined to be subject to the Yucca Mountain Project's quality assurance (QA) program, as indicated in *Technical Work Plan for: Performance Assessment Unsaturated Zone,* TWP-NBS-HS-000003 REV 02 (BSC 2002 [160819], Section 8.2, Work Package (WP) AUZM11). Approved QA procedures identified in the TWP (BSC 2002 [160819], Section 4) have been used to conduct and document the activities described in this model report. The TWP also identifies the methods used to control the electronic management of data (BSC 2002 [160819], Section 8.4, WP AUZM11) during the modeling and documentation activities.

This Model Report provides information pertaining to radionuclide transport through a natural barrier that is important to the demonstration of compliance with the post-closure performance objectives prescribed in 10 CFR 63.113 [156605]. Therefore it is classified as a "Quality Level – 1" with regard to importance to waste isolation, as defined in AP-2.22Q, *Classification Criteria and Maintenance of the Monitored Geologic Repository Q-List*. The report contributes to the analysis and modeling data used to support performance assessment (PA); the conclusions do not directly impact engineered features important to safety, as defined in AP-2.22Q.

INTENTIONALLY LEFT BLANK

3. USE OF SOFTWARE

The major software codes and software routines used in this study are listed in Table 3-1. These software have been baselined in accordance with AP-SI.1Q, *Software Management*, are appropriate for the intended use, have been used strictly in the range of validation and were obtained from the Software Configuration Management (SCM). The iTOUGH2 V4.0 (LBNL 1999 [139918]) and TOUGH2 V1.11MEOS9NTV1.0 (LBNL 1999 [113943]) programs are the primary software used to represent physical processes for the Drift-Scale Radionuclide Transport models. Flow simulations were performed with iTOUGH2 V4.0 (LBNL 1999 [139918]) and flow and transport calculations were performed using TOUGH2 V1.11MEOS9NTV1.0 (LBNL 1999 [113943]). The routine CutDrift V1.0 (LBNL 2000 [152816]) was used to cut a cylindrical drift shape into the rectangular grid. The routine AddBound V1.0 (LBNL 2000 [152823]) was used to generate boundary grids for water and tracers to enter and leave the model grid. The routine EXT V1.0 (LBNL 1999 [134141]) was used to postprocess the results of iTOUGH2 V4.0 (LBNL 1999 [139918]) for graphical display of the flow field results.

Table 3-1. Qualified Software Used in this Report

Software Name	Version	Software Tracking Number	DIRS
iTOUGH2	4.0	10003-4.0-00	139918
CutDrift	1.0	10375-1.0-00	152816
AddBound	1.0	10357-1.0-00	152823
EXT	1.0	10047-1.0-00	134141
TOUGH2	1.11MEOS9NTV1.0	10065-1.11MEOS9NTV1.0-00	113943

Excel (v. 97-SR-1) and Mathcad (v. 11.0) spreadsheets and visual display graphics programs (Tecplot v. 7.0-4.0 for MS-WINDOWS) were also used. All information needed to reproduce the work using these standard software programs, including the input, computation, and output, is included in this report. Excel calculations are documented in Attachments I through IX and XII. Mathcad calculations are discussed in Sections 6.4.3, 6.4.4, 6.4.6, and Attachments X and XII.

INTENTIONALLY LEFT BLANK

4. INPUTS

4.1 DATA AND PARAMETERS

This section provides documentation for direct inputs to the Model Report. Other inputs are identified in the sections where they are used. Data input to the Model Report are referred to by Data Tracking Number (DTN); technical information input is identified by reference. This format allows for all data of similar use in the Model Report to be kept in a single location, for readability of the document and simplicity for downstream users.

Source DTNs for the hydrological and transport properties used in the calculations that feed total system performance assessment (TSPA) (see Section 6.4) are listed in Table 4.1-1. These data are summarized in Tables 4.1-2a through 4.1-2e for the repository unsaturated zone (UZ) model layers tsw33, tsw34, tsw35, and tsw36 (Topopah Spring Tuff upper lithophysal, middle nonlithophysal, lower lithophysal, and lower nonlithophysal welded units, respectively). This report uses the same parameter and data values as other TSPA feeds.

4.1.1 Fracture Frequency

Data for the mean and standard deviation of fracture frequency and fracture porosity for the tsw33, tsw34, tsw35, and tsw36 (see Table 4.1-2a) are given in Table 7 of the report, *Analysis of Hydrologic Properties Data* (BSC 2003 [161773]; DTN: LB0205REVUZPRP.001 [159525]). See Section 6.4.5 for a complete discussion of the uncertainty treatment for fracture frequency and fracture porosity. Fracture frequency data in the repository host rock provides estimates for the standard deviation of fracture frequency for the tsw33 and tsw34 model units, but not for the tsw35 or tsw36. Data from other units shown in Table 4.1-2b are used to develop uncertainty data for the tsw35 and tsw36.

4.1.2 Unsaturated Zone Flow

Data on UZ flow in the repository were developed using the UZ Flow Model. The flow data used are for the lower, mean, and upper bound flow fields for the glacial transition climate. These data, which include the fracture and matrix flux and the fracture and matrix water saturations, are available in DTN: LB03023DSSCP9I.001 [163044] (BSC 2003 [163045]). The glacial transition lower, mean, and upper infiltration scenarios cover a range of conditions that encompass all of the monsoon scenarios and all but the present-day lower infiltration scenario. Furthermore, the majority of the compliance period (2,000 to 10,000 years) is modeled as being under glacial transition climate. Because of the predominance in time and wide range of the glacial transition infiltration scenarios, these three cases are used as representative for the low, mean, and high scenarios for the entire compliance period. In conjunction with the mountain-scale flow model results, a distribution for flow focusing in the fracture continuum is also used to account for sub gridblock scale heterogeneity for the mountain-scale flow fields.

4.1.3 Fracture Hydrologic Characteristics

The flow-focusing effect is represented in the fracture fluxes and water saturations, requiring the van Genuchten pore size distribution factor (m) shown in Table 4.1-2c. This parameter is not treated as uncertain because of the uncertainty already investigated through flow model calibration (BSC 2003 [160240] and [163045]). Fracture residual water saturation (Table 4.1-2c) is needed to define the effective saturation used in the van Genuchten relative permeability model and is treated as an uncertain parameter. The flow-focusing correlation, documented in Bodvarsson et al. (2003 [163443], Figure 13), is given by the following:

$$P = -0.3137F^4 + 5.4998F^3 - 35.66F^2 + 102.3F - 11.434$$

where F is the flow focusing factor and P is the cumulative probability for the value of F (Bodvarsson et al. 2003 [163443], Figure 13). See Section 6.4.5 for a complete discussion of the uncertainty treatment for water flux, saturation, and flow focusing.

4.1.4 Matrix Hydrologic Characteristics

Data for matrix porosity and permeability (Table 4.1-2d and Table 4.1-2e) are also used to evaluate matrix diffusion. See Section 6.4.5 for a complete discussion of the uncertainty treatment.

4.1.5 Diffusion in Fractured Rock

Mass transport in the rock fractures immediately in contact with the drift is treated as a steady-state diffusion process, as described in Section 6.4.1. Diffusion will occur through rock fractures immediately adjacent to a drift due to the residual water content (or greater) that is present in all fractures. Due to the limited direct information available concerning diffusion coefficients in partially saturated fractures, diffusion coefficients determined for the rock matrix are used as the expected values for diffusion coefficients in the neighboring partially saturated fractures. See Assumption 1 and Section 6.4.5 for a discussion of the justification for this approximation. The effects of changes in water saturation on diffusion are captured through the following correlation (Reimus et al. 2002 [163008], Equation 2.5)

$$\log(D_m) = -3.49 + 1.38\theta_m + 0.165\log(k_w)$$

where D_m is the effective diffusion coefficient in cm^2/s, θ_m is the matrix water content, and k_w is the effective permeability to water in m^2. These data are the basis for all of the UZ flow and transport models used for LA.

4.1.6 Diffusion in the Invert

Mass transport in the invert is modeled as a diffusion process. The water-filled pore space is treated as a single continuum. A correlation for the diffusion coefficient is given in the report, *Invert Diffusion Properties Model* (BSC 2001 [156700], pp. 23–25). The crushed tuff used for the invert will be "a native material from the development of the emplacement drifts" (refer to design information by BSC (2003 [164069]); characteristics of the crushed tuff by CRWMS M&O (2000 [136255], Section 6.5)). Therefore, the matrix porosity of the granular material will be the same as the matrix porosity, ϕ_m, from the repository host rock. The matrix porosity characteristics for the invert are taken from the tsw36 (see Table 4.1-2d), as used in BSC (2002 [161619], Section 5.9). The expected value and range for the intergranular porosity of the crushed tuff, ϕ_{Ig}, is shown in Table 4.1-2f (BSC 2002 [161619], Tables 6-1 and 6-2). Uncertainty for ϕ_{Ig} is discussed in Section 6.4.5. The uncertainty in the free-water diffusion coefficient is based on data from Weast and Astle (1979 [102865]), which provides 38 free-water diffusion coefficients for 19 electrolytes in a range of aqueous solutions (see Table 4.1-2g). These diffusion coefficients range in value from 7.1×10^{-10} m^2/s to 3.87×10^{-9} m^2/s. This is a sufficiently wide range of free-water diffusion coefficients for radionuclides, based on reported values discussed in Section 6.4.5. See Section 6.4.5 for a complete discussion of the uncertainty treatment for diffusive mass transfer in the invert.

The correlation for the diffusive mass transfer coefficient is given by (BSC 2001 [156700], pp. 23–25):

$$\log\left(\frac{D_{eI}}{D_0}\right) = 1.849 \log \theta_I$$

where D_{eI} is the invert diffusive mass transfer coefficient, D_0 is the free-water diffusion coefficient, and θ_I is the invert water content.

4.1.7 Design Information

Design information on invert characteristics, cited in the in-drift configuration IED, are given as follows:

Design data on the dimensions of the drift and invert, cited in the in-drift configuration IED, are given in Figure 4.1-1 (BSC 2003 [164101]).

Information concerning the design layout is also needed. The percentages of each waste emplacement panel (1, 2, 3, and 4) within each of the four rock units (tsw33, tsw34, tsw35, and tsw36) is calculated from information on drift areas by geologic unit in BSC (2003 [164491] 800-IED-WIS0-00103-000-00Ab). The total drift areas and percentages in each host rock unit are shown in Table 4.1-2h.

Table 4.1-1. Inputs

Input	Type	Description
LB0205REVUZPRP.001 [159525]	Data	Fracture frequency and porosity
LB0208UZDSCPLI.002 [161788]	Data	Matrix permeabilities, fracture van Genuchten *m*, and fracture residual saturation – lower infiltration scenario.
LB0208UZDSCPMI.002 [161243]	Data	Matrix permeabilities, fracture van Genuchten *m*, and fracture residual saturation – mean infiltration scenario.
LB0302UZDSCPUI.002 [161787]	Data	Matrix permeabilities, fracture van Genuchten *m*, and fracture residual saturation – upper infiltration scenario.
LB03023DSSCP9I.001 [163044]	Data	Fracture and matrix flux and saturation, and matrix relative permeability (glacial transition climate, all infiltration scenarios)
Bodvarsson et al. 2003 [163443]	Technical Information	Flow focusing factor correlation
LB0207REVUZPRP.002 [159672]	Data	Matrix porosity, standard deviation for matrix porosity
Weast and Astle 1979 [102865]	Technical Information	Diffusion coefficients in aqueous solution
Reimus et al. 2002 [163008]	Technical information	Correlation for diffusion coefficient in rock matrix
BSC 2001 [156700], pp. 23–25	Technical Information	Correlation for diffusion coefficient in invert materials
BSC 2002 [161619], Section 4.1.3	Technical Information	Intergranular porosity of invert
BSC 2003 [164101] 800-IED-WIS0-00302-000-00A	Design information	Emplacement drift committed materials
BSC 2003 [164491] 800-IED-WIS0-00103-000-00Ab	Design Information	Repository design layout information
BSC 2003 [164069], 800-IED-EBS0-00201-000-00A	Design Information	Emplacement drift configuration

Table 4.1-2a. Fracture Frequency and Porosity Data for the Repository Host Rock

UZ Model Layer	Frequency (m^{-1})		porosity	
	F	σ_f	Mean (-)	Std (-)
tsw33	0.81	1.03	5.8E-3	-
tsw34	4.32	3.42	8.5E-3	2.50E-03
tsw35	3.16	-	9.6E-3	-
tsw3[67]	4.02	-	1.3E-2	-

DTN: LB0205REVUZPRP.001 [159525]; BSC 2003 [161773]

NOTE: Fracture properties developed from field data (Std refers to standard deviation for porosity)

Table 4.1-2b. Fracture Frequency for Rock Units with Data on Standard Deviation

Fracture frequency data		
UZ Model Layer	Frequency (m^{-1})	
	F	σ_f
tcw11	0.92	0.94
tcw12	1.91	2.09
tcw13	2.79	1.43
ptn21	0.67	0.92
ptn24	0.46	0.45
ptn25	0.52	0.6
ptn26	0.97	0.84
tsw31	2.17	2.37
tsw32	1.12	1.09
tsw33	0.81	1.03
tsw34	4.32	3.42

DTN: LB0205REVUZPRP.001 [159525]; BSC 2003 [161773]

Table 4.1-2c. Fracture van Genuchten *m* and Residual Saturation, All Infiltration Cases

UZ Model Layer	Hydrogeologic Units	Fracture van Genuchten m	Fracture Residual Saturation
tsw33	TUL	0.633	0.01
tsw34	TMN	0.633	0.01
tsw35	TLL	0.633	0.01
tsw3[67]	TM2 & TM1	0.633	0.01

DTNs: LB0208UZDSCPLI.002 [161788]; LB0208UZDSCPMI.002 [161243]; and LB0302UZDSCPUI.002 [161787]

Table 4.1-2d. Matrix Porosity Average and Standard Deviation, All Infiltration Cases

UZ Model Layer	Hydrogeologic Units	Average Matrix Porosity	Standard Deviation for Matrix Porosity
tsw33	TUL	0.155	0.030
tsw34	TMN	0.111	0.020
tsw35	TLL	0.131	0.031
tsw3[67]	TM2 & TM1	0.103	0.025

DTN: LB0207REVUZPRP.002 [159672]; BSC 2003 [161773]

Table 4.1-2e. Matrix Permeability, All Infiltration Cases

UZ Model Layer	Hydrogeologic Units	Average Matrix Permeability (m^2) – lower infiltration case	Average Matrix Permeability (m^2) – mean infiltration case	Average Matrix Permeability (m^2) – upper infiltration case
tsw33	TUL	1.60E-18	6.57E-18	2.39E-17
tsw34	TMN	1.38E-19	1.77E-19	2.96E-19
tsw35	TLL	2.33E-18	4.48E-18	8.55E-18
tsw3[67]	TM2 & TM1	5.58E-19	2.00E-19	7.41E-19

DTNs: LB0208UZDSCPLI.002 [161788]; LB0208UZDSCPMI.002 [161243]; and LB0302UZDSCPUI.002 [161787]

Table 4.1-2f. Intergranular Porosity of the Invert

Mean	Range
0.45	0.4 to 0.48

Source: BSC 2002 [161619], Section 4.1.3

Table 4.1-2g. Free-Water Diffusion Coefficients

Electrolytes	Solute concentration (molarity)		
	0.01	**0.1**	**1**
HCl	n.a.	3.05	3.436
HBr	n.a.	3.156	3.87
LiCl	1.312	1.269	1.302
LiBr	n.a.	1.279	1.404
$LiNO_3$	1.276	1.24	1.293
NaCl	1.545	1.483	1.484
NaBr	n.a.	1.517	1.596
NaI	n.a.	1.52	1.662
KCl	1.917	1.844	1.892
KBr	n.a.	1.874	1.975
KI	n.a.	1.865	2.065
KNO_3	1.846	n.a.	n.a.
$KClO_4$	1.79	n.a.	n.a.
$CaCl_2$	1.188	1.11	1.203
$BaCl_2$	1.265	1.159	1.179
Na_2SO_4	1.123	n.a.	n.a.
$MgSO_4$	0.71	n.a.	n.a.
$LaCl_3$	1.105	n.a.	n.a.
$K_4Fe(CN)_4$	1.183	n.a.	n.a.

Source: Weast and Astle 1979 [102865], p. F-62.

NOTE: Diffusion coefficient values for strong electrolytes = actual value × 10^5 cm^2/s

n.a. = data not available

Table 4.1-2h. Drift Areas and Percentage of Each Rock Unit within Waste Emplacement Panels

Panel	Drift Area (m^2)	%tsw33	%tsw34	%tsw35	%tsw36
1	298850	0	40	60	0
2	1477867	0	5	91	4
3	1862136	12	22	66	0
4	1344299	0	0	95	5

Source: BSC (2003 [164491], 800-IED-WIS0-00103-000-00Ab) (see also Attachment VIII)

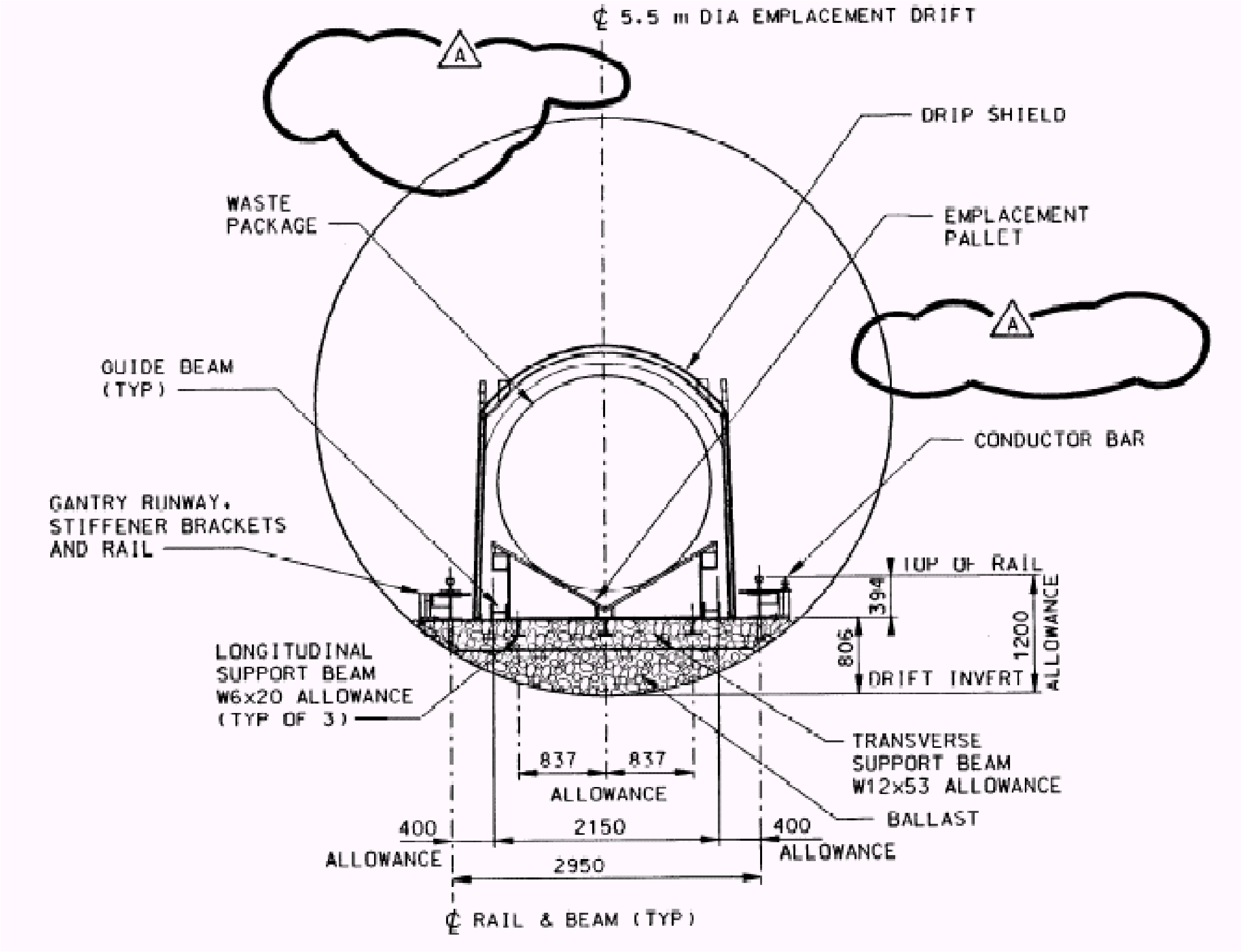

Source: BSC 2003 [164101]

Figure 4.1-1. In-Drift Configuration – all dimensions are in mm unless otherwise noted

4.2 CRITERIA

The licensing criteria for postclosure performance assessment are stated in 10 CFR 63.114 [156605]. The requirements to be satisfied by TSPA are identified in the Yucca Mountain *Project Requirements Document* (Canori and Leitner 2003 [161770]). The acceptance criteria that will be used by the Nuclear Regulatory Commission (NRC) to determine whether the technical requirements have been met are identified in *Yucca Mountain Review Plan, Final Report* (YMRP; NRC 2003 [163274]). The pertinent requirements and criteria for this model report are summarized in Table 4.2-1.

Table 4.2-1. Project Requirements and YMRP Acceptance Criteria Applicable to this Model Report

Requirement Number[a]	Requirement Title[a]	10 CFR 63 Link	YMRP Acceptance Criteria
PRD-002/T-015	Requirements for Performance Assessment	10 CFR 63.114(a-c; e-g)	Criteria 1 to 4 for *Flow Paths in the Unsaturated Zone* [b]
PRD-002/T-016	Requirements for Multiple Barriers	10 CFR 63.115(b,c)	Criteria 1 to 3 for *Demonstration of Multiple Barriers* [c]

NOTES: [a] from Canori and Leitner (2003 [161770])

[b] from NRC (2003 [163274], Section 2.2.1.3.7.3)

[c] from NRC (2003 [163274], Section 2.2.1.1.3)

The acceptance criteria identified in Section 2.2.1.3.7.3 of the YMRP (NRC 2003 [163274]) are given below, followed by a short description of their applicability to this Model Report:

- Acceptance Criterion 1, *System Description and Model Integration Are Adequate* (also refer to Sections 6.4 and 6.4.1 of this Model Report):

  Transport relationships at the interface between the waste emplacement drift and the rock are accounted for in a manner consistent with the various flow and transport model abstractions used in the TSPA. The methodology accounts for important design features and physical phenomena at a level consistent with the available data and uncertainty, such that the potential for radionuclide transport in the unsaturated zone (UZ) is not underestimated. In particular, this model provides suitable estimates of the boundary conditions for the UZ mountain-scale transport abstraction, in terms of the partitioning of radionuclide releases from waste emplacement drifts to the fractures and rock matrix supporting the inclusion of related features, events, and processes (FEPs).

- Acceptance Criterion 3, *Data Uncertainty Is Characterized and Propagated through the Model Abstraction* (also refer to Section 6.4.6 of this Model Report):

  The parameters used in and derived by the seepage process model are technically defensible; they are based on and consistent with available data from Yucca Mountain; uncertainties and variabilities are evaluated and reasonably accounted for and adequately represented. Uncertainty is adequately represented in parameter development for conceptual models, process-level models, and alternative conceptual models, considered in developing the abstraction of radionuclide transport in the UZ.

- Acceptance Criterion 4, *Model Uncertainty Is Characterized and Propagated through the Model Abstraction* (also refer to Section 6.7 of this Model Report):

  Alternative modeling approaches of FEPs are considered and are consistent with available data and current scientific understanding, and the results and limitations are appropriately considered in the abstraction. Conceptual model uncertainties are adequately defined and documented, and the effects on conclusions regarding performance are properly assessed. Appropriate alternative modeling approaches are consistent with available data and current scientific knowledge, and appropriately consider their results and limitations.

- Acceptance Criterion 5, *Model Abstraction Output is Supported by Objective Comparisons* (also refer to Section 6.7 of this Model Report)

  Models implemented in this TSPA abstraction provide results consistent with output from detailed process-level models. Outputs of radionuclide transport in the UZ abstractions reasonably produce or bound the results of corresponding process-level models. Sensitivity analyses or bounding analyses are provided, to support the TSPA abstraction of radionuclide transport in the UZ, that cover ranges consistent with site data, field or laboratory experiments and tests.

The acceptance criteria identified in Sections 2.2.1.1.3 of the YMRP (NRC 2003 [163274]) are given below, followed by a short description of their applicability to this Model Report:

- Acceptance Criterion 1, *Identification of Barriers Is Adequate* (also refer to Sections 6.3.3.4, 6.4.1, 6.4.6, and 8 of this Model Report):

  The unsaturated rock layers below the repository (and above the water table) is a natural barrier important to waste isolation. This barrier functions by delaying radionuclide movement. The barrier capability is determined by the hydrological and transport properties as implemented in this model for UZ transport.

- Acceptance Criterion 2, Description of Barrier Capability to Isolate Waste Is Acceptable (also refer to Sections 6.3.3.4, 6.4.1, 6.4.6, and 8 of this Model Report):

  The capability of the identified barrier to substantially delay the movement of radionuclides is adequately identified and described for the time period over which the barrier is effective. The uncertainty associated with barrier capabilities is adequately described.

- Acceptance Criterion 3, Technical Basis for Barrier Capability Is Adequately Presented (also refer to Sections 6.3.3.4, 6.4.1, 6.4.6, and 8 of this Model Report):

  The technical bases are consistent with the technical basis for the PA. The technical basis for assertions of barrier capability is commensurate with the importance of each barrier's capability and the associated uncertainties.

4.3 CODES AND STANDARDS

No specific formally established standards have been identified as applying to this modeling activity.

5. ASSUMPTIONS

The following assumptions are used in this model report:

1. Diffusion in the rock matrix may be used as limiting upper values for diffusion in fractures.

Diffusion coefficients in fracture water have not been directly determined. Generally speaking, diffusion in unsaturated geologic materials has been found to be sensitive to water content (Conca and Wright 1990 [101582], p. 1,055; Bear 1972 [156269], pp. 117–118). Experimental evidence concerning diffusion in unsaturated granular materials is presented in Conca and Wright (1990 [101582]). These experiments were performed on nonporous granular materials in which diffusion occurred through water films along the granular surfaces. The water content of these materials were on the order of 0.5 to 5 percent and diffusion coefficients ranged from about 10^{-13} m^2/s to 10^{-11} m^2/s (Conca and Wright 1990 [101582], Figures 10–13). The analogous water content of a fracture continuum is the fracture water saturation, which is also roughly in this range (see Attachment VII). The range for matrix diffusion coefficients is about an order of magnitude larger (see Figure 6.4-15). This information suggests that the use of diffusion coefficients in the rock matrix as surrogates for diffusion coefficients in the fractures is conservative. Fractures in the welded tuff repository host rock are different than the nonporous granular materials investigated by Conca and Wright (1990 [101582]) due to differences in geometry and the connection to a porous rock matrix. Therefore, limiting values for diffusion coefficients in the fractures are taken to be the effective diffusion coefficients in the neighboring rock matrix. This assumption is used in Sections 6.3.2.2 and 6.4.5 and does not require further confirmation because the assumption represents a conservative bound.

2. Standard deviation of fracture frequency may be derived from the correlation with the mean value.

Values for fracture frequency and the standard deviation for fracture frequency have been determined for several hydrogeologic model units in the unsaturated zone. These data show a strong correlation (see Figure 6.4-13). For two of the hydrogeologic model units addressed in this report (the tsw35 and tsw36), estimates of the mean fracture frequency are available, but not for the standard deviations. The correlation is used to derive estimated standard deviations for fracture frequency for these units. This assumption, used in Section 6.4.5, is considered adequate does not require further confirmation given the other greater uncertainties concerning fracture aperture, fracture water content, and the general fracture flow patterns around a waste emplacement drift.

3. A correlation between permeability, porosity, and effective diffusion coefficient developed for water-saturated rock matrix is extended to unsaturated conditions by using the effective permeability and water content in place of the permeability and porosity.

This extension to unsaturated conditions is appropriate because for unsaturated flow, the character of the gas phase is not significant other than the space that it occupies. The gas phase could be replaced by solid (rock mineral) which would result in exact equivalence between the unsaturated water content and porosity and effective unsaturated permeability and permeability. This assumption, used in Section 6.4.5, is considered adequate does not require further confirmation because, as discussed for Assumption 1, the treatment of diffusion represents a conservative bound.

6. DRIFT-SCALE RADIONUCLIDE TRANSPORT MODEL

6.1 INTRODUCTION

Hydrogeology at Yucca Mountain

Yucca Mountain consists of alternating layers of welded and nonwelded volcanic tuffs. The repository horizon lies in the unsaturated zone (UZ), approximately 300 m below the ground surface and 300 m above the water table. This horizon consists of welded tuffs composed of a dense porous rock matrix, which is highly fractured. Fracture permeability in the welded tuffs is on the order of darcies ($\sim 10^{-12}$ m^2), and the rock matrix permeability is on the order of microdarcies ($\sim 10^{-18}$ m^2) (BSC 2001 [161316], Table 13). Given these rock characteristics and the estimated range of water percolation rates of 1 to 11 mm/yr (USGS 2001 [160355], Table 6-9), most of the water flux in the repository host rock is expected to flow in the fractures with a smaller component flowing through the rock matrix. Although most of the flow is in the fractures, more than 99% of the water volume resides in the rock matrix due to the larger porosity and water saturation in the matrix compared to the fractures. The key scientific notebooks (with relevant pages) used in this study are presented in Table 6.1-1.

Table 6.1-1. Scientific Notebooks Used in this Model Report

LBNL Scientific Notebook ID	M&O Scientific Notebook ID	Relevant Pages	Citation
YMP-LBNL-SZ-JEH-1	SN-LBNL-SCI-205-V1	115–181; 193–194	Houseworth 2003 [163233]
YMP-LBNL-SZ-JEH-2	SN-LBNL-SCI-239-V1	211–231	Wang 2003 [163234]
YMP-LBNL-DSRT-JEH-1	SN-LBNL-SCI-236-V1	5–145	Wang 2003 [163234]

Drift Shadow Alternative Model

The phenomenon of flow diversion around a cavity was investigated for a homogeneous porous medium by Philip et al. (1989 [105743]). This diversion of flow was shown to result in flow velocities in a zone beneath the drift that are reduced relative to the undisturbed flow velocities away from the drift. In particular, the flow velocity at the base of the drift is exactly zero. The zone beneath the drift was also found to have lower water saturation than the undisturbed zone. This region of reduced flow velocity and water saturation beneath the drift is known as the drift shadow (Philip et al. 1989 [105743]).

For a quasi-linear representation of the hydrogeologic properties, Philip et al. (1989 [105743]) found that the extent of the drift shadow is a function of the characteristic sorptive length scale and the drift radius. The quasi-linear model is a special case in which the logarithm of the relative permeability is linearly proportional to the capillary pressure, where the constant of proportionality is equal to 2, divided by the sorptive length scale. The shape of the drift shadow is governed by the ratio of the drift radius to the sorptive length scale. This ratio is a measure of the relative importance of gravitational forces compared with the capillary forces that define flow patterns around the drift. Philip et al. (1989 [105743], p. 24) showed that the drift shadow becomes more elongated (relative to coordinates scaled by the drift radius) as the dimensionless ratio increases (i.e., the gravitational gradient becomes more dominant). Diagrams showing contours of equal flow velocity are given in Philip et al. (1989 [105743], Figure 3). Bordering the shadow, near the edge of the drift, a zone of enhanced flow occurs where the flow diverted from the top of the drift is focused.

Capillary effects are much stronger in the matrix than in the fractures of a fractured rock. Based on the results of Philip et al. (1989 [105743]), the fracture continuum is expected to behave as a gravity-dominated system and the rock matrix as a capillary-dominated system. Therefore, the reduction in flow below the drift is expected to be much more significant for the fracture continuum than for the matrix continuum. Furthermore, the very low water content of the fracture continuum below the drift, caused by very low saturation and porosity (compared to the matrix continuum), means that the vast majority of the water immediately below the drift will be in the rock matrix.

In this report, the drift shadow model results suggest the use of the fracture-matrix partitioning model described below. This model is used as an alternative model for qualitative comparison with the Fracture-Matrix Partitioning Model described below. Comparisons between expected results for transport based on the fracture-matrix partitioning model method and the drift shadow model are used for model validation in Section 7.

Fracture-Matrix Partitioning (Primary) Model

Results of the drift shadow model rely on the use of the dual-continuum approach for drift-scale flow and transport in a fractured rock beneath a waste emplacement drift. A fracture-matrix partitioning model considers the case in which fracture flow occurs in a region close to the base of the waste emplacement drift, relaxing the reliance on the dual-continuum process description of flow around a waste emplacement drift. Under these conditions, the partitioning of radionuclides from the waste emplacement drift to the rock fractures and matrix is an important process, given the more active hydrologic environment beneath waste emplacement drifts in this model. The fracture-matrix partitioning model only establishes the fraction of radionuclides released to the rock fractures and matrix. The output of this model can then be used in combination with the TSPA models for radionuclide release rates from drifts and radionuclide transport. The transport model and the associated flow model used in TSPA are mountain-scale models that do not represent the drifts and, therefore, do not include any effects of the drift shadow on flow or radionuclide transport beneath waste emplacement drifts.

6.2 FEATURES, EVENTS, AND PROCESSES

The following table of features, events, and processes (FEPs) were taken from the License Application (LA) FEP List (DTN: MO0301SEPFEPS1.000 [161496]). The LA FEP List is a revision to the previous project FEP list (Freeze et al. 2001 [154365]) used to develop the list of included FEPs in the *Technical Work Plan for: Performance Assessment Unsaturated Zone* (BSC 2002 [160819], Table 2-6). The selected FEPs are those taken from the LA FEP List that are associated with the subject matter of this report. The results of this model are part of the basis for the treatment of FEPs as discussed in the *Total System Performance Assessment-License Application Methods and Approach* (BSC 2002 [160146], Section 3.2.2) and the set of abstraction reports given in *Technical Work Plan for: Performance Assessment Unsaturated*

Zone (BSC 2002 [160819], Table 2-6). The cross reference for each FEP to the relevant sections of this report is also given below (Table 6.2-1).

Complete or partial treatment of FEPs is provided herein. The results of this and other model reports are used to fully document the technical basis for the include/exclude status of these FEPs for TSPA-LA. The UZ department's documentation for the included FEPs listed in Table 6.1-1 is compiled from this and other model reports and can be found in the model abstraction reports as described in Sections 2.1.2 and 2.4 of the TWP (BSC 2002 [160819]) and the FEPs report as described in Section 1.12.10 of the TWP (BSC 2002 [160819]). Excluded FEPs are to be documented in the FEPs report as described in Section 1.12.10 of the TWP (BSC 2002 [160819]).

Table 6.2-1. Features, Events, and Processes Addressed in This Report

LA FEP Number	FEP Name	Cross Reference Section
1.2.02.01.0A	Fractures	6.3.2.3 and 6.4.5
1.3.01.00.0A	Climate change, global	6.4.6
1.4.01.01.0A	Climate modification increases recharge	6.4.6
2.1.08.01.0A	Water influx at the repository	6.3.2.2 and 6.4.5
2.1.08.02.0A	Enhanced influx at the repository	6.4.5
2.2.03.01.0A	Stratigraphy	6.4.5
2.2.03.02.0A	Rock properties of host rock and other units	6.3.2.3 and 6.4.5
2.2.07.02.0A	Unsaturated groundwater flow in the geosphere	6.3.3 and 6.4.1
2.2.07.04.0A	Focusing of unsaturated flow (fingers, weeps)	6.4.5
2.2.07.08.0A	Fracture flow in the UZ	6.3.3 and 6.4.1
2.2.07.15.0B	Advection and dispersion in the UZ	6.3.3.2 and 6.4.1
2.2.07.20.0A	Flow diversion around repository drifts	6.3.3.1 and 6.4.1
2.2.07.21.0A	Drift shadow forms below repository	6.3.3.1 and 6.4.1
2.2.08.05.0A	Diffusion in the UZ	6.3.2.3 and 6.4.5
2.2.08.08.0B	Matrix diffusion in the UZ	6.3.2.3 and 6.4.5
2.2.08.09.0B	Sorption in the UZ	6.3.2.3

6.2.1 Included FEPs

The following FEP statements are the TSPA Disposition statements for included FEPs. Only FEP 2.2.07.21.0A is exclusively included in this model report. The remainder of the included FEPs are also included in other UZ model reports that support TSPA. Note that FEPs 1.3.01.00.0A, 2.2.07.20.0A, 2.2.08.08.0B, and 2.2.08.09.0B are addressed, but not included, in the output of this model report for TSPA, and are not discussed below.

FEP 2.2.07.21.0A, "Drift shadow forms below repository," is included in TSPA through the results of this model report. This is included through the fracture-matrix partitioning model for the fraction of releases from a waste emplacement drift without seepage to the fractures of the underlying rock mass (see Tables 6.4-6 and 6.4-7). This boundary condition (initiation of geosphere transport in the rock matrix or fractures) is found to control, in large part, the general behavior of radionuclide transport through the drift shadow zone. Based on these results, additional effects of the drift shadow on radionuclide transport are not further considered in TSPA. In particular, the reduction in flow over a region beneath the waste emplacement drift scaled by the size of the drift is not further considered. The fraction of the releases from a drift without seepage to the fractures is represented as an uncertain parameter, caused by uncertainty in rock fracture and matrix properties, invert properties, diffusion characteristics in the rock and invert, and hydrological conditions beneath the drift. Distributions that represent the effects of this uncertainty in the fraction released to fractures are developed for use in TSPA as a probabilistic parameter applied to the total radionuclide flux entering the rock from waste emplacement drifts.

FEP 2.2.07.08.0A, “Fracture flow in the UZ,” is included in TSPA through the results of this model report. Advective transport in fractures, based on fracture flow (parameter q_f in Table 6.4-5) as computed in the UZ flow model (BSC 2002 [160819], Section 1.10), is included as part of the model for radionuclide transport from the waste emplacement drift to the rock. This is included through the fracture-matrix partitioning model for the fraction of releases from a waste emplacement drift without seepage to the fractures of the underlying rock mass (see Tables 6.4-6 and 6.4-7). The fraction of the releases from a drift without seepage to the fractures is represented as an uncertain parameter, caused in part by uncertainty in fracture flow. Distributions that represent the effects of this uncertainty in the fraction released to fractures are developed for use in TSPA as a probabilistic parameter applied to the total radionuclide flux entering the rock from waste emplacement drifts.

FEP 1.2.02.01.0A, “Fractures” is included in TSPA through the results of this model report. This is included through the fracture-matrix partitioning model for the fraction of releases from a waste emplacement drift without seepage to the fractures of the underlying rock mass (see Tables 6.4-6 and 6.4-7). The fraction of the releases from a drift without seepage to the fractures is represented as an uncertain parameter, caused in part by uncertainty in fracture characteristics (parameters f, m, and ϕ_f in Table 6.4-5).. Distributions that represent the effects of this uncertainty in the fraction released to fractures are developed for use in TSPA as a probabilistic parameter applied to the total radionuclide flux entering the rock from waste emplacement drifts.

FEP 2.1.08.02.0A, “Enhanced Influx at the Repository,” is included in TSPA through the results of this model report. This is included through the fracture-matrix partitioning model for the fraction of releases from a waste emplacement drift without seepage to the fractures of the underlying rock mass (see Tables 6.4-6 and 6.4-7). Local flow focusing in fractures is included as part of the model for radionuclide transport from the waste emplacement drift to the rock (parameter F in Table 6.4-5). The fraction of the releases from a drift without seepage to the fractures is represented as an uncertain parameter, caused in part by uncertainty in flow focusing. Distributions that represent the effects of this uncertainty in the fraction released to fractures are developed for use in TSPA as a probabilistic parameter applied to the total radionuclide flux entering the rock from waste emplacement drifts.

FEP 2.1.08.01.0A, “Water Influx at the Repository,” is included in TSPA through the results of this model report. This is included through the fracture-matrix partitioning model for the fraction of releases from a waste emplacement drift without seepage to the fractures of the underlying rock mass (see Tables 6.4-6 and 6.4-7). Water influx through both the fractures and porous rock matrix is included as part of the model for radionuclide transport from the waste emplacement drift to the rock (parameters q_m and q_f in Table 6.4-5). The fraction of the releases from a drift without seepage to the fractures is represented as an uncertain parameter, caused in part by uncertainty in water flux in the fractures and matrix. Distributions that represent the effects of this uncertainty in the fraction released to fractures are developed for use in TSPA as a probabilistic parameter applied to the total radionuclide flux entering the rock from waste emplacement drifts.

FEP 2.2.07.15.0B, "Advection and Dispersion in the UZ," is included in TSPA through the results of this model report. This is included through the fracture-matrix partitioning model for the fraction of releases from a waste emplacement drift without seepage to the fractures of the underlying rock mass (see Tables 6.4-6 and 6.4-7). Advective transport in fractures and matrix, based on flow as computed in the UZ flow model (BSC 2002 [160819], Section 1.10), is included as part of the model for radionuclide transport from the waste emplacement drift to the rock (parameters q_m and q_f in Table 6.4-5). Diffusive transport in fractures is also included (parameter D_m in Table 2.4-5), but hydrodynamic dispersion is not further considered. The fraction of the releases from a drift without seepage to the fractures is represented as an uncertain parameter, caused in part by uncertainty in fracture and matrix flow. Distributions that represent the effects of this uncertainty in the fraction released to fractures are developed for use in TSPA as a probabilistic parameter applied to the total radionuclide flux entering the rock from waste emplacement drifts.

FEP 2.2.03.01.0A, "Stratigraphy" is included in TSPA through the results of this model report. This is included through the fracture-matrix partitioning model for the fraction of releases from a waste emplacement drift without seepage to the fractures of the underlying rock mass (see Tables 6.4-6 and 6.4-7). The fraction of the releases from a drift without seepage to the fractures is represented as an uncertain parameter, caused in part by uncertainty in rock characteristics based on stratigraphy (see Table 4.1-2h). Distributions that represent the effects of this uncertainty in the fraction released to fractures are developed for use in TSPA as a probabilistic parameter applied to the total radionuclide flux entering the rock from waste emplacement drifts.

FEP 2.2.07.02.0A, "Unsaturated Groundwater Flow in the Geosphere," is included in TSPA through the results of this model report. This is included through the fracture-matrix partitioning model for the fraction of releases from a waste emplacement drift without seepage to the fractures of the underlying rock mass (see Tables 6.4-6 and 6.4-7). Unsaturated flow in the geosphere, based on unsaturated flow as computed in the UZ flow model (BSC 2002 [160819], Section 1.10), is included as part of the model for radionuclide transport from the waste emplacement drift to the rock (parameters q_m and q_f in Table 6.4-5). The fraction of the releases from a drift without seepage to the fractures is represented as an uncertain parameter, caused in part by uncertainty in unsaturated flow. Distributions that represent the effects of this uncertainty in the fraction released to fractures are developed for use in TSPA as a probabilistic parameter applied to the total radionuclide flux entering the rock from waste emplacement drifts.

FEP 1.4.01.01.0A, "Climate Modification Increases Recharge," is included in TSPA through the results of this model report. This is included through the fracture-matrix partitioning model for the fraction of releases from a waste emplacement drift without seepage to the fractures of the underlying rock mass (see Tables 6.4-6 and 6.4-7). Unsaturated flow in the vicinity of the repository is treated for the case of the glacial-transition climate, based on flow fields as computed in the UZ flow model (BSC 2002 [160819], Section 1.10), is included as part of the model for radionuclide transport from the waste emplacement drift to the rock (parameters q_m and q_f in Table 6.4-5). The fraction of the releases from a drift without seepage to the fractures is represented as an uncertain parameter, caused in part by uncertainty in unsaturated flow under the glacial-transition climate. The effects of this uncertainty in the fraction released to fractures are developed for use in TSPA as independent parameter distributions for the total radionuclide flux entering the rock from waste emplacement drifts under lower-mean and upper infiltration conditions.

FEP 2.2.07.04.0A, "Focusing of Unsaturated Flow (fingers, weeps)," is included in TSPA through the results of this model report. This is included through the fracture-matrix partitioning model for the fraction of releases from a waste emplacement drift without seepage to the fractures of the underlying rock mass (see Tables 6.4-6 and 6.4-7). Local flow focusing in fractures is included as part of the model for radionuclide transport from the waste emplacement drift to the rock (parameter F in Table 6.4-5). The fraction of the releases from a drift without seepage to the fractures is represented as an uncertain parameter, caused in part by uncertainty in flow focusing. Distributions that represent the effects of this uncertainty in the fraction released to fractures are developed for use in TSPA as a probabilistic parameter applied to the total radionuclide flux entering the rock from waste emplacement drifts.

FEP 2.2.03.02.0A, "Rock Properties of Host Rock and Other Units" is included in TSPA through the results of this model report. This is included through the fracture-matrix partitioning model for the fraction of releases from a waste emplacement drift without seepage to the fractures of the underlying rock mass (see Tables 6.4-6 and 6.4-7). The fraction of the releases from a drift without seepage to the fractures is represented as an uncertain parameter, caused in part by uncertainty in rock host characteristics (parameters f, m, ϕ_f, ϕ_m, k_m in Table 6.4-5). Distributions that represent the effects of this uncertainty in the fraction released to fractures are developed for use in TSPA as a probabilistic parameter applied to the total radionuclide flux entering the rock from waste emplacement drifts.

FEP 2.2.08.05.0A, "Diffusion in the UZ," is included in TSPA through the results of this model report. This is included through the fracture-matrix partitioning model for the fraction of releases from a waste emplacement drift without seepage to the fractures of the underlying rock mass (see Tables 6.4-6 and 6.4-7). Diffusive transport in fractures is included as part of the model for radionuclide transport from the waste emplacement drift to the rock (parameter D_m in Table 6.4-5). The fraction of the releases from a drift without seepage to the fractures is represented as an uncertain parameter, caused in part by uncertainty in diffusion in fractures. Distributions that represent the effects of this uncertainty in the fraction released to fractures are developed for use in TSPA as a probabilistic parameter applied to the total radionuclide flux entering the rock from waste emplacement drifts.

6.3 DRIFT SHADOW ALTERNATIVE MODEL

6.3.1 Conceptual Model and Numerical Implementation

The dual-permeability conceptual model is used to simulate flow and transport in fractured rock. The dual-permeability model allows for flow and transport in a fracture continuum and a matrix continuum with advective and diffusive exchange between these continua. The conceptual model for fracture-matrix exchange also incorporates the active fracture model (Liu et al. 1998 [105729]), in which the fraction of flowing fractures is postulated to be a function of fracture saturation. This type of behavior is a result of flow instabilities caused by gravitational instability in combination with spatially heterogeneous properties, which leads to water flow in only a portion of the connected fracture system. One consequence of the active fracture model is a reduction in fracture-matrix interaction, needed to calibrate the dual-permeability flow model to observed matrix water saturations and potentials at Yucca Mountain (Bandurraga and Bodvarsson 1999 [103949]). The conceptual flow and transport models are implemented numerically using an integral finite-difference method. Flow calculations are carried out to steady-flow conditions using the iTOUGH2 V4.0 EOS9 module (Pruess et al. 1999 [160778]), which simulates unsaturated flow according to Richards' equation (Richards 1931 [104252]). The flow model calibration has been performed using the TOUGH family of software (BSC 2001 [161316]), thus the compatibility of the parameters between the parameter development and their implementation in this report lead to the selection of the iTOUGH2 V4.0 software over other possible software and computational methods. Transport calculations are then performed for steady-state flow conditions using the EOS9nT module of TOUGH2 (TOUGH2 V1.11MEOS9NTV1.0 in Table 3-1) (Moridis et al. 1999 [123093]). The transport module first solves Richards equation to establish the steady-state flow field. The solute concentrations are sufficiently small such that they have no dynamic effects on the flow (e.g., the density or viscosity). This allows transport equations to be decoupled from flow equations. Transport equations are solved using a Laplace transform method (Moridis et al. 1999 [123093], Section 3.2) applicable to steady-state flow conditions. Compatibility between the flow calculations with iTOUGH2 V4.0 and the transport calculations with TOUGH2 V.11MEOS9NTV1.0 lead to the selection of the TOUGH2 V4.0 software over other possible software and computational methods. Other direct finite difference approaches for treating the time dependence of the transport problem were not used because the Laplace transform method provides a semi-analytical treatment of the time derivatives that eliminates the need for time discretization or any restrictions on time-step size.

An important factor in the drift shadow problem, as discussed in Section 6.1, is the diversion of percolation flux around the drift such that water does not enter the drift. A considerable amount of theoretical and experimental work has been conducted to evaluate seepage for the waste emplacement drifts at Yucca Mountain (Wang and Bodvarsson 2003 [163215]; Finsterle et al. 2003 [163214]; Li and Tsang 2003 [163714]; CRWMS M&O 2001 [154291]). This work indicates that the percolation flux encountering a drift will be completely diverted if the percolation flux is less than a value known as the seepage threshold. The seepage threshold depends on the capillary properties of the fracture system, the size and shape of the drift, and the heterogeneity in fracture properties.

The drift shadow model is used in this report as an alternative model to the fracture-matrix partitioning model discussed in Section 6.4. Results of the drift shadow model are used for qualitative comparison with the fracture-matrix partitioning model as presented in Section 7. The model calculations were carried out using property sets (discussed in Section 6.3.2.3) available at the time the original calculations were performed (Houseworth 2003 [163233]). Additional documentation of the work presented in Section 6.3 is provided in Scientific Notebook by Houseworth (2003 [163233], pp. 115–181; 193–194).

6.3.2 Numerical Grid, Boundary Conditions, and Parameter Development

6.3.2.1 Numerical Grid

The calculations presented here are for a two-dimensional, homogeneous, dual-permeability model of an emplacement drift. Figure 6.3-1 shows the grid employed in the calculations. The area around the 5 m diameter drift uses a refined grid of 0.2 m × 0.2 m. Farther from the drift, the grid coarsens to approximately 2 m × 2 m. The drift is represented by two grid blocks that provide horizontal and vertical connections to the bordering rock grids after removing the grid blocks originally generated in the drift region. The depth to the bottom of the drift shadow model was chosen roughly on the character of the flow fields. At 45 meters below the drift, the flow field is found to have nearly returned to the unperturbed state.

The 5 m drift diameter used in this calculation differs from the 5.5 m drift diameter in the current repository design. This smaller diameter may be used because the effects of a smaller drift diameter, given no drift seepage, will result in a conservative estimate of the effects of a drift on transport beneath the drift.

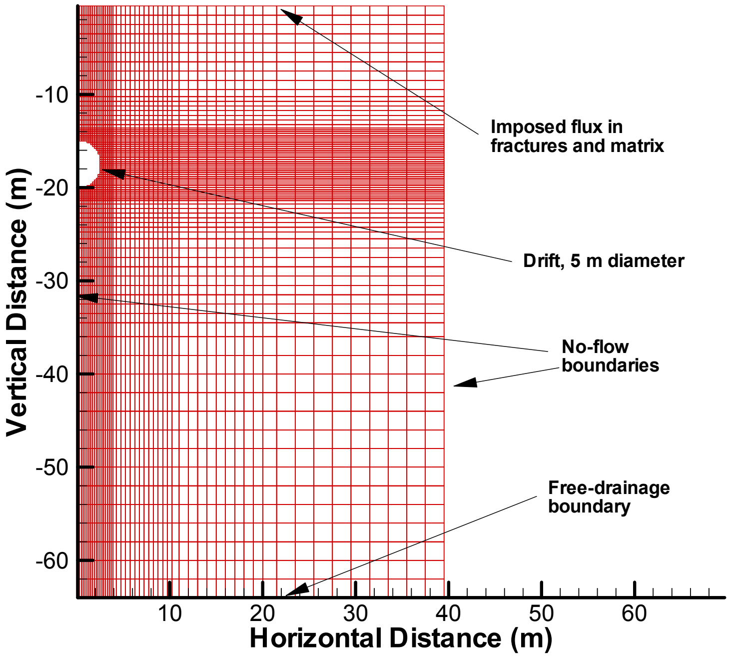

Output-DTN: LB0307DSRADTRN.001

Figure 6.3-1. Grid and Boundary Conditions

6.3.2.2 Boundary Conditions

As shown in Figure 6.3-1, the model uses a no-flow symmetry condition along the vertical centerline of the drift. Similarly, the far lateral boundary is a no-flow boundary due to the symmetry condition reflecting the periodic, 81 m drift spacing. The bottom boundary condition is free gravity drainage (no capillary pressure gradient). The center of the drift is 17.5 m below the top of the model domain, and the drift has a radius of 2.5 m. Hydrological properties are assigned to the drift such that the capillary pressure is zero for all values of water saturation.

Flow is introduced at the top boundary at a prescribed flow rate. For the dual-continuum model calculations, flow rates are prescribed separately for the fracture and matrix continua. This is necessary to develop a flow field compatible with results from the mountain-scale unsaturated zone flow model. The flow rates in Table 6.3-1 were chosen to cover a range of total flows while keeping matrix saturations within the range of observed values, approximately 0.85 to 0.95 (BSC 2001 [158726], Table 6-22). For higher total percolation rates expected for future climates, BSC (2001 [158726], Tables 6-23 and 6-24) shows that the percentage of the total percolation moving in the matrix is lower, however the absolute matrix flux increases as expected under wetter climate conditions. Therefore, the percentage of total flux in the matrix is adjusted to allow for more flow in the matrix than found at the lower percolation rates, short of saturating the matrix. Table 6.3-1 gives the values of flow rates investigated here. Note the cited fracture flow rate and matrix flow rate in Table 6.3-1 and elsewhere in this report refer to the flow rate maintained at the upper boundary of the model. Because of fracture-matrix interaction and flow diversion, the local flow rates at other locations in the model will vary.

Table 6.3-1. Flow Rates Investigated

Total Flow Rate (mm/yr)	Fracture Flow Rate (mm/yr)	Matrix Flow Rate (mm/yr)
10	9.85	0.15
10	9.15	0.85
100	99.55	0.45
100	98.4	1.6
300	299.0	1.0

Output-DTN: LB0307DSRADTRN.001

6.3.2.3 Parameters

Capillary pressure and relative permeability functions of saturation for the fracture and matrix continua are based on the van Genuchten formulation (van Genuchten 1980 [100610]). The property set for the tsw35 hydrogeologic unit (BSC 2001 [161316]), which corresponds to the lower lithophysal unit of the Topopah Spring tuff, is used in the flow calculations. This property set is used because about 80% of the waste emplacement areas in the current repository design reside in this unit (see Table 4.1-2h). The hydrological data are summarized in Tables 6.3-2a and 6.3-2b for the Topopah Spring Tuff Lower Lithophysal unit, one of the repository host rock units for waste emplacement drifts. Matrix and mountain-scale fracture properties are given in DTN: LB997141233129.001 [104055].

The calibrated property set for dual-permeability flow and transport calculations is based on permeability values obtained by calibrating a mountain-scale model against saturation, water potential, and pneumatic pressure data, using a large-scale model of Yucca Mountain (Bandurraga and Bodvarsson 1999 [103949]; Ahlers et al. 1999 [109715]). Permeability measured at the drift scale has been found to be roughly one order of magnitude smaller than that inferred from measurements at the mountain scale (BSC 2001 [161316], Section 6.2). This difference results from the difference in sampling volume between mountain-scale and drift-scale measurements. Mountain-scale measurements capture the sparse, but highly permeable, fracture pathways not present in the typical smaller sampling volume. Because of the smaller length scales addressed in this model (tens of meters rather than hundreds of meters), the drift-scale fracture permeability is believed to be more appropriate. Drift-scale fracture permeability, shown in Table 6.3-2c, was derived in the Calibrated Properties Model (BSC 2001 [161316], DTN: LB990861233129.001 [110226]). All other properties at the drift scale were kept the same as the site-scale properties, as recommended in BSC (2001 [161316], Section 6.2). However, for fracture-matrix interaction to be approximately the same for the mountain-scale and drift-scale properties, the drift-scale active fracture parameter, γ, must be increased from 0.41 to 0.81. An evaluation of the mountain-scale versus drift-scale properties with respect to the active fracture parameter is discussed further in Section 6.3.3.1.

Table 6.3-2a. Hydrological Properties for the tsw35—Matrix Properties (Drift-Scale and Mountain-Scale)

Permeability	**Porosity**	**van Genuchten α**	**van Genuchten m (λ)**	**Residual saturation**	**Satiated saturation**	**Rock grain density**
k_m (m^2)	ϕ_m (-)	α_m (1/Pa)	m_m (-)	S_{lrm} (-)	S_{lsm} (-)	ρ_g (kg/m^3)
3.04E-17	0.131	6.44E-6	0.236	0.12	1.00	2540

DTN: LB997141233129.001 [104055]; BSC 2001 [161316]

Table 6.3-2b. Hydrological Properties for the tsw35—Fracture Properties (Mountain-Scale Permeability)

Mountain-scale permeability	**Porosity**	**van Genuchten α**	**van Genuchten m (α)**	**Residual saturation**	**Satiated saturation**	**Active fracture parameter**	**Frequency**	**Fracture to matrix connection area**
k_f (m^2)	ϕ_f (-)	α_f (1/Pa)	m_f (-)	S_{lrf} (-)	S_{lsf} (-)	γ (-)	f (1/m)	A (m^2/m^3)
4.51E-11	1.5E-2	7.39E-4	0.611	0.01	1.00	0.41	3.16	9.68

DTN: LB997141233129.001 [104055]; BSC 2001 [161316]; BSC 2001 [159725]

Table 6.3-2c. Hydrological Properties for the tsw35—Drift-Scale Fracture Permeability

Drift-Scale Permeability
k_f (m^2)
1.29E-12

DTN: LB990861233129.001 [110226];
BSC 2001 [161316]

Transport calculations require the specification of matrix diffusion and sorption parameters. For Total System Performance Assessment (TSPA), sorption and diffusion parameters have been characterized using a statistical approach to account for the variability found in measured values (BSC 2001 [160828]). The parameters used in the calculations reported here have been chosen to be the expected (mean) values used in the site recommendation base case (CRWMS M&O 2000 [153246], Section 3.7.3). The drift-shadow transport calculations presented here are for technetium, neptunium, and plutonium. These radionuclides were chosen because of their significance in dose calculations for TSPA (CRWMS M&O 2000 [153246], Figure 4.1-19a). Under the oxidizing conditions expected in the UZ, the aqueous form of technetium is the negatively charged pertechnetate ion (TcO_4^-), which is nonsorbing. Under the relevant geochemical conditions, aqueous neptunium has been found to be weakly sorbing to the volcanic rock, and aqueous plutonium has been found to be strongly sorbing (BSC 2001 [160828], Section 6.4.4.1.4). Therefore, the aqueous radionuclides investigated here span the range of expected sorption behavior. Matrix sorption coefficients are given in DTN: LA0003AM831341.001 [148751]. Implementation of sorption coefficients in a transport model also requires specification of the rock bulk density. Rock bulk density in the tsw35 is given in DTN: LB997141233129.001 [104055]. Note that sorption is only accounted for in the matrix because values for sorption in the fractures have not been measured and are difficult to estimate. Also, sensitivity studies indicate that sorption in the fractures will only have a significant effect if the sorption coefficients are very large. This is a result of transport in the fractures which is, in general, orders of magnitude faster than matrix transport. Consequently, sorption in the fractures will only affect travel time if it is strong enough to reduce the transport velocities by orders of magnitude.

Values for the effective diffusion coefficients in the matrix are taken from DTN: LA0003JC831362.001 [149557]. The effective diffusion coefficient for technetium in tuff matrix is found to be smaller than for neptunium or plutonium. This is postulated to be a result of the large size and negative charge of the pertechnetate ion, leading to exclusion from a portion of the matrix pore space and a lower tortuosity. Parameters used for transport are given in Table 6.3-3.

Table 6.3-3. Transport Properties for the tsw35

	Matrix Diffusion Coefficient (m^2/s)	**Matrix Sorption Coefficient (m^3/kg)**
Technetium	3.2×10^{-11}	0
Neptunium	1.6×10^{-10}	3.0×10^{-4}
Plutonium	1.6×10^{-10}	3.75×10^{-2}

DTNs: LA0003AM831341.001 [148751] and
LA0003JC831362.001 [149557]

For diffusion in the fractures, a representative average diffusion coefficient in water, 1.6×10^{-9} m^2/s, is adjusted by the tortuosity, where the fracture tortuosity is approximated by the matrix tortuosity (see Section 4.1.5 and 6.4.5). The free-water diffusion coefficient is based on the average of the values given in Table 4.1-2g. No sorption is accounted for in the fractures owing to the limited information and likely limited effects on transport.

Hydrodynamic dispersion is not expected to play a significant role in the transport of radionuclides in the fractures, because of the predominant role of differential advection resulting from fracture-matrix interaction as the main dispersive mechanism. The dispersive effects of fracture-matrix interaction are explicitly modeled, so they do not need to be represented in the form of a dispersion coefficient. Low velocities and short correlation lengths in the matrix make hydrodynamic dispersion negligible compared to molecular diffusion, which is included. With this in mind, hydrodynamic dispersion is not included in the model.

The transport of aqueous radionuclides is calculated without including the effects of radioactive decay. For technetium, neptunium, and certain isotopes of plutonium, the half-lives are long relative to the transport times in the drift-shadow model.

Parameters used here for the drift-shadow model are from previous work for the Site Recommendation. Parameters for the License Application have changed, however, the general character of the rock remains the same, i.e., the fractures and matrix in the repository host rock are distinct continua with large differences in permeability, porosity, and capillary pressure characteristics. Differences in parameters between Site Recommendation and License Application do not impact the qualitative behavior of flow and transport in the drift shadow. In particular, transport of radionuclides released in the drift shadow will be orders of magnitude longer than transport of radionuclides released to unperturbed fracture flow for either parameter set. Given that the drift shadow model presented here is only used for qualitative comparison with the fracture-matrix partitioning model discussed in Section 6.4, the older parameter set is adequate for the intended use of this alternative model.

6.3.3 Results of Analysis

6.3.3.1 Flow Field Results and Parameter Sets

Unsaturated flow calculations were performed for a dual-continuum model using the mountain-scale and drift-scale property sets shown in Table 6.3-2a–c and the flow rates shown in Table 6.3-1. The van Genuchten relative permeability relationship is used for these TOUGH2 calculations. The current repository design locates about 80% of the emplacement drifts in the tsw35 hydrogeologic unit (see Attachment VIII). Results of flow calculations using the mountain-scale property set are shown in Figure 6.3-2.

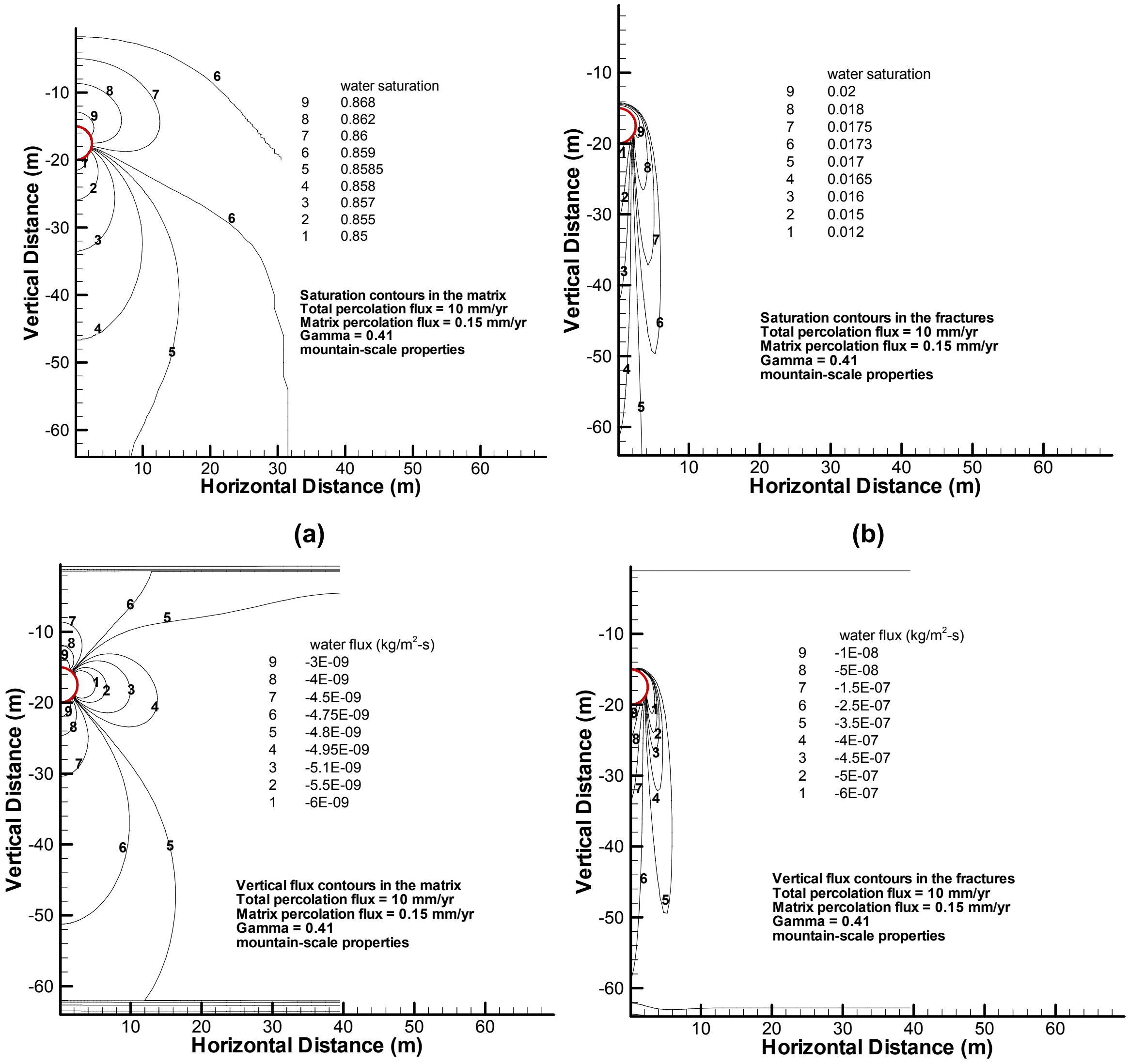

(a) (b)

(c) (d)

Output-DTN: LB0307DSRADTRN.002

Figure 6.3-2. Fracture and Matrix Vertical Flux and Saturation Contours Using Mountain-Scale Property Set: (a) Matrix Saturation; (b) Fracture Saturation; (c) Matrix Flux; (d) Fracture Flux

The drift shadow is seen to be long and narrow for gravity-dominated fracture flow (Figures 6.3-2b and 6.3-2d), resulting in a substantial decrease in fracture flow for several drift diameters below the drift. For example, the flow rate within about three drift diameters, on the drift centerline below the emplacement drift, is less than 50 percent of the undisturbed flow rate. The matrix, on the other hand, has a much shorter drift shadow (Figures 6.3-2a and 6.3-2c), with the flow rate in the matrix less than 50 percent of the undisturbed flow rate within approximately 0.2 drift diameters below the bottom of the drift (Figure 6.3-2c).

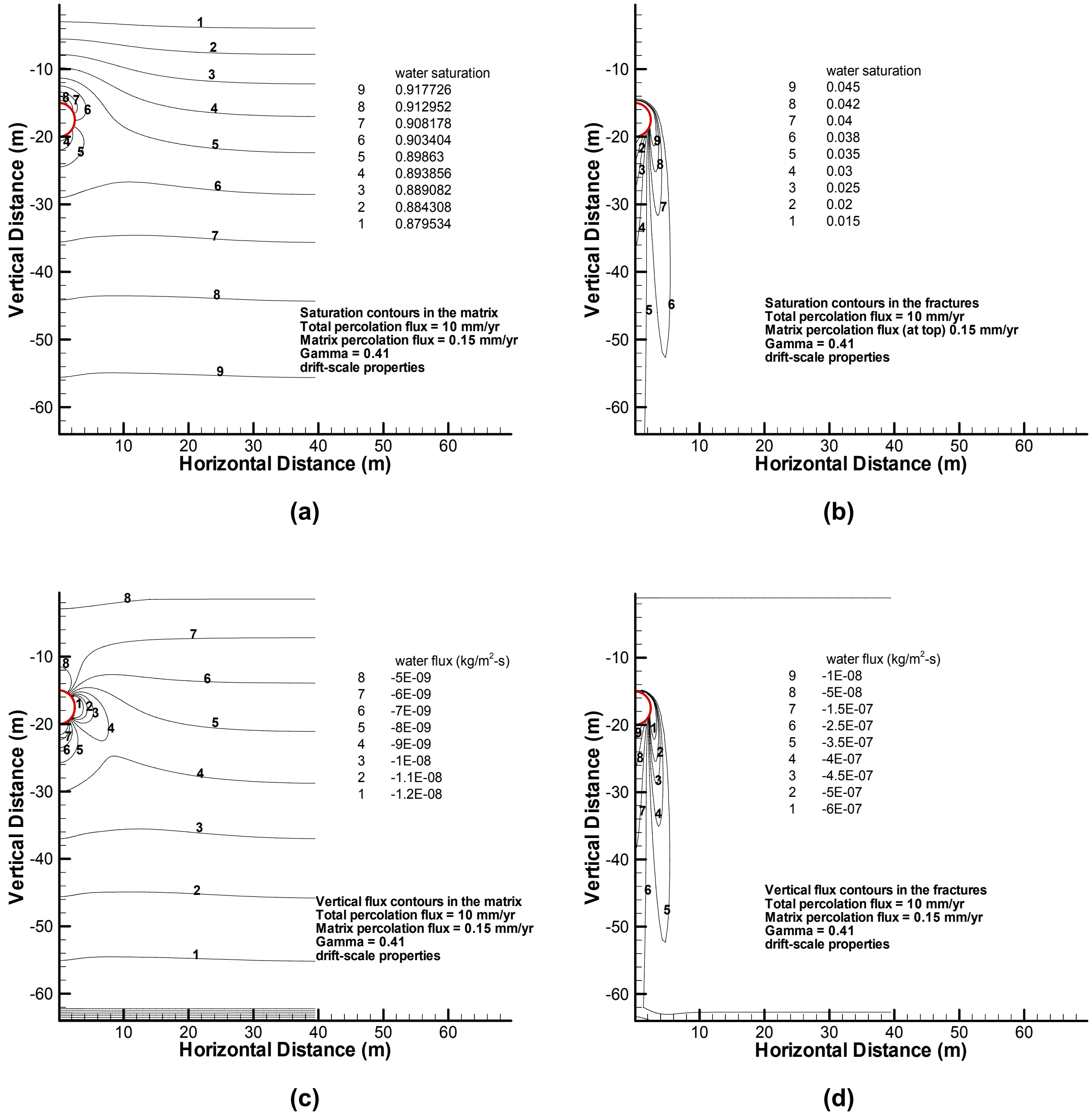

(a) (b)

(c) (d)

Output-DTN: LB0307DSRADTRN.002

Figure 6.3-3. Fracture and Matrix Vertical Flux and Saturation Contours using Drift-Scale Property Set and $\gamma = 0.41$ (a) Matrix Saturation; (b) Fracture Saturation; (c) Matrix Flux; (d); Fracture Flux

The original drift-scale property set is the same as the modified drift-scale property set with the exception of the active fracture parameter, γ. In the original drift-scale property set, γ is assigned a value of 0.41, which is the same as for the mountain-scale property set. The vertical flow and water saturation contours for the original drift-scale property set are shown in Figure 6.3-3. However, as shown by comparing Figures 6.3-2 and 6.3-3, the resulting flow and saturation contours are substantially altered for the drift-scale property set. In particular, global vertical gradients of matrix water saturation and flow appearing in Figures 6.3-3a and 6.3-3c contrasts with the corresponding plots in Figures 6.3-2a and 6.3-2c. The water saturation contours in Figure 6.3-3 indicate a much greater degree of fracture-matrix interaction than that found for the mountain-scale property set. This can be seen by the increase of matrix water saturation with depth. Given that the matrix properties are unchanged, the only mechanism that would explain this pattern is an increase in water flux from the fractures to the matrix. The flow model calibration against measured values of matrix water potential and saturation was conducted for the mountain-scale property set. Therefore, the original drift-scale property does not appear to be consistent with the field data.

The differences in fracture-matrix interaction found for mountain-scale and drift-scale parameters may be understood from the van Genuchten relationships as modified for the active fracture model. As proposed in Liu et al. (1998 [105729], Equation 1), the fraction of active fractures, f_a, is defined by

$$f_a = S_e^{\gamma} \qquad \text{(Eq. 1)}$$

where γ is an empirical parameter of the active fracture model. S_e is the effective fracture saturation defined by

$$S_e = \frac{S_f - S_r}{1 - S_r} \qquad \text{(Eq. 2)}$$

where S_f is the fracture water saturation and S_r is the residual fracture water saturation. The active fracture parameter, γ, is constrained to be less than or equal to one such that the saturation of the active fractures is less than or equal to one. Liu et al. (1998 [105729], Equations 5 and 9) derive the following relationships for fracture capillary pressure, P_c, and relative permeability, k_r, using the van Genuchten formulation (van Genuchten 1980 [100610]) in combination with the active fracture concept:

$$P_c(S_e) = \frac{1}{\alpha}\left[S_e^{(\gamma-1)/m} - 1\right]^{1-m} \qquad \text{(Eq. 3)}$$

$$k_r(S_e) = S_e^{(1+\gamma)/2}\left[1 - \left\{1 - S_e^{(1-\gamma)/m}\right\}^{m}\right]^{2} \qquad \text{(Eq. 4)}$$

Figures 6.3-2 and 6.3-3 show that fracture water saturation is expected to be low, in the range of 0.01 to 0.05. The effective water saturation range is even lower in magnitude. Therefore, it is appropriate to consider an expansion of the capillary pressure and relative permeability functions for low water saturation. The first-order expansions of the capillary pressure and relative permeability functions for low water saturation (such that $S^{(1-\gamma)/m}$ is small) are

$$P_c(S_e) \approx \frac{1}{\alpha} S_e^{\left(\frac{1-m}{m}\right)(\gamma-1)} \qquad \text{(Eq. 5)}$$

$$k_r(S_e) \approx m^2 S_e^{\frac{4(1-\gamma)+m(1+\gamma)}{2m}} \qquad \text{(Eq. 6)}$$

Flux in the fractures, q_f, can be approximated as free gravity drainage, i.e., the flux in the fractures equals the effective hydraulic conductivity. The effective hydraulic conductivity of the fractures is equal to the product of the saturated hydraulic conductivity, K_s, times the relative permeability. Using this approximation, the fracture saturation is given by

$$S_e \approx \left(\frac{q_f}{K_s m^2} \right)^{\frac{2m}{4(1-\gamma)+m(1+\gamma)}} \tag{Eq. 7}$$

Substituting this into Equation 5 gives

$$P_c \approx \frac{1}{\alpha} \left(\frac{K_s m^2}{q_f} \right)^{\frac{2(1-\gamma)(1-m)}{4(1-\gamma)+m(1+\gamma)}} \tag{Eq. 8}$$

Note that the exponent of K_s is always positive. This relationship shows that for a fixed q_f, as K_s decreases, P_c also decreases. This leads to a larger pressure difference between the fractures and matrix and, therefore, greater fracture-to-matrix imbibition flow as K_s decreases. This is consistent with the changes in fracture-matrix interaction observed in Figures 6.3-2 and 6.3-3 using the mountain-scale and drift-scale fracture permeabilities.

The noted increase in fracture-matrix interaction suggests that the fracture-matrix interaction parameter, γ, needs to be modified for use with the lower drift-scale fracture permeability. Measurements to establish γ at the drift scale are not available. However, one of the key calibration metrics used to establish the value of γ for the mountain-scale flow model is matrix saturation (BSC 2001 [161316], Section 6). Figure 6.3-4 shows the matrix saturation contours using the drift-scale property set over a range of values for γ. Increasing the value of γ reduces fracture-matrix interaction. The matrix water saturation contours for the drift-scale properties with γ set to 0.81 (Figure 6.3-4d) appear to be consistent with saturation contours for the mountain-scale property set (Figure 6.3-4a). Therefore, the modified drift-scale parameter set is believed to be more consistent with field observations. Note that the current calibrated properties values (BSC 2003 [160240], Section 6) were developed using the lower drift-scale fracture permeabilities, and the values of gamma have increased from the previous values for the repository host rock units (BSC 2001 [161316], Section 6). This is true even though matrix permeabilities are reduced in the current property set, which if everything else was held constant, would lead to a lower value of gamma.

Calibration of the UZ Flow Model (Bandurraga and Bodvarsson 1999 [103949], Section 4) and comparisons of geochemical composition of perched water (water from the fracture continuum) and matrix pore water (BSC 2002 [160247], Section 7.5) suggest that the fracture and matrix continua are only weakly connected. The UZ Flow Model requires reduced fracture-matrix interaction areas for calibration against field measurements of water saturation and potential (Liu et al. 1998 [105729], Section 1). Perched water and matrix pore waters are found to be significantly different in composition (BSC 2002 [160247], Section 7.5), indicating a lack of geochemical equilibrium between the fracture and matrix continua. Although the hydrological and geochemical evidence indicates that the fracture and matrix continua are only weakly coupled, quantitative estimates of parameters reflecting this aspect of the fractured rock system are uncertain. Furthermore, this aspect of the system has a large impact on radionuclide transport in the drift shadow and beyond.

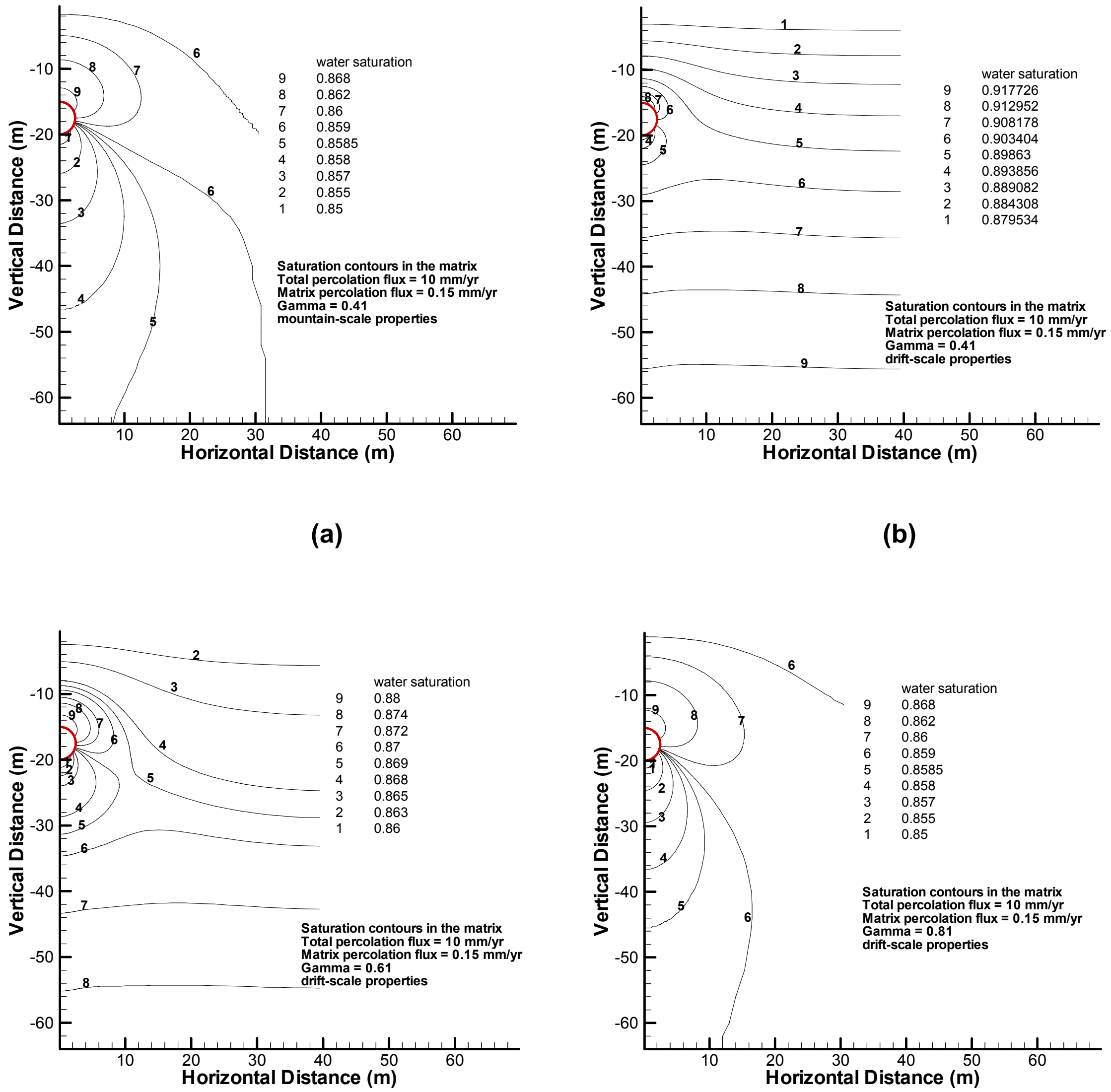

(a) (b)

(c) (d)

Output-DTN: LB0307DSRADTRN.002

Figure 6.3-4. Matrix Saturation Contours Using Different Property Sets: (a) Mountain-Scale; (b) Drift-Scale, γ = 0.41; (c) Drift-Scale, γ = 0.61; (d); Drift-Scale, γ = 0.81

Flow calculations for percolation rates of 10 mm/yr and 100 mm/yr have been performed and are used in the transport calculations discussed below. Flow behavior for higher total percolation rates also have been investigated. Complete diversion of seepage is found for total percolation rates up to 300 mm/yr. Between the 300 and 350 mm/yr total percolation rate, gravitational forces overcome the seepage threshold and water enters the drift.

6.3.3.2 Transport Results

Transport calculations were run for a dual-permeability flow and transport system using the EOS9nT module of TOUGH2 (Moridis et al. 1999 [123093]). In all cases, 1 kg of radionuclide is available for release from the waste emplacement drift. Connections are made from two cells inside the drift, where the radionuclides originate, to the fractures and rock matrix cells adjacent to the bottom of the drift and within 1 meter of the drift centerline. Radionuclides enter the fracture and matrix cells from the drift cells at rates determined by diffusive transport processes, because water does not flow through the drift cells.

Breakthrough curves for transport to the bottom of the model (45 m below the bottom of the emplacement drift, as seen in Figure 6.3-1) are shown for technetium, neptunium, and plutonium in Figures 6.3-5a through 6.3-5d. These figures compare the transport results for total percolation rates of 10 mm/yr and 100 mm/yr for two matrix percolation cases each (see Table 6.3-1).

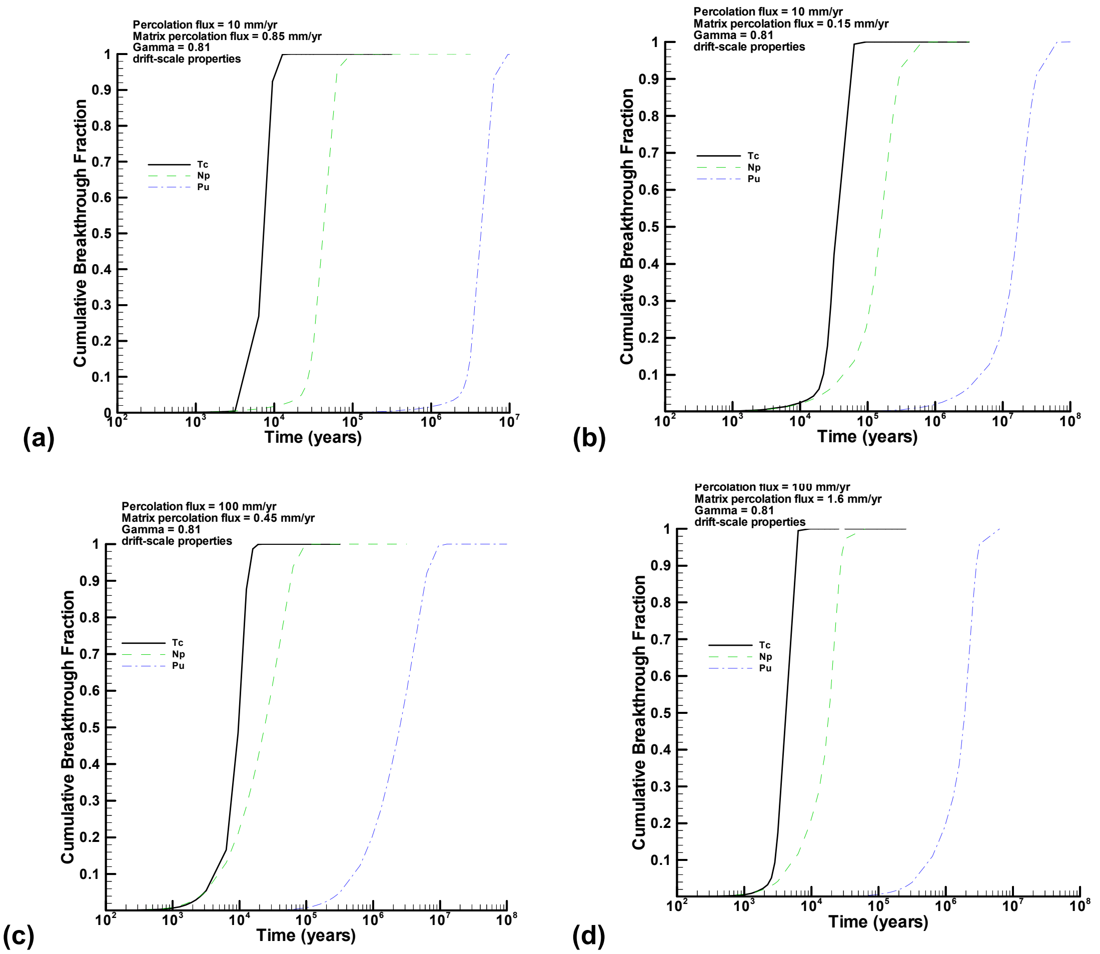

Output-DTN: LB0307DSRADTRN.002

Figure 6.3-5. Breakthrough Curves for Drift Shadow Transport: (a) Total Percolation Flux = 10 mm/yr, Matrix Percolation Flux = 0.15 mm/yr; (b) Total Percolation Flux = 10 mm/yr, Matrix Percolation Flux = 0.85 mm/yr; (c) Total Percolation Flux = 100 mm/yr, Matrix Percolation Flux = 0.45 mm/yr; (d) Total Percolation Flux = 100 mm/yr, Matrix Percolation Flux = 1.6 mm/yr

A comparison of the 50% breakthrough with approximate matrix advection-transport times can be made (Table 6.3-4). Approximate advection-transport times are computed from the flux introduced to the matrix divided by the approximate water content and retardation factor. Advective transport times are approximate, because flow rates vary as a result of the drift shadow effect and in response to fracture-matrix exchange. Nevertheless, flow patterns discussed earlier indicate that the variations in flux and water saturation in the matrix are minor. Therefore, the approximate advective transport time is considered reasonable. The retardation factor is given by the relationship (derived from Freeze and Cherry 1979 [101173], p. 404)

$$R = 1 + \frac{\rho_m (1-\phi) K_d}{\phi S_w} \qquad \text{(Eq. 9)}$$

where ρ_m is the grain density (2,540 kg/m^3), ϕ is the porosity (0.131), K_d is the sorption coefficient (see Table 6.3-3), and S_w is the water saturation (see Table 6.3-4).

Table 6.3-4. Advective Transport Times and Computed Transport Times

Radionuclide	Total Percolation Flux (mm/yr)	Matrix Percolation Flux (mm/yr)	Water Saturation	Retardation Factor	Advective Travel Time in Matrix (years)	50% Breakthrough Time (years) (Output-DTN: LB0307DSRADTRN.002)
Technetium	10	0.15	0.86	1	3.4E+04	3.6E+04
Neptunium	10	0.15	0.86	6.9	2.3E+05	1.6E+05
Plutonium	10	0.15	0.86	740	2.5E+07	1.7E+07
Technetium	10	0.85	0.96	1	6.7E+03	7.5E+03
Neptunium	10	0.85	0.96	6.3	4.2E+04	4.4E+04
Plutonium	10	0.85	0.96	660	4.4E+06	4.6E+06
Technetium	100	0.45	0.94	1	1.2E+04	9.6E+03
Neptunium	100	0.45	0.94	6.4	7.9E+04	2.4E+04
Plutonium	100	0.45	0.94	670	8.3E+06	2.5E+06
Technetium	100	1.60	0.98	1	3.6E+03	4.4E+03
Neptunium	100	1.60	0.98	6.2	2.2E+04	1.8E+04
Plutonium	100	1.60	0.98	650	2.3E+06	1.9E+06

Output DTN: LB0307DSRADTRN.002

In general, the advective travel time in the matrix is close to the value of the 50% breakthrough time for all percolation fluxes, suggesting that transport in the drift shadow is dominated by matrix advection. Because of the diversion of flow around the drift, radionuclides move from the drift to the rock by diffusion. Diffusive releases preferentially enter the matrix rather than the fractures because the water content (porosity times water saturation) in the matrix is roughly 1,000 times larger than in the fractures immediately beneath the drift. In some cases, the 50% breakthrough time is longer than the advective travel time. This happens for some of the technetium breakthrough curves (such as the case for 10 mm/yr total flux with 0.85 mm/yr flux in the matrix) because the computed advective travel times in Table 6.3-4 ignore the hydrodynamic effects of the drift shadow. For neptunium and plutonium, some of the 50% breakthrough times are shorter than the advective travel times because of diffusive exchange between the matrix and the fractures. This occurs for the sorbing radionuclides, which have longer advective travel times and have more time for diffusive release from the matrix to the fractures. In the fractures, travel times are relatively short.

6.3.3.4 Transport Sensitivity Analysis

Figure 6.3-6 compares breakthrough curves for technetium under different total percolation flux and matrix flux cases. The breakthrough curve sensitivity to total percolation flux is found to be low, with much greater sensitivity to the rate of percolation flux in the matrix. This result further substantiates the hypothesis that transport in the drift shadow is predominantly in the matrix.

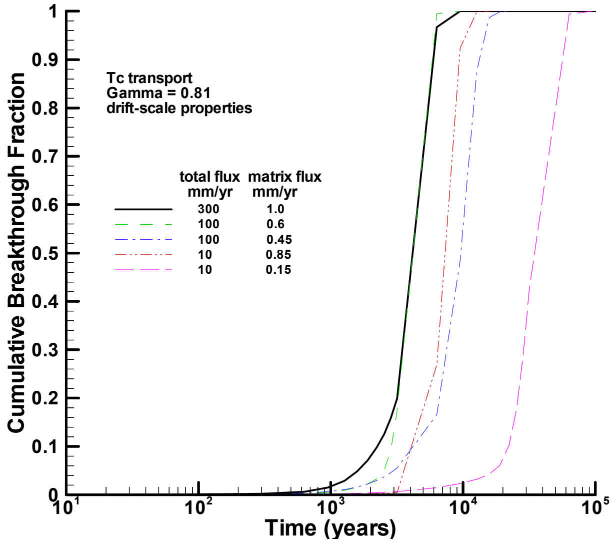

Output-DTN: LB0307DSRADTRN.002

Figure 6.3-6. Technetium Transport as a Function of Total Percolation Flux and Matrix Percolation Flux

Figures 6.3-7a and 6.3-7b compare Tc transport in the drift shadow to transport in the unperturbed flow field for 10 mm/yr and 100 mm/yr total percolation fluxes. The releases in the unperturbed flow field were made in cells near the right-hand boundary of the model, at the same vertical coordinate as the bottom of the drift. Two types of releases were investigated; releases that are initiated in the fractures and releases that are initiated in the matrix. The drift-shadow breakthrough curve is shown for comparison. These results clearly demonstrate that releases to fractures transport at much greater velocities. These results also indicate that the drift-shadow effect is approximately equivalent to initiation of transport in the matrix. The dynamics of the drift shadow flow field have only a second-order effect on the breakthrough curves.

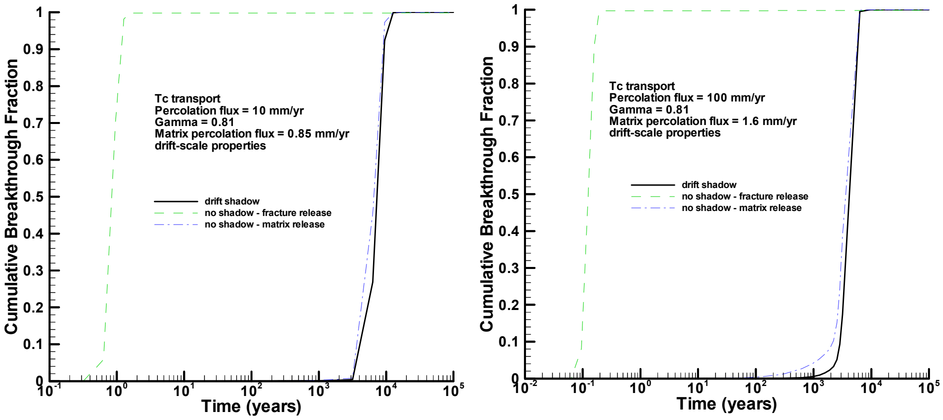

(a) (b)

Output-DTN: LB0307DSRADTRN.002

Figure 6.3-7. Sensitivity Calculations Comparing Drift Shadow Transport with Transport in Unperturbed Flow Field: (a) Total Percolation Flux = 10 mm/yr, Matrix Percolation Flux = 0.85 mm/yr; (b) Total Percolation Flux = 100 mm/yr, Matrix Percolation Flux = 1.6 mm/yr

Figure 6.3-8 shows a sensitivity calculation for the effects of the active fracture parameter, γ, on breakthrough curves. This figure clearly shows that fracture-matrix interaction is a key factor in the rate of transport in the drift shadow. As γ is reduced, the amount of fracture-matrix interaction increases, resulting in greater matrix-to-fracture diffusive exchange. Increased interaction results in more transport in the fractures and, therefore, more rapid transport through the drift shadow.

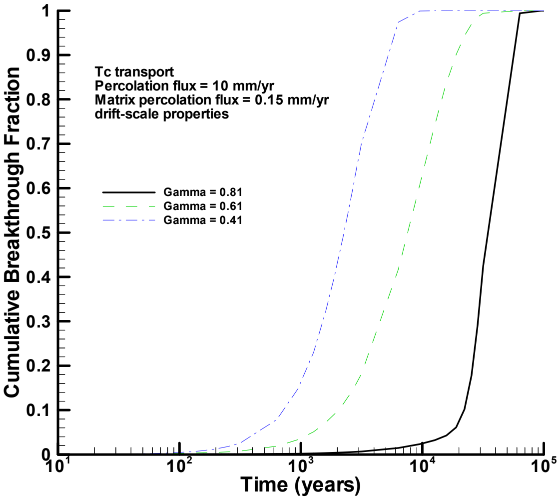

Output-DTN: LB0307DSRADTRN.002

Figure 6.3-8. Sensitivity Calculation for Technetium Transport Using Different Values of γ

6.4 FRACTURE-MATRIX PARTITIONING MODEL

Results of sensitivity studies presented in Section 6.3 suggest that the main effect of the drift shadow is on the initiation of transport in the matrix. The fracture-matrix partitioning model presented here focuses on the partitioning of releases from drifts between the rock fractures and matrix. The fracture-matrix partitioning model sets unperturbed fracture flow directly below the base of waste emplacement drifts. This approximation in neglecting the drift shadow effect on flow is based on the idea that the drift shadow may not be as spatially extensive as presented in Section 6.3, due to heterogeneity and anisotropy in fracture characteristics, as well as discrete fracture effects. As in Section 6.3, the fracture-matrix partitioning model is limited to drifts without seepage or other sources of water that may result in advective-dominated transport in the drift invert, i.e., transport through the drift invert to the rock is dominated by diffusion. For the initial release of radionuclides, the transient concentration front passing from the invert into the rock will initially be dominated by diffusion. But as the concentration approaches a steady condition, transport in the rock will be dominated by advection. This is due to the reduction in the radionuclide concentration gradient at the drift wall over time for a steady radionuclide source concentration. The radionuclide concentration gradient at the drift wall relaxes for greater offset between the drift wall and the flowing fracture. The water content of the matrix is always dominant over the water content of the fractures, so diffusive exchange between the invert and the rock will predominantly enter the matrix. However, for the steady transport condition following the initial transient period, the final distribution of releases becomes a function of the water content and flux in the fractures and matrix. Because the unperturbed flux (no effects of the drift on the flow field) in the repository host rock is predominantly in the fractures, the distribution of releases from the invert between the fractures and matrix is controlled by the relative influence of the flux and the water content of the fractures and matrix.

Note that calculations reported in BSC (2002 [161619], Sections 6.6–6.8) indicate that even without drift seepage, water will enter the drift laterally from the rock into the crushed tuff invert as a result of capillary forces. The predicted flow pattern shows water entering laterally from the rock into the invert along the sides and then flowing out of the invert at the bottom of the drift. This flow is restricted to the micropores of the crushed tuff and the rock matrix (BSC 2002 [161619], Section 6.11). The crushed tuff micropores are assigned the same capillary and permeability characteristics as the rock matrix, so from the perspective of flow, the rock matrix and micropores of the crushed tuff invert constitute a uniform and continuous flow domain. Flow exchange from the crushed tuff micropores with the rock fractures and macropores of the crushed tuff is excluded by capillary pressure differences. A similar flow pattern between the rock fractures and crushed tuff macropores is not predicted due to the weaker capillarity of the fractures and the capillary barrier presented by the crushed tuff macropores relative to the rock fractures. The predicted micropore-matrix flow will lead to greater partitioning of radionuclide flux from the invert into the rock matrix than would be predicted by the fracture-matrix partitioning model, which is based on pure diffusive transport through the invert. Therefore, the neglect of this flow is conservative for the prediction of radionuclide partitioning from the drift into the rock fractures and matrix, and subsequent effects on radionuclide transport through the unsaturated zone.

The results of the fracture-matrix partitioning model are to be used in TSPA in combination with the radionuclide release rates and the mountain-scale radionuclide transport model.

6.4.1 Model Development

Figure 6.4-1 shows a diagram of the fracture-matrix partitioning model given this conceptual background. Beneath the waste package, the invert ranges in depth from 675 mm to 806 mm, with an average depth of 741 mm. The total invert depth variation is approximately 17% of the average depth beneath the waste package. Sensitivity to invert thickness is included in the model, but the second-order effects of the curvature of the drift-rock interface are not included. Rather than include the entire invert-rock interface, the model is restricted to a domain from the centerline of a fracture to a boundary at the midpoint between fractures (Figure 6.4-2). The boundary along the fracture centerline and the boundary along the midpoint between fractures are approximate symmetry boundaries. The top and bottom boundaries correspond to the top and bottom of the invert.

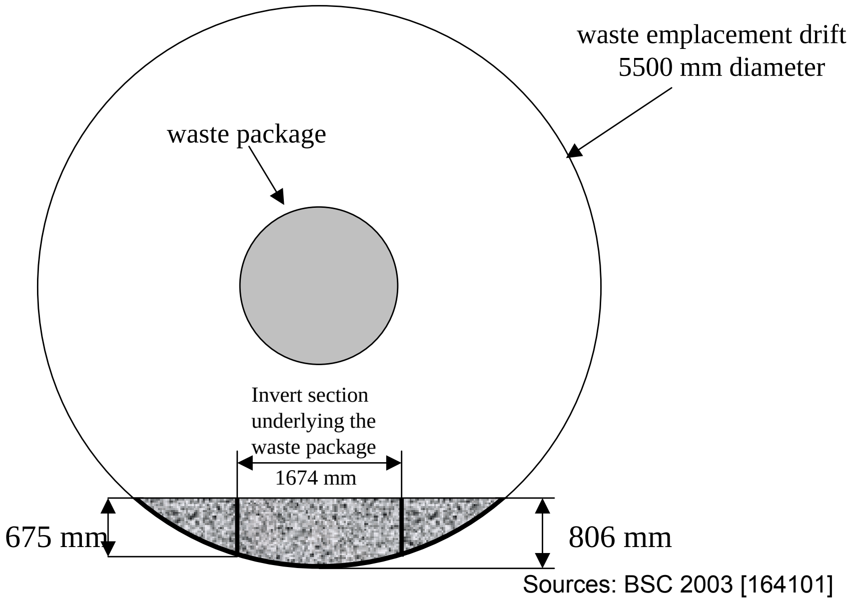

Sources: BSC 2003 [164101]

Figure 6.4-1. Schematic of Waste Emplacement Drift Configuration

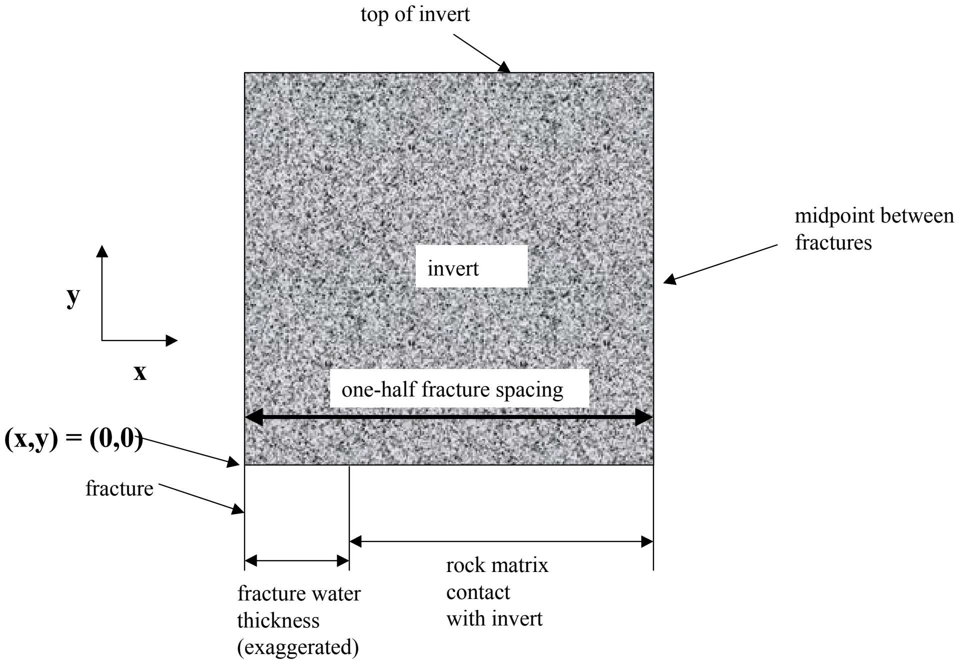

Figure 6.4-2. Schematic Diagram of Modeling Domain

The governing equation for steady diffusion in a homogeneous invert is (Crank 1975 [122990], Equation 1.3, Section 1.3)

$$\nabla^2 C(x, y) = 0 \qquad \text{(Eq. 10)}$$

where C is the mass concentration of radionuclide and x and y are spatial coordinates.

The boundary condition at the top of the invert has a fixed radionuclide concentration,

$$C(x, y_m) = C_m \qquad \text{(Eq. 11)}$$

where y_m is the y coordinate for the top of the invert and C_m is the radionuclide concentration at the top of the invert. No-flux boundary conditions are imposed on the lateral boundaries as a result of symmetry along these boundaries:

$$\frac{\partial C}{\partial x}(0, y) = 0 \qquad \text{(Eq. 12)}$$

$$\frac{\partial C}{\partial x}(h_f, y) = 0 \qquad \text{(Eq. 13)}$$

where h_f is the x coordinate for the midpoint between fractures.

The boundary condition at the bottom of the invert is that the diffusive flux of radionuclides from the invert is equal to the flux in the rock. To determine this flux, one must establish the location of fracture flow relative to the waste emplacement drift. The high permeability and low capillary pressure of the fractures in the repository host rock are conditions conducive to gravity-driven flow. For fracture flow to move around the drift and contact the invert at a point underneath a waste package, the trajectory needs to be approximately 3 to 1 horizontal to vertical motion. Furthermore, the vertical projection for the portion of the invert beneath the waste package available for contact with horizontal flow is only about 13 cm (see Figure 6.4-1). Thus, flow in vertical fractures is not expected to have a sufficient lateral flow component to result in fracture flow immediately beneath a waste emplacement drift. However, under certain circumstances related to the local fracture connectivity, subhorizontal fractures may be capable of redirecting flow in a fracture network in a near-horizontal direction. Under these circumstances, the extent of the drift shadow could be substantially reduced compared with the model results presented in Sections 6.3.3.1 and 6.3.3.2.

The limitation on where fracture flow may occur beneath a waste emplacement drift is associated with the probability of the location of a subhorizontal fracture beneath a waste emplacement drift in association with a vertical fracture. Because of fracture spacing and the random relationship between fracture locations and the drift, the distance of a subhorizontal fracture connection to a vertical fracture beneath the waste emplacement drift, Δy_f, lies between 0 and the fracture spacing (see Figure 6.4-3). This distance (Δy_f) has a uniform distribution, so the expected value for the distance to the closest potential fracture flow beneath a waste emplacement drift is one-half the fracture spacing.

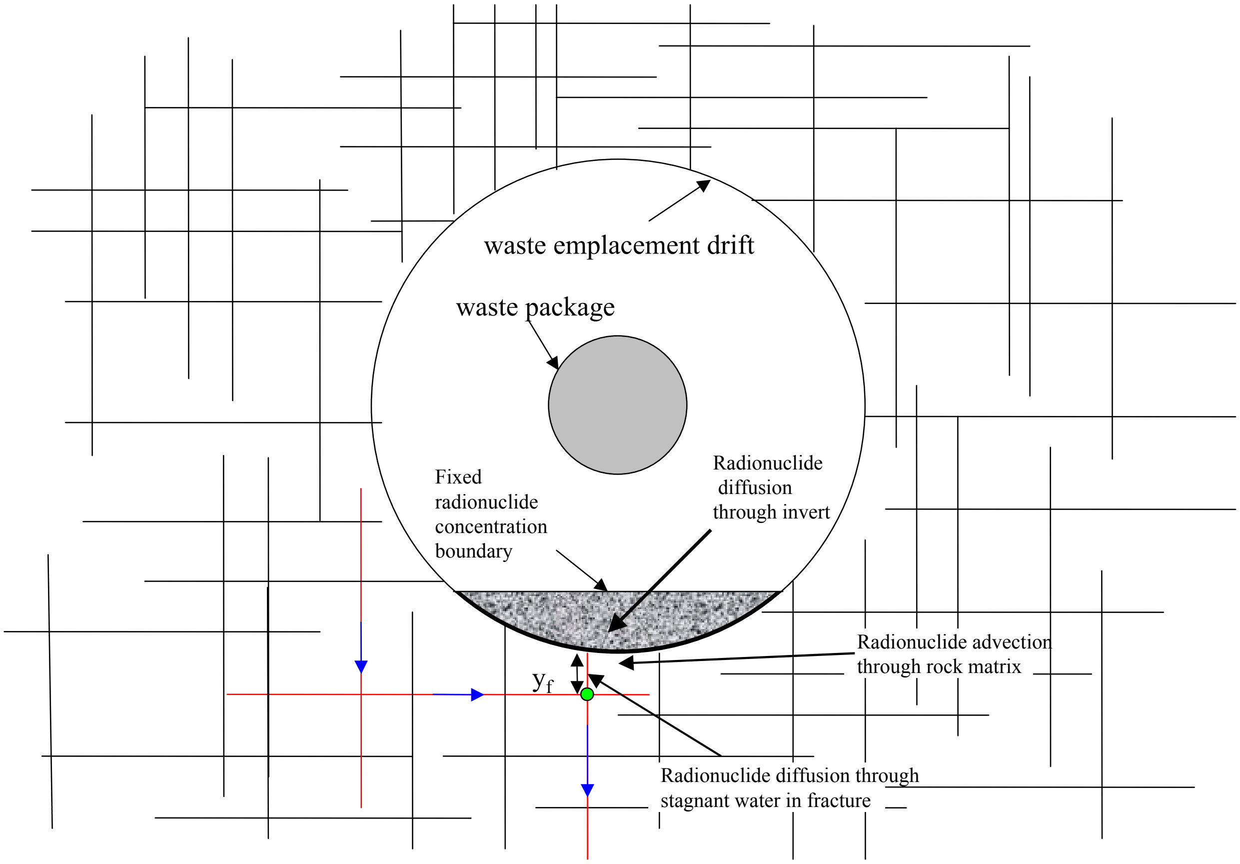

Figure 6.4-3. Schematic of Fracture Network, Waste Emplacement Drift, and Transport Processes

The radionuclide mass flux along any streamline through this connection (green circle in Figure 6.4-3), under steady flow and constant concentration conditions, will be equal to the fracture water flux times the concentration. Given that the water in the fracture between the drift and the connection is not flowing, the flux into the connection is diffusive. The steady-state flux balance along a fracture streamline is given by

$$-D_{ef}\left(\frac{C(x,0)-C_{fn}(x)}{\Delta y_f}\right)=q_{wf}C_{fn}(x) \quad \text{for} \quad 0<x<b \qquad \text{(Eq. 14)}$$

where D_{ef} is the diffusion coefficient for steady diffusive flux in the fracture, C_{fn} is the radionuclide mass concentration at the connection point in the fracture network, and b is the half-water thickness in the fracture. Because the fracture is identified discretely rather than as a continuum, the local water flux in the discrete fracture, q_{wf}, is equal to the continuum fracture flux (e.g., from a dual-permeability flow model) divided by the fracture water content. Note that q_{wf} is negative. Solving Equation 14 for C_{fn} gives

$$C_{fn}(x) = \frac{C(x,0)}{1 + \dfrac{(-q_{wf})\Delta y_f}{D_{ef}}} \quad \text{for} \quad 0 < x < b \qquad \text{(Eq. 15)}$$

Therefore, the radionuclide mass flux, $q_{rad}(x)$, into the fracture at the drift wall may be expressed as

$$q_{rad}(x) = q_{wf} C_{fn}(x) = \frac{q_{wf} C(x,0)}{1 - \dfrac{q_{wf}\Delta y_f}{D_{ef}}} \quad \text{for} \quad 0 < x < b \qquad \text{(Eq. 16)}$$

Note that the effects of fracture-matrix exchange are neglected. However, neglecting this mechanism leads to greater radionuclide partitioning into the fracture at the drift wall.

Owing to the continuity of the matrix, the flux into the matrix is equal to the matrix water flux, q_m, times the radionuclide concentration at the drift boundary,

$$q_{rad}(x) = q_m C(x,0) \quad \text{for} \quad b < x < h_f \qquad \text{(Eq. 17)}$$

Therefore, the balance between diffusive flux in the invert and the flux into the rock may be written in the form

$$-D_{eI}\frac{\partial C}{\partial y}(x,0) = q(x)C(x,0) \qquad \text{(Eq. 18)}$$

where D_{eI} is the effective diffusive mass-transfer coefficient for steady diffusive flux in the invert. The generalized water flux function, $q(x)$, is given by

$$q(x) = \frac{q_{wf}}{1 - \dfrac{q_{wf}\Delta y_f}{D_{ef}}} = q_{fe} \quad \text{for} \quad 0 < x < b \qquad \text{(Eq. 19)}$$

$$q(x) = q_m \quad \text{for} \quad b < x < h_f \qquad \text{(Eq. 20)}$$

A schematic water flux profile is shown in Figure 6.4-4. In the fracture water ($x = 0$ to $x = b$), the equivalent “flux”, q_{fe} , is given by Equation 19. The water flux in the matrix ($x = b$ to $x = h_f$) is given by Equation 20.

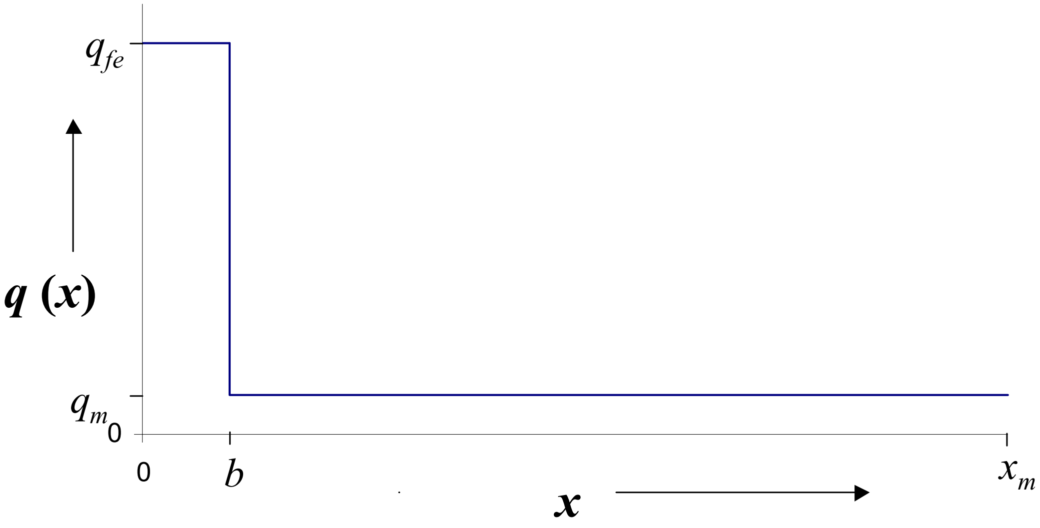

Figure 6.4-4. Schematic Generalized Water Flux Profile at the Drift Wall

Note that the fracture-matrix partitioning model does not include any representation of the air that is present in an unsaturated fracture at the invert-rock interface. Aqueous radionuclides cannot enter the rock through the gas phase, therefore, the presence of air in the fracture represents a barrier to radionuclide transfer to the rock. The justification for not including this feature of the unsaturated fracture in the model is given in Section 6.5.

6.4.2 Dimensionless Representation

The model described by Equations 10–13 and 18–20 can be put into a dimensionless form, which reduces the number of independent parameters that need to be considered. The dimensionless concentration, C_d, is defined by

$$C_d = \frac{C}{C_m} - 1 \qquad \text{(Eq. 21)}$$

The range of C_d varies between 0 and -1. The reason for the normalization by subtracting 1 is to simplify the boundary condition at the top of the invert. The dimensionless distance coordinates, x_d and y_d, are given by

$$x_d = \frac{x}{h_f} \qquad \text{(Eq. 22)}$$

and

$$y_d = y_{dm} - \frac{y}{h_f} \qquad \text{(Eq. 23)}$$

where x_d varies between 0 and 1 and y_d between 0 and $y_{dm} = \dfrac{y_m}{h_f}$.

Writing Equations 10 through 13 and 18 in terms of the dimensionless variables gives

$$\nabla_d^2 C_d(x_d, y_d) = 0 \qquad \text{(Eq. 24)}$$

$$C_d(x_d, 0) = 0 \qquad \text{(Eq. 25)}$$

$$\frac{\partial C_d}{\partial x_d}(0, y_d) = 0 \qquad \text{(Eq. 26)}$$

$$\frac{\partial C_d}{\partial x_d}(1, y_d) = 0 \qquad \text{(Eq. 27)}$$

$$\frac{\partial C_d}{\partial y_d}(x_d, y_{dm}) = q_d(x_d)(C_d(x_d, y_{dm}) + 1) \qquad \text{(Eq. 28)}$$

where the dimensionless Laplacian operator is defined by $\nabla_d^2 \equiv \dfrac{\partial^2}{\partial x_d^2} + \dfrac{\partial^2}{\partial y_d^2}$ and the dimensionless flux, $q_d(x_d)$, on the right-hand side of Equation 28 is defined as follows:

$$q_d = Pe_{fe} = \frac{q_{fe} h_f}{D_{eI}} \quad \text{for} \quad 0 < x_d < b_d \qquad \text{(Eq. 29)}$$

$$q_d = Pe_m = \frac{q_m h_f}{D_{eI}} \quad \text{for} \quad b_d < x_d \leq 1 \qquad \text{(Eq. 30)}$$

$$q_d = \frac{1}{2}(Pe_{fe} + Pe_m) \quad \text{for} \quad x_d = b_d \qquad \text{(Eq. 31)}$$

where

$$b_d = \frac{b}{h_f} \qquad \text{(Eq. 32)}$$

Based on the dimensionless form in Equations 24 through 32, the following dimensionless groups may be identified:

$Pe_m \equiv$ matrix – invert mass transfer Peclet number

$Pe_{fe} \equiv$ fracture – invert mass transfer Peclet number

$\theta_f = b_d \equiv$ fracture water content

$y_{dm} \equiv$ dimensionless invert depth.

6.4.3 Solution Method

The solution of Equation 24 subject to the boundary conditions defined in Equations 25–28 may be obtained using an expansion in cosines and hyperbolic tangent functions. The general solution that satisfies Equation 24 and boundary conditions, Equations 25–27 is

$$C_d(x_d, y_d) = B_0 y_d + \sum_{j=1}^{\infty} B_j \cos(j\pi x_d)\sinh(j\pi y_d) \qquad \text{(Eq. 33)}$$

which may be verified by direct substitution. Substituting Equation 33 into Equation 28 gives

$$A_0\left(1 - q_d\left(x_d\right)y_{dm}\right) + \sum_{j=1}^{\infty} A_j \, cos\left(j\,\pi\, x_d\right)\left[j\,\pi - q_d\left(x_d\right) tanh\left(j\,\pi\, y_{dm}\right)\right] = q_d\left(x_d\right) \qquad \text{(Eq. 34)}$$

or

$$\sum_{j=0}^{\infty} M_{ij} A_j = q_{di} \qquad \text{(Eq. 35)}$$

where

$$M_{i0} = \left(1 - q_d\left(x_{di}\right)y_{dm}\right) \qquad \text{(Eq. 36)}$$

$$M_{ij} = \cos(j\pi x_{di})[j\pi - q_d(x_{di})\tanh(j\pi y_{dm})] \quad \text{for} \quad i > 0 \qquad \text{(Eq. 37)}$$

$$q_{di} = q_d(x_{di}) \qquad \text{(Eq. 38)}$$

$$A_j = B_j \cosh(j\pi y_{dm}) \qquad \text{(Eq. 39)}$$

The transformation from B_j to A_j is introduced to eliminate numerical difficulties in the evaluation of $\cosh(j\,\pi\, y_{dm})$ and $\sinh(j\pi y_{dm})$ for large j. The concentration at the invert-rock interface may be written as

$$C_d(x_d, y_{dm}) = A_0 y_{dm} + \sum_{j=1}^{\infty} A_j \cos(j\pi x_d)\tanh(j\pi y_{dm}) \qquad \text{(Eq. 40)}$$

The usual Fourier method for determining the coefficients, A_j, cannot be used because of the term in Equation 34 that involves the product of the cosine and the dimensionless flux. However, a Fourier solution does exist, because if the steady concentration at the boundary $y_d = y_{dm}$ were known, then the coefficients could be determined through standard methods using the orthogonality properties of the cosine series. An alternative method to determine the coefficients may be developed by noting that a finite range for n is expected to be sufficient in practice based on the similarity of this solution method with Fourier series and the known convergence characteristics of the Fourier series (Weinberger 1965 [163216], Section 18). For a finite sum from $j = 0$ to $j = j_{max}$, Equation 34 may be considered as a set of $j_{max}+1$ linear equations, corresponding to the set of points $x_{d0} \ldots x_{dj_{\max}}$, in $j_{max}+1$ unknowns, $A_0 \ldots A_{j_{\max}}$, as shown in Equation 35. This solution method will be referred to as the discrete transform method. See Attachment XII for a demonstration of the equivalence of the discrete transform method with the standard Fourier series method. Alternative solution methods include direct numerical approaches, such as the finite difference method. These methods were not selected because the solution to the problem is amenable using the semi-analytic approach presented here.

The cumulative dimensionless flux in the fracture, F_{df}, and in the matrix, F_{dm}, may be calculated by integrating the diffusive flux on the left hand side of Equation 28 over x_d. Equation 33 is used for $C_d(x_d, y_d)$ to compute the derivative evaluated at y_{dm}. The result is

$$F_{dfD} = b_d A_0 + \sum_{j=1}^{j_{\max}} A_j \sin(j\pi b_d) \qquad \text{(Eq. 41)}$$

$$F_{dmD} = (1 - b_d)A_0 - \sum_{j=1}^{j_{\max}} A_j \sin(j\,\pi\, b_d) \qquad \text{(Eq. 42)}$$

The cumulative dimensionless flux in the fracture, F_{df}, and in the matrix, F_{dm}, may also be calculated by integrating the advective flux on the right-hand side of Equation 28 over x_d. Equation 40 is used for $C_d(x_d, y_{dm})$ and the flux in Equations 29 and 30 for the fracture and matrix, respectively.

$$F_{dfA} = Pe_{fe}\left(b_d\left(1 + A_0 y_{dm}\right) + \sum_{j=1}^{j_{max}} \frac{A_j}{j\pi} tanh\left(j\,\pi\, y_{dm}\right) sin\left(j\,\pi\, b_d\right)\right) \qquad \text{(Eq. 43)}$$

$$F_{dmA} = Pe_m\left(\left(1 - b_d\right)\left(1 + A_0 y_{dm}\right) - \sum_{j=1}^{j_{max}} \frac{A_j}{j\pi} tanh\left(j\,\pi\, y_{dm}\right) sin\left(j\,\pi\, b_d\right)\right) \qquad \text{(Eq. 44)}$$

6.4.4 Solution Behavior

A typical case is investigated here to provide insight into the solution behavior. This case, called nominal case 1, is parameterized as shown in Table 6.4-1.

Table 6.4-1. Parameters for Nominal Case

Parameter	Value
fracture water content	0.0001
fracture Peclet number	-1
matrix Peclet number	-0.004
dimensionless invert depth	4

Output-DTN: LB0307FMRADTRN.001

The computational details leading to the results for the cases summarized here are given in a scientific notebook by Wang (2003 [163234], SN-LBNL-SCI-236-V1, pp. 5–118). An example of the nominal-case calculations is presented in Attachment X.

The concentration profile at the drift wall is shown for a nominal case 1 in Figure 6.4-5. The concentration drop at the left boundary results from the higher radionuclide mass flux entering the fracture. Lateral diffusive mass flux in the invert leads to additional radionuclide mass transfer into the fracture. The flux profile is shown in Figure 6.4-6, which shows the large flux near $x_d = 0$ in the fracture zone. The matrix flux near the fracture is depressed on account of the reduced radionuclide concentration in the invert.

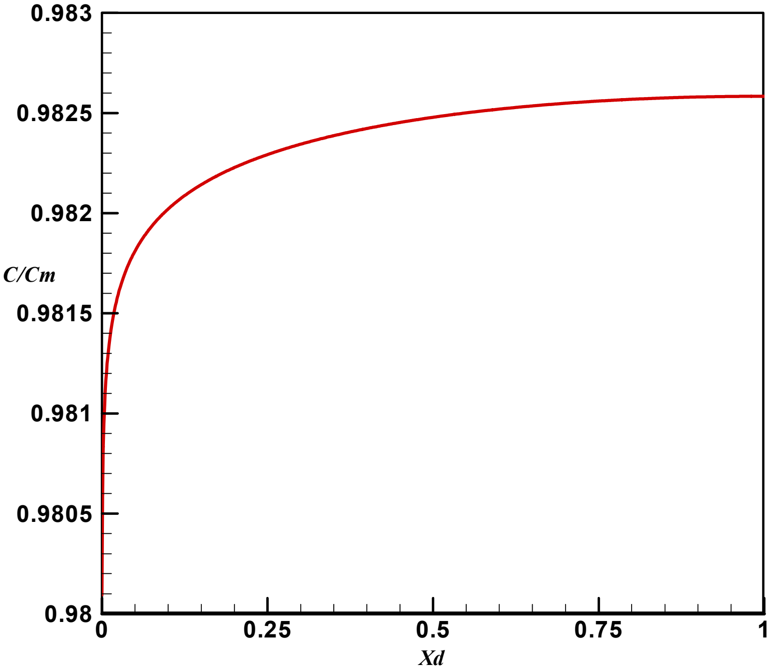

Output-DTN: LB0307FMRADTRN.001

Figure 6.4-5. Plot of C/Cm at the Solution Locations for the Fourier Coefficients—Nominal Case 1

Dimensionless flux ratios are computed for both the flux in the invert at the drift wall and for the flux in the rock at the drift wall. The flux ratio on the invert side of the boundary is given by

$$P_{rI} = \frac{F_{dfD}}{F_{dfD} + F_{dmD}}$$

and the flux ratio in the rock at the drift wall is given by

$$P_r = \frac{F_{dfA}}{F_{dfA} + F_{dmA}},$$

as computed from Equations 41 through 44. The diffusive and advective flux ratios are 0.024 and 0.022, respectively. The discrepancy between these flux terms provides an estimator for the accuracy of the discrete transform solution. For an infinite number of terms, the two flux ratios would be equal.

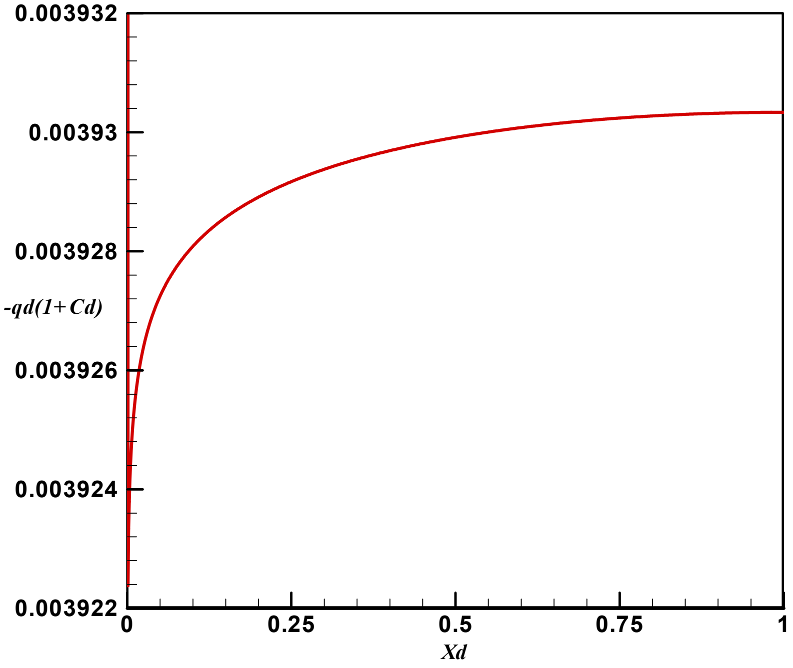

Output-DTN: LB0307FMRADTRN.001

Figure 6.4-6. Plot of Negative of Local Dimensionless Flux at the Solution Points for the Discrete Transform Coefficients—Nominal Case 1

The solution of Equation 35 may be evaluated through a comparison of the left-hand side and right-hand side at intermediate points to the solution points used for computing the discrete transform coefficients. Figure 6.4-7 provides this comparison at different scales, to give a perspective on the entire solution as well as the fit near the fracture where rapid changes in the function occur. The series approximation to the curve is seen to have greater error and oscillations about the target function near the fracture, with a rapid reduction in differences moving away from the fracture.

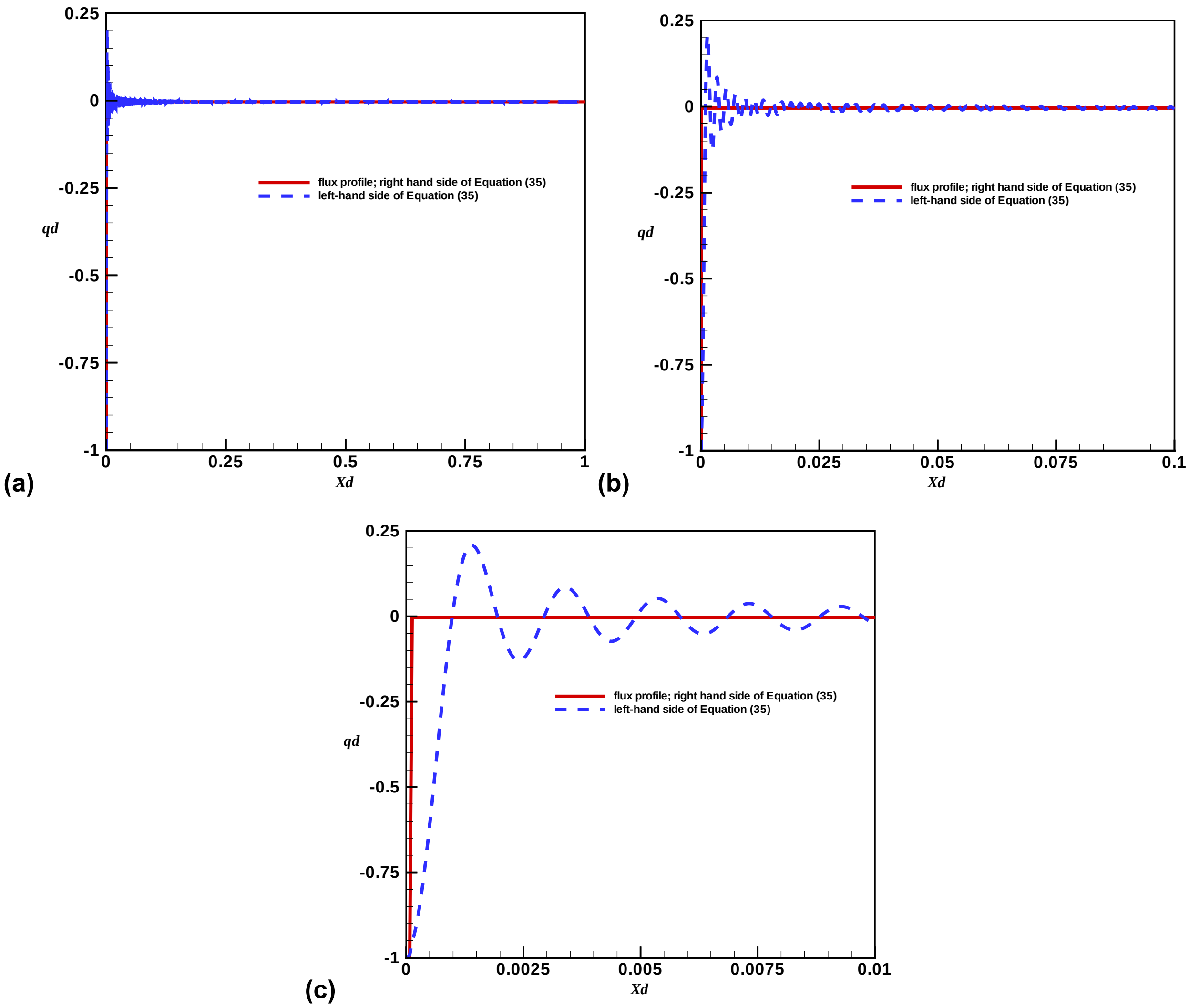

Output-DTN: LB0307FMRADTRN.001

Figure 6.4-7. Comparison Plot at Intermediate Points to Solution for Discrete Transform Coefficients, q_d, right-hand side of Equation (35) (Solid Red Line) left-hand side of Equation (35) (Dotted Blue Line) for 1,024 Terms (a) Entire Domain, (b) Region Near Fracture, and (c) Fracture Close-Up – Nominal Case 1

The solution accuracy may also be evaluated through comparisons of the invert and rock flux terms at the drift wall. For the solution points (x_d) in the equation for the discrete transform coefficients, the flux in the invert and in the rock at the drift wall are identical. However, deviations between these flux terms at intermediate locations provide an indication of solution accuracy. In Figure 6.4-8, the comparison of these two fluxes is made at intermediate values of x_d. This comparison points out that the calculations for diffusive flux in the invert are subject to oscillations of greater magnitude than the calculation for advective flux in the rock. This suggests that the advective flux ratio will provide a more accurate estimate than the diffusive flux ratio.

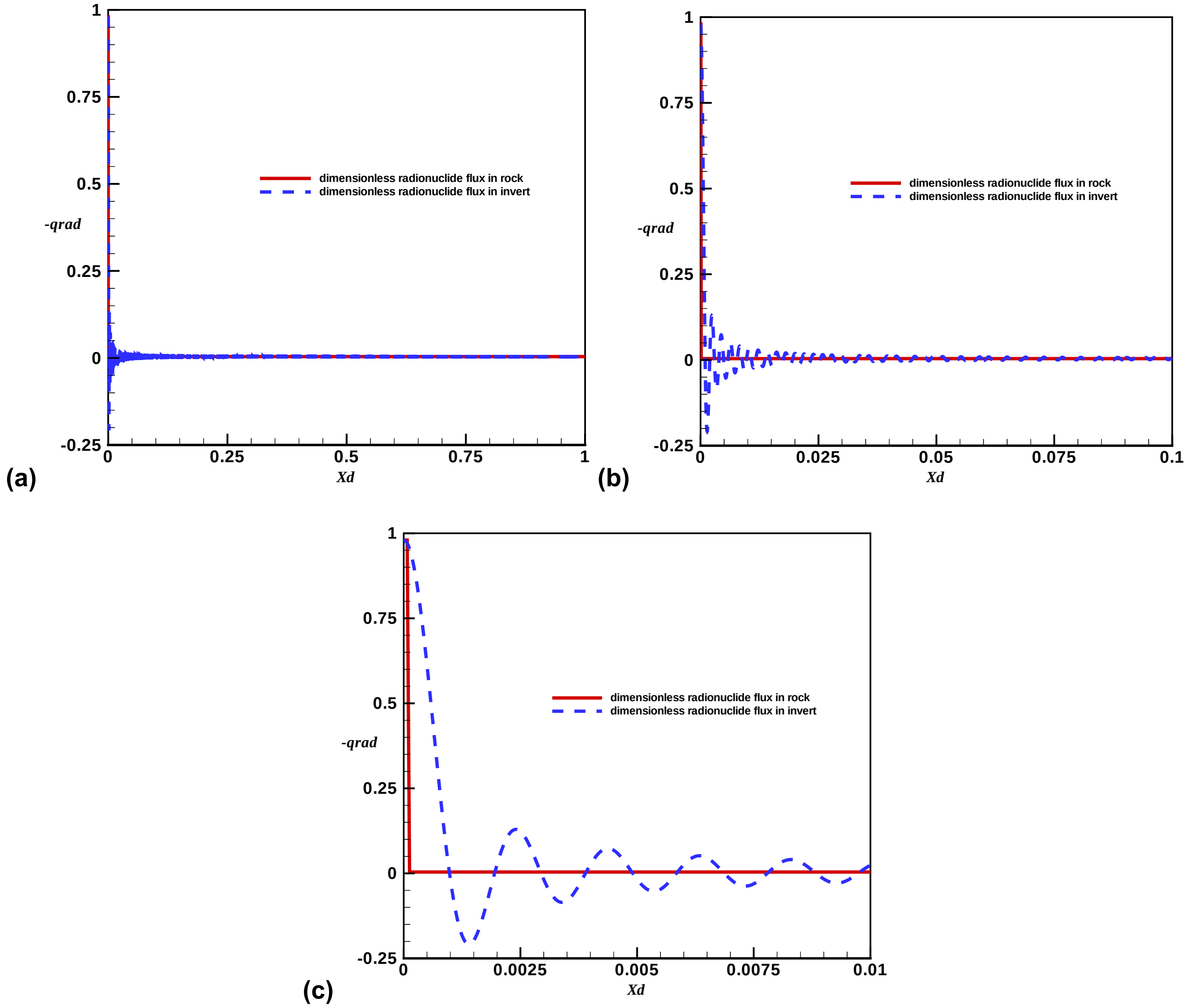

Output-DTN: LB0307FMRADTRN.001

Figure 6.4-8. Comparison Plot of Flux in the Invert (Dotted Blue Line) and Rock (Solid Red Line) at the Drift Wall for 1,024 Terms: (a) Entire Domain, (b) Region Near Fracture, and (c) Fracture Close-Up – Nominal Case 1

The behavior of the solution with successively larger numbers of coefficients is shown in Figures 6.4-9 and 6.4-10. The solutions are seen to generally improve with larger numbers of coefficients. Table 6.4-2 gives the change in the dimensionless flux ratio over a range of 1,024 to 4,096 Fourier coefficients. The value of the flux ratio as computed from the advective flux in the rock is found to change by less than 2% as compared to 4% for the diffusive flux ratio. The variability of the results (to be shown below) is on the order of a factor of 10, so the accuracy of the solution with 1,024 points is sufficient. Because of the greater stability of the flux ratio as computed from the advective flux in the rock, this ratio will be used to determine the flux ratios.

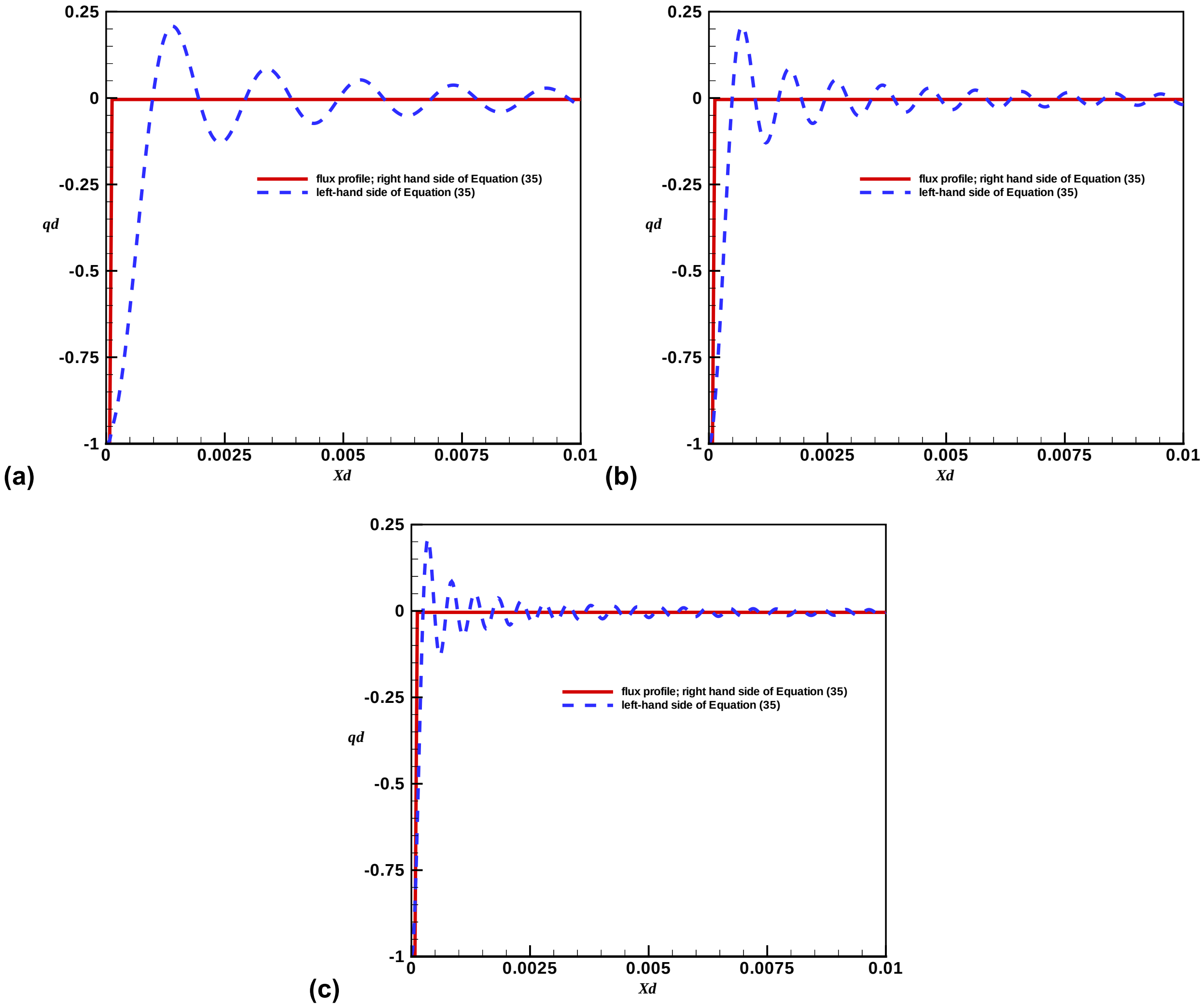

Output-DTN: LB0307FMRADTRN.001

Figure 6.4-9. Comparison Plot at Intermediate Points to Solution for Discrete Transform Coefficients, showing q_d, right-hand side of Equation (35) (Solid Red Line) left-hand side of Equation (35) (Dotted Blue Line): (a) 1,024 Points, (b) 2,048 Points, and (c) 4,096 Points – Nominal Case 1

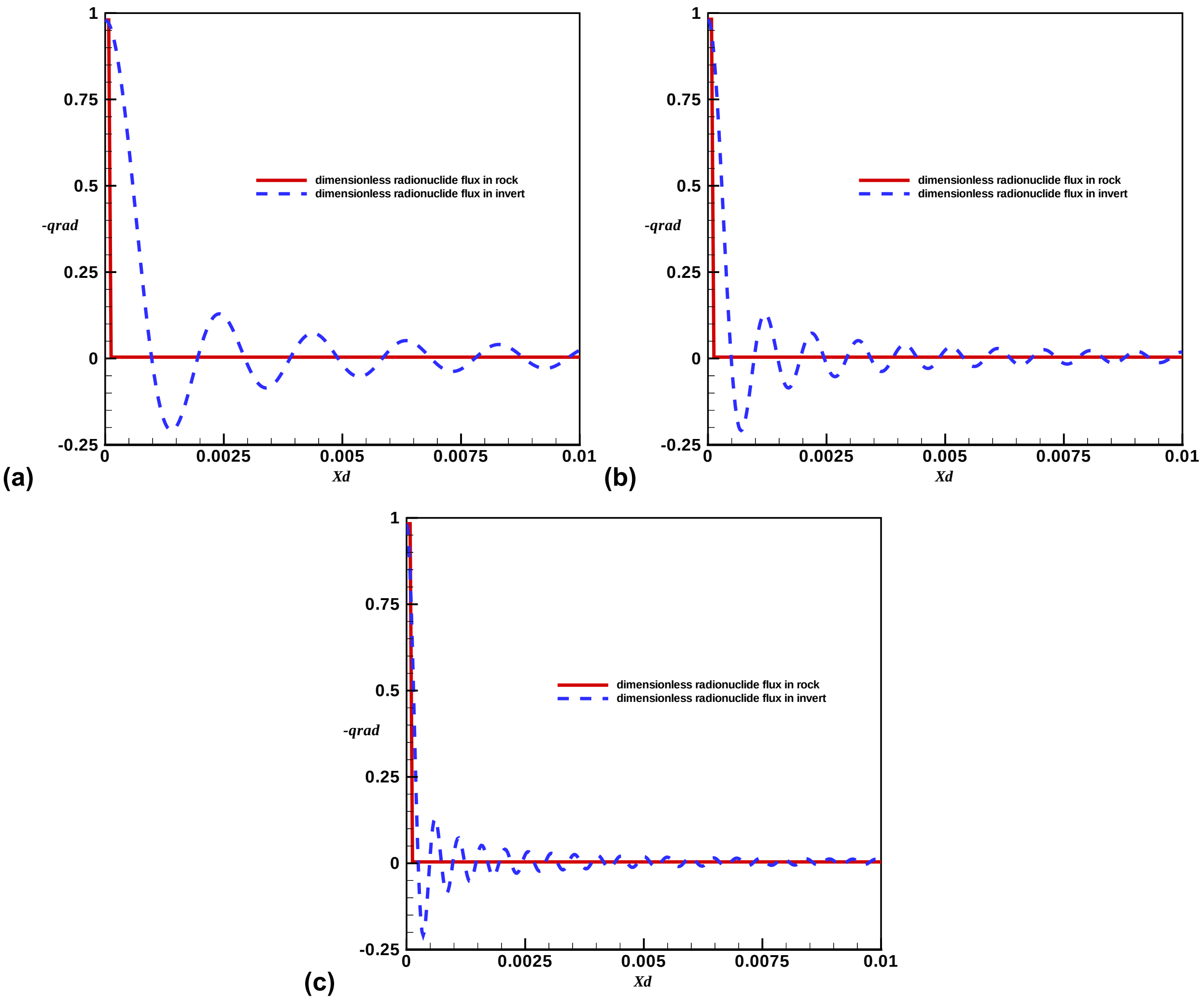

Output-DTN: LB0307FMRADTRN.001

Figure 6.4-10. Comparison Plot of Flux in the Invert (Solid Red Line) and Rock (Dotted Blue Line) at the Drift Wall: (a) 1,024 Points, (b) 2,048 Points, and (c) 4,096 Points – Nominal Case 1

Table 6.4-2. Advective and Diffusive Flux Ratios for Nominal Case 1

Nominal Case 1 Results		
Number of Fourier Coefficients	Advective Flux Ratio in Rock	Diffusive Flux Ratio in Invert
1024	0.02434	0.02211
2048	0.02436	0.02301
4096	0.02438	0.02213

Output-DTN: LB0307FMRADTRN.001

Similar behavior is found for nominal case 2 with fracture water content of 0.0005 and all other parameters unchanged. Figures 6.4-11 and 6.4-12 show similar convergence characteristics for Nominal Case 2 as compared with Nominal Case 1. Again, the advective flux ratio is seen to be more stable in Table 6.4-3 over the selected number of coefficients.

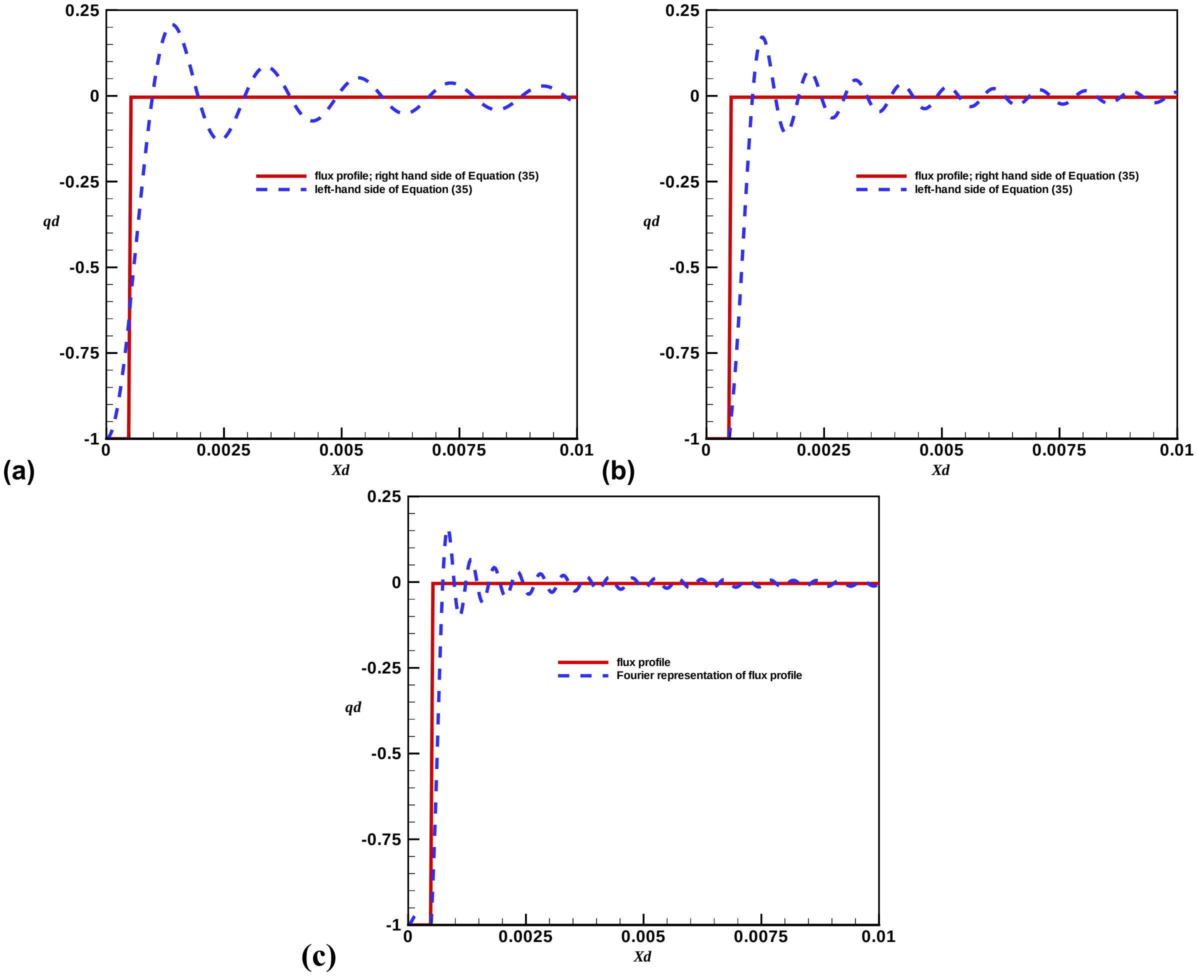

Output-DTN: LB0307FMRADTRN.001

Figure 6.4-11. Comparison Plot at Intermediate Points to Solution for Discrete Transform Coefficients, showing q_d, right-hand side of Equation (35) (Solid Red Line) left-hand side of Equation (35) (Dotted Blue Line): (a) 1,024 Points, (b) 2,048 Points, and (c) 4,096 Points – Nominal Case 2

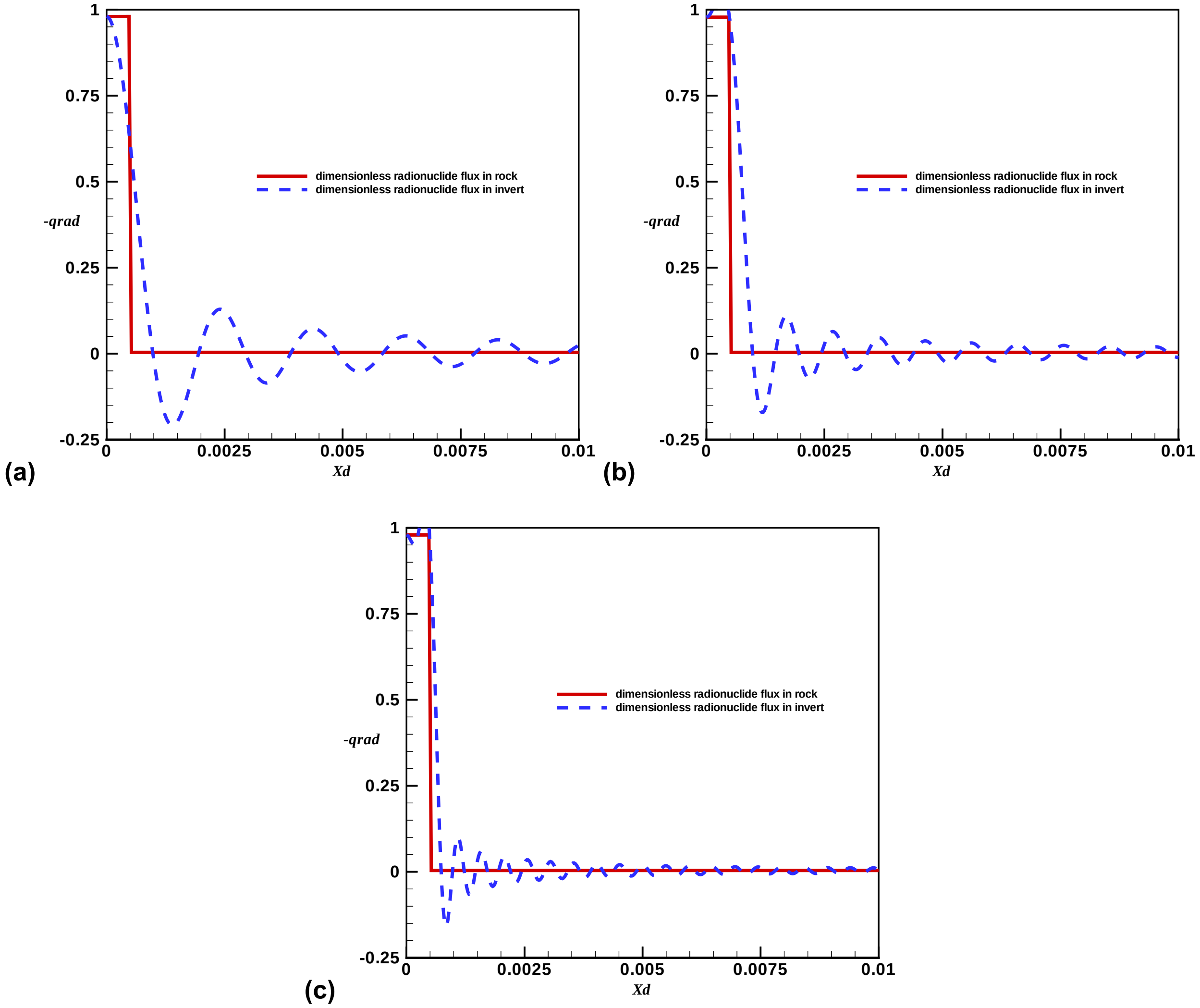

Output-DTN: LB0307FMRADTRN.001

Figure 6.4-12. Comparison Plot of Flux in the Invert (Solid Red Line) and Rock (Dotted Blue Line) at the Drift Wall: (a) 1,024 Points, (b) 2,048 Points, and (c) 4,096 Points – Nominal Case 2

Table 6.4-3. Advective and Diffusive Flux Ratios for Nominal Case 2

Nominal Case 2 Results		
Number of Fourier Coefficients	**Advective Flux Ratio in Rock**	**Diffusive Flux Ratio in Invert**
1024	0.1109	0.0965
2048	0.1108	0.1096
4096	0.1109	0.1108

Output-DTN: LB0307FMRADTRN.001

6.4.5 Model Parameterization and Sampling

The dimensionless invert depth is computed from the invert depth divided by the half of the fracture spacing, $h_f d$. Fracture half-spacing may be computed from

$$h_f = \frac{1}{2} f^{-1} \qquad \text{(Eq. 45)}$$

where f is the fracture frequency. The fracture frequency mean and standard deviation for the repository host rock units (BSC 2003 [161773]; DTN: LB0205REVUZPRP.001 [159525]) are used to derive a sampled set of fracture spacings (see Section 4.1). A correlation of the data from all the model units having both the mean and the standard deviation in fracture frequency is shown in Figure 6.4-13. This figure shows a strong correlation between the average fracture frequency and the standard deviation in fracture frequency. The standard deviation in fracture frequency for the tsw35 and tsw36 are computed from the correlation in Figure 6.4-13. Fracture frequency is modeled as a lognormal distribution to account for the semi-infinite range of the fracture frequency. Details of the sampling method are given in Attachment I.

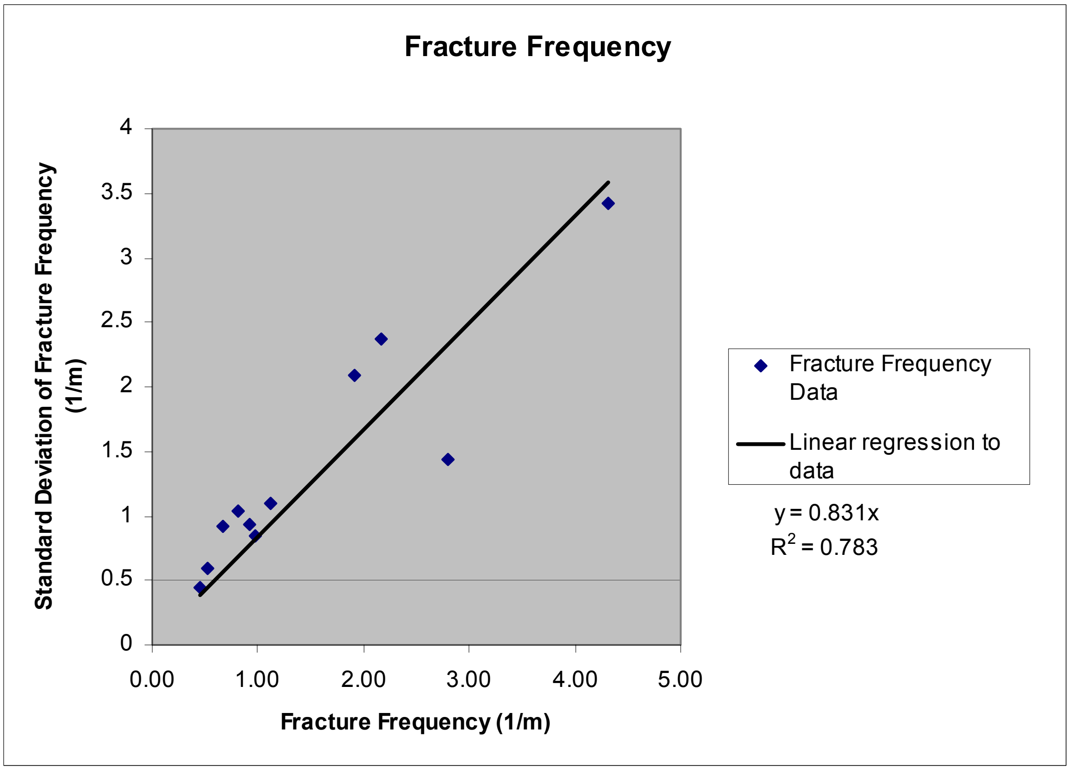

Output-DTN: LB0307FMRADTRN.001

Figure 6.4-13. Fracture Frequency Correlation

Fracture and matrix flux and water saturation values are taken from the output of the UZ Flow Model for the repository host rock (see Section 4.1). These provide over 400 fracture and matrix flux pairs in the repository host rock, as shown in Attachment II. The flow model output also provides the matrix relative permeability, which is used below for computing matrix diffusion.

In addition to the average flow rates predicted by the mountain-scale model, flow focusing at the drift scale is including through a flow-focusing factor. This factor (see Section 4.1) is sampled and used in combination with the sampled fracture flux from the mountain-scale model (Bodvarsson et al. 2003 [163443], Figure 13).

$$P = -0.3137F^4 + 5.4998F^3 - 35.66F^2 + 102.3F - 11.434 \qquad \text{(Eq. 46)}$$

where F is the flow focusing factor and P is the cumulative probability for the value of F. Details of the sampling method are given in Attachment III. Fracture saturations are adjusted for flow focusing through the van Genuchten relationship and the approximation of unit gradient flow in the fractures:

$$q_f = \frac{k_f g}{\nu} S_{fn}^{\frac{1}{2}} \left[1 - \left(1 - S_{fn}^{\frac{1}{m}} \right)^m \right]^2 \qquad \text{(Eq. 47)}$$

where g is the acceleration of gravity, ν is the kinematic viscosity of water, S_{fn} is the normalized fracture saturation $\frac{S_f - S_{fr}}{1 - S_{fr}}$, S_f is the physical fracture saturation, S_{fr} is the residual fracture saturation (S_{fr} is a significant fraction of the typical ambient S_f), m is the van Genuchten pore size distribution factor, and q_f is the fracture water flux. Adjusting q_f by the flow focusing factor, F, gives

$$Fq_f = \frac{k_f g}{\nu} S_{fna}^{\frac{1}{2}} \left[1 - \left(1 - S_{fna}^{\frac{1}{m}} \right)^m \right]^2 \qquad \text{(Eq. 48)}$$

where S_{fna} is the adjusted normalized fracture saturation. Taking the ratio of Equations 48 to 47 gives

$$F = \frac{S_{fna}^{\frac{1}{2}} \left[1 - \left(1 - S_{fna}^{\frac{1}{m}} \right)^m \right]^2}{S_{fn}^{\frac{1}{2}} \left[1 - \left(1 - S_{fn}^{\frac{1}{m}} \right)^m \right]^2} \qquad \text{(Eq. 49)}$$

Using the fact that fracture saturations are low, the numerator may be expanded for small S_{fna} (such that $S_{fna}^{\frac{1}{m}}$ is small) and solved for S_{fna} , as detailed in Attachment XI:

$$S_{fna} = \left[\left(\frac{F}{m^2} \right) S_{fn}^{\frac{1}{2}} \left\{ 1 - \left(1 - S_{fn}^{\frac{1}{m}} \right)^m \right\}^2 \right]^{\frac{2m}{4+m}} \quad \text{(Eq. 50)}$$

Fracture porosity is needed to define the fracture water velocity and to define the fracture water content in contact with the drift invert. A standard deviation in fracture porosity is available only for the tsw34 model unit. The standard deviation for the other host rock units are computed from the ratio of the standard deviation to the mean in the tsw34, multiplied by the average porosity for each host rock unit. The fracture porosity is described by a beta distribution to reflect the physical limits of 0 and 1 for this parameter. Details of the sampling method are given in Attachment III. A similar sampling is performed for matrix porosity as described in Attachment IV.

The fracture saturation at the drift wall is given the same value as that in the flowing fracture beneath the drift. Although physical saturations are reported from the flow model, flow calibrations are based on permeability and capillary pressure relationships that are a function of normalized saturation. Therefore the uncertainty in the normalized fracture saturation is accounted for via the lower, mean, and upper infiltration cases, but this does not account for uncertainty in the residual saturation. The value for residual water saturation in fractures is available in the calibrated hydrological property sets (DTN: LB03023DSSCP9I.001 [163044]), which for all infiltration cases is 0.01. Currently, there are no data from Yucca Mountain that could be used to assess the uncertainty in residual fracture saturation. In general, experiments may be expected to overestimate residual wetting-phase saturations because it is difficult to assess the end of a drainage process. The wetting phase tends to maintain continuity during the drainage process (Dullien et al. 1986 [163221], p. 201), which leads to drainage experiments that only asymptotically approach residual saturation at an ever-decreasing rate. Therefore, the time scales for laboratory experiments become a factor in the determination of the residual saturation. Dullien et al. (1986 [163221], p. 203) investigated residual wetting-phase saturation in sandstones and found that with increasing capillary pressure, the wetting-phase saturation continued to drop, and no “irreducible” saturation could be determined. The uncertainty in residual saturation in fractures is modeled using a log-uniform distribution with a range of 0.001 to 0.1. This distribution has a median of 0.01 and spans the range of residual saturation values measured for higher permeability capillary media (Dombrowski and Brownell 1954 [163222], Figure 7, p. 1,213). Sampling for fracture water saturation, including the uncertainty in residual saturation is described in Attachment VII. The magnitude of the residual water saturation is found to be a significant fraction of the typical total fracture water saturation.

The invert diffusion coefficient was developed based on an empirical correlation with the water content (BSC 2001 [156700], pp. 23–25):

$$\log\left(\frac{D_{eI}}{D_0} \right) = 1.849 \log \theta_I \quad \text{(Eq. 51)}$$

where D_0 is the diffusion coefficient in water factor and θ_I is the invert water content. The coefficient in this correlation, 1.849 was more recently updated to a value of 1.863 (BSC 2002

[161619]). For a typical invert water content of 0.046, the change in exponent results in a difference in D_{eI} of about 4 percent. However, the total uncertainty range for D_{eI} spans a factor of 43 due to uncertainties in invert water content and the free-water diffusion coefficient (see Attachment V). Therefore, the effect of the difference in the exponent is negligible. The invert water content is found to be essentially equal to the intergranular solid content (1 minus the intergranular porosity) times the matrix porosity of the invert material grains, or $\left(1-\phi_{Ig}\right)\phi_m$ (BSC 2002 [161619], Sections 6.4.3 and 6.4.4). The tuff matrix material for the invert will be taken from the tsw36 repository host rock horizon (BSC 2002 [161619], Section 5.9). Therefore, the matrix porosity in the invert is sampled based on the variability in matrix porosity in the Tptpln lithostratigraphic unit, which is equivalent to the TM2 and TM1 hydrogeologic units (*Analysis of Hydrologic Properties Data*, BSC 2003 [161773], Table 4). A suitable range of values for the intergranular porosity is estimated to be 0.4 to 0.48 (BSC 2002 [161619], Section 4.1.3). Intergranular porosity is sampled as a uniform random distribution over the range identified in Section 4.1.1. The uncertainty in D_0 is based on the range of values for strong electrolyte diffusion coefficients in aqueous solution (Weast and Astle 1979 [102865]) given in Section 4.1.1. This is a sufficiently wide range of free-water diffusion coefficients for radionuclides, based on reported values of 2.2×10^{-9} m^2/s for tritiated water (Sato et al. 2001 [164047]), 1.9×10^{-9} m^2/s for pertechnetate (TcO_4^-) (Sato et al. 1996 [163213]), and 1.1×10^{-9} m^2/s for bicarbonate (Newman 1973 [148719]). These are sampled as a lognormal distribution to account for the semi-infinite range of this parameter. Details concerning the sampling methods used for the diffusive mass transfer coefficient are given in Attachment V.

Diffusion coefficients in fracture water have not been directly determined. Generally speaking, diffusion in unsaturated geologic materials has been found to be sensitive to water content (Conca and Wright 1990 [101582], p. 1,055; Bear 1972 [156269], pp. 117–118). Experimental evidence concerning diffusion in unsaturated granular materials is presented in Conca and Wright (1990 [101582]). These experiments were performed on nonporous granular materials in which diffusion occurred through water films along the granular surfaces. The water content of these materials were on the order of 0.5 to 5 percent and diffusion coefficients ranged from about 10^{-13} m^2/s to 10^{-11} m^2/s (Conca and Wright 1990 [101582], Figures 10–13). The analogous water content of a fracture continuum is the fracture water saturation, which is also roughly in this range (see Attachment VII). The range for matrix diffusion coefficients is about an order of magnitude larger (see Figure 6.4-15). This information suggests that the use of diffusion coefficients in the rock matrix as surrogates for diffusion coefficients in the fractures is conservative. Fractures in the welded tuff repository host rock are different than the nonporous granular materials investigated by Conca and Wright (1990 [101582]) due to differences in geometry and the connection to a porous rock matrix. As discussed in Section 4.1.5, limiting values for diffusion coefficients in the fractures are taken to be the effective diffusion coefficients in the neighboring rock matrix. Distributions for matrix diffusion coefficients for cations and anions are given in Attachment IX. Additional corroborative information on diffusion coefficients in rock matrix is given in Reimus et al. (2002 [163008]), where a correlation for diffusion in the rock matrix was developed based on laboratory and field data. The correlation establishes a quantitative relationship between the porosity and permeability of a saturated rock matrix to the effective diffusion coefficient. This correlation may be extended for unsaturated conditions by using the water content as an equivalent parameter for porosity under saturated conditions and the unsaturated effective permeability for the saturated permeability.

This extension to unsaturated conditions is appropriate because for unsaturated flow, the character of the gas phase is not significant other than the space that it occupies. The gas phase could be replaced by solid (rock mineral) which would result in exact equivalence between the unsaturated water content and porosity and effective unsaturated permeability and permeability. The correlation is then (Reimus et al. 2002 [163008], Equation 2.5)

$$\log(D_m) = -3.49 + 1.38\theta_m + 0.165\log(k_w) \tag{Eq. 52}$$

where D_m is the effective diffusion coefficient in cm^2/s, θ_m is the matrix water content, and k_w is the effective permeability to water in m^2. The data from Reimus et al. (2002 [163008]) suggests that the range of diffusion coefficients for tritium, bicarbonate, and pertechnetate individually are roughly similar to the range of mean values for each. This suggests that a single broad distribution scaled by the range of values between cations and anions from DTN: LA0003JC831362.001 [149557] would provide a better representation of the uncertainty in matrix diffusion. To capture this in a single distribution, consider the following transformation:

$$X = \log\left(\frac{D_0}{D_m}\right) \tag{Eq. 53}$$

where D_0 is the limiting upper value for D_m. This value is given in DTN: LA0003JC831362.001 [149557] as 10^{-9} m^2/s. The average for X is

$$\mu_X = \log(D_0) - \overline{\log(D_m)} \tag{Eq. 54}$$

If we stipulate that the variable X ranges from 0 to infinity, then D_m is constrained to be less than 10^{-9} m^2/s.

Given the semi-infinite range for X, it can be sampled as a lognormal distribution. This introduces the second logarithmic transformation, Y,

$$Y = \ln(X) \tag{Eq. 55}$$

The mean for Y is taken to be

$$\mu_Y = \ln(\mu_X) \tag{Eq. 56}$$

such that the mean is unchanged by the transformation to a lognormal distribution. The distribution of diffusion coefficients based on Equations 53 and 55 and a normal distribution for Y is called the "primary distribution". Distribution parameters for Y may be obtained by setting $\overline{\log(D_m)}$ to be the log of the geometric mean of the mean values in DTN: LA0003JC831362.001 [149557] and then adjusting the standard deviation for Y such that it covers the range of values represented by cations and anions in DTN: LA0003JC831362.001 [149557]. The standard deviation of 0.3 for Y results in a spread for the distribution that is representative of the spread of values in DTN: LA0003JC831362.001 [149557], as shown in Figure 6.4-14.

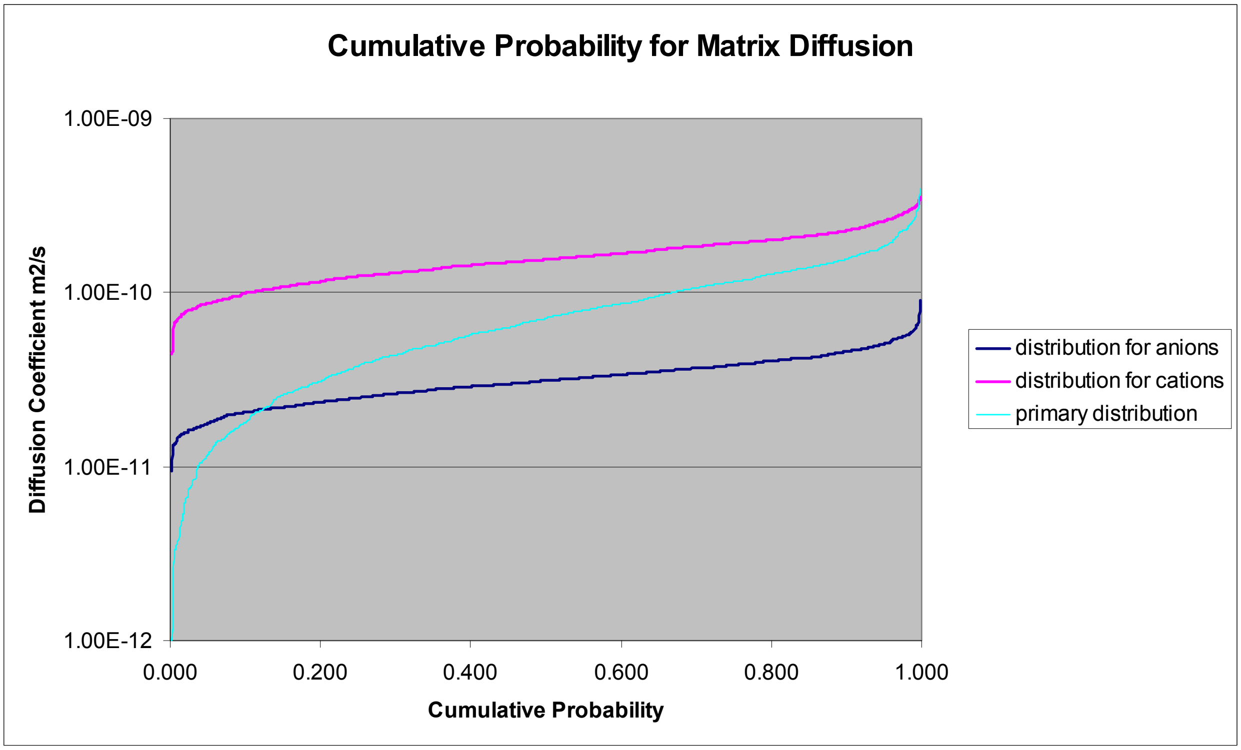

DTN: LA0003JC831362.001 [149557]
Output DTN: LB0307FMRADTRN.001

Figure 6.4-14. Cumulative Probability for Matrix Diffusion

See Attachment IX for a discussion of the methods used to generate the distributions for cations, anions, and the Reimus correlation. The range of values for the UZ may be examined using 5th and 95th percentile values for water content and effective matrix permeability. Doing this, the a "low" distribution may be computed based on Equation 52 by assigning the mean using the 5th percentile water content and effective matrix permeability and a "high" distribution may be based on the 95th percentile of values of these quantities. The results are shown in Figure 6.4-15.

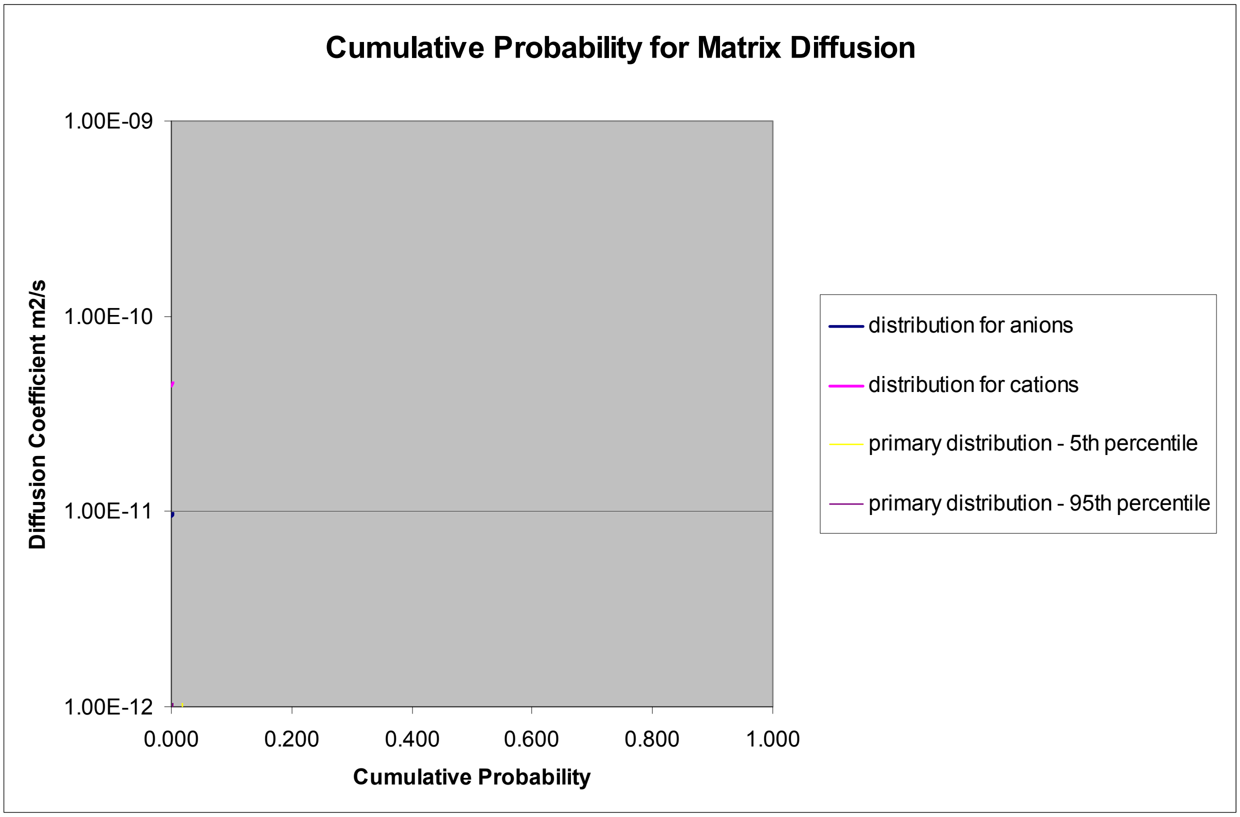

DTN: LA0003JC831362.001 [149557]
Output DTN: LB0307FMRADTRN.001

Figure 6.4-15. Comparison of Cation/Anion Distributions with Primary Distributions at 5th and 95th Percentile for Effective Permeability, Mean Glacial Transition Climate

See Attachment IX for a discussion of the methods used to generate the low and high distributions for the Reimus correlation. The data used to develop the distributions in DTN: LA0003JC831362.001 [149557] were from diffusion measurements under saturated conditions. As a consequence, the generally lower values represented by the Reimus distributions are expected. The comparison with measured diffusion coefficients for tritium, technetium, and bicarbonate (Table 6.4-4) is given in Figure 6.4-16. Again, the correlations for the UZ are lower than the measured values, which were all performed under saturated conditions.

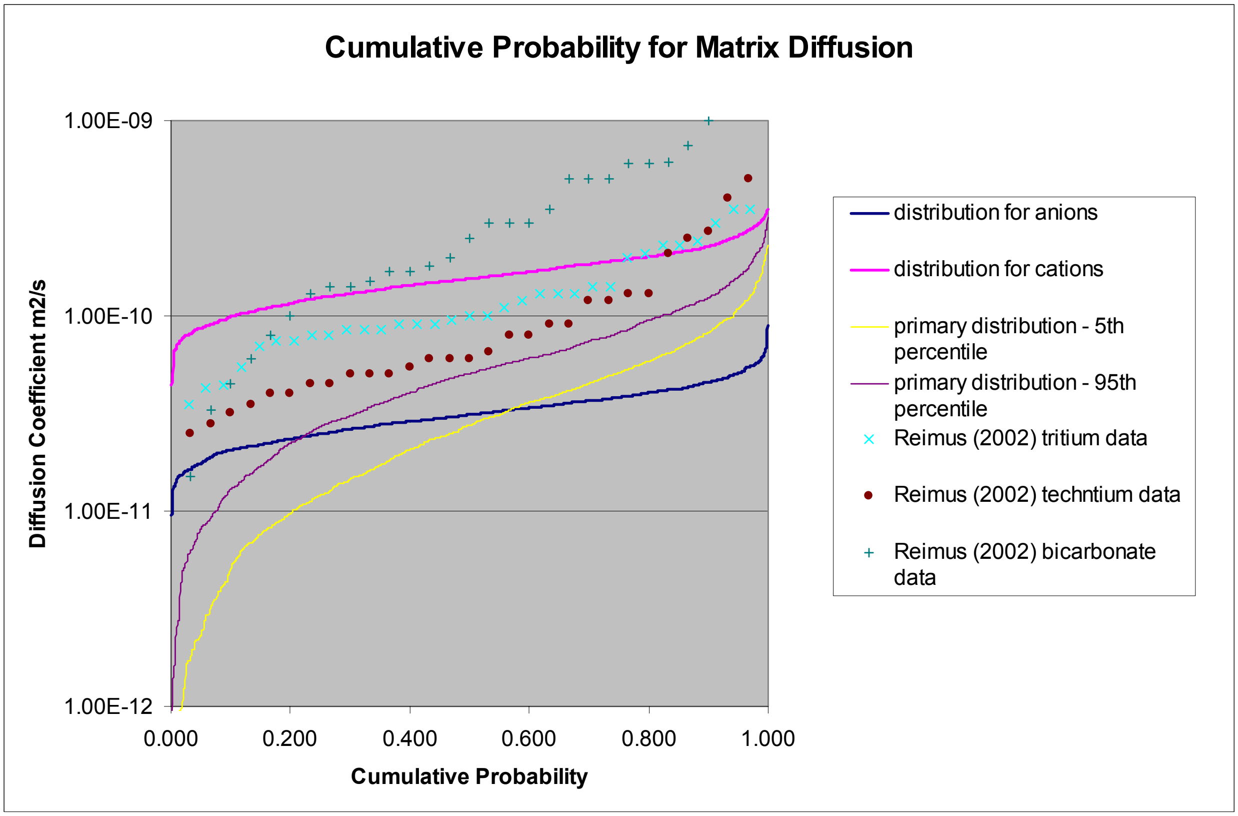

DTN: LA0003JC831362.001 [149557]
Output DTN: LB0307FMRADTRN.001

Source: Reimus et al. 2002 [163008], Table 2-4

Figure 6.4-16. Comparison of the Distributions with Diffusion Data

Table 6.4-4. Diffusion Data from Reimus et al. (2002 [163008], Table 2-4)

Sample Description	^{3}H Diffusion coefficient, cm^{2}/s	^{99}Tc Diffusion coefficient, cm^{2}/s	^{14}C Diffusion coefficient, cm^{2}/s
UE20c 2856D	1.10E-06	8.00E-07	6.00E-07
UE20c 2856E	8.50E-07	6.00E-07	4.50E-07
UE20c 2856F	9.00E-07	5.00E-07	3.30E-07
UE20c 2856F	2.30E-06	2.50E-06	1.70E-06
UE20c 2856F	1.30E-06	1.20E-06	8.00E-07
UE20c 2858A	1.20E-06	9.00E-07	3.00E-06
UE20c 2858A	1.00E-06	4.00E-07	1.70E-06
UE20c 2809A	7.50E-07	na	na
UE20c 2809B*	1.40E-06	na	na
UE20c 2751A	1.40E-06	6.00E-07	5.00E-06
UE20c 2751B*	1.30E-06	5.00E-07	5.00E-06
UE20c 2908A	3.00E-06	2.70E-06	1.30E-06
UE20c 2908D*	2.40E-06	2.10E-06	2.50E-06
UE20f 2842	5.50E-07	5.00E-07	1.50E-07
UE18t 1003A	1.30E-06	na	na
UE18t 1003B*	7.00E-07	na	na
UE18t 1387.5A	8.50E-07	4.50E-07	3.00E-06
UE18t 1387.5A	8.50E-07	6.50E-07	1.80E-06
UE18t 1387.5B	8.00E-07	6.00E-07	6.10E-06
UE18t 1387.5B	9.50E-07	9.00E-07	3.00E-06
UE18t 1390	9.00E-07	5.50E-07	7.50E-06
UE18t 1390	7.50E-07	4.00E-07	1.10E-05
UE18r 2228A	4.40E-07	3.50E-07	6.00E-06
UE18r 2228A	4.30E-07	3.20E-07	6.00E-06
UE18r 2228B	3.50E-07	1.30E-06	2.00E-05
PM1 4823A	3.50E-06	1.20E-06	1.50E-06
PM1 4823B*	3.50E-06	1.30E-06	5.00E-06
PM2 4177A	2.10E-06	8.00E-07	1.40E-06
PM2 4177A	8.00E-07	2.50E-07	1.40E-06
PM2 4177B	2.30E-06	5.00E-06	3.50E-06
PM2 4177B	9.00E-07	4.50E-07	1.00E-06
PM2 4177C*	2.00E-06	4.00E-06	1.00E-05
PM2 4177C*	1.00E-06	2.80E-07	2.00E-06

NOTE: * Denotes diffusion cell with a mineralized fracture surface.
na = data not available

See Attachment IX for a discussion of the methods used to compare these distributions with the measurements.

Sampling for the matrix water saturation is described below. Water content is derived from the local water saturation times the sampled matrix porosity (as discussed above) for the model unit. The effective permeability is computed from the relative permeability and matrix permeability

$$k_w = k_m k_{rw} \tag{Eq. 57}$$

where k_m is the saturated permeability of the matrix and k_{rw} is the relative permeability from the flow model output. The matrix permeability is not sampled because the flow and saturation information is consistent only with the mean values. Details concerning the sampling methods used for the matrix diffusion coefficient are given in Attachment VI.

The parameters derived are combined to provide values of the dimensionless parameters identified in Section 6.4.2 across the flow model grid locations within the repository host rock. Computation of these parameters across the grid locations is described in Attachment VII.

A summary table of the parameters used for the fracture-matrix partitioning model, initially presented in Section 4 of this report, are given in Table 6.4-5.

Table 6.4-5. Inputs for the Fracture-Matrix Partitioning Model

Input Name	Input Description	Input Source	Value or Distribution	Type of Uncertainty
f	fracture frequency	LB0205REVUZPRP.001 [159525]	log-normal	epistemic
S_{fr}	fracture residual saturation	LB03023DSSCP9I.001 [163044]	log-uniform	epistemic
S_f	fracture saturation	LB03023DSSCP9I.001 [163044]	empirical	epistemic
F	flow focusing factor	Bodvarsson et al. 2003 [163443], Figure 13	empirical	epistemic
m	fracture van Genuchten pore size distribution parameter	LB03023DSSCP9I.001 [163044]	single value	na
q_{wf}	water flux in fracture	LB03023DSSCP9I.001 [163044]	empirical	epistemic
ϕ_f	fracture porosity	LB0205REVUZPRP.001 [159525]	beta	epistemic
ϕ_m	matrix porosity	LB0207REVUZPRP.002 [159672]	beta	epistemic
k_m	matrix saturated permeability	LB03023DSSCP9I.001 [163044]	empirical	epistemic
k_{rm}	matrix relative permeability	LB03023DSSCP9I.001 [163044]	empirical	epistemic
D_m	diffusion in rock matrix	Reimus et al. 2002 [163008], Equation 2.5	ln-log normal	epistemic
q_m	water flux in matrix	LB03023DSSCP9I.001 [163044]	empirical	epistemic
ϕ_{Ig}	invert intergranular porosity	BSC 2002 [161619], Section 4.1.3	uniform	epistemic
D_0	free-water diffusion coefficient	Weast and Astle 1979 [102865], p. F-62	log-normal	epistemic
D_{el}	Invert diffusion correlation	BSC 2001 [156700], pp. 23–25	na	na
y_m	invert depth	BSC 2003 [164101]	uniform	epistemic
na	waste emplacement areas in each host rock unit	BSC 2003 [164491]	single value	na

NOTE: na = not applicable

6.4.6 Model Results

Calculations are performed for the lower, mean, and upper scenarios of the glacial transition climate. This climate is the largest fraction of the compliance period and is the portion of the compliance period when radionuclide transport is more probable. Furthermore, average infiltration rates for the glacial transition scenarios range from 2.5 to 33 mm/yr (*Simulation of Net Infiltration for Modern and Potential Future Climates*, USGS 2001 [160355], Table 6-18). This range nearly encompasses the entire average infiltration range infiltration scenarios from monsoon and present-day climates, which range from 1.3 to 19.8 mm/yr (USGS 2001 [160355], Tables 6-9 and 6-13). Therefore, using results derived for the glacial transition climate for the lower, mean, and upper infiltration scenarios, respectively, under modern and monsoon climate, are not expected to result in an underestimate of radionuclide transport.

As discussed in Section 6.4.5, parameter uncertainty is included in the model development through sampling of the 433 different repository locations that have been assigned parameters. The sampling is performed to provide a representation of the frequency distribution of the fraction of the total radionuclide flux from a drift that enters the fractures. A set of 24 samples were randomly selected for each climate scenario. This total number of samples allows for taking one sample each from the tsw33 and tsw36 host rock horizons in a representative proportion to the tsw34 (3 samples) and the tsw35 (19 samples), based on the repository layout. Estimation theory indicates that for 95% confidence limits, 24 samples provide an estimate of the mean that is within

$$\pm \frac{1.96}{\sqrt{24-1}} S = \pm 0.41 S \qquad \text{(Eq. 58)}$$

(Hogg and Craig 1978 [163236], pp. 212–215), where S is the sample standard deviation. The details of the sampling methods used for each infiltration case are given in Attachment VIII.

Computed results for each climate scenario are shown in Figures 6.4-17a-c. Calculation details are given in Wang (2003 [163234], SN-LBNL-SCI-236-V1, pp. 101–145), but the method used is the same as discussed in Section 6.4.4 and Attachment X. The 24 values for each climate scenario provide a basis for developing a distribution for sampling in TSPA. Results for the lower and mean infiltration scenarios are more similar and, in general, have larger releases to the fractures than the higher infiltration case. This difference primarily results from the influence of the higher matrix flux on the transport from the drift into the rock matrix under this infiltration scenario. The variation in fracture flux and water saturation among the different infiltration scenarios is found to have a second-order effect on fracture-matrix partitioning.

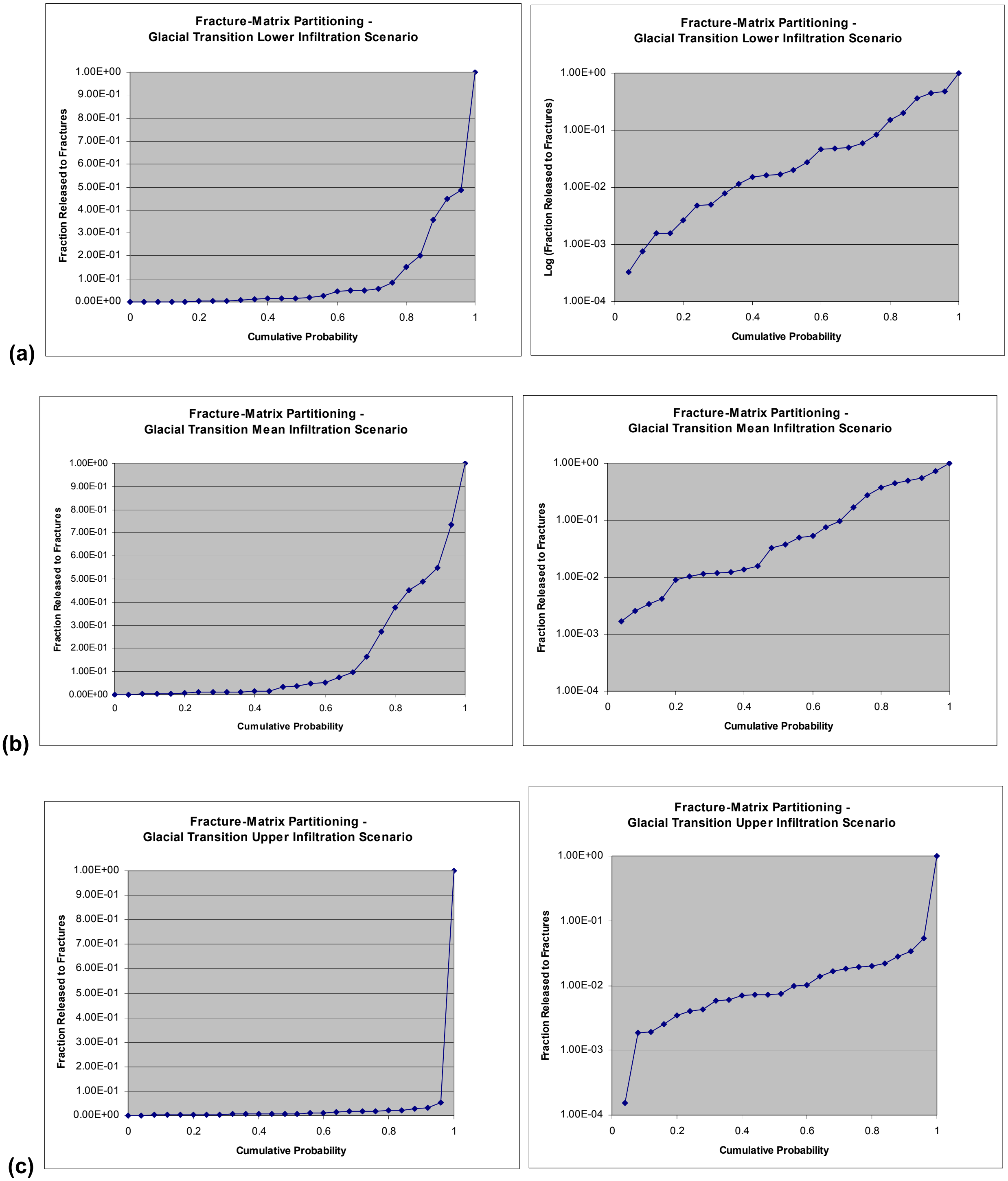

Output DTN: LB0307FMRADTRN.001

Figure 6.4-17. Fracture-Matrix Partitioning Distributions for the (a) Lower, (b) Mean, and (c) Upper Glacial-Transition Infiltration Scenarios – linear scale on left-hand side; logarithmic scale on right-hand side

Distributions are based on the values for fracture-matrix partitioning and then ordered to establish an empirical cumulative probability distribution. The distribution for the upper scenario has smaller releases to the fractures because of the larger advective flux in the matrix. The average matrix flux for the upper infiltration scenario is 0.08 mm/yr. compared with average matrix fluxes for the mean and lower scenarios of 0.035 and 0.027 mm/yr, respectively. Furthermore, the median matrix fluxes for the upper, mean, and lower infiltration scenarios are 6.6, 1.6, and 1.6 mm/yr, respectively. The similarity of the matrix flux for the lower and mean scenarios is the main reason for the similarity in the flux partitioning between the fractures and matrix. The other factors, such as the fracture Peclet number and fracture water content, tend to be random variables defined by the invert and fracture diffusion coefficients, offset of fracture flow from the drift, and residual fracture saturation not strongly affected by the infiltration scenario. Figures 6.4-17a–c show that the lower and mean scenarios result in distributions similar to the upper scenario. A comparison of the lower and mean scenarios is given in Figure 6.4-18.

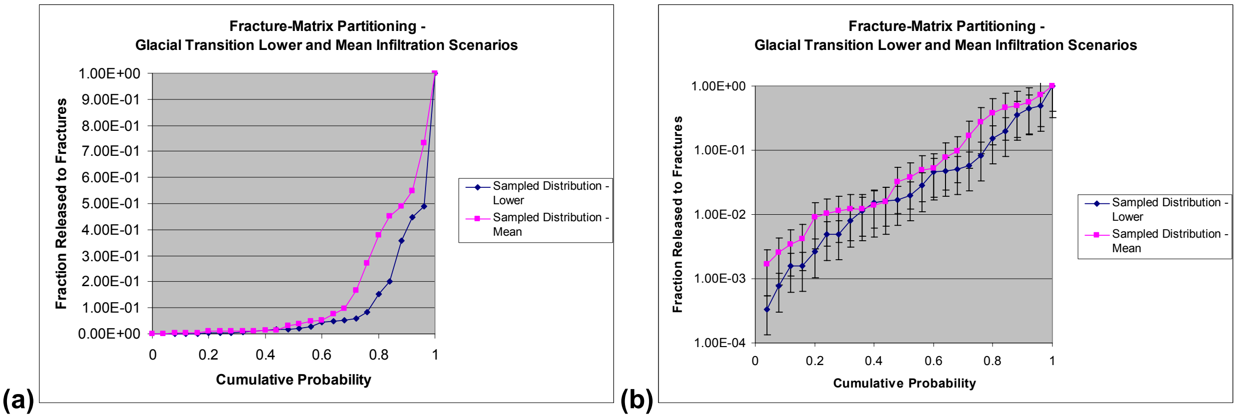

Output DTN: LB0307FMRADTRN.001

Figure 6.4-18. Comparison of Lower and Mean Scenarios – (a) linear scale on left-hand side; (b) logarithmic scale on right-hand side

The comparisons in Figure 6.4-18a show on a linear scale that the distributions are fairly similar. The logarithmic plot shows the comparison with error bars set by the relative error in the mean. The overlap of the confidence limits for the lower and mean cases suggests combining these distributions into a single distribution. This distribution is shown in Figure 6.4-19.

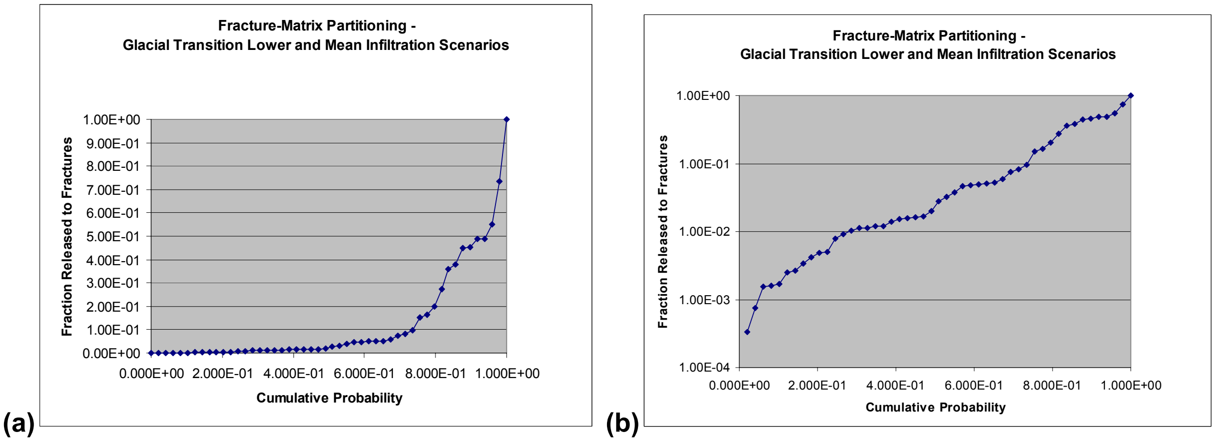

Output DTN: LB0307FMRADTRN.001

Figure 6.4-19. Composite Distribution from the Lower and Mean Scenarios – (a) linear scale on left-hand side; (b) logarithmic scale on right-hand side

The uncertainty in the sampled distributions is shown in Figure 6.4-20. This uncertainty is based on the 95th percentile confidence interval estimates as presented in Equation 58.

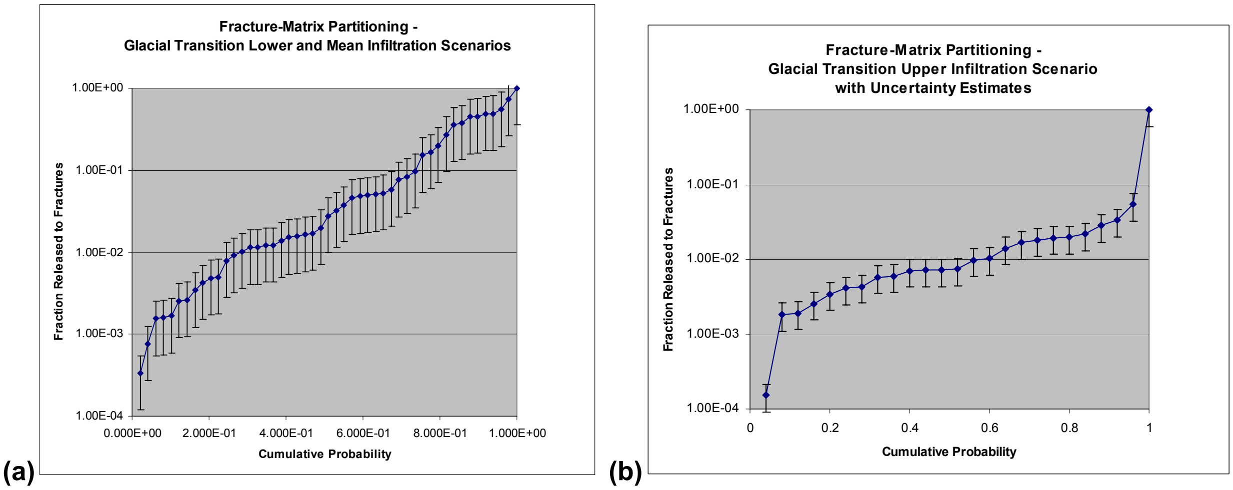

Output DTN: LB0307FMRADTRN.001

Figure 6.4-20. Fracture-Matrix Partitioning Distributions with 95th Percentile Confidence Intervals: (a) Composite Distribution for the Lower and Mean Infiltration Scenarios and (b) Distribution for the Upper Infiltration Scenario

The combined distribution for lower and mean infiltration scenarios under the glacial transition climate spans average infiltration rates from 2.5 to 17.8 mm/yr (*Simulation of Net Infiltration for Modern and Potential Future Climates,* USGS 2001 [160355], Table 6-18). Present-day and monsoon climates range from 1.3 to 19.8 mm/yr (USGS 2001 [160355], Tables 6-9 and 6-13). Therefore, the combined distribution given in Figure 6.4-20a is applicable over all climates and infiltration scenarios except for the glacial transition upper infiltration case. For the glacial transition upper infiltration scenario, the distribution shown in Figures 6.4-20b is applicable. The following sampling scheme accounts for the uncertainty in the sampled distributions shown in Figure 6.4-20:

1. Randomly select a mean value for the fracture matrix partitioning factor for all climate scenarios except the upper glacial transition climate from Table 6.4-6(a). For the upper glacial transition climate scenario, pick the mean from Table 6.4-6(b).

2. Select the fracture-matrix partitioning coefficient from a beta distribution with a range from 0 to 1, a mean value selected in step 1), and a standard deviation of the beta distribution based on the mean times the percentage from Table 6.4-7(a) times 1.96^{-1} for all climate scenarios except the upper glacial transition climate. The percentage is multiplied by 1.96^{-1} because the 95th percentile represents 1.96 standard deviations. For the upper glacial transition climate scenario, the standard deviation is the mean times the percentage from Table 6.4-7(b) times 1.96^{-1}.

Table 6.4-6. Cumulative Distributions for Fracture-Matrix Partitioning Factor: (a) Composite Distribution for the Glacial Transition Lower and Mean Infiltration Scenarios; (b) Distribution for the Glacial Transition Upper Infiltration Scenario

(a) Lower and Mean Infiltration Scenario		**(b) Upper Infiltration Scenario**	
Cumulative Probability	**Sampled Distribution**	**Cumulative Probability**	**Sampled Distribution**
0.000E+00	0.00	0	0.00
2.041E-02	3.33E-04	0.040	1.53E-04
4.082E-02	7.60E-04	0.080	1.84E-03
6.122E-02	1.55E-03	0.120	1.91E-03
8.163E-02	1.58E-03	0.160	2.56E-03
1.020E-01	1.67E-03	0.200	3.45E-03
1.224E-01	2.53E-03	0.240	4.08E-03
1.429E-01	2.63E-03	0.280	4.32E-03
1.633E-01	3.41E-03	0.320	5.79E-03
1.837E-01	4.22E-03	0.360	5.98E-03
2.041E-01	4.86E-03	0.400	7.08E-03
2.245E-01	4.97E-03	0.440	7.14E-03
2.449E-01	7.86E-03	0.480	7.21E-03
2.653E-01	9.08E-03	0.520	7.37E-03
2.857E-01	1.02E-02	0.560	9.81E-03
3.061E-01	1.139E-02	0.600	1.02E-02
3.265E-01	1.141E-02	0.640	1.40E-02
3.469E-01	1.209E-02	0.680	1.68E-02
3.673E-01	1.214E-02	0.720	1.82E-02
3.878E-01	1.39E-02	0.760	1.95E-02
4.082E-01	1.52E-02	0.800	1.98E-02
4.286E-01	1.55E-02	0.840	2.18E-02
4.490E-01	1.63E-02	0.880	2.83E-02
4.694E-01	1.69E-02	0.920	3.34E-02
4.898E-01	1.99E-02	0.960	5.44E-02
5.102E-01	2.79E-02	1	1.00E+00
5.306E-01	3.24E-02		
5.510E-01	3.77E-02		
5.714E-01	4.63E-02		
5.918E-01	4.82E-02		
6.122E-01	4.94E-02		
6.327E-01	5.04E-02		
6.531E-01	5.26E-02		
6.735E-01	5.85E-02		
6.939E-01	7.61E-02		
7.143E-01	8.34E-02		
7.347E-01	9.68E-02		
7.551E-01	1.52E-01		
7.755E-01	1.66E-01		
7.959E-01	2.00E-01		
8.163E-01	2.72E-01		
8.367E-01	3.58E-01		
8.571E-01	3.77E-01		
8.776E-01	4.49E-01		
8.980E-01	4.53E-01		
9.184E-01	4.88E-01		
9.388E-01	4.90E-01		
9.592E-01	5.50E-01		
9.796E-01	7.34E-01		
1.000E+00	1.00E+00		

Output DTN: LB0307FMRADTRN.001

NOTE: A fourth significant figure is given for the sampled distribution values where three significant figures results in a repeated value.

Table 6.4-7. Statistics for the Fracture-Matrix Partitioning Factor Distributions: (a) Lower and Mean Infiltration Scenarios for Glacial Transition Climate; (b) Upper Infiltration Scenario for Glacial Transition Climate.

	(a) Lower and Mean Infiltration Scenario	**(b) Upper Infiltration Scenario**
Average of Fracture—Matrix Partitioning Factors	1.16E-01	1.27E-02
Standard Deviation of Fracture-Matrix Partitioning Factors	1.82E-01	1.25E-02
95th Percentile Confidence Interval (Equation 58)	7.45E-02	5.11E-03
95th Percentile Confidence Interval—Percentage of Average	64.5%	40.2%

Output DTN: LB0307FMRADTRN.001

6.5 EFFECTS OF AIR IN FRACTURE

The results found for the model as discussed in Section 6.4 may be compared with the first-order model predictions from Equations 43 and 44. The fracture-matrix partitioning ratio, P_r, to first order is:

$$P_r = \frac{Pe_{fe} b_d}{Pe_m \left(1 - b_d\right) + Pe_{fe} b_d} \qquad \text{(Eq. 59)}$$

A comparison of the predictions for the fracture-matrix partitioning model based on Equation 59 with the results in Section 6.4 are given below. Inputs for this calculation are presented in Attachment VIII.

Table 6.5-1. Comparison of First-Order Model to Full Model

	Average Fracture-Matrix Partitioning Ratio	
	Full model	**First-order model**
Lower case	8.61E-02	8.92E-02
Mean case	1.45E-01	1.51E-01
Upper case	1.27E-02	1.33E-02

The results indicate that the first-order model explains most of the partitioning behavior. The first-order model is independent of the Fourier coefficients, as shown in Equation 59. Therefore, the solution is not sensitive to the details of the boundary conditions and location of the water film along the invert-rock boundary.

If the air gap in the fracture is included, the first-order solution becomes:

$$P_{ra} = \frac{Pe_{fe} b_d}{Pe_m \left(1 - \phi_f\right) + Pe_{fe} b_d} \qquad \text{(Eq. 60)}$$

where P_{ra} is the partitioning ratio including the air gap and ϕ_f is the fracture porosity. Equation 60 may be written in terms of P_r giving,

$$P_{ra} = \frac{P_r}{1 - \left(1 - P_r\right)\left(\dfrac{\phi_f - b_d}{1 - b_d}\right)} \qquad \text{(Eq. 61)}$$

The ratio of P_{ra} to P_r is unity for $P_r = 1$ and is largest for $P_r = 0$. The maximum ratio is

$$\frac{P_{ra}}{P_r} = \frac{1 - b_d}{1 - \phi_f} \qquad \text{(Eq. 62)}$$

However, ϕ_f and b_d are both much less than 1 so Equation 60 may be approximated as,

$$\frac{P_{ra}}{P_r} = 1 + \phi_f - b_d \qquad \text{(Eq. 63)}$$

Therefore, the maximum relative error is,

$$\frac{P_{ra} - P_r}{P_r} = \phi_f - b_d \qquad \text{(Eq. 64)}$$

which is less than the fracture porosity. This result supports the model approximation that the solution is not sensitive to the placement of the no-flux boundary either immediately adjacent to the water film (as in the model presented in Section 6.4) or displaced from this water film by an air gap in the fracture.

6.6 ADVECTIVE RELEASES FROM DRIFTS (DRIFTS WITH SEEPAGE)

For cases with water seeping into drifts, the rates of seepage are expected to be large with respect to the capacity for the matrix to conduct water. This is a result of the seepage threshold that tends to prevent seepage for locations where the percolation flux is low. Once the seepage threshold is exceeded, the seepage flux into the drift tends to be larger than the average percolation flux. Given that flux in the repository host rock is mainly in the fractures (more than 99%), the seepage flux in the drifts may be expected to predominantly enter the fractures at the base of the drift. These considerations lead to the hypothesis that under most circumstances, radionuclides released from drifts with seepage will be preferentially carried by the flow into the fractures. An approximate modeling treatment for fracture-matrix partitioning is to have all of the radionuclides released from drifts with seepage enter the fractures in the underlying rock.

6.7 COMPARISON OF FRACTURE-MATRIX PARTITIONING MODEL AND DRIFT SHADOW MODEL

Sections 6.3 and 6.4 present two models concerning the behavior of flow and transport in the region beneath waste emplacement drifts. In Section 6.3, the drift shadow model uses the dual-continuum method to show that a substantial perturbation to the flow field exists beneath waste emplacement drifts. A large zone of reduced flow is found for the fracture continuum, with a much smaller perturbation to the flow for the matrix continuum. The transport through the drift shadow is found to be much slower than transport initiated in unperturbed fracture flow. Sensitivity studies indicate that this behavior is largely due to initiation of transport in the matrix and the subsequent slow migration of radionuclides through the matrix to the fractures.

The fracture-matrix partitioning model presented in Section 6.4 is based on the premise that fracture flow around a drift does not behave like a homogeneous continuum, but that heterogeneity, anisotropy, and discrete fracture effects may results in water movement in the fractures much closer to the waste emplacement drift than found in Section 6.3. With the approximation of fracture flow close to the base of the waste emplacement drift, partitioning of releases from the drifts is not necessarily dominated by the relatively large matrix water content as compared with the fracture water content. The dynamics of the flow field in this model result in a competition between the fracture and matrix continua for radionuclide releases, and that leads to greater partitioning of the releases to the fractures. The greater releases of radionuclides to fractures and the more active flow system in the fracture-matrix partitioning model leads to more rapid transport of radionuclides in the UZ. Therefore, the fracture-matrix partitioning model was chosen to provide input for TSPA so that radionuclide transport in the unsaturated zone is not underestimated.

INTENTIONALLY LEFT BLANK

7. VALIDATION

Validation for the Drift-Scale Radionuclide Transport Model is divided into two parts. The first part concerns the validation of the process model. The second part concerns the validation of the abstraction model. Required process model validation methods are identified in BSC (2002 [160819], Attachment I, Section I-5). The methods identified are corroboration with alternative models, independent technical reviews, and publication in a refereed professional journal. At a minimum, one or more methods of model validation is required, per AP-SIII.10Q, *Models.* Note that the model validation presented in Section 7 deviates from the technical work plan (BSC 2002 [160819], Section I-5) in that an independent technical review specifically for model validation has not been conducted, nor publication in a peer-reviewed journal. Model validation for the process model was performed using corroboration with alternative models. Relevant existing data, analog site information, and laboratory testing are not available for validation of the drift-scale radionuclide transport model, therefore validation methods requiring corroborative data are not used. This validation section addresses corroboration with alternative models. In particular, BSC (2002 [160819], p. 60, Attachment I) states for corroboration with alternative models:

> Results of the case in which flow is undisturbed immediately below the drift will be evaluated. A comparison of this case with the dual-continuum model provides information on the sensitivity of the radionuclide partitioning to matrix and fractures upon leaving the waste emplacement drift, as a function of the flow field characteristics. The alternative model that results in greater radionuclide releases to the fractures will be implemented in TSPA so that radionuclide transport in the unsaturated zone is not underestimated. Available TSPA or process model sensitivity analyses may be used to justify validation criteria. A discussion of the model uncertainties will also be provided.

The validation method for the abstraction model specified in BSC (2002 [160819], p. 61, Attachment I) is corroboration of abstraction model with process model. In particular, BSC (2002 [160819], Attachment I, Section I-5) states for corroboration of abstraction model with process model:

> The main validation for an abstraction model is to show that it can provide results sufficiently close to the predictions of the supporting process model. The supporting process model in turn is validated to ensure appropriate representation of the physical processes and relevant parameters. In this way, the abstraction model is validated to represent the relevant processes in TSPA. In this case the supporting process model will be the one chosen for implementation in TSPA (see immediately above). Agreement within 20% will be the criterion for accepting the Drift-Scale Radionuclide Transport Abstraction Model as having been validated sufficiently for the purposes of LA (License Application).

7.1 PROCESS MODEL VALIDATION

The validation of the fracture-matrix partitioning model is based on comparisons with the drift shadow dual-continuum model.

The drift shadow model presented in Section 6.3 provides a detailed process-level description of the phenomena of unsaturated flow and transport in a fractured rock near a waste emplacement drift (Houseworth et al. 2003 [164394]). This model accounts for the presence of fractures and a porous rock matrix using a standard process-based description of unsaturated flow in a dual continuum that predicts the hydrodynamic effects of a waste emplacement drift on unsaturated flow patterns. The model parameters are based on the drift-scale calibrated properties parameter set, with an adjustment to the active fracture parameter as discussed in Section 6.3 to account for the effects of the lower fracture permeability on fracture-matrix interaction. Similarly, transport is modeled using a standard process-based description for an unsaturated dual-continuum using parameters applicable to advection, diffusion, sorption, and fracture-matrix interaction. The model uses the same conceptual basis as described in CRWMS M&O (2000 [141187]). The fundamental process representations for flow and transport used by the drift shadow model are the same as those used for other drift-scale models as discussed by BSC (2003 [163226]; 2003 [162267]; 2003 [162050]; 2003 [161530]; and 2003 [162318]), as well as mountain-scale models as discussed by BSC (2003 [163045]; 2001 [161340]; and CRWMS M&O 2000 [144454]). Therefore, a precedent exists for the approach used in the drift shadow model for describing flow and transport in a fractured rock.

The primary reason for not directly using the drift shadow model is that there is presently a lack of relevant observational data, the principal point of contention being the representation of processes in the fractures. The theory of flow and transport in a porous medium such as the rock matrix is well supported in the scientific literature through laboratory measurements and field tests. However, the scientific basis for the theory of unsaturated flow and transport in fractured rock is less well developed. Furthermore, not all features of fractured rock have been explored in the drift shadow model. For example, heterogeneity of the fracture network and potential effects of discrete fractures may lead to a reduction in the extent of the drift shadow. Given the potentially large effect of drift-scale transport on radionuclide transport rates through the UZ, the fracture-matrix partitioning model has been developed that limits the reliance on process descriptions of flow and transport in the fractures near a waste emplacement drift. This necessarily results in approximations from the standpoint of the theoretical framework used for the drift shadow model. The fracture-matrix partitioning model uses the following approximations that lead to greater flow and transport in fractures beneath a waste emplacement drift:

1. Fracture flow occurs beneath a waste emplacement drift within a distance less than the fracture spacing. Given fracture spacings that are, on average, less than one meter, the zone of reduced flow is greatly reduced in comparison with the shadow zone predicted by the drift shadow model.

2. The initial transient period, which is initially dominated by diffusive transfer into the rock, is not treated. This initial radionuclide partitioning ratio will be equal to the

water content ratio of the fractures and matrix, and will only asymptotically approach the predicted fracture-matrix partitioning ratio.

3. The effects of dryout during the boiling and rewetting periods are ignored, during which fracture water saturations are disproportionately reduced in comparison with the matrix. This will lead to preferential entry of radionuclides to the matrix during this thermally perturbed period.

The fracture-matrix partitioning model is discussed in detail in Section 6.4, with specific information on boundary conditions given in Section 6.4.1 and information on solution convergence in Section 6.4.4. Given that the model is steady-state, initial conditions are not applicable. Model calibration was not performed.

The results of the fracture matrix partitioning model clearly lead to more rapid radionuclide transport through the UZ as compared with the drift shadow model. The probability distribution for the partitioning ratio between the fractures and matrix for the drift interface model allows a non-zero fraction of the releases initially into the fractures, which will lead to relative rapid transport through the UZ for that release fraction. By comparison, the drift shadow model predicts significantly longer transport times for essentially all radionuclides.

In summary, the fracture-matrix partitioning model is valid based on the following results:

1. The transport results shown in Figure 6.3-7 demonstrate that releases to the matrix in an undisturbed flow field behave similarly to transport through the drift shadow. The figure also shows that releases to fractures in an undisturbed flow field travel through the model domain in about one year compared with several thousand years for releases to the matrix or the drift shadow.

2. The drift shadow model results in Figures 6.3-5 and 6.3-6 shows that transport times through the model domain are thousands to tens of thousands of years for essentially all radionuclides under a wide range of fracture and matrix flow conditions.

3. As can be seen in Table 6.4-5, the fracture-matrix partitioning model gives a distribution of releases to fractures of ranging from roughly 0.1% to 50% for the 5th to 95th percentile values, with a mean of 11.6% for all climates scenarios except for the glacial-transition upper climate scenario. The distribution of releases for the glacial-transition upper climate scenario is roughly 0.02% to 5% for the 5th to 95th percentile values, with an average of 1.27%. These releases to undisturbed fracture flow will result in transport through the near-drift region (drift-shadow model domain) that are orders of magnitude faster than releases to the matrix or in the drift shadow model.

Therefore, based on points 1, 2, and 3, the fracture-matrix partitioning model will result in a fast component of transport not found in the drift shadow model and leads to a conservative representation of drift-scale transport as compared to the drift shadow model. This satisfies the model validation requirement presented in the technical work plan that (BSC 2002 [160819], p. 60, Attachment I) “The alternative model that results in greater radionuclide releases to the fractures will be implemented in TSPA so that radionuclide transport in the unsaturated zone is not underestimated.” This provides the best possible validation of the model at the present time, due to the lack of data available for validation of the drift-scale radionuclide transport model. The collection of data or analog information is still needed such that validation of the drift-scale radionuclide transport model can be made at a level comparable to the validation documented for other models in the unsaturated zone (e.g., drift seepage model, unsaturated zone flow model, unsaturated zone transport model).

7.2 ABSTRACTION MODEL VALIDATION

The abstraction model for use in TSPA are the distributions that result from the fracture-matrix partitioning model, as described in Section 6.4.6. These distributions are shown in Figure 6.4-20 and tabulated in Table 6.4-5. The validation of the abstraction model is based on the direct sampling of these distributions in TSPA. As such, the abstraction model predictions for the fraction of releases to the fractures are statistically identical to the results of the fracture-matrix partitioning model and therefore lie within 20% of the process model predictions for the fraction of releases to the fractures, which is within the criterion for abstraction model validation. Therefore, the abstraction model is valid.

8. CONCLUSIONS

The diversion of percolating water around a waste emplacement drift results in an environment of greatly diminished flow inside the drift. In such an environment, the primary transport mechanism for radionuclides to migrate from the drift to the surrounding rock is by diffusion. Because of the relatively large water content of the matrix in comparison with the fractures, diffusive releases from waste emplacement drifts are highly partitioned to the matrix. Transport time for radionuclides initiated in the matrix has been found to be orders of magnitude longer than for radionuclides initiated in undisturbed fracture flow. The average (or 50%) breakthrough times in the submodel presented in Section 6.3.3.2 are dominated by matrix advection. Simulation results show that for these cases, most of the radionuclide mass still remains in the matrix at breakthrough. Therefore, the effects of the drift shadow on transport extend beyond the existing model boundary. For radionuclide releases from drifts without seepage, the results presented in this section indicate that transport times to the water table will be thousands to tens of thousands of years for nonsorbing radionuclides (such as technetium). For sorbing radionuclides, the transport times are considerably longer, according to the degree of sorption. For a weakly sorbing radionuclide such as neptunium, transport times are tens of thousands to hundreds of thousands of years. For a strongly sorbing radionuclide such as plutonium, transport times range from millions to tens of millions of years.

Sensitivity calculations show that the main effect of the drift shadow on transport is that radionuclide transport is initiated in the matrix. Subsequent effects of the drift shadow on the dynamics of the fracture or matrix flow fields have much less influence on transport. The long transport pathways in the matrix primarily result from initiation of transport in the matrix combined with the relatively “disconnected” nature of the fracture and matrix continua. Varying degrees of fracture-matrix interaction in the dual-permeability model are shown to have a significant influence on transport in the drift shadow.

The lack of observational evidence for the drift shadow has led to the development of the fracture-matrix partitioning model. In this model, the sensitivity results from the drift shadow model are used to focus the discussion of drift-scale transport on the behavior of radionuclide releases from drifts without seepage. In particular, the most important factor is the initiation of transport in the fractures or the matrix. The fracture-matrix partitioning model allows for undisturbed fracture flow to occur some distance beneath the drift, flow that is scaled by the fracture spacing to account for uncertainty in the drift shadow effect. Additional uncertainty is captured through sampling distributions for the following factors:

1. Fracture and matrix flux and saturation and matrix effective permeability over a wide range of average flow rates representing uncertainty in the UZ flow fields

2. Flow-focusing effects to account for uncertainty in variations in flow at the drift scale, which is smaller than the spatial resolution of the mountain-scale flow model

3. Invert thickness, porosity characteristics, and molecular diffusion rates that influence diffusive characteristics of the invert

4. Matrix diffusion rates, including the influence of partial matrix saturation

5. Fracture and matrix porosity and fracture residual saturation.

The fracture-matrix partitioning model assesses the fraction of releases from drifts without seepage to the fractures and matrix in the underlying rock. This assessment is based on a steady-state transport model where radionuclides diffuse through the crushed tuff invert in the drift to the fractures and matrix in the underlying rock. Due to the discrete nature of fractures and blockage of fracture flow by the drift, fracture flow is offset from the base of the drift by a fraction of the fracture spacing. Conversely, the continuous nature of the rock matrix leads to advective flux in the rock immediately below the drift. Thus, diffusive releases from the invert are transported away from the drift by advection in the rock matrix and by diffusion through the fractures to the point where fracture flow begins. The developed partitioning distributions are shown in Figure 6.4-20. These distributions are a result of uncertainties in the inputs (see Table 6.4-5). Similarity in the partitioning distribution for the lower and mean infiltration scenarios leads to the composite distribution for the fracture-matrix partitioning in 6.4-20a. The upper infiltration scenario leads to a distinct distribution as shown in 6.4-20b. Uncertainties in the distributions resulting from sampling uncertainties are indicated by the error bars in Figure 6.4-20. Implementation of these distribution in TSPA is given by the following steps:

1. Randomly select a mean value for the fracture matrix partitioning factor for all climate scenarios except the upper glacial transition climate from Table 6.4-6(a). For the upper glacial transition climate scenario, pick the mean from Table 6.4-6(b).

2. Select the fracture-matrix partitioning coefficient from a beta distribution with a range from 0 to 1, a mean value selected in step 1), and a standard deviation of the beta distribution based on the mean times the percentage from Table 6.4-7(a) times 1.96^{-1} for all climate scenarios except the upper glacial transition climate. The percentage is multiplied by 1.96^{-1} because the 95th percentile represents 1.96 standard deviations. For the upper glacial transition climate scenario, the standard deviation is the mean times the percentage from Table 6.4-7(b) times 1.96^{-1}.

The abstraction for drifts with seepage is discussed in Section 6.6. This abstraction conservatively allocates all of the releases from drifts with seepage into the fractures.

Output from this report for the drift shadow model is captured in Output-DTNs: LB0307DSRADTRN.001 and LB0307DSRADTRN.002 and in Output-DTN: LB0307FMRADTRN.001 for the fracture-matrix partitioning model.

Following release from the drifts to the rock, the radionuclide transport process is simulated using the particle-tracking model, which does not account for the effects of the drift on the flow field (CRWMS M&O 2000 [141418]). Thus, radionuclides are transported from the drifts in the undisturbed, UZ flow field. Use of these results for the partitioning of fracture-matrix releases is restricted to drifts with radionuclide releases dominated by diffusion, which in general are drifts without seepage. For drifts with seepage, the analysis in Section 6.5 indicates that advective-dominated releases are generally expected and that for this case, an adequate approximation is that all radionuclide releases enter the fracture continuum.

Barrier Description

The findings in this model report support the conclusion that for drifts without seepage, radionuclide releases from the drift to the rock will be preferentially partitioned to the rock matrix. Furthermore, initiation of transport in the rock matrix has a significant effect on the subsequent transport through the unsaturated zone. The difference in transport times through the drift-scale model domain for radionuclide transport initiated in rock matrix versus the fractures for undisturbed flow conditions is thousands to tens of thousands of years. The preferential release of radionuclides from drifts without seepage to the rock matrix results in substantial delays in radionuclide transport, leading to the conclusion that the presence of the drift, with or without a drift shadow, plays an important role in the delay of radionuclide transport. The magnitude of this effect on performance of the repository is a function of fraction of drifts that do not seep.

INTENTIONALLY LEFT BLANK

9. INPUTS AND REFERENCES

The following is a list of the references cited in this document. Column 1 represents the unique six digit numerical identifier (the Document Input Reference System [DIRS] number), which is placed in the text following the reference callout (e.g., BSC 2002 [160819]). The purpose of these numbers is to assist the reader in locating a specific reference. Within the reference list, multiple sources by the same author (e.g., BSC 2002) are sorted alphabetically by title.

9.1 DOCUMENTS CITED

103280 Abramowitz, M. and Stegun, I.A., eds. 1972. *Handbook of Mathematical Functions with Formulas, Graphs, and Mathematical Tables*. National Bureau of Standards, Applied Mathematics Series. 55, 1046. Washington, D.C.: U.S. Department of Commerce. TIC: 229060.

109715 Ahlers, C.F.; Finsterle, S.; and Bodvarsson, G.S. 1999. "Characterization and Prediction of Subsurface Pneumatic Response at Yucca Mountain, Nevada." *Journal of Contaminant Hydrology, 38*, (1-3), 47-68. New York, New York: Elsevier. TIC: 244160.

103949 Bandurraga, T.M. and Bodvarsson, G.S. 1999. "Calibrating Hydrogeologic Parameters for the 3-D Site-Scale Unsaturated Zone Model of Yucca Mountain, Nevada." *Journal of Contaminant Hydrology, 38*, (1-3), 25-46. New York, New York: Elsevier. TIC: 244160.

156269 Bear, J. 1972. *Dynamics of Fluids in Porous Media*. Environmental Science Series. Biswas, A.K., ed. New York, New York: Elsevier. TIC: 217356.

163443 Bodvarsson, G.S.; Wu, Y-S.; and Zhang, K. 2003. "Development of Discrete Flow Paths in Unsaturated Fractures at Yucca Mountain." *Journal of Contaminant Hydrology, 62-63*, 23-42. New York, New York: Elsevier. TIC: 254205.

159725 BSC (Bechtel SAIC Company) 2001. *Analysis of Hydrologic Properties Data*. ANL-NBS-HS-000002 REV 00 ICN 01. Las Vegas, Nevada: Bechtel SAIC Company. ACC: MOL.20020429.0296.

161316 BSC (Bechtel SAIC Company) 2001. *Calibrated Properties Model*. MDL-NBS-HS-000003 REV 00 ICN 01. Las Vegas, Nevada: Bechtel SAIC Company. ACC: MOL.20020311.0012.

156700 BSC (Bechtel SAIC Company) 2001. *Invert Diffusion Properties Model*. ANL-EBS-MD-000031 REV 01 ICN 01. Las Vegas, Nevada: Bechtel SAIC Company. ACC: MOL.20010801.0315.

161340 BSC (Bechtel SAIC Company) 2001. *Radionuclide Transport Models Under Ambient Conditions*. MDL-NBS-HS-000008 REV 00 ICN 01. Las Vegas, Nevada: Bechtel SAIC Company. ACC: MOL.20020409.0011.

160828 BSC (Bechtel SAIC Company) 2001. *Unsaturated Zone and Saturated Zone Transport Properties (U0100)*. ANL-NBS-HS-000019 REV 00 ICN 02. Las Vegas, Nevada: Bechtel SAIC Company. ACC: MOL.20020311.0017.

158726 BSC (Bechtel SAIC Company) 2001. *UZ Flow Models and Submodels*. MDL-NBS-HS-000006 REV 00 ICN 01. Las Vegas, Nevada: Bechtel SAIC Company. ACC: MOL.20020417.0382.

161619 BSC (Bechtel SAIC Company) 2002. *Advection Versus Diffusion in the Invert*. ANL-EBS-MD-000063 REV 00F. Las Vegas, Nevada: Bechtel SAIC Company. ACC: MOL.20030812.0379. TBV-5400

160247 BSC (Bechtel SAIC Company) 2002. *Analysis of Geochemical Data for the Unsaturated Zone*. ANL-NBS-HS-000017 REV 00 ICN 02. Las Vegas, Nevada: Bechtel SAIC Company. ACC: MOL.20020314.0051.

160819 BSC (Bechtel SAIC Company) 2002. *Technical Work Plan for: Performance Assessment Unsaturated Zone*. TWP-NBS-HS-000003 REV 02. Las Vegas, Nevada: Bechtel SAIC Company. ACC: MOL.20030102.0108.

160146 BSC (Bechtel SAIC Company) 2002. *Total System Performance Assessment-License Application Methods and Approach*. TDR-WIS-PA-000006 REV 00. Las Vegas, Nevada: Bechtel SAIC Company. ACC: MOL.20020923.0175.

161773 BSC (Bechtel SAIC Company) 2003. *Analysis of Hydrologic Properties Data*. MDL-NBS-HS-000014 REV 00. Las Vegas, Nevada: Bechtel SAIC Company. ACC: DOC.20030404.0004.

160240 BSC (Bechtel SAIC Company) 2003. *Calibrated Properties Model*. MDL-NBS-HS-000003 REV 01. Las Vegas, Nevada: Bechtel SAIC Company. ACC: DOC.20030219.0001.

162318 BSC (Bechtel SAIC Company) 2003. *Drift Scale THM Model*. MDL-NBS-HS-000017 REV 00. Las Vegas, Nevada: Bechtel SAIC Company. ACC: DOC.20030818.0003.

161530 BSC (Bechtel SAIC Company) 2003. *Drift-Scale Coupled Processes (DST and TH Seepage) Models*. MDL-NBS-HS-000015 REV 00. Las Vegas, Nevada: Bechtel SAIC Company. URN-1087

162050 BSC (Bechtel SAIC Company) 2003. *Drift-Scale Coupled Processes (DST and THC Seepage) Models*. MDL-NBS-HS-000001 REV 02. Las Vegas, Nevada: Bechtel SAIC Company. ACC: DOC.20030804.0004.

164101 BSC (Bechtel SAIC Company) 2003. *Repository Design Project, Repository/PA IED Emplacement Drift Committed Materials (2)*. 800-IED-WIS0-00302-000-00A. Las Vegas, Nevada: Bechtel SAIC Company. ACC: ENG.20030627.0004.

164069 BSC (Bechtel SAIC Company) 2003. *Repository Design Project, Repository/PA IED Emplacement Drift Configuration 1 of 2*. 800-IED-EBS0-00201-000-00A. Las Vegas, Nevada: Bechtel SAIC Company. ACC: ENG.20030630.0002.

164491 BSC (Bechtel SAIC Company) 2003. *Repository Design Project, Repository/PA IED Subsurface Facilities*. 800-IED-WIS0-00103-000-00Ab. Las Vegas, Nevada: Bechtel SAIC Company. ACC: MOL.20030813.0178. TBV-5397

162267 BSC (Bechtel SAIC Company) 2003. *Seepage Calibration Model and Seepage Testing Data*. MDL-NBS-HS-000004 REV 02. Las Vegas, Nevada: Bechtel SAIC Company. ACC: DOC.20030408.0004.

163226 BSC (Bechtel SAIC Company) 2003. *Seepage Model for PA Including Drift Collapse*. MDL-NBS-HS-000002 REV 02. Las Vegas, Nevada: Bechtel SAIC Company. ACC: DOC.20030709.0001.

163045 BSC (Bechtel SAIC Company) 2003. *UZ Flow Models and Submodels*. MDL-NBS-HS-000006 REV 01. Las Vegas, Nevada: Bechtel SAIC Company. ACC: DOC.20030818.0002.

161770 Canori, G.F. and Leitner, M.M. 2003. *Project Requirements Document*. TER-MGR-MD-000001 REV 01. Las Vegas, Nevada: Bechtel SAIC Company. ACC: DOC.20030404.0003.

101582 Conca, J.L. and Wright, J. 1990. "Diffusion Coefficients in Gravel Under Unsaturated Conditions." *Water Resources Research, 26*, (5), 1055-1066. Washington, D.C.: American Geophysical Union. TIC: 237421.

122990 Crank, J. 1975. *The Mathematics of Diffusion*. 2nd Edition. 1983 Reprint. Oxford, England: Clarendon Press. TIC: 9662.

141187 CRWMS M&O (Civilian Radioactive Waste Management System Management and Operating Contractor) 2000. *Conceptual and Numerical Models for UZ Flow and Transport*. MDL-NBS-HS-000005 REV 00. Las Vegas, Nevada: CRWMS M&O. ACC: MOL.19990721.0526.

136255 CRWMS M&O 2000. *Invert Configuration and Drip Shield Interface*. TDR-EDS-ST-000001 REV 00. Las Vegas, Nevada: CRWMS M&O. ACC: MOL.20000505.0232.

144454 CRWMS M&O 2000. *Mountain-Scale Coupled Processes (TH) Models*. MDL-NBS-HS-000007 REV 00. Las Vegas, Nevada: CRWMS M&O. ACC: MOL.19990721.0528.

141418 CRWMS M&O 2000. *Particle Tracking Model and Abstraction of Transport Processes*. ANL-NBS-HS-000026 REV 00. Las Vegas, Nevada: CRWMS M&O. ACC: MOL.20000502.0237.

153246 CRWMS M&O 2000. *Total System Performance Assessment for the Site Recommendation*. TDR-WIS-PA-000001 REV 00 ICN 01. Las Vegas, Nevada: CRWMS M&O. ACC: MOL.20001220.0045.

154291 CRWMS M&O 2001. *Abstraction of Drift Seepage*. ANL-NBS-MD-000005 REV 01. Las Vegas, Nevada: CRWMS M&O. ACC: MOL.20010309.0019.

163222 Dombrowski, H.S. and Brownell, L.E. 1954. "Residual Equilibrium Saturation of Porous Media." *Industrial & Engineering Chemistry, 46*, (6), 1207-1219. Easton, Pennsylvania: American Chemical Society. TIC: 254309.

163221 Dullien, F.A.L.; Lai, F.S.Y.; and MacDonald, I.F. 1986. "Hydraulic Continuity of Residual Wetting Phase in Porous Media." *Journal of Colloid and Interface Science, 109*, (1), 201-218. New York, New York: Academic Press. TIC: 254308.

163214 Finsterle, S.; Ahlers, C.F.; Trautz, R.C.; and Cook, P.J. 2003. "Inverse and Predictive Modeling of Seepage into Underground Openings." *Journal of Contaminant Hydrology, 62-63*, 89-109. New York, New York: Elsevier. TIC: 254205.

154365 Freeze, G.A.; Brodsky, N.S.; and Swift, P.N. 2001. *The Development of Information Catalogued in REV00 of the YMP FEP Database*. TDR-WIS-MD-000003 REV 00 ICN 01. Las Vegas, Nevada: Bechtel SAIC Company. ACC: MOL.20010301.0237.

101173 Freeze, R.A. and Cherry, J.A. 1979. *Groundwater*. Englewood Cliffs, New Jersey: Prentice-Hall. TIC: 217571.

163236 Hogg, R.V. and Craig, A.T. 1978. *Introduction to Mathematical Statistics*. 4th Edition. New York, New York: Macmillan. TIC: 254311.

163233 Houseworth, J. 2003. UZ PMR for SR - Shadow Zone. Scientific Notebook SN-LBNL-SCI-205-V1. ACC: MOL.20030319.0086.

164394 Houseworth, J.E.; Finsterle, S.; and Bodvarsson, G.S. 2003. "Flow and Transport in the Drift Shadow in a Dual-Continuum Model." *Journal of Contaminant Hydrology, 62-63*, 133-156. New York, New York: Elsevier. TIC: 254205.

163714 Li, G. and Tsang, C-F. 2003. "Seepage into Drifts with Mechanical Degradation." *Journal of Contaminant Hydrology, 62-63*, 157-172. New York, New York: Elsevier. TIC: 254205.

105729 Liu, H.H.; Doughty, C.; and Bodvarsson, G.S. 1998. "An Active Fracture Model for Unsaturated Flow and Transport in Fractured Rocks." *Water Resources Research, 34*, (10), 2633-2646. Washington, D.C.: American Geophysical Union. TIC: 243012.

123093 Moridis, G.J.; Wu, Y-S.; and Pruess, K. 1999. *EOS9nT: A TOUGH2 Module for the Simulation of Water Flow and Solute/Colloid Transport in the Subsurface*. LBNL-42351. Berkeley, California: Lawrence Berkeley National Laboratory. TIC: 246520.

148719 Newman, J. 1973. *Electrochemical Systems*. Englewood Cliffs, New Jersey: Prentice-Hall. TIC: 210201.

163274 NRC (U.S. Nuclear Regulatory Commission) 2003. *Yucca Mountain Review Plan, Final Report*. NUREG-1804, Rev. 2. Washington, D.C.: U.S. Nuclear Regulatory Commission, Office of Nuclear Material Safety and Safeguards. TIC: 254568.

105743 Philip, J.R.; Knight, J.H.; and Waechter, R.T. 1989. "Unsaturated Seepage and Subterranean Holes: Conspectus, and Exclusion Problem for Circular Cylindrical Cavities." *Water Resources Research, 25*, (1), 16-28. Washington, D.C.: American Geophysical Union. TIC: 239117.

160778 Pruess, K.; Oldenburg, C.; and Moridis, G. 1999. *TOUGH2 User's Guide, Version 2.0*. LBNL-43134. Berkeley, California: Lawrence Berkeley National Laboratory. TIC: 253038.

163008 Reimus, P.W.; Ware, S.D.; Benedict, F.C.; Warren, R.G.; Humphrey, A.; Adams, A.; Wilson, B.; and Gonzales, D. 2002. *Diffusive and Advective Transport of {superscript 3}H, {superscript 14}C, and {superscript 99}Tc in Saturated, Fractured Volcanic Rocks from Pahute Mesa, Nevada*. LA-13891-MS. Los Alamos, New Mexico: Los Alamos National Laboratory. TIC: 253905.

104252 Richards, L.A. 1931. "Capillary Conduction of Liquids Through Porous Mediums." *Physics, 1*, 318-333. [New York, New York: American Physical Society]. TIC: 225383.

163213 Sato, H.; Yui, M.; and Yoshikawa, H. 1996. "Ionic Diffusion Coefficients of Cs+, Pb{superscript 2}+, Sm{superscript 3}+, Ni{superscript 2}+, SeO{superscript 2-}{subscript 4} and TcO{superscript -}{subscript 4} in Free Water Determined from Conductivity Measurements." *Journal of Nuclear Science and Technology, 33*, (12), 950-955. Tokyo, Japan: Atomic Energy Society of Japan. TIC: 254307.

164047 Sato, S.; Otsuka, T.; Kuroda, Y.; Higashihara, T.; and Ohashi, H. 2001. "Diffusion of Helium in Water-Saturated, Compacted Sodium Montmorillonite." *Journal of Nuclear Science and Technology, 38*, (7), 577-580. [Tokyo, Japan: Atomic Energy Society of Japan]. TIC: 254463.

160355 USGS (U.S. Geological Survey) 2001. *Simulation of Net Infiltration for Modern and Potential Future Climates*. ANL-NBS-HS-000032 REV 00 ICN 02. Denver, Colorado: U.S. Geological Survey. ACC: MOL.20011119.0334.

100610 van Genuchten, M.T. 1980. "A Closed-Form Equation for Predicting the Hydraulic Conductivity of Unsaturated Soils." *Soil Science Society of America Journal, 44*, (5), 892-898. Madison, Wisconsin: Soil Science Society of America. TIC: 217327.

163234 Wang, J.S. 2003. Scientific Notebooks Referenced in Model Report U0230, Drift-Scale Radionuclide Transport, MDL-NBS-HS-000016 REV 00." Interoffice correspondence from J.S. Wang (BSC) to File, August 18, 2003, with attachments. ACC: MOL.20030818.0293.

163215 Wang, J.S.Y. and Bodvarsson, G.S. 2003. "Evolution of the Unsaturated Zone Testing at Yucca Mountain." *Journal of Contaminant Hydrology, 62-63*, 337-360. New York, New York: Elsevier. TIC: 254205.

102865 Weast, R.C. and Astle, M.J., eds. 1979. *CRC Handbook of Chemistry and Physics*. 60th Edition. 2nd Printing 1980. Boca Raton, Florida: CRC Press. TIC: 245312.

163216 Weinberger, H.F. 1965. *A First Course in Partial Differential Equations*. New York, New York: John Wiley & Sons. TIC: 254310.

Software Cited

139918 LBNL (Lawrence Berkeley National Laboratory) 09/16/1999. *Software Code: iTOUGH2*. V4.0. SUN, DEC. 10003-4.0-00.

134141 LBNL (Lawrence Berkeley National Laboratory) 1999. *Software Code: EXT*. V1.0. Sun. 10047-1.0-00.

113943 LBNL (Lawrence Berkeley National Laboratory) 1999. *Software Code: TOUGH2*. V1.11 MEOS9nTV1.0. MAC, SUN, DEC/Alpha, PC. 10065-1.11MEOS9NTV1.0-00.

152823 LBNL (Lawrence Berkeley National Laboratory) 2000. Soft*ware Routine: AddBound*. V1.0. SUN w/Unix OS. 10357-1.0-00.

152816 LBNL (Lawrence Berkeley National Laboratory) 2000. *Software Routine: CutDrift*. V1.0. SUN w/Unix OS. 10375-1.0-00.

9.2 CODES, STANDARDS, REGULATIONS, AND PROCEDURES

156605 10 CFR 63. Energy: Disposal of High-Level Radioactive Wastes in a Geologic Repository at Yucca Mountain, Nevada. Readily available.

AP-2.22Q, Rev. 1. *Classification Analyses and Maintenance of the Q-List*. Washington, D.C.: U.S. Department of Energy, Office of Civilian Radioactive Waste Management. ACC: DOC.20030807.0002.

AP-SI.1Q, Rev. 5, ICN 1. *Software Management.* Washington, D.C.: U.S. Department of Energy, Office of Civilian Radioactive Waste Management. ACC: DOC.20030708.0001.

AP-SIII.10Q, Rev. 1, ICN 2. *Models.* Washington, D.C.: U.S. Department of Energy, Office of Civilian Radioactive Waste Management. ACC: DOC.20030627.0003.

9.3 SOURCE DATA, LISTED BY DATA TRACKING NUMBER

148751 LA0003AM831341.001. Probability Distributions for Sorption Coefficients (Kd's). Submittal date: 03/29/2000.

149557 LA0003JC831362.001. Preliminary Matrix Diffusion Coefficients for Yucca Mountain Tuffs. Submittal date: 4/10/2000.

159525 LB0205REVUZPRP.001. Fracture Properties for UZ Model Layers Developed from Field Data. Submittal date: 05/14/2002.

159672 LB0207REVUZPRP.002. Matrix Properties for UZ Model Layers Developed from Field and Laboratory Data. Submittal date: 07/15/2002.

161788 LB0208UZDSCPLI.002. Drift-Scale Calibrated Property Sets: Lower Infiltration Data Summary. Submittal date: 08/26/2002.

161243 LB0208UZDSCPMI.002. Drift-Scale Calibrated Property Sets: Mean Infiltration Data Summary. Submittal date: 08/26/2002.

163044 LB03023DSSCP9I.001. 3-D Site Scale UZ Flow Field Simulations for 9 Infiltration Scenarios. Submittal date: 02/28/2003.

161787 LB0302UZDSCPUI.002. Drift-Scale Calibrated Property Sets: Upper Filtration Data Summary. Submittal date: 02/05/2003.

110226 LB990861233129.001. Drift Scale Calibrated 1-D Property Set, FY99. Submittal date: 08/06/1999.

104055 LB997141233129.001. Calibrated Basecase Infiltration 1-D Parameter Set for the UZ Flow and Transport Model, FY99. Submittal date: 07/21/1999.

161496 MO0301SEPFEPS1.000. LA FEP List. Submittal date: 01/21/2003.

9.4 OUTPUT DATA, LISTED BY DATA TRACKING NUMBER

LB0307DSRADTRN.001. Drift Shadow Model: Simulations. Submittal date: 07/24/2003.

LB0307DSRADTRN.002. Drift Shadow Model: Data Summaries. Submittal date: 07/24/2003.

LB0307FMRADTRN.001. Fracture-Matrix Partitioning Model: Spreadsheet Calculations. Submittal date: 07/31/2003.

INTENTIONALLY LEFT BLANK

ATTACHMENT I – SAMPLING FOR FRACTURE FREQUENCY (OR FRACTURE SPACING)

This attachment provides additional information pertaining to Section 6.4.5 of the main text. Fracture frequency sampling uses the mean and standard deviations as given in Table I-1. The standard deviations for the tsw35 and tsw36 units are computed using the correlation shown in Figure 6.4-13. The mean and standard deviation for the natural logarithm of f is related to the mean and standard deviation for f through the following relationships (Hogg and Craig 1978 [163236], pp. 180 and 432) (see Attachment XI for detailed derivation):

$$\mu_{\ln(f)} = \ln\left(\mu_f\right) - \frac{1}{2}\ln\left(1+\frac{\sigma_f^2}{\mu_f^2}\right) \qquad \text{(Eq. I-1)}$$

$$\sigma_{\ln(f)} = \sqrt{\ln\left(1+\frac{\sigma_f^2}{\mu_f^2}\right)} \qquad \text{(Eq. I-2)}$$

Table I-1. Fracture Frequency and Standard Deviation

	Frequency (m^{-1})	Std Dev Frequency (m^{-1})	Equation I-1	Equation I-2
UZ Model Layer	μ_f	σ_f	$\mu_{\ln(f)}$	$\sigma_{\ln(f)}$
tsw33	0.81	1.03	-0.692	0.981
tsw34	4.32	3.42	1.22	0.698
tsw35	3.16	2.63	0.887	0.725
tsw3[67]	4.02	3.34	1.13	0.725

Source: DTN: LB0205REVUZPRP.001 [159525]; and Output-DTN: LB0307FMRADTRN.001

The sampling for the lognormal distribution uses the rational approximation of the inverse cumulative probability distribution for a Gaussian random variable as given in Equation 26.2.23 of Abramowitz and Stegun (1972 [103280]). See Scientific Notebook by Wang (2003 [163234], SN-LBNL-SCI-236-V1, pp. 40–42) for a discussion of the generation of Gaussian random numbers. Table I-2 presents a portion of the output from the formulation as performed in an Excel spreadsheet for the tsw35 model unit. See Wang (2003 [163234], SN-LBNL-SCI-236-V1, p. 46) and Output-DTN: LB0307FMRADTRN.001 for the complete output.

The sequence of calculations are as follows:

Column A: Uniform random numbers generated by the Excel spreadsheet function RAND() and saved. These are the cumulative probabilities, p.

Column B: The normalized Gaussian random number corresponding to the cumulative probability in Column A.

Column C: The corresponding random natural logarithm of fracture frequency is derived from the normalized Gaussian random variable through the normalization definition:

$$f = x_p \sigma_{\ln(f)} + \mu_{\ln(f)} \qquad \text{(Eq. I-3)}$$

where $\mu_{\ln(f)}$ and $\sigma_{\ln(f)}$ are defined in Equations I-1 and I-2.

In Excel, this is

Crn=Brn*Irn+Hrn

Column D: This column calculates the fracture frequency through the identity

$$f = \exp(\ln(f)) \qquad \text{(Eq. I-5)}$$

In Excel, this is

Drn=exp(Crn)

Column E: The fracture half-spacing, in millimeters, is computed from the fracture frequency based on the relationship

$$h_f = \frac{1000}{2f} \qquad \text{(Eq. I-6)}$$

In Excel, this is

Ern=1000/(2*Drn)

Column F: Uniform random numbers generated by the Excel spreadsheet function RAND() and saved.

Column G: The distance beneath the drift where fracture flow occurs, in millimeters, is defined by a uniform random distribution between 0 and the fracture spacing. Therefore, this is just the uniform random number between 0 and 1 in Column O, multiplied by the corresponding fracture spacing. In Excel, this is

Grn=2*Ern*Frn

Column H: Contains the value of $\mu_{\ln(f)}$ as computed from Equation I-1

Column I: Contains the value of $\sigma_{\ln(f)}$ as computed from Equation I-2.

Table I-2. Fracture Frequency and Spacing in the tsw35

	A	B	C	D	E	F	G	H	I
1	Fixed Uniform Random Number (P)	x_P - norm. Gaussian random number	x – Gaussian random number	Fracture frequency (m^{-1})	Fracture Half-Spacing (mm)	Fixed Uniform Random Number (P)	Distance for fracture flow beneath drift (mm)	mean ln(f) tsw35	Standard deviation ln(f) tsw35
2	5.8511E-01	2.1459E-01	1.04E+00	2.84E+00	1.76E+02	4.5126E-01	1.59E+02	8.87E-01	7.25E-01
3	5.4439E-01	1.1124E-01	9.68E-01	2.63E+00	1.90E+02	9.1458E-01	3.48E+02		
4	6.4091E-01	3.6045E-01	1.15E+00	3.15E+00	1.59E+02	3.3211E-01	1.05E+02		
5	5.9792E-01	2.4755E-01	1.07E+00	2.91E+00	1.72E+02	8.5178E-01	2.93E+02		
6	3.5424E-01	-3.7345E-01	6.16E-01	1.85E+00	2.70E+02	5.2193E-01	2.82E+02		
7	2.0906E-01	-8.0950E-01	3.00E-01	1.35E+00	3.70E+02	6.2457E-02	4.63E+01		
8	3.6657E-01	-3.4052E-01	6.40E-01	1.90E+00	2.64E+02	6.0227E-01	3.18E+02		
9	2.4803E-01	-6.8040E-01	3.94E-01	1.48E+00	3.37E+02	9.8595E-02	6.65E+01		
10	1.3127E-01	-1.1205E+00	7.47E-02	1.08E+00	4.64E+02	5.1294E-01	4.76E+02		
11	3.9488E-01	-2.6619E-01	6.94E-01	2.00E+00	2.50E+02	7.5245E-01	3.76E+02		
12	3.5507E-01	-3.7123E-01	6.18E-01	1.85E+00	2.70E+02	5.5208E-02	2.98E+01		
13	3.2690E-01	-4.4805E-01	5.62E-01	1.75E+00	2.85E+02	4.1146E-01	2.35E+02		
14	7.3161E-01	6.1735E-01	1.33E+00	3.80E+00	1.32E+02	1.6819E-01	4.43E+01		
15	3.7473E-01	-3.1891E-01	6.56E-01	1.93E+00	2.60E+02	1.0001E-03	5.19E-01		
16	4.3275E-01	-1.6904E-01	7.64E-01	2.15E+00	2.33E+02	3.3327E-02	1.55E+01		
17	2.2638E-01	-7.5058E-01	3.43E-01	1.41E+00	3.55E+02	5.1599E-01	3.66E+02		
18	4.8791E-01	-3.0228E-02	8.65E-01	2.38E+00	2.11E+02	7.7558E-01	3.27E+02		
19	9.6566E-01	1.8210E+00	2.21E+00	9.09E+00	5.50E+01	1.4702E-01	1.62E+01		
20	9.9064E-01	2.3515E+00	2.59E+00	1.34E+01	3.74E+01	7.1911E-02	5.38E+00		
21	7.6046E-01	7.0750E-01	1.40E+00	4.05E+00	1.23E+02	4.8032E-01	1.18E+02		
22	6.5544E-01	3.9961E-01	1.18E+00	3.24E+00	1.54E+02	4.3202E-01	1.33E+02		
23	2.8080E-01	-5.8009E-01	4.66E-01	1.59E+00	3.14E+02	6.6853E-02	4.19E+01		
24	9.7585E-01	1.9751E+00	2.32E+00	1.02E+01	4.92E+01	7.7782E-01	7.65E+01		
25	9.9035E-01	2.3403E+00	2.58E+00	1.32E+01	3.77E+01	1.9658E-01	1.48E+01		
26	4.8014E-01	-4.9667E-02	8.51E-01	2.34E+00	2.13E+02	8.7179E-01	3.72E+02		
27	6.7670E-01	4.5806E-01	1.22E+00	3.38E+00	1.48E+02	1.0364E-01	3.06E+01		
28	6.7628E-02	-1.4940E+00	-1.96E-01	8.22E-01	6.08E+02	5.7641E-02	7.01E+01		
29	3.8513E-01	-2.9160E-01	6.76E-01	1.97E+00	2.54E+02	3.0107E-01	1.53E+02		
30	6.0259E-01	2.5965E-01	1.08E+00	2.93E+00	1.71E+02	9.8363E-01	3.36E+02		

Output-DTN: LB0307FMRADTRN.001

INTENTIONALLY LEFT BLANK

ATTACHMENT II – FRACTURE AND MATRIX FLUXES AND WATER SATURATIONS

This attachment provides additional information pertaining to Section 6.4.5 of the main text. Fracture and matrix water saturations and fluxes and matrix relative permeabilities are available from the UZ Flow Model results. As discussed in Section 4.1.1, the lower, mean, and upper infiltration scenarios for the glacial transition climate are evaluated. Table II-1 gives an example of the fluxes, saturations, and matrix relative permeabilities for mean infiltration scenario for model grid cells within the waste emplacement horizon, excluding fault zones. The values are arranged by rock unit (tsw33, tsw34, tsw35, and tsw36). The flux for a given cell is a vector with three components; therefore, the component with the maximum fracture flux (and corresponding matrix flux) was selected for each cell. See Scientific Notebook by Wang (2003 [163234], SN-LBNL-SCI-236-V1, pp. 47–52) for a discussion of how these values were extracted from the 3-D flow fields. Table II-1 gives a portion of the values extracted for the tsw33 and tsw34 model units. See Wang (2003 [163234], SN-LBNL-SCI-236-V1, pp. 50–53) and Output-DTN: LB0307FMRADTRN.001 for the complete output.

Table II-1. Fracture and Matrix Fluxes, Saturations, and Matrix Relative Permeability—Glacial Transition Mean

	A	B	C	D	E	F	G	H
1	**Rock Unit**	**Fracture Cell Name**	**Fracture Flux (mm/yr)**	**Fracture Saturation**	**Matrix Cell Name**	**Matrix Flux (mm/yr)**	**Matrix Saturation**	**Matrix Relative Permeability**
2	tsw33	F012Bl76	5.3967E+00	1.3240E-02	M012Bl76	2.4032E-01	9.3761E-01	1.1223E-01
3	tsw33	F012Bl78	5.7350E+00	1.3264E-02	M012Bl78	1.4520E-01	9.0879E-01	7.1708E-02
4	tsw33	F012Cl72	4.8155E+00	1.3061E-02	M012Cl72	1.3236E+00	9.9786E-01	5.4681E-01
5	tsw33	F012Cl74	6.6185E+00	1.3454E-02	M012Cl74	5.1798E-01	9.7267E-01	2.1822E-01
6	tsw33	F012Cm70	9.7583E+00	1.3937E-02	M012Cm70	5.0937E-01	9.7432E-01	2.2678E-01
7	tsw33	F012Dg58	1.0083E+01	1.4374E-02	M012Dg58	2.2577E-01	9.3205E-01	1.0250E-01
8	tsw33	F012Dl68	1.3328E+01	1.4453E-02	M012Dl68	5.3696E-01	9.7656E-01	2.3933E-01
9	tsw33	F012Dl70	6.9879E+00	1.3254E-02	M012Dl70	5.5948E-01	9.7693E-01	2.4154E-01
10	tsw33	F012Dl71	3.5104E+00	1.2386E-02	M012Dl71	1.2656E+00	9.9586E-01	4.7057E-01
11	tsw33	F012Dl75	4.4996E+00	1.2746E-02	M012Dl75	2.6302E-01	9.4760E-01	1.3303E-01
12	tsw33	F012Dl77	4.2020E+00	1.2657E-02	M012Dl77	2.1155E-01	9.3789E-01	1.1275E-01
13	tsw33	F012Dl79	5.5142E+00	1.3038E-02	M012Dl79	4.4544E-01	9.6898E-01	2.0103E-01
14	tsw33	F012Ef89	1.8602E+01	1.4758E-02	M012Ef89	1.4086E-01	9.5004E-01	1.3891E-01
15	tsw33	F012Eg 2	1.5102E+01	1.5319E-02	M012Eg 2	1.1983E-01	9.2449E-01	9.0951E-02
16	tsw33	F012Eg14	4.0953E+00	1.2794E-02	M012Eg14	5.8384E-02	9.0131E-01	6.4266E-02
17	tsw33	F012Eg25	4.2045E+00	1.2854E-02	M012Eg25	5.3101E-02	8.5649E-01	3.4394E-02
18	tsw33	F012Eg36	6.6068E+00	1.3531E-02	M012Eg36	1.1091E-01	9.1961E-01	8.4365E-02
19	tsw33	F012Eg47	7.4195E+00	1.3779E-02	M012Eg47	1.6404E-01	9.1500E-01	7.8658E-02
20	tsw33	F012Eh 1	2.5267E+01	1.6781E-02	M012Eh 1	1.8512E-01	9.3937E-01	1.1556E-01
21	tsw33	F012El73	4.1465E+00	1.2600E-02	M012El73	4.8153E-01	9.7170E-01	2.1347E-01
22	tsw33	F012Fg26	4.5607E+00	1.2340E-02	M012Fg26	1.0880E-01	9.4168E-01	1.2012E-01
23	tsw33	F012Fg59	3.4216E+01	1.6465E-02	M012Fg59	3.2473E-01	9.6741E-01	1.9434E-01
24	tsw33	F012Fg70	3.3638E+01	1.6356E-02	M012Fg70	2.1330E-01	9.5857E-01	1.6265E-01
25	tsw33	F012Fg80	2.0564E+01	1.6174E-02	M012Fg80	1.4723E-01	9.3185E-01	1.0217E-01
26	tsw33	F012Fg90	1.9384E+01	1.6000E-02	M012Fg90	1.3500E-01	9.2880E-01	9.7324E-02
27	tsw34	F0013g 3	3.5168E+00	1.4929E-02	M0013g 3	1.2727E-02	9.5988E-01	2.0111E-01
28	tsw34	F0013g48	2.6890E+01	2.2664E-02	M0013g48	1.5652E-02	9.7120E-01	2.5171E-01
29	tsw34	F0013g91	1.4310E+01	1.9454E-02	M0013g91	1.4594E-02	9.6798E-01	2.3541E-01
30	tsw34	F0013h 2	9.6354E+00	1.9077E-02	M0013h 2	6.9779E-02	9.6752E-01	2.3319E-01

Output DTN: LB0307FMRADTRN.001

INTENTIONALLY LEFT BLANK

ATTACHMENT III – SAMPLING FOR FLOW FOCUSING FACTOR

This attachment provides additional information pertaining to Section 6.4.5 of the main text. The cumulative probability distribution for the flow focusing factor is given by Bodvarsson et al. (2003 [163443], Figure 13):

$$P = -0.3137F^4 + 5.4998F^3 - 35.66F^2 + 102.3F - 11.434 \qquad \text{(Eq. III-1)}$$

where F is the flow focusing factor and *P* is the cumulative probability in as a percentage. The correlation is limited to a range of *F* between approximately 0.12 to 5. The equation is evaluated and interpolated to evenly spaced values of *P*, 1, 2, 3, …, 100. Then, the factor is sampled using a uniform random number scaled between 1 and 100 and truncated to an integer. This factor does not depend on any particular properties of the host rock. Table III-1 presents a portion of the output from the formulation as performed in an Excel spreadsheet. See Wang (2003 [163234], SN-LBNL-SCI-236-V1, p. 54) and DTN: LB0307FMRADTRN.001 for the complete output.

The sequence of calculations are described here:

Column A: This column contains a series of values for the normalized flux generated between 0.12 and 5.02.

Column B: The cumulative probability is computed from the relationship given in Equation III-1 In Excel, this is calculated as

Brn=-11.434 +102.3*Arn-35.66*Arn^2+5.4998*Arn^3-0.3137*Arn^4

Column C: A series of evenly spaced values of the cumulative probability.

Column D: The normalized flux is interpolated to the evenly spaced values in Column C. This is done using the following Excel formula:

Drn=Arn+(Crn-Brn)*((A(rn+1)-Arn)/(B(rn+1)-Brn))

Column E: A uniform random number between 1 and 100 is used to randomly select a normalized flux. The Excel formula is

Ern=1+99*RAND(),

which is copied and saved in Column E.

Column F: Round off the random number to an integer. The Excel formula is

Frn=ROUND(Ern,0)

Column G: Use the random integer to find the corresponding normalized flux. The Excel formula is

Grn=INDEX(D$3:D$103,Frn)

Table III-1. Flow-Focusing Factor

	A	B	C	D	E	F	G
1	**Normalized Flux**	**Cumulative Probability (%)**	**Cumulative Probability (%)**	**Interpolated Normalized Flux**	**Fixed Uniform Random Number**	**Uniform Random Integer**	**Flow Focusing Factor**
2	1.16E-01	8.81E-07	0.00E+00	1.16E-01	7.8382E+01	78	1.47E+00
3	1.20E-01	3.38E-01	1.00E+00	1.27E-01	9.1213E+01	91	2.10E+00
4	1.30E-01	1.27E+00	2.00E+00	1.38E-01	5.2710E+01	53	8.51E-01
5	1.40E-01	2.20E+00	3.00E+00	1.49E-01	6.2073E+01	62	1.04E+00
6	1.50E-01	3.13E+00	4.00E+00	1.60E-01	3.7861E+01	38	5.96E-01
7	1.60E-01	4.04E+00	5.00E+00	1.71E-01	2.6944E+01	27	4.38E-01
8	1.80E-01	5.86E+00	6.00E+00	1.82E-01	2.0972E+01	21	3.60E-01
9	1.90E-01	6.75E+00	7.00E+00	1.93E-01	5.6278E+01	56	9.09E-01
10	2.00E-01	7.64E+00	8.00E+00	2.04E-01	8.8144E+01	88	1.91E+00
11	2.10E-01	8.53E+00	9.00E+00	2.15E-01	8.6708E+01	87	1.85E+00
12	2.20E-01	9.40E+00	1.00E+01	2.27E-01	8.6516E+00	9	2.15E-01
13	2.30E-01	1.03E+01	1.10E+01	2.38E-01	8.9982E+01	90	2.03E+00
14	2.40E-01	1.11E+01	1.20E+01	2.50E-01	6.3578E+01	64	1.08E+00
15	2.60E-01	1.28E+01	1.30E+01	2.62E-01	5.0222E+01	50	7.95E-01
16	2.70E-01	1.37E+01	1.40E+01	2.74E-01	5.7781E+01	58	9.49E-01
17	2.80E-01	1.45E+01	1.50E+01	2.86E-01	3.7505E+01	38	5.96E-01
18	2.90E-01	1.54E+01	1.60E+01	2.98E-01	4.0043E+01	40	6.27E-01
19	3.00E-01	1.62E+01	1.70E+01	3.10E-01	1.1477E+01	11	2.38E-01
20	3.10E-01	1.70E+01	1.80E+01	3.22E-01	3.7317E+00	4	1.60E-01
21	3.30E-01	1.86E+01	1.90E+01	3.35E-01	4.9257E+00	5	1.71E-01
22	3.40E-01	1.94E+01	2.00E+01	3.47E-01	6.5344E+01	65	1.10E+00
23	3.50E-01	2.02E+01	2.10E+01	3.60E-01	2.9530E+01	30	4.79E-01
24	3.60E-01	2.10E+01	2.20E+01	3.72E-01	4.2111E+01	42	6.59E-01
25	3.80E-01	2.26E+01	2.30E+01	3.85E-01	4.7234E+01	47	7.42E-01
26	3.90E-01	2.34E+01	2.40E+01	3.98E-01	7.4482E+01	74	1.34E+00
27	4.00E-01	2.41E+01	2.50E+01	4.12E-01	7.9962E+01	80	1.55E+00
28	4.20E-01	2.56E+01	2.60E+01	4.25E-01	4.3791E+01	44	6.92E-01
29	4.30E-01	2.64E+01	2.70E+01	4.38E-01	1.5301E+01	15	2.86E-01
30	4.40E-01	2.71E+01	2.80E+01	4.52E-01	8.8079E+01	88	1.91E+00

Output-DTN: LB0307FMRADTRN.001

ATTACHMENT IV – SAMPLING FOR FRACTURE AND MATRIX POROSITY

This attachment provides additional information pertaining to Section 6.4.5 of the main text. Fracture and matrix average porosity values and standard deviations are given in Section 4.1.1. No standard deviations are available for fracture porosity in the tsw33, tsw35, and tsw36. Therefore, values were computed such that the ratio of the standard deviation to the mean in these units is the same as the ratio for the tsw34. The average and standard deviations for fracture and matrix porosities are given in Table IV-1.

Table IV-1. Fracture and Matrix Porosity Data

UZ Model Layer	Average fracture porosity[a] (-)	Fracture porosity Std deviation[a] (-)	Average Matrix Porosity[b]	Standard Deviation for Matrix Porosity[b]
tsw33	5.8E-3	1.71E-03[c]	0.155	0.030
tsw34	8.5E-3	2.50E-03	0.111	0.020
tsw35	9.6E-3	2.82E-03[c]	0.131	0.031
tsw3[67]	1.3E-2	3.82E-03[c]	0.103	0.025

[a] DTN: LB0205REVUZPRP.001 [159525]
[b] DTN: LB0207REVUZPRP.002 [159672]
[c] Derived values – see text above.

Porosities are modeled using the beta distribution, with the mean values and standard deviations as indicated in Table IV-1 and for all cases, a maximum of 1 and a minimum of 0.

The sampling for the beta distribution uses the approximation for the inverse as given in Equation 26.5.22 of Abramowitz and Stegun (1972 [103280]). This method requires the generation of a Gaussian random number. Gaussian random numbers are computed using the rational approximation for the inverse cumulative probability distribution for a Gaussian random variable, as given in Equation 26.2.23 of Abramowitz and Stegun (1972 [103280]). See Scientific Notebook by Wang (2003 [163234], SN-LBNL-SCI-236-V1, pp. 40–42) for a discussion of the generation of Gaussian random numbers. Table IV-2 presents a portion of the output from the formulation as performed in an Excel spreadsheet for the fracture and matrix porosities of the tsw35 model unit. See Wang (2003 [163234], SN-LBNL-SCI-236-V1, p. 59) and DTN: LB0307FMRADTRN.001 for the complete output.

The sequence of calculations are as follows:

Column A: Uniform random numbers generated by the Excel spreadsheet function RAND() and saved. These are the cumulative probabilities, *p*.

Column B: The normalized Gaussian random number corresponding to the cumulative probability in Column A.

Column C: The parameter λ in the beta inverse function is given by Abramowitz and Stegun (1972 [103280], Equation 26.5.22):

$$\lambda = \frac{y_p^2 - 3}{6} \qquad \text{(Eq. IV-6)}$$

where y_p is defined in Column B. In Excel, this is

Crn=(Brn^2-3)/6

Column D: The parameter w in the beta inverse function is given by Abramowitz and Stegun (1972 [103280], Equation 26.5.22):

$$w = \frac{y_p (h + \lambda)^{\frac{1}{2}}}{h} - \left(\frac{1}{2b - 1} - \frac{1}{2a - 1} \right)\left(\lambda + \frac{5}{6} - \frac{2}{3h} \right) \qquad \text{(Eq. IV-7)}$$

In Excel, this is

Drn= (Brn*(($J$2+Crn)^0.5)/$J$2)-((2*$I$2-1)^(-1)-(2*$H$2-1)^(-1))*(Crn+(5/6)-2/(3*$J$2))

Column E: The beta random number, x_p, is given by Abramowitz and Stegun (1972 [103280], Equation 26.5.22):

$$x_p \approx \frac{a}{a + be^{2w}} \qquad \text{(Eq. IV-8)}$$

In Excel, this is

Ern=$H$2/($H$2+$I$2*EXP(2*Drn))

Column F: Contains the value of the mean porosity, μ_ϕ, from Table IV-1

Column G: Contains the value of the porosity standard deviation, σ_ϕ, from Table IV-1

Column H: The beta distribution parameter a is derived from Abramowitz and Stegun (1972 [103280], Equation 26.1.33) (see Attachment XI for a detailed derivation of Equations (IV-3) and (IV-4)):

$$a = \mu_\phi \left[\frac{\mu_\phi (1 - \mu_\phi)}{\sigma_\phi^2} - 1 \right] \qquad \text{(Eq. IV-3)}$$

In Excel, this is

H2=F2*((F2*(1-F2)/G2^2)-1)

Column I: The beta distribution parameter b is given by Abramowitz and Stegun (1972 [103280], Equation 26.1.33):

$$b = \left(1 - \mu_\phi\right)\left[\frac{\mu_\phi\left(1 - \mu_\phi\right)}{\sigma_\phi^2} - 1\right] \qquad \text{(Eq. IV-4)}$$

In Excel, this is

I2=(1-F2)*((F2*(1-F2)/G2^2)-1)

Column J: The parameter *h* in the beta inverse function is given by Abramowitz and Stegun (1972 [103280], Equation 26.5.22):

$$h = 2\left(\frac{1}{2a-1} + \frac{1}{2b-1}\right)^{-1} \qquad \text{(Eq. IV-5)}$$

In Excel, this is

J2=2*((2*H2-1)^(-1)+(2*I2-1)^(-1))^(-1)

Table IV-2a. Fracture Porosity in the tsw35

	A	B	C	D	E	F	G	H	I	J
1	**Fixed Uniform Random Number (P)**	**y_P - normalized Gaussian random number**	**Beta inverse param. -λ**	**Beta inverse param. - w**	**x_P - Beta random number (Fracture Porosity)**	**mean fracture porosity - tsw35**	**standard deviation fracture porosity - tsw35**	**Beta dist. Param. - a**	**Beta dist. Param. - b**	**Beta inverse param. - h**
2	6.1798E-01	2.9975E-01	-4.8503E-01	6.02E-02	8.52E-03	9.60E-03	2.82E-03	1.15E+01	1.18E+03	4.35E+01
3	4.6680E-01	-8.3116E-02	-4.9885E-01	1.88E-03	9.56E-03					
4	6.3399E-01	3.4200E-01	-4.8051E-01	6.68E-02	8.41E-03					
5	6.5133E-01	3.8846E-01	-4.7485E-01	7.41E-02	8.29E-03					
6	8.7752E-01	1.1628E+00	-2.7465E-01	2.00E-01	6.45E-03					
7	3.6128E-01	-3.5460E-01	-4.7904E-01	-3.82E-02	1.04E-02					
8	3.3315E-01	-4.3080E-01	-4.6907E-01	-4.92E-02	1.06E-02					
9	5.7646E-02	-1.5752E+00	-8.6467E-02	-2.06E-01	1.44E-02					
10	3.4838E-01	-3.8926E-01	-4.7475E-01	-4.32E-02	1.05E-02					
11	6.3949E-01	3.5665E-01	-4.7880E-01	6.91E-02	8.37E-03					
12	6.3466E-01	3.4378E-01	-4.8030E-01	6.71E-02	8.40E-03					
13	2.1067E-01	-8.0391E-01	-3.9229E-01	-1.02E-01	1.18E-02					
14	1.8567E-01	-8.9384E-01	-3.6684E-01	-1.15E-01	1.20E-02					
15	6.9110E-01	4.9856E-01	-4.5857E-01	9.15E-02	8.01E-03					
16	5.2111E-01	5.2811E-02	-4.9954E-01	2.23E-02	9.18E-03					
17	7.6460E-02	-1.4296E+00	-1.5940E-01	-1.87E-01	1.39E-02					
18	1.2759E-01	-1.1380E+00	-2.8418E-01	-1.48E-01	1.29E-02					
19	2.2382E-01	-7.5911E-01	-4.0396E-01	-9.59E-02	1.16E-02					
20	3.9235E-01	-2.7278E-01	-4.8760E-01	-2.62E-02	1.01E-02					
21	4.7861E-01	-5.3507E-02	-4.9952E-01	6.31E-03	9.48E-03					
22	2.9629E-01	-5.3472E-01	-4.5235E-01	-6.42E-02	1.09E-02					
23	2.9692E-02	-1.8858E+00	9.2682E-02	-2.45E-01	1.56E-02					
24	8.1567E-01	8.9887E-01	-3.6534E-01	1.56E-01	7.04E-03					
25	9.1682E-01	1.3842E+00	-1.8064E-01	2.38E-01	5.98E-03					
26	3.2410E-01	-4.5583E-01	-4.6537E-01	-5.28E-02	1.07E-02					
27	2.3452E-01	-7.2378E-01	-4.1269E-01	-9.09E-02	1.15E-02					
28	4.4601E-01	-1.3546E-01	-4.9694E-01	-5.93E-03	9.71E-03					
29	4.5832E-01	-1.0442E-01	-4.9818E-01	-1.30E-03	9.62E-03					
30	3.6776E-01	-3.3734E-01	-4.8103E-01	-3.57E-02	1.03E-02					

Output-DTN: LB0307FMRADTRN.001

Table IV-2b. Matrix Porosity in the tsw35

	A	B	C	D	E	F	G	G	I	J
1	**Fixed Uniform Random Number (P)**	**y_P - normalized Gaussian random number**	**Beta inverse param. -λ**	**Beta inverse param. - w**	**x_P - Beta random number (Matrix Porosity)**	**mean matrix porosity - tsw35**	**standard deviation matrix porosity - tsw35**	**Beta dist. Param. - a**	**Beta dist. Param. - b**	**Beta inverse param. - h**
2	8.2838E-01	9.4770E-01	-3.5031E-01	1.45E-01	1.01E-01	1.31E-01	3.10E-02	1.54E+01	1.02E+02	5.19E+01
3	1.4598E-01	-1.0538E+00	-3.1491E-01	-1.31E-01	1.64E-01					
4	9.2170E-01	1.4169E+00	-1.6542E-01	2.15E-01	8.93E-02					
5	2.3816E-01	-7.1196E-01	-4.1552E-01	-8.68E-02	1.52E-01					
6	1.9194E-01	-8.7064E-01	-3.7367E-01	-1.08E-01	1.57E-01					
7	2.3945E-01	-7.0779E-01	-4.1651E-01	-8.62E-02	1.52E-01					
8	8.6837E-01	1.1188E+00	-2.9138E-01	1.70E-01	9.69E-02					
9	5.1569E-01	3.9223E-02	-4.9974E-01	1.46E-02	1.28E-01					
10	7.6814E-01	7.3249E-01	-4.1058E-01	1.13E-01	1.07E-01					
11	1.3291E-01	-1.1128E+00	-2.9361E-01	-1.39E-01	1.66E-01					
12	5.2042E-01	5.1084E-02	-4.9957E-01	1.63E-02	1.27E-01					
13	3.0449E-01	-5.1112E-01	-4.5646E-01	-6.02E-02	1.45E-01					
14	6.2932E-01	3.2962E-01	-4.8189E-01	5.52E-02	1.19E-01					
15	7.8249E-01	7.8041E-01	-3.9849E-01	1.20E-01	1.06E-01					
16	2.1576E-02	-2.0227E+00	1.8187E-01	-2.52E-01	2.00E-01					
17	1.0799E-01	-1.2374E+00	-2.4479E-01	-1.55E-01	1.70E-01					
18	7.6286E-01	7.1526E-01	-4.1473E-01	1.10E-01	1.08E-01					
19	2.3410E-01	-7.2515E-01	-4.1236E-01	-8.85E-02	1.53E-01					
20	3.1982E-01	-4.6778E-01	-4.6353E-01	-5.44E-02	1.44E-01					
21	1.5005E-01	-1.0362E+00	-3.2104E-01	-1.29E-01	1.63E-01					
22	8.6802E-01	1.1172E+00	-2.9199E-01	1.70E-01	9.69E-02					
23	6.3793E-02	-1.5240E+00	-1.1290E-01	-1.91E-01	1.81E-01					
24	7.1773E-01	5.7574E-01	-4.4475E-01	9.03E-02	1.12E-01					
25	2.6452E-02	-1.9361E+00	1.2476E-01	-2.42E-01	1.96E-01					
26	1.2687E-03	-3.0192E+00	1.0192E+00	-3.70E-01	2.40E-01					
27	6.7080E-01	4.4170E-01	-4.6748E-01	7.11E-02	1.16E-01					
28	1.7696E-01	-9.2694E-01	-3.5680E-01	-1.15E-01	1.59E-01					
29	8.9801E-02	-1.3422E+00	-1.9975E-01	-1.68E-01	1.74E-01					
30	1.4850E-01	-1.0429E+00	-3.1873E-01	-1.30E-01	1.64E-01					

Output-DTN: LB0307FMRADTRN.001

INTENTIONALLY LEFT BLANK

ATTACHMENT V – SAMPLING FOR INVERT DIFFUSIVE MASS TRANSFER COEFFICIENTS

This attachment provides additional information pertaining to Section 6.4.5 of the main text. The invert diffusive mass-transfer coefficient is based upon the correlation presented in BSC (2001 [156700], pp. 23–25):

$$\log\left(\frac{D_{eI}}{D_0}\right) = 1.849 \log \theta_I \qquad \text{(Eq. V-1)}$$

where D_{eI} is the invert diffusive mass-transfer coefficient, D_0 is the coefficient of diffusion in water, and θ_I is the invert water content. As discussed in Section 6.4.5, the invert water content is related to the invert grain microporosity, times the fraction of the bulk volume occupied by the grains, i.e.:

$$\theta_I = (1 - \phi_{Ig})\phi_m \qquad \text{(Eq. V-2)}$$

where ϕ_{Ig} is the intergranular porosity of the invert and ϕ_m is the microporosity of the grains. The invert material is planned to be taken from the tsw36 unit, and the sampling for the porosity of this material is discussed in Attachment IV. The intergranular porosity has an expected value of 0.45 (BSC 2002 [161619], Section 4.13) and a range from 0.4 to 0.48. A distribution representative of these characteristics can be produced by noting that a uniform random sample between 0.4 and 0.45 will on average produce a value of 0.425. Similarly, a uniform random sample between 0.45 and 0.48 will on average produce a value of 0.465. If samples are drawn from these two distributions in some proportion, x , for the range of 0.4 to 0.45 and (1-x) for the range of 0.45 to 0.48, then an overall average of 0.45 will be achieved if $x = 0.375$.

Table V-1 presents a portion of the output from the formulation as performed in an Excel spreadsheet for the fracture and matrix porosities of the tsw35 model unit. See Wang (2003 [163234], SN-LBNL-SCI-236-V1, p. 64) and DTN: LB0307FMRADTRN.001 for the complete output. The sequence of calculations are as follows:

Column A: Uniform random numbers generated by the Excel spreadsheet function RAND() and saved.

Column B: Scale the random number in Column B to between 0.4 and 0.45

Brn=0.4+Arn*0.05

Column C: Uniform random numbers generated by the Excel spreadsheet function RAND() and saved.

Column D: Scale the random number in Column E to between 0.45 and 0.48

Drn=0.45+Crn*0.03

Column E: Calculate the weighted average of columns C B and F D to give the invert intergranular porosity.

Ern=0.375*Brn+0.625*Drn

The statistical properties for the diffusion coefficient in water, D_0, are derived from the data from Weast and Astle 1979 [102865], presented in Section 4.1.1. The diffusion coefficient is sampled as a lognormal distribution, with the mean and standard deviation of log(D_0) being 4.69 and 0.150, respectively, where D_0 is in mm/yr.

See Scientific Notebook by Wang (2003 [163234], SN-LBNL-SCI-236-V1, pp. 40–42) for a discussion of the generation of Gaussian random numbers. Table V-2 presents a portion of the output from the formulation as performed in an Excel spreadsheet for the diffusion coefficient. See Wang (2003 [163234], SN-LBNL-SCI-236-V1, p. 67) and DTN: LB0307FMRADTRN.001 for the complete output

The sequence of calculations are as follows:

Column A: Uniform random numbers generated by the Excel spreadsheet function RAND() and saved. These are the cumulative probabilities, p.

Column B: The normalized Gaussian random number corresponding to the cumulative probability in Column A.

Column C: The corresponding random base-10 logarithm of fracture frequency is derived from the normalized Gaussian random variable through the normalization definition:

$$f = x_p \sigma_{\log(D_0)} + \mu_{\log(D_0)} \qquad \text{(Eq. V-3)}$$

where $\mu_{\log(D_0)}$ and $\sigma_{\log(D_0)}$ are the mean and variance of $\log(D_0)$.

In Excel, this is

Crn=Brn*$F$2+$E$2

Column D: This column calculates the diffusion coefficient through the identity

$$D_0 = 10^{\log(D_0)} \qquad \text{(Eq. V-4)}$$

In Excel, this is

Drn=10^(Crn)

Table V-1. Intergranular Porosity

	A	B	C	D	E
1	Fixed Uniform Random Number (P)	Random Porosity between 0.4 and 0.45	Fixed Uniform Random Number (P)	Random Porosity between 0.45 and 0.48	Intergranular porosity
2	4.1774E-01	4.2089E-01	4.7017E-01	4.6411E-01	4.48E-01
3	8.1015E-01	4.4051E-01	3.8268E-01	4.6148E-01	4.54E-01
4	7.0390E-01	4.3519E-01	2.6241E-01	4.5787E-01	4.49E-01
5	1.9219E-01	4.0961E-01	1.5264E-01	4.5458E-01	4.38E-01
6	6.8994E-01	4.3450E-01	7.1428E-01	4.7143E-01	4.58E-01
7	1.5716E-01	4.0786E-01	8.3342E-02	4.5250E-01	4.36E-01
8	6.6607E-01	4.3330E-01	4.5951E-01	4.6379E-01	4.52E-01
9	6.5736E-01	4.3287E-01	5.7148E-02	4.5171E-01	4.45E-01
10	1.0713E-01	4.0536E-01	2.5464E-01	4.5764E-01	4.38E-01
11	2.9326E-01	4.1466E-01	1.8206E-01	4.5546E-01	4.40E-01
12	2.8986E-01	4.1449E-01	4.8610E-01	4.6458E-01	4.46E-01
13	8.9896E-01	4.4495E-01	8.8812E-01	4.7664E-01	4.65E-01
14	9.2404E-01	4.4620E-01	2.3375E-01	4.5701E-01	4.53E-01
15	2.1126E-01	4.1056E-01	4.6330E-01	4.6390E-01	4.44E-01
16	9.7667E-01	4.4883E-01	1.5419E-01	4.5463E-01	4.52E-01
17	8.7149E-02	4.0436E-01	3.6447E-02	4.5109E-01	4.34E-01
18	1.0232E-01	4.0512E-01	9.8288E-01	4.7949E-01	4.52E-01
19	9.1436E-02	4.0457E-01	2.3091E-01	4.5693E-01	4.37E-01
20	2.0876E-01	4.1044E-01	1.6027E-01	4.5481E-01	4.38E-01
21	4.6890E-01	4.2344E-01	9.6731E-01	4.7902E-01	4.58E-01
22	2.4024E-01	4.1201E-01	4.6734E-01	4.6402E-01	4.45E-01
23	7.3021E-01	4.3651E-01	9.8400E-01	4.7952E-01	4.63E-01
24	5.9356E-01	4.2968E-01	8.7017E-02	4.5261E-01	4.44E-01
25	5.8208E-01	4.2910E-01	8.1004E-01	4.7430E-01	4.57E-01
26	8.3132E-01	4.4157E-01	6.2164E-01	4.6865E-01	4.58E-01
27	6.5032E-01	4.3252E-01	3.1289E-01	4.5939E-01	4.49E-01
28	3.9302E-02	4.0197E-01	1.1715E-01	4.5351E-01	4.34E-01
29	1.9354E-01	4.0968E-01	7.8522E-01	4.7356E-01	4.50E-01
30	7.4822E-03	4.0037E-01	8.6992E-01	4.7610E-01	4.48E-01

Output-DTN: LB0307FMRADTRN.001

Table V-2. Free-Water Diffusion Coefficients

	A	B	C	D	E	F
1	**Fixed Uniform Random Number (P)**	**x_P - norm. Gaussian random number**	**x - Gaussian random number**	**Free-water Diffusion Coefficient (mm^2/yr)**	**mean log(D_0) (mm^2/yr)**	**standard deviation log(D_0)**
2	8.6421E-01	1.0995E+00	4.85E+00	7.16E+04	4.69E+00	1.50E-01
3	2.3687E-01	-7.1615E-01	4.58E+00	3.82E+04		
4	4.7360E-01	-6.6043E-02	4.68E+00	4.79E+04		
5	4.7725E-01	-5.6898E-02	4.68E+00	4.80E+04		
6	3.1923E-01	-4.6944E-01	4.62E+00	4.16E+04		
7	3.2902E-01	-4.4220E-01	4.62E+00	4.20E+04		
8	4.9136E-01	-2.1600E-02	4.69E+00	4.86E+04		
9	8.4999E-01	1.0364E+00	4.85E+00	7.01E+04		
10	9.5489E-01	1.6946E+00	4.94E+00	8.79E+04		
11	2.0629E-01	-8.1919E-01	4.57E+00	3.69E+04		
12	1.4971E-01	-1.0377E+00	4.53E+00	3.42E+04		
13	5.3725E-01	9.3274E-02	4.70E+00	5.06E+04		
14	5.0698E-01	1.7446E-02	4.69E+00	4.93E+04		
15	2.5667E-01	-6.5333E-01	4.59E+00	3.91E+04		
16	9.7563E-01	1.9712E+00	4.99E+00	9.68E+04		
17	8.2452E-01	9.3265E-01	4.83E+00	6.76E+04		
18	8.5117E-01	1.0414E+00	4.85E+00	7.02E+04		
19	5.1257E-01	3.1418E-02	4.69E+00	4.95E+04		
20	1.2745E-01	-1.1386E+00	4.52E+00	3.31E+04		
21	5.9803E-01	2.4783E-01	4.73E+00	5.34E+04		
22	4.2537E-01	-1.8780E-01	4.66E+00	4.59E+04		
23	8.0602E-01	8.6319E-01	4.82E+00	6.60E+04		
24	1.7123E-01	-9.4925E-01	4.55E+00	3.53E+04		
25	8.3000E-01	9.5408E-01	4.83E+00	6.81E+04		
26	6.0404E-01	2.6339E-01	4.73E+00	5.36E+04		
27	4.4891E-01	-1.2814E-01	4.67E+00	4.69E+04		
28	9.1953E-01	1.4022E+00	4.90E+00	7.95E+04		
29	9.5815E-01	1.7300E+00	4.95E+00	8.90E+04		
30	1.7662E-01	-9.2825E-01	4.55E+00	3.55E+04		

Output-DTN: LB0307FMRADTRN.001

The invert diffusion coefficient is computed using the intergranular porosity and matrix porosity from tsw36 (Attachment IV), Equations V-1 and V-2, and the free-water diffusion coefficient. Table V-2 presents a portion of the output from the formulation as performed in an Excel spreadsheet for the invert diffusive mass transfer coefficient. See Wang (2003 [163234], SN-LBNL-SCI-236-V1, p. 69) and DTN: LB0307FMRADTRN.001 for the complete output. The ratio of the maximum to minimum of the sampled diffusion coefficients spans a factor of approximately 43.

The sequence of calculations are described here:

Column A: Intergranular Porosity

Column B: Matrix Porosity (tsw36)

Column C: Invert water content computed from Equation V-2. In Excel, this is

Crn=(1-Arn)*Brn

Column D: Free-water diffusion coefficient

Column E: Invert diffusive mass transfer coefficient computed from Equation V-1. In Excel, this is

Ern=Drn*Crn^1.849

Table V-3. Invert Diffusive Mass Transfer Coefficients

	A	**B**	**C**	**D**	**E**
1	**Intergranular Porosity**	**Matrix Porosity - tsw36**	**Invert Water Content**	**Free-Water Diffusion Coefficient (mm/r)**	**Invert Diffusive Mass Transfer Coefficient (mm^2/yr)**
2	4.48E-01	1.51E-01	8.34E-02	7.16E+04	7.25E+02
3	4.54E-01	9.24E-02	5.05E-02	3.82E+04	1.53E+02
4	4.49E-01	8.54E-02	4.70E-02	4.79E+04	1.68E+02
5	4.38E-01	9.61E-02	5.40E-02	4.80E+04	2.18E+02
6	4.58E-01	8.26E-02	4.48E-02	4.16E+04	1.34E+02
7	4.36E-01	1.35E-01	7.60E-02	4.20E+04	3.58E+02
8	4.52E-01	1.09E-01	5.99E-02	4.86E+04	2.67E+02
9	4.45E-01	8.37E-02	4.65E-02	7.01E+04	2.41E+02
10	4.38E-01	1.23E-01	6.89E-02	8.79E+04	6.24E+02
11	4.40E-01	1.31E-01	7.31E-02	3.69E+04	2.93E+02
12	4.46E-01	6.76E-02	3.75E-02	3.42E+04	7.89E+01
13	4.65E-01	1.15E-01	6.18E-02	5.06E+04	2.94E+02
14	4.53E-01	1.05E-01	5.76E-02	4.93E+04	2.51E+02
15	4.44E-01	1.75E-01	9.71E-02	3.91E+04	5.24E+02
16	4.52E-01	7.95E-02	4.35E-02	9.68E+04	2.94E+02
17	4.34E-01	5.44E-02	3.08E-02	6.76E+04	1.09E+02
18	4.52E-01	1.33E-01	7.27E-02	7.02E+04	5.51E+02
19	4.37E-01	1.12E-01	6.30E-02	4.95E+04	2.99E+02
20	4.38E-01	1.32E-01	7.39E-02	3.31E+04	2.68E+02
21	4.58E-01	1.33E-01	7.18E-02	5.34E+04	4.10E+02
22	4.45E-01	9.39E-02	5.22E-02	4.59E+04	1.95E+02
23	4.63E-01	1.38E-01	7.42E-02	6.60E+04	5.38E+02
24	4.44E-01	1.09E-01	6.08E-02	3.53E+04	1.99E+02
25	4.57E-01	3.70E-02	2.01E-02	6.81E+04	4.94E+01
26	4.58E-01	1.23E-01	6.67E-02	5.36E+04	3.59E+02
27	4.49E-01	4.55E-02	2.51E-02	4.69E+04	5.14E+01
28	4.34E-01	1.02E-01	5.79E-02	7.95E+04	4.09E+02
29	4.50E-01	5.68E-02	3.13E-02	8.90E+04	1.47E+02
30	4.48E-01	1.25E-01	6.90E-02	3.55E+04	2.53E+02

Output-DTN: LB0307FMRADTRN.001

ATTACHMENT VI – SAMPLING FOR MATRIX DIFFUSION COEFFICIENTS

This attachment provides additional information pertaining to Section 6.4.5 of the main text. Matrix diffusion coefficients are derived based on the correlation discussed in Section 6.4.5 (Equation 52):

$$\log(D_m) = -3.49 + 1.38\theta_m + 0.165\log(k_w) \tag{Eq. VI-1}$$

where D_m is in cm^2/s and k_w is in m^2. The water-content values of the matrix are derived from the matrix porosities given in Attachment IV, times the matrix water saturations given in Attachment II. The effective permeability to water is derived using the equation given in Section 6.4.5 (Equation 57):

$$k_w = k_m k_{rw} \tag{Eq. VI-2}$$

where the matrix permeabilities are given in Table 4.1-2e. A portion of the output from the above relationship for matrix diffusion coefficient for each of the model grid locations are shown in Table VI-1. See Wang (2003 [163234], SN-LBNL-SCI-236-V1, p. 84) and DTN: LB0307FMRADTRN.001 for the complete output.

The sequence of calculations is given here:

Column A: Cell name from Attachment II.

Column B: Matrix water saturation from Attachment II.

Column C: Matrix porosity from Attachment IV.

Column D: Matrix water content equals matrix water saturation, times matrix porosity. In Excel, this is

Drn=Brn*Crn

Column E: Matrix relative permeability from Attachment II

Column F: The effective permeability is computed using Equation VI-2. In Excel, this is

Frm=$N$2*Ern

Column G: The logarithm of the mean matrix diffusion coefficient is computed using Equation VI-1. In Excel, this is

Grn=-3.49+1.38*Drn+0.165*LOG(Frn)

Column H: The matrix diffusion coefficient is computed from the identity

$$D_m = 10^{\log(D_m)} \tag{Eq. VI-3}$$

and converted from cm^2/s to mm^2/yr. In Excel, this is

Hrn=(10^Grn)*100*3600*24*365.25

Column I: Uniform random numbers generated by the Excel spreadsheet function RAND() and saved. These are the cumulative probabilities, p.

Column J: The normalized Gaussian random number corresponding to the cumulative probability in Column H.

Column K: The distributed random variable, Y, in Equation 55 is defined by

$$Y = \ln\left(\log\left(\frac{D_0}{D_m}\right)\right) \quad \text{(Eq. VI-4)}$$

where D_m is given in Column G and $D_0 = 10^{-9}$ m^2/s = 31557.6 mm^2/yr. In Excel, this is

Krn=ln(log(31558/Hrn))

Column L: The corresponding random value of Y is derived from the normalized Gaussian random variable through the normalization definition:

$$Y = x_p \sigma_Y + \overline{Y} \quad \text{(Eq. VI-5)}$$

where $\overline{Y}$ and σ_Y are the mean and variance for Y. As discussed in Section 6.4.5, σ_Y =0.3.

In Excel, this is

Lrn=Jrn*Orn+Krn

Column M: Inverting Equation VI-4, the random value of Y is transformed back to a diffusion coefficient through the relationship

$$D_m = D_0 10^{-\exp(Y)}$$

In Excel, this is

Mrn=31558*10^(-exp(Lrn))

Column N: Matrix permeability from Table 4.1-2e

Column O: Standard deviation for Y

Table VI-1. Matrix Diffusion Coefficients in the tsw35, Mean Infiltration Scenario

	A	B	C	D	E	F	G	H	I	J	K	L	M	N	O
1	Cell Name	Matrix Water Saturation	Matrix Porosity	Matrix Water Content	Relative Permeability	Effective Permeability m^2	$\log(D_m)$ cm^2/s	D_m mm^2/yr	Fixed Uniform Random Number (P)	Normalized Gaussian Random Number	Mean of Y	Sampled Y	Sampled D_m mm^2/yr	Permeability m^2	Std Dev Y
2	F0014f19	8.5119E-01	1.01E-01	8.64E-02	1.1513E-02	5.16E-20	-6.55E+00	8.83E+02	2.8703E-02	-1.9006E+00	4.40E-01	-1.30E-01	4.18E+03	4.48E-18	3.00E-01
3	F0014f31	8.3762E-01	1.64E-01	1.37E-01	9.1980E-03	4.12E-20	-6.50E+00	1.00E+03	1.0475E-01	-1.2551E+00	4.05E-01	2.83E-02	2.95E+03		
4	F0014f67	8.3178E-01	8.93E-02	7.43E-02	8.3545E-03	3.74E-20	-6.59E+00	8.06E+02	9.7688E-01	1.9937E+00	4.66E-01	1.06E+00	4.00E+01		
5	F0014f80	8.3701E-01	1.52E-01	1.27E-01	9.1054E-03	4.08E-20	-6.51E+00	9.67E+02	1.9728E-01	-8.5123E-01	4.15E-01	1.59E-01	2.12E+03		
6	F0014g17	8.3776E-01	1.57E-01	1.32E-01	9.2192E-03	4.13E-20	-6.51E+00	9.84E+02	6.8327E-01	4.7643E-01	4.10E-01	5.53E-01	5.77E+02		
7	F0014g83	8.3757E-01	1.52E-01	1.27E-01	9.1904E-03	4.12E-20	-6.51E+00	9.69E+02	5.6143E-01	1.5428E-01	4.14E-01	4.60E-01	8.21E+02		
8	F0014h13	8.3672E-01	9.69E-02	8.11E-02	9.0624E-03	4.06E-20	-6.58E+00	8.34E+02	4.4206E-02	-1.7042E+00	4.56E-01	-5.53E-02	3.57E+03		
9	F0014h21	8.3566E-01	1.28E-01	1.07E-01	8.9063E-03	3.99E-20	-6.54E+00	9.03E+02	3.6072E-01	-3.5609E-01	4.34E-01	3.27E-01	1.29E+03		
10	F0014h67	8.4732E-01	1.07E-01	9.10E-02	1.0797E-02	4.84E-20	-6.55E+00	8.86E+02	8.3538E-01	9.7559E-01	4.39E-01	7.32E-01	2.63E+02		
11	F0014h77	8.4210E-01	1.66E-01	1.40E-01	9.9040E-03	4.44E-20	-6.49E+00	1.02E+03	4.6970E-01	-7.5832E-02	3.99E-01	3.76E-01	1.10E+03		
12	F0014h82	8.3832E-01	1.27E-01	1.07E-01	9.3047E-03	4.17E-20	-6.54E+00	9.09E+02	1.4114E-01	-1.0752E+00	4.32E-01	1.09E-01	2.42E+03		
13	F0014i13	8.3837E-01	1.45E-01	1.22E-01	9.3129E-03	4.17E-20	-6.52E+00	9.54E+02	3.7451E-01	-3.1949E-01	4.18E-01	3.23E-01	1.31E+03		
14	F0014i18	8.3830E-01	1.19E-01	9.97E-02	9.3013E-03	4.17E-20	-6.55E+00	8.89E+02	2.6836E-01	-6.1745E-01	4.38E-01	2.53E-01	1.63E+03		
15	F0014i48	8.3729E-01	1.06E-01	8.88E-02	9.1484E-03	4.10E-20	-6.57E+00	8.56E+02	7.5006E-01	6.7438E-01	4.49E-01	6.51E-01	3.81E+02		
16	F0014l54	8.3708E-01	2.00E-01	1.67E-01	9.1172E-03	4.08E-20	-6.46E+00	1.10E+03	5.5094E-01	1.2776E-01	3.77E-01	4.16E-01	9.63E+02		
17	F0014l56	8.3869E-01	1.70E-01	1.43E-01	9.3628E-03	4.19E-20	-6.49E+00	1.02E+03	4.1410E-02	-1.7349E+00	3.99E-01	-1.22E-01	4.11E+03		
18	F0014l57	8.3979E-01	1.08E-01	9.06E-02	9.5337E-03	4.27E-20	-6.56E+00	8.67E+02	8.9647E-01	1.2619E+00	4.45E-01	8.24E-01	1.66E+02		
19	F0014m62	8.4322E-01	1.53E-01	1.29E-01	1.0090E-02	4.52E-20	-6.50E+00	9.88E+02	4.7281E-01	-6.8031E-02	4.08E-01	3.88E-01	1.06E+03		
20	F0014m63	8.3760E-01	1.44E-01	1.21E-01	9.1946E-03	4.12E-20	-6.52E+00	9.48E+02	6.9257E-01	5.0273E-01	4.20E-01	5.71E-01	5.36E+02		
21	F0014m64	8.4056E-01	1.63E-01	1.37E-01	9.6557E-03	4.33E-20	-6.50E+00	1.01E+03	8.9833E-01	1.2723E+00	4.03E-01	7.84E-01	2.03E+02		
22	F0014m65	8.4299E-01	9.69E-02	8.17E-02	1.0051E-02	4.50E-20	-6.57E+00	8.51E+02	7.1121E-01	5.5653E-01	4.51E-01	6.18E-01	4.41E+02		
23	F0014n24	8.6049E-01	1.81E-01	1.56E-01	1.3442E-02	6.02E-20	-6.45E+00	1.13E+03	9.5768E-01	1.7248E+00	3.69E-01	8.87E-01	1.18E+02		
24	F0014n26	8.5652E-01	1.12E-01	9.57E-02	1.2580E-02	5.64E-20	-6.53E+00	9.23E+02	6.3064E-01	3.3310E-01	4.28E-01	5.28E-01	6.37E+02		
25	F0014o29	8.4453E-01	1.96E-01	1.66E-01	1.0310E-02	4.62E-20	-6.45E+00	1.12E+03	7.0273E-01	5.3187E-01	3.72E-01	5.32E-01	6.26E+02		
26	F0014o31	8.5044E-01	2.40E-01	2.04E-01	1.1370E-02	5.09E-20	-6.39E+00	1.28E+03	7.1114E-01	5.5635E-01	3.30E-01	4.97E-01	7.16E+02		
27	F014Af20	8.3851E-01	1.16E-01	9.70E-02	9.3349E-03	4.18E-20	-6.55E+00	8.82E+02	3.6621E-01	-3.4147E-01	4.41E-01	3.38E-01	1.25E+03		
28	F014Af43	8.3937E-01	1.59E-01	1.34E-01	9.4685E-03	4.24E-20	-6.50E+00	9.94E+02	7.4439E-01	6.5661E-01	4.07E-01	6.04E-01	4.68E+02		
29	F014Af56	8.3128E-01	1.74E-01	1.45E-01	8.2857E-03	3.71E-20	-6.50E+00	1.01E+03	8.2489E-01	9.3409E-01	4.03E-01	6.83E-01	3.30E+02		
30	F014Af68	8.3726E-01	1.64E-01	1.37E-01	9.1432E-03	4.10E-20	-6.50E+00	9.98E+02	4.9809E-01	-4.7678E-03	4.05E-01	4.04E-01	1.00E+03		

Output-DTN: LB0307FMRADTRN.001

INTENTIONALLY LEFT BLANK

ATTACHMENT VII – SAMPLING FOR FRACTURE AND MATRIX PECLET NUMBERS, FRACTURE WATER CONTENT, AND DIMENSIONLESS INVERT DEPTH

This attachment provides additional information pertaining to Section 6.4.5 of the main text. Fracture Peclet numbers are computed using Equations 19 and 29 from the main text. These are:

$$q_{fe} = \frac{q_{wf}}{1 + \frac{(-q_{wf})\Delta y_f}{D_{ef}}} \qquad \text{(Eq. VII-1)}$$

and

$$Pe_{fe} = \frac{q_{fe} h_f}{D_{eI}} \qquad \text{(Eq. VII-2)}$$

Fracture flow is adjusted using the flow focusing factor in Attachment III

$$q_{wfa} = q_{wf} F \qquad \text{(Eq. VII-3)}$$

and the fracture saturation is adjusted as shown in Equation 50 in the main text.

$$S_{fna} = \left[\left(\frac{F}{m^2} \right) S_{fn}^{\frac{1}{2}} \left\{ 1 - \left(1 - S_{fn}^{\frac{1}{m}} \right)^m \right\}^2 \right]^{\frac{2m}{4+m}} \qquad \text{(Eq. VII-4)}$$

where S_{fn} is the normalized fracture saturation

$$S_{fn} = \frac{S_f - S_{fr}}{1 - S_{fr}} \qquad \text{(Eq. VII-5)}$$

and the adjusted physical saturation, S_{fa}, is given by

$$S_{fa} = S_{fr} + (1 - S_{fr}) S_{fna} \qquad \text{(Eq. VII-6)}$$

The fixed parameters used are given in Table 4.1-2c.

The fracture residual saturation is sampled as discussed in Section 6.4.5. A portion of the output for the sampling of fracture residual saturation is shown in Table VII-1. See Wang (2003 [163234], SN-LBNL-SCI-236-V1, p. 62) and DTN: LB0307FMRADTRN.001 for the complete output.

The sequence of calculations is as follows:

Column A: Uniform random numbers generated by the Excel spreadsheet function RAND() and saved.

Column B: The uniform random number in Column A, which ranges between 0 and 1, is converted to a uniform random number between -3 and -1. In Excel, this is

Brn=-3+2*Arn

Column C: The sampled S_{fr} is computed from the relationship

$$S_{fr} = 10^{RN}$$

where RN is the random number between -3 and -1 in Column B. In Excel, this is

Crn=10^Brn

Table VII-1. Sampled Fracture Residual Saturations

	A	B	C
1	**Fixed Uniform Random Number**	**Uniform Random Number between -3 and -1**	**Sampled S_{fr}**
2	9.5775E-01	-1.0845E+00	8.2318E-02
3	9.4855E-01	-1.1029E+00	7.8906E-02
4	8.4093E-01	-1.3181E+00	4.8068E-02
5	8.1139E-01	-1.3772E+00	4.1954E-02
6	2.4515E-01	-2.5097E+00	3.0924E-03
7	6.0656E-01	-1.7869E+00	1.6335E-02
8	1.6459E-01	-2.6708E+00	2.1339E-03
9	8.3698E-01	-1.3260E+00	4.7201E-02
10	1.7917E-01	-2.6417E+00	2.2821E-03
11	7.5053E-01	-1.4989E+00	3.1700E-02
12	3.5867E-01	-2.2827E+00	5.2161E-03
13	9.4585E-01	-1.1083E+00	7.7927E-02
14	7.8309E-01	-1.4338E+00	3.6828E-02
15	4.9868E-01	-2.0026E+00	9.9396E-03
16	8.3823E-01	-1.3235E+00	4.7475E-02
17	5.1569E-01	-1.9686E+00	1.0749E-02
18	5.2289E-01	-1.9542E+00	1.1112E-02
19	9.0574E-01	-1.1885E+00	6.4787E-02
20	4.4778E-01	-2.1044E+00	7.8627E-03
21	6.5841E-01	-1.6832E+00	2.0740E-02
22	6.1984E-01	-1.7603E+00	1.7365E-02
23	5.8284E-02	-2.8834E+00	1.3079E-03
24	9.6211E-01	-1.0758E+00	8.3987E-02
25	9.6423E-01	-1.0715E+00	8.4814E-02
26	2.8823E-01	-2.4235E+00	3.7711E-03
27	6.7397E-01	-1.6521E+00	2.2281E-02
28	2.0593E-01	-2.5881E+00	2.5815E-03
29	4.4110E-01	-2.1178E+00	7.6241E-03
30	4.4855E-01	-2.1029E+00	7.8905E-03

Output-DTN: LB0307FMRADTRN.001

A portion of the output for the fracture flux and water content sampling for the mean infiltration scenario are shown in Table VII-2. See Wang (2003 [163234], SN-LBNL-SCI-236-V1, p. 88) and DTN: LB0307FMRADTRN.001 for the complete output.

The sequence of calculations is given here:

Column A: Rock unit.

Column B: Cell name.

Column C: Fracture flux (negative of) from Attachment II.

Column D: Flow focusing factor from Attachment III.

Column E: Fracture saturation from Attachment II.

Column F: Fracture normalized saturation using Equation VII-5. In Excel this is

Frn=(Ern-$M$2)/(1-$M$2)

Column G: Adjusted normalized fracture saturation using Equation VII-4. In Excel, this is

Grn= ((Drn/($N$2^2))*Frn^0.5*(1-(1-Frn^(1/$N$2))^$N$2)^2)^(2*$N$2/(4+$N$2))

Column H: Sampled fracture residual saturation (see above).

Column I: Adjusted physical fracture saturation using Equation VII-6. In Excel, this is

Irn= Hrn+Grn*(1-Hrn)

Column J: Fracture porosity from Attachment IV.

Column K: Adjusted fracture water velocity, which is equal to the fracture flux, times the flow-focusing factor, divided by the fracture porosity and the adjusted physical fracture saturation. In Excel, this is

Krn= Drn*Crn/(Irn*Jrn)

Column L: Fracture water content. In Excel, this is

Lrn=Irn*Jrn

Column M: Fracture residual saturation from Table 4.1-2c.

Column N: Fracture van Genuchten pore size distribution factor, *m*, from Table 4.1-2c.

Table VII-2. Fracture Flux and Water Content for Mean Infiltration Scenario

	A	B	C	D	E	F	G	H	I	J	K	L	M	N
1	**Rock Unit**	**Cell Name**	**q_f (mm/yr)**	**F**	**S_f**	**S_{fn}**	**S_{fna}**	**Sampled S_{fr}**	**S_{fa}**	**φ_f**	**q_{wf} (mm/yr)**	**Fracture Water Content**	**S_{fr}**	***m***
2	tsw33	F012Bl76	-5.3967E+00	1.47E+00	1.32E-02	3.27E-03	3.64E-03	8.2318E-02	8.57E-02	5.98E-03	-1.55E+04	5.12E-04	0.01	0.633
3	tsw33	F012Bl78	-5.7350E+00	2.10E+00	1.33E-02	3.30E-03	4.04E-03	7.8906E-02	8.26E-02	4.70E-03	-3.11E+04	3.89E-04		
4	tsw33	F012Cl72	-4.8155E+00	8.51E-01	1.31E-02	3.09E-03	2.96E-03	4.8068E-02	5.09E-02	7.40E-03	-1.09E+04	3.77E-04		
5	tsw33	F012Cl74	-6.6185E+00	1.04E+00	1.35E-02	3.49E-03	3.52E-03	4.1954E-02	4.53E-02	4.21E-03	-3.59E+04	1.91E-04		
6	tsw33	F012Cm70	-9.7583E+00	5.96E-01	1.39E-02	3.98E-03	3.45E-03	3.0924E-03	6.53E-03	3.62E-03	-2.46E+05	2.36E-05		
7	tsw33	F012Dg58	-1.0083E+01	4.38E-01	1.44E-02	4.42E-03	3.53E-03	1.6335E-02	1.98E-02	5.48E-03	-4.07E+04	1.09E-04		
8	tsw33	F012Dl68	-1.3328E+01	3.60E-01	1.45E-02	4.50E-03	3.40E-03	2.1339E-03	5.53E-03	8.18E-03	-1.06E+05	4.52E-05		
9	tsw33	F012Dl70	-6.9879E+00	9.09E-01	1.33E-02	3.29E-03	3.20E-03	4.7201E-02	5.03E-02	2.82E-03	-4.49E+04	1.41E-04		
10	tsw33	F012Dl71	-3.5104E+00	1.91E+00	1.24E-02	2.41E-03	2.88E-03	2.2821E-03	5.15E-03	6.95E-03	-1.87E+05	3.58E-05		
11	tsw33	F012Dl75	-4.4996E+00	1.85E+00	1.27E-02	2.77E-03	3.28E-03	3.1700E-02	3.49E-02	5.49E-03	-4.36E+04	1.91E-04		
12	tsw33	F012Dl77	-4.2020E+00	2.15E-01	1.27E-02	2.68E-03	1.76E-03	5.2161E-03	6.97E-03	4.11E-03	-3.16E+04	2.86E-05		
13	tsw33	F012Dl79	-5.5142E+00	2.03E+00	1.30E-02	3.07E-03	3.73E-03	7.7927E-02	8.14E-02	4.79E-03	-2.88E+04	3.90E-04		
14	tsw33	F012Ef89	-1.8602E+01	1.08E+00	1.48E-02	4.81E-03	4.91E-03	3.6828E-02	4.16E-02	5.88E-03	-8.23E+04	2.44E-04		
15	tsw33	F012Eg 2	-1.5102E+01	7.95E-01	1.53E-02	5.37E-03	5.05E-03	9.9396E-03	1.49E-02	6.52E-03	-1.23E+05	9.75E-05		
16	tsw33	F012Eg14	-4.0953E+00	9.49E-01	1.28E-02	2.82E-03	2.78E-03	4.7475E-02	5.01E-02	4.80E-03	-1.62E+04	2.41E-04		
17	tsw33	F012Eg25	-4.2045E+00	5.96E-01	1.29E-02	2.88E-03	2.50E-03	1.0749E-02	1.32E-02	4.03E-03	-4.71E+04	5.32E-05		
18	tsw33	F012Eg36	-6.6068E+00	6.27E-01	1.35E-02	3.57E-03	3.14E-03	1.1112E-02	1.42E-02	4.52E-03	-6.44E+04	6.43E-05		
19	tsw33	F012Eg47	-7.4195E+00	2.38E-01	1.38E-02	3.82E-03	2.58E-03	6.4787E-02	6.72E-02	4.84E-03	-5.44E+03	3.25E-04		
20	tsw33	F012Eh 1	-2.5267E+01	1.60E-01	1.68E-02	6.85E-03	4.15E-03	7.8627E-03	1.20E-02	6.55E-03	-5.14E+04	7.84E-05		
21	tsw33	F012El73	-4.1465E+00	1.71E-01	1.26E-02	2.63E-03	1.62E-03	2.0740E-02	2.23E-02	8.15E-03	-3.89E+03	1.82E-04		
22	tsw33	F012Fg26	-4.5607E+00	1.10E+00	1.23E-02	2.36E-03	2.43E-03	1.7365E-02	1.98E-02	3.55E-03	-7.18E+04	7.02E-05		
23	tsw33	F012Fg59	-3.4216E+01	4.79E-01	1.65E-02	6.53E-03	5.34E-03	1.3079E-03	6.64E-03	7.72E-03	-3.20E+05	5.13E-05		
24	tsw33	F012Fg70	-3.3638E+01	6.59E-01	1.64E-02	6.42E-03	5.73E-03	8.3987E-02	8.92E-02	4.17E-03	-5.95E+04	3.73E-04		
25	tsw33	F012Fg80	-2.0564E+01	7.42E-01	1.62E-02	6.24E-03	5.75E-03	8.4814E-02	9.01E-02	6.26E-03	-2.71E+04	5.64E-04		
26	tsw33	F012Fg90	-1.9384E+01	1.34E+00	1.60E-02	6.06E-03	6.57E-03	3.7711E-03	1.03E-02	3.97E-03	-6.36E+05	4.10E-05		
27	tsw34	F0013g 3	-3.5168E+00	1.55E+00	1.49E-02	4.98E-03	5.61E-03	2.2281E-02	2.78E-02	1.13E-02	-1.73E+04	3.15E-04		
28	tsw34	F0013g48	-2.6890E+01	6.92E-01	2.27E-02	1.28E-02	1.16E-02	2.5815E-03	1.41E-02	1.16E-02	-1.13E+05	1.64E-04		
29	tsw34	F0013g91	-1.4310E+01	2.86E-01	1.95E-02	9.55E-03	6.78E-03	7.6241E-03	1.44E-02	8.94E-03	-3.18E+04	1.28E-04		
30	tsw34	F0013h 2	-9.6354E+00	1.91E+00	1.91E-02	9.17E-03	1.09E-02	7.8905E-03	1.87E-02	4.37E-03	-2.25E+05	8.19E-05		

Output-DTN: LB0307FMRADTRN.001

A portion of the output for the fracture Peclet number is shown in Table VII-3 for the mean infiltration scenario. See Wang (2003 [163234], SN-LBNL-SCI-236-V1, p. 89) and DTN: LB0307FMRADTRN.001 for the complete output.

The sequence of calculations is given here:

Column A: Rock unit.

Column B: Cell name.

Column C: The adjusted fracture flux (q_{wf}) as shown in Table VII-2.

Column D: Fracture half-spacing from Attachment I.

Column E: Distance to fracture flow below drift from Attachment I.

Column F: Effective diffusion coefficient in the fracture from Attachment VI.

Column G: Effective fracture velocity using Equation VII-1. In Excel, this is

Grn= Crn/(1+(-Crn*Ern/Frn))

Column H: Diffusive mass transfer coefficient for the invert from Attachment V.

Column I: Fracture Peclet number computed using Equation VII-2. In Excel, this is

Irn= Grn*Drn/Hrn

Table VII-3. Fracture Peclet Number for the Mean Infiltration Scenario

	A	B	C	D	E	F	G	H	I
1	**Rock Unit**	**Cell Name**	**q_{wf} (mm/yr)**	**h_f (mm)**	**Δy_f (mm)**	**D_{ef} (mm^2/yr)**	**q_{fe} (mm/yr)**	**D_{el} (mm^2/yr)**	**Pe_{fe}**
2	tsw33	F012Bl76	-1.55E+04	1.26E+03	5.70E+02	3.31E+02	-5.81E-01	7.25E+02	-1.01E+00
3	tsw33	F012Bl78	-3.11E+04	4.14E+03	4.88E+03	2.27E+03	-4.65E-01	1.53E+02	-1.26E+01
4	tsw33	F012Cl72	-1.09E+04	4.60E+02	5.36E+02	6.23E+02	-1.16E+00	1.68E+02	-3.18E+00
5	tsw33	F012Cl74	-3.59E+04	1.35E+03	1.59E+03	2.53E+03	-1.59E+00	2.18E+02	-9.90E+00
6	tsw33	F012Cm70	-2.46E+05	1.84E+03	1.83E+03	4.63E+03	-2.53E+00	1.34E+02	-3.49E+01
7	tsw33	F012Dg58	-4.07E+04	8.46E+02	1.27E+03	7.77E+02	-6.13E-01	3.58E+02	-1.45E+00
8	tsw33	F012Dl68	-1.06E+05	4.10E+02	5.88E+02	1.12E+03	-1.91E+00	2.67E+02	-2.93E+00
9	tsw33	F012Dl70	-4.49E+04	8.27E+02	1.18E+02	5.82E+01	-4.95E-01	2.41E+02	-1.70E+00
10	tsw33	F012Dl71	-1.87E+05	5.00E+02	1.88E+01	3.80E+03	-2.02E+02	6.24E+02	-1.62E+02
11	tsw33	F012Dl75	-4.36E+04	2.84E+03	5.37E+03	2.54E+03	-4.73E-01	2.93E+02	-4.60E+00
12	tsw33	F012Dl77	-3.16E+04	4.09E+02	6.79E+02	2.80E+03	-4.12E+00	7.89E+01	-2.14E+01
13	tsw33	F012Dl79	-2.88E+04	2.55E+03	3.22E+03	1.54E+03	-4.78E-01	2.94E+02	-4.16E+00
14	tsw33	F012Ef89	-8.23E+04	3.36E+02	5.01E+02	2.82E+03	-5.62E+00	2.51E+02	-7.51E+00
15	tsw33	F012Eg 2	-1.23E+05	1.10E+03	5.94E+02	6.67E+02	-1.12E+00	5.24E+02	-2.36E+00
16	tsw33	F012Eg14	-1.62E+04	4.82E+02	5.22E+01	1.09E+03	-2.08E+01	2.94E+02	-3.40E+01
17	tsw33	F012Eg25	-4.71E+04	7.49E+02	7.20E+02	3.05E+02	-4.24E-01	1.09E+02	-2.93E+00
18	tsw33	F012Eg36	-6.44E+04	6.35E+02	4.83E+02	7.93E+02	-1.64E+00	5.51E+02	-1.89E+00
19	tsw33	F012Eg47	-5.44E+03	1.60E+03	7.33E+02	8.73E+02	-1.19E+00	2.99E+02	-6.39E+00
20	tsw33	F012Eh 1	-5.14E+04	1.49E+03	1.36E+03	1.58E+03	-1.16E+00	2.68E+02	-6.48E+00
21	tsw33	F012El73	-3.89E+03	6.33E+02	7.25E+02	3.81E+03	-5.25E+00	4.10E+02	-8.11E+00
22	tsw33	F012Fg26	-7.18E+04	1.79E+03	2.45E+03	1.29E+03	-5.25E-01	1.95E+02	-4.82E+00
23	tsw33	F012Fg59	-3.20E+05	1.21E+03	3.60E+02	2.41E+03	-6.68E+00	5.38E+02	-1.51E+01
24	tsw33	F012Fg70	-5.95E+04	1.94E+03	1.23E+03	3.09E+03	-2.51E+00	1.99E+02	-2.45E+01
25	tsw33	F012Fg80	-2.71E+04	2.17E+02	2.59E+01	1.36E+03	-5.22E+01	4.94E+01	-2.30E+02
26	tsw33	F012Fg90	-6.36E+05	1.23E+03	2.41E+03	3.28E+03	-1.36E+00	3.59E+02	-4.66E+00
27	tsw34	F0013g 3	-1.73E+04	1.48E+02	2.91E+02	3.13E+01	-1.07E-01	5.14E+01	-3.10E-01
28	tsw34	F0013g48	-1.13E+05	1.66E+02	1.45E+01	8.82E+01	-6.08E+00	4.09E+02	-2.47E+00
29	tsw34	F0013g91	-3.18E+04	1.66E+02	8.55E+01	1.90E+03	-2.22E+01	1.47E+02	-2.50E+01
30	tsw34	F0013h 2	-2.25E+05	1.85E+02	1.12E+02	6.04E+02	-5.38E+00	2.53E+02	-3.93E+00

Output-DTN: LB0307FMRADTRN.001

The matrix Peclet number is computed using Equation 30 from the main text, which is

$$Pe_m = \frac{q_m h_f}{D_{eI}} \qquad \text{(Eq. VII-7)}$$

An example of the sampling for the matrix Peclet number is shown in Table VII-4. See Wang (2003 [163234], SN-LBNL-SCI-236-V1, p. 91) for the file directory information containing the complete results.

The sequence of calculations is as follows:

Column A: Rock unit.

Column B: Cell name.

Column C: Matrix flux from Attachment II.

Column D: Fracture half-spacing from Attachment I.

Column E: Diffusive mass-transfer coefficient for the invert from Attachment V.

Column F: Matrix Peclet number computed using Equation VII-7. In Excel, this is

Frn= Crn*Drn/Ern

Table VII-4. Matrix Peclet Numbers for Mean Infiltration Scenario

	A	B	C	D	E	F
1	**Rock Unit**	**Cell Name**	**q_m (mm/yr)**	**h_f (mm)**	**D_{el} (mm^2/yr)**	**Pe_m**
2	tsw33	M012Bl76	-2.4032E-01	1.26E+03	7.25E+02	-4.18E-01
3	tsw33	M012Bl78	-1.4520E-01	4.14E+03	1.53E+02	-3.93E+00
4	tsw33	M012Cl72	-1.3236E+00	4.60E+02	1.68E+02	-3.63E+00
5	tsw33	M012Cl74	-5.1798E-01	1.35E+03	2.18E+02	-3.22E+00
6	tsw33	M012Cm70	-5.0937E-01	1.84E+03	1.34E+02	-7.02E+00
7	tsw33	M012Dg58	-2.2577E-01	8.46E+02	3.58E+02	-5.34E-01
8	tsw33	M012Dl68	-5.3696E-01	4.10E+02	2.67E+02	-8.25E-01
9	tsw33	M012Dl70	-5.5948E-01	8.27E+02	2.41E+02	-1.92E+00
10	tsw33	M012Dl71	-1.2656E+00	5.00E+02	6.24E+02	-1.01E+00
11	tsw33	M012Dl75	-2.6302E-01	2.84E+03	2.93E+02	-2.55E+00
12	tsw33	M012Dl77	-2.1155E-01	4.09E+02	7.89E+01	-1.10E+00
13	tsw33	M012Dl79	-4.4544E-01	2.55E+03	2.94E+02	-3.87E+00
14	tsw33	M012Ef89	-1.4086E-01	3.36E+02	2.51E+02	-1.88E-01
15	tsw33	M012Eg 2	-1.1983E-01	1.10E+03	5.24E+02	-2.51E-01
16	tsw33	M012Eg14	-5.8384E-02	4.82E+02	2.94E+02	-9.55E-02
17	tsw33	M012Eg25	-5.3101E-02	7.49E+02	1.09E+02	-3.67E-01
18	tsw33	M012Eg36	-1.1091E-01	6.35E+02	5.51E+02	-1.28E-01
19	tsw33	M012Eg47	-1.6404E-01	1.60E+03	2.99E+02	-8.81E-01
20	tsw33	M012Eh 1	-1.8512E-01	1.49E+03	2.68E+02	-1.03E+00
21	tsw33	M012El73	-4.8153E-01	6.33E+02	4.10E+02	-7.44E-01
22	tsw33	M012Fg26	-1.0880E-01	1.79E+03	1.95E+02	-9.99E-01
23	tsw33	M012Fg59	-3.2473E-01	1.21E+03	5.38E+02	-7.32E-01
24	tsw33	M012Fg70	-2.1330E-01	1.94E+03	1.99E+02	-2.08E+00
25	tsw33	M012Fg80	-1.4723E-01	2.17E+02	4.94E+01	-6.47E-01
26	tsw33	M012Fg90	-1.3500E-01	1.23E+03	3.59E+02	-4.61E-01
27	tsw34	M0013g 3	-1.2727E-02	1.48E+02	5.14E+01	-3.67E-02
28	tsw34	M0013g48	-1.5652E-02	1.66E+02	4.09E+02	-6.35E-03
29	tsw34	M0013g91	-1.4594E-02	1.66E+02	1.47E+02	-1.65E-02
30	tsw34	M0013h 2	-6.9779E-02	1.85E+02	2.53E+02	-5.10E-02

Output-DTN: LB0307FMRADTRN.001

The dimensionless invert depth is computed from the invert depth, divided by the fracture half-spacing. The variation in the invert depth is sampled as a uniform random number between 675 mm and 806 mm (see Figure 6.4-1). A portion of the output for the dimensionless invert depth is shown in Table VII-5. See Wang (2003 [163234], SN-LBNL-SCI-236-V1, p. 94) and DTN: LB0307FMRADTRN.001 for the complete output.

The sequence of calculations is as follows:

Column A: Rock unit.

Column B: Cell name.

Column C: Uniform random numbers generated by the Excel spreadsheet function RAND() and saved.

Column D: Generate random invert depth between 675 and 806 mm. In Excel, this is

Drn= 675+(806-675)*Crn

Column E: Fracture half-spacing from Attachment I.

Column F: Dimensionless invert depth is computed from the ratio of the invert depth to the fracture half-spacing. In Excel, this is

Frn= Drn/Ern

Table VII-5. Dimensionless Invert Depth (Independent of Infiltration Scenario).

	A	B	C	D	E	F
1	**Rock Unit**	**Cell Name**	**Fixed Uniform Random Number**	**Invert Depth (mm)**	**h_f (mm)**	**Dimensionless Invert Depth**
2	tsw33	F012Bl76	5.3041E-01	7.44E+02	1.26E+03	5.91E-01
3	tsw33	F012Bl78	1.7330E-01	6.98E+02	4.14E+03	1.68E-01
4	tsw33	F012Cl72	2.3364E-01	7.06E+02	4.60E+02	1.53E+00
5	tsw33	F012Cl74	7.5332E-01	7.74E+02	1.35E+03	5.72E-01
6	tsw33	F012Cm70	5.8412E-01	7.52E+02	1.84E+03	4.08E-01
7	tsw33	F012Dg58	8.0829E-01	7.81E+02	8.46E+02	9.23E-01
8	tsw33	F012Dl68	4.2416E-01	7.31E+02	4.10E+02	1.78E+00
9	tsw33	F012Dl70	8.3845E-01	7.85E+02	8.27E+02	9.50E-01
10	tsw33	F012Dl71	6.5790E-01	7.61E+02	5.00E+02	1.52E+00
11	tsw33	F012Dl75	4.3296E-01	7.32E+02	2.84E+03	2.57E-01
12	tsw33	F012Dl77	2.7310E-01	7.11E+02	4.09E+02	1.74E+00
13	tsw33	F012Dl79	3.7391E-01	7.24E+02	2.55E+03	2.83E-01
14	tsw33	F012Ef89	3.6039E-01	7.22E+02	3.36E+02	2.15E+00
15	tsw33	F012Eg 2	6.4304E-01	7.59E+02	1.10E+03	6.91E-01
16	tsw33	F012Eg14	5.1883E-01	7.43E+02	4.82E+02	1.54E+00
17	tsw33	F012Eg25	6.3216E-01	7.58E+02	7.49E+02	1.01E+00
18	tsw33	F012Eg36	6.1548E-01	7.56E+02	6.35E+02	1.19E+00
19	tsw33	F012Eg47	8.8158E-01	7.90E+02	1.60E+03	4.93E-01
20	tsw33	F012Eh 1	1.8140E-01	6.99E+02	1.49E+03	4.68E-01
21	tsw33	F012El73	7.6937E-01	7.76E+02	6.33E+02	1.23E+00
22	tsw33	F012Fg26	2.3021E-01	7.05E+02	1.79E+03	3.94E-01
23	tsw33	F012Fg59	1.1181E-01	6.90E+02	1.21E+03	5.69E-01
24	tsw33	F012Fg70	3.0337E-01	7.15E+02	1.94E+03	3.68E-01
25	tsw33	F012Fg80	6.3025E-01	7.58E+02	2.17E+02	3.49E+00
26	tsw33	F012Fg90	9.3048E-01	7.97E+02	1.23E+03	6.50E-01
27	tsw34	F0013g 3	4.4532E-01	7.33E+02	1.48E+02	4.94E+00
28	tsw34	F0013g48	6.5840E-01	7.61E+02	1.66E+02	4.58E+00
29	tsw34	F0013g91	3.3859E-01	7.19E+02	1.66E+02	4.34E+00
30	tsw34	F0013h 2	5.0435E-01	7.41E+02	1.85E+02	4.01E+00

Output-DTN: LB0307FMRADTRN.001

ATTACHMENT VIII – SAMPLING FOR THE PARAMETER SETS USED IN THE CALCULATION OF FRACTURE-MATRIX RADIONUCLIDE FLUX DISTRIBUTIONS FROM WASTE EMPLACEMENT DRIFTS

This attachment provides additional information pertaining to Sections 6.4.6 and 6.5 of the main text. Each case investigated for the calculation of the radionuclide fracture-matrix flux fraction, for radionuclide transport from the waste emplacement drift invert into the rock, requires four dimensionless parameters. These were the parameters given at the end of Section 6.4.2; they are repeated here:

$Pe_m \equiv$ matrix – invert mass transfer Peclet number

$Pe_{fe} \equiv$ fracture – invert mass transfer Peclet number

$\theta_f \equiv$ fracture water content

$y_{dm} \equiv$ dimensionless invert depth

The design information in Table 4.1-2h (BSC 2003 [164491], 800-IED-WIS0-00103-000-00Ab) may be used to compute the percentage of total waste-emplacement drift area in each of the four rock units (tsw33, tsw34, tsw35, and tsw36). The total percentage of waste emplacement in each of the four rock units is shown in the following table:

	Drift Area (m^2)	**%tsw33**	**%tsw34**	**%tsw35**	**%tsw36**	**Drift Area tsw33 (m^2)**	**Drift Area tsw34 (m^2)**	**Drift Area tsw35 (m^2)**	**Drift Area tsw36 (m^2)**	**Total Drift Area (m^2)**
Panel 1	298850	0	40	60	0	0	119172	179678	0	
Panel 2	1477867	0	5	91	4	0	80213	1341147	56507	
Panel 3	1862136	12	22	66	0	224398	416618	1221120	0	
Panel 4	1344299	0	0	95	5	0	0	1271323	72976	
						224398	616003	4013268	129483	4983152
			Overall Fractions =			4.5%	12.4%	80.5%	2.6%	

The percentages are rounded to the nearest percent, except for tsw33, which is truncated to 4% such that the total is 100%. For a total of 24 samples, this leads to the following expected number of samples in each rock unit:

Rock unit	number of samples in each rock unit
Tsw33	1
Tsw34	3
Tsw35	19
Tsw36	1

Random sampling for each of these dimensionless parameters at every model grid across a laterally continuous section through the repository horizon is presented in Attachment VII. These parameters are assembled and sampled to provide the cases computed for fracture-matrix release fractions. The sampling selects 24 random parameter sets from each infiltration scenario. To ensure sampling from all host rock units, one random sample is drawn from each of the tsw33 and tsw36, three random samples from the tsw34, and 19 random samples from the tsw35. The Peclet numbers and fracture water film thicknesses selected here are used as inputs for the calculations performed in Section 6.5. A portion of the output for the sampled values are given in Table VIII-1. See Wang (2003 [163234], SN-LBNL-SCI-236-V1, p. 100) and DTN: LB0307FMRADTRN.001 for the complete output.

The sequence of calculations is given here:

Column A: Rock unit.

Column B: Fracture cell name.

Column C: Matrix cell name.

Column D: Fracture Peclet number from Attachment VII.

Column E: Matrix Peclet number from Attachment VII.

Column F: Fracture water content from Attachment VII.

Column G: Dimensionless invert depth from Attachment VII.

Column H: Uniform random numbers generated by the Excel spreadsheet function RAND() and saved.

Column I: Convert cumulative probability in Column H to an integer between 1 and 25 for the tsw33, between 26 and 95 for the tsw34, between 96 and 428 for the tsw35 and between 429 and 433 for the tsw36. In Excel, this is

Irn= INT(1+25*Hrn) for the tsw33 in row 2

Irn= INT(26+95*Hrn) for the tsw34 in rows 3, 4, and 5

Irn= INT(96+428*Hrn) for the tsw35 in rows 6 through 24

Irn= INT(429+433*Hrn) for the tsw36 in row 25

Column J: Find selected rock type from Column A. In Excel, this is

Jrn= INDEX(A$2:A$434,$Irn)

Column K: Find selected Fracture Peclet number from Column D. In Excel, this is

Krn= INDEX(D$2:D$434,$Irn)

Column L: Find selected Matrix Peclet number from Column E. In Excel, this is

Lrn= INDEX(E$2:E$434,$Irn)

Column M: Find selected fracture water content from Column F. In Excel, this is

Mrn= INDEX(F$2:F$434,$Irn)

Column N: Find selected dimensionless invert depth from Column G. In Excel, this is

Nrn= INDEX(G$2:G$434,$Irn)

Values selected in columns K, L, and M are used as input for the calculations discussed in Section 6.5.

Table VIII-1. Sampled Parameter Sets for Mean Infiltration Scenarios

	A	B	C	D	E	F	G	H	I	J	K	L	M	N	O
1	**Rock Unit**	**Fracture Cell Name**	**Matrix Cell Name**	**Fracture Peclet Number, Pe_{ef}**	**Matrix Peclet Number, Pe_m**	**Fracture Water Content, θ_f**	**Dimensionless Invert Depth, y_{dm}**	**Fixed Uniform Random Number**	**Uniform Random Integer ranging over cells in each rock unit**	**Selected Rock Type**	**Selected Fracture Peclet Number, Pe_{fe}**	**Selected Matrix Peclet Number, Pe_m**	**Selected Fracture Water Content, θ_f**	**Selected Dimensionless Invert Depth, y_{dm}**	**Case Number**
2	tsw33	F012Bl76	M012Bl76	-1.01E+00	-4.18E-01	5.12E-04	5.91E-01	3.2628E-01	9	tsw33	-1.62E+02	-1.01E+00	3.58E-05	1.52E+00	1
3	tsw33	F012Bl78	M012Bl78	-1.26E+01	-3.93E+00	3.89E-04	1.68E-01	9.4126E-01	91	tsw34	-4.05E+01	-2.62E-02	4.27E-04	3.62E+00	2
4	tsw33	F012Cl72	M012Cl72	-3.18E+00	-3.63E+00	3.77E-04	1.53E+00	5.0552E-01	61	tsw34	-2.87E+00	-5.99E-03	4.18E-04	8.14E+00	3
5	tsw33	F012Cl74	M012Cl74	-9.90E+00	-3.22E+00	1.91E-04	5.72E-01	5.7828E-01	66	tsw34	-2.45E+00	-4.48E-03	6.15E-05	7.78E+00	4
6	tsw33	F012Cm70	M012Cm70	-3.49E+01	-7.02E+00	2.36E-05	4.08E-01	5.8022E-01	289	tsw35	-4.37E+01	-1.90E-02	5.84E-04	3.91E+00	5
7	tsw33	F012Dg58	M012Dg58	-1.45E+00	-5.34E-01	1.09E-04	9.23E-01	5.2025E-01	269	tsw35	-6.49E+00	-1.33E-02	2.23E-04	5.38E+00	6
8	tsw33	F012Dl68	M012Dl68	-2.93E+00	-8.25E-01	4.52E-05	1.78E+00	6.5149E-01	312	tsw35	-1.47E+00	-3.96E-02	4.51E-05	1.17E+00	7
9	tsw33	F012Dl70	M012Dl70	-1.70E+00	-1.92E+00	1.41E-04	9.50E-01	8.8356E-01	390	tsw35	-8.82E-01	-2.00E-02	7.78E-05	1.92E+00	8
10	tsw33	F012Dl71	M012Dl71	-1.62E+02	-1.01E+00	3.58E-05	1.52E+00	3.2712E-01	204	tsw35	-2.29E+01	-6.15E-02	1.57E-04	1.59E+00	9
11	tsw33	F012Dl75	M012Dl75	-4.60E+00	-2.55E+00	1.91E-04	2.57E-01	9.5806E-01	415	tsw35	-8.53E+00	-3.56E-02	5.23E-05	1.68E+00	10
12	tsw33	F012Dl77	M012Dl77	-2.14E+01	-1.10E+00	2.86E-05	1.74E+00	4.3343E-01	240	tsw35	-1.66E+00	-5.90E-03	5.62E-05	6.82E+00	11
13	tsw33	F012Dl79	M012Dl79	-4.16E+00	-3.87E+00	3.90E-04	2.83E-01	5.3805E-01	275	tsw35	-2.63E+00	-6.72E-03	9.60E-04	5.35E+00	12
14	tsw33	F012Ef89	M012Ef89	-7.51E+00	-1.88E-01	2.44E-04	2.15E+00	8.3590E-01	374	tsw35	-4.99E+00	-1.13E-02	1.19E-04	1.69E+00	13
15	tsw33	F012Eg 2	M012Eg 2	-2.36E+00	-2.51E-01	9.75E-05	6.91E-01	5.9247E-01	293	tsw35	-1.20E+02	-7.27E-03	7.44E-05	3.62E+00	14
16	tsw33	F012Eg14	M012Eg14	-3.40E+01	-9.55E-02	2.41E-04	1.54E+00	4.0651E-01	231	tsw35	-9.89E-01	-3.08E-02	4.39E-04	2.17E+00	15
17	tsw33	F012Eg25	M012Eg25	-2.93E+00	-3.67E-01	5.32E-05	1.01E+00	3.3043E-01	206	tsw35	-1.95E+00	-1.85E-02	1.10E-04	1.08E+00	16
18	tsw33	F012Eg36	M012Eg36	-1.89E+00	-1.28E-01	6.43E-05	1.19E+00	4.4509E-02	110	tsw35	-3.46E+01	-7.85E-03	6.74E-04	3.32E+00	17
19	tsw33	F012Eg47	M012Eg47	-6.39E+00	-8.81E-01	3.25E-04	4.93E-01	5.7180E-01	286	tsw35	-3.34E+00	-2.03E-02	5.61E-05	2.99E+00	18
20	tsw33	F012Eh 1	M012Eh 1	-6.48E+00	-1.03E+00	7.84E-05	4.68E-01	8.5478E-01	380	tsw35	-2.09E-01	-9.65E-03	1.17E-04	2.36E+00	19
21	tsw33	F012El73	M012El73	-8.11E+00	-7.44E-01	1.82E-04	1.23E+00	2.3670E-01	174	tsw35	-4.59E+00	-2.77E-02	6.28E-05	1.33E+00	20
22	tsw33	F012Fg26	M012Fg26	-4.82E+00	-9.99E-01	7.02E-05	3.94E-01	6.6134E-01	316	tsw35	-1.14E+01	-8.15E-03	6.06E-04	5.43E+00	21
23	tsw33	F012Fg59	M012Fg59	-1.51E+01	-7.32E-01	5.13E-05	5.69E-01	2.3843E-01	175	tsw35	-3.26E+00	-7.18E-03	8.70E-05	4.54E+00	22
24	tsw33	F012Fg70	M012Fg70	-2.45E+01	-2.08E+00	3.73E-04	3.68E-01	8.1817E-01	368	tsw35	-6.11E+00	-6.35E-02	1.29E-04	9.09E-01	23
25	tsw33	F012Fg80	M012Fg80	-2.30E+02	-6.47E-01	5.64E-04	3.49E+00	4.2699E-01	431	tsw36	-7.60E+00	-1.16E-02	1.28E-04	3.65E+00	24
26	tsw33	F012Fg90	M012Fg90	-4.66E+00	-4.61E-01	4.10E-05	6.50E-01								
27	tsw34	F0013g 3	M0013g 3	-3.10E-01	-3.67E-02	3.15E-04	4.94E+00								
28	tsw34	F0013g48	M0013g48	-2.47E+00	-6.35E-03	1.64E-04	4.58E+00								
29	tsw34	F0013g91	M0013g91	-2.50E+01	-1.65E-02	1.28E-04	4.34E+00								
30	tsw34	F0013h 2	M0013h 2	-3.93E+00	-5.10E-02	8.19E-05	4.01E+00								

Output-DTN: LB0307FMRADTRN.001

ATTACHMENT IX – DISTRIBUTIONS FOR MATRIX DIFFUSION AND MEASURED MATRIX DIFFUSION COEFFICIENTS

This attachment provides additional information pertaining to Section 6.4.5 of the main text. Anion and cation distributions for matrix diffusion coefficients are sampled from a beta distribution, using the distribution statistics shown here:

Table IX-1. Matrix Diffusion Distributions

Solute	Min (m^2/s)	Max (m^2/s)	Mean (m^2/s)	Std Dev (m^2/s)	Distribution Type
Anions	0	1.0 E-9	3.2 E-11	1.0 E-11	Beta
Cations	0	1.0 E-9	1.6 E-10	0.5 E-10	Beta

DTN: LA0003JC831362.001 [149557]

The distributions are generated by sampling 1,000 values from each beta distribution. The sampling for the beta distribution uses the approximation for the inverse as given in Equation 26.5.22 of Abramowitz and Stegun (1972 [103280]). This method requires the generation of a Gaussian random number. Gaussian random numbers are computed using the rational approximation for the inverse cumulative probability distribution for a Gaussian random variable, as given in Equation 26.2.23 of Abramowitz and Stegun (1972 [103280]). See Scientific Notebook by Wang (2003 [163234], SN-LBNL-SCI-236-V1, pp. 40–42) for a discussion of the generation of Gaussian random numbers. A portion of the output with the results for anions are given in Table IX-2. See Wang (2003 [163234], SN-LBNL-SCI-236-V1, p. 75) and Output-DTN: LB0307FMRADTRN.001 for the complete output. The sequence of calculations is given here:

Column A: Uniform random numbers generated by the Excel spreadsheet function RAND() and saved. These are the cumulative probabilities, p.

Column B: The normalized Gaussian random number corresponding to the cumulative probability in Column A.

Column C: The parameter λ in the beta inverse function is given by Abramowitz and Stegun (1972 [103280], Equation 26.5.22)

$$\lambda = \frac{y_p^2 - 3}{6} \qquad \text{(Eq. IX-1)}$$

where y_p is defined in Column B. In Excel, this is

Crn=(Brn^2-3)/6

Column D: The parameter w in the beta inverse function is given by Abramowitz and Stegun (1972 [103280], Equation 26.5.22)

$$w = \frac{y_p (h+\lambda)^{\frac{1}{2}}}{h} - \left(\frac{1}{2b-1} - \frac{1}{2a-1}\right)\left(\lambda + \frac{5}{6} - \frac{2}{3h}\right) \qquad \text{(Eq. IX-2)}$$

In Excel, this is

Drn= (Brn*(($K$2+Crn)^0.5)/$K$2)-((2*$J$2-1)^(-1)-(2*$I$2-1)^(-1))*(Crn+(5/6)-2/(3*$K$2))

Column E: The beta random number, x_p, is given by Abramowitz and Stegun (1972 [103280], Equation 26.5.22)

$$x_p \approx \frac{a}{a+be^{2w}} \qquad \text{(Eq. XI-3)}$$

In Excel, this is

Ern=$I$2/($I$2+$J$2*EXP(2*Drn))

Column F: Contains the ordered values computed in Column E.

Column G: Contains the value of the mean matrix diffusion coefficient, μ_{D_m} , from Table 4.1-2f.

Column H: Contains the value of the matrix diffusion coefficient standard deviation, σ_{D_m} , from Table 4.1-2f.

Column I: The beta distribution parameter *a* is derived from by Abramowitz and Stegun (1972 [103280], Equation 26.1.33) (for detailed derivation, see Attachment XI)

$$a = \mu_{D_m}\left[\frac{\mu_{D_m}\left(1-\mu_{D_m}\right)}{\sigma_{D_m}^2} - 1\right] \qquad \text{(Eq. IX-4)}$$

In Excel, this is

I2=G2*((G2*(1-G2)/H2^2)-1)

Column J: The beta distribution parameter *b* is derived from Abramowitz and Stegun (1972 [103280], Equation 26.1.33) (for detailed derivation, see Attachment XI)

$$b = \left(1-\mu_{D_m}\right)\left[\frac{\mu_{D_m}\left(1-\mu_{D_m}\right)}{\sigma_{D_m}^2} - 1\right] \qquad \text{(Eq. IX-5)}$$

In Excel, this is

J2=(1-G2)*((G2*(1-G2)/H2^2)-1)

Column K: The parameter *h* in the beta inverse function is given by Abramowitz and Stegun (1972 [103280], Equation 26.5.22)

$$h = 2\left(\frac{1}{2a-1} + \frac{1}{2b-1} \right)^{-1} \qquad \text{(Eq. IX-6)}$$

In Excel, this is

K2=2*((2*I2-1)^(-1)+(2*J2-1)^(-1))^(-1)

Table IX-2. Anion Matrix Diffusion Coefficient Distribution

	A	B	C	D	E	F	G	H	I	J	K
1	**Fixed Uniform Random Number (P)**	**y_P - normalized Gaussian random number**	**lambda**	**w**	**x_P - Beta random number (Dm, m^2/s)**	**Ordered Distribution (Dm, m^2/s)**	**mean Dm - m^2/s**	**standard deviation Dm m^2/s**	**a**	**b**	**h**
2	5.7681E-01	1.9336E-01	-4.94E-01	4.73E-02	2.91E-11	9.49E-12	3.20E-11	1.00E-11	1.02E+01	3.20E+11	3.90E+01
3	1.5444E-02	-2.1589E+00	2.77E-01	-2.91E-01	5.73E-11	9.78E-12					
4	8.9037E-01	1.2287E+00	-2.48E-01	2.25E-01	2.04E-11	1.23E-11					
5	5.6024E-01	1.5127E-01	-4.96E-01	4.05E-02	2.95E-11	1.32E-11					
6	3.7359E-01	-3.2192E-01	-4.83E-01	-3.41E-02	3.43E-11	1.33E-11					
7	2.4730E-01	-6.8273E-01	-4.22E-01	-8.86E-02	3.82E-11	1.34E-11					
8	9.0546E-01	1.3135E+00	-2.12E-01	2.41E-01	1.98E-11	1.35E-11					
9	7.0270E-01	5.3178E-01	-4.53E-01	1.03E-01	2.60E-11	1.37E-11					
10	4.1033E-01	-2.2629E-01	-4.91E-01	-1.94E-02	3.33E-11	1.41E-11					
11	1.0581E-01	-1.2493E+00	-2.40E-01	-1.70E-01	4.50E-11	1.42E-11					
12	3.9859E-01	-2.5657E-01	-4.89E-01	-2.41E-02	3.36E-11	1.49E-11					
13	8.0209E-01	8.4894E-01	-3.80E-01	1.58E-01	2.33E-11	1.49E-11					
14	5.1719E-01	4.2995E-02	-5.00E-01	2.31E-02	3.06E-11	1.49E-11					
15	5.6921E-01	1.7402E-01	-4.95E-01	4.42E-02	2.93E-11	1.50E-11					
16	4.4208E-01	-1.4540E-01	-4.96E-01	-6.73E-03	3.24E-11	1.52E-11					
17	8.4520E-01	1.0160E+00	-3.28E-01	1.87E-01	2.20E-11	1.53E-11					
18	9.3388E-01	1.5056E+00	-1.22E-01	2.76E-01	1.84E-11	1.53E-11					
19	8.3627E-01	9.7919E-01	-3.40E-01	1.81E-01	2.23E-11	1.53E-11					
20	2.0787E-01	-8.1365E-01	-3.90E-01	-1.08E-01	3.97E-11	1.54E-11					
21	6.9208E-01	5.0136E-01	-4.58E-01	9.82E-02	2.63E-11	1.57E-11					
22	5.2997E-01	7.5015E-02	-4.99E-01	2.82E-02	3.02E-11	1.57E-11					
23	8.1050E-02	-1.3983E+00	-1.74E-01	-1.91E-01	4.68E-11	1.58E-11					
24	2.0226E-01	-8.3341E-01	-3.84E-01	-1.11E-01	3.99E-11	1.58E-11					
25	6.0195E-01	2.5798E-01	-4.89E-01	5.79E-02	2.85E-11	1.59E-11					
26	9.4478E-01	1.5966E+00	-7.52E-02	2.94E-01	1.78E-11	1.61E-11					
27	9.0122E-01	1.2887E+00	-2.23E-01	2.36E-01	1.99E-11	1.61E-11					
28	6.8250E-02	-1.4892E+00	-1.30E-01	-2.03E-01	4.80E-11	1.62E-11					
29	4.9429E-01	-1.4281E-02	-5.00E-01	1.40E-02	3.11E-11	1.63E-11					
30	5.9879E-01	2.4979E-01	-4.90E-01	5.65E-02	2.86E-11	1.63E-11					

Output-DTN: LB0307FMRADTRN.001

The Reimus et al. (2002 [163008]) correlation is sampled according to the scheme outlined in Section 6.4.5 and Equations 51 through 55 which are shown here:

$$\log(D_m) = -3.49 + 1.38\theta_m + 0.165\log(k_w) \tag{Eq. IX-7}$$

$$X = \log\left(\frac{D_0}{D_m}\right) \tag{Eq. IX-8}$$

$$\mu_X = \log(D_0) - \overline{\log(D_m)} \tag{Eq. IX-9}$$

$$Y = \ln(X) \tag{Eq. IX-10}$$

$$\mu_Y = \ln(\mu_X) \tag{Eq. IX-11}$$

Here, D_0 is a limiting value of D_m taken to be 10^{-9} m^2/s (see Table 4.1-2f). The sampling follows a lognormal distribution scheme for the variable X, in which the variable Y in Equation IX-10 is normally distributed. This sampled variable is reduced to the matrix diffusion coefficient using Equations IX-8 and IX-10. Gaussian random numbers are computed using the rational approximation for the inverse cumulative probability distribution for a Gaussian random variable as given in Equation 26.2.23 of Abramowitz and Stegun (1972 [103280]). See Scientific Notebook by Wang (2003 [163234], SN-LBNL-SCI-236-V1, pp. 40–42) for a discussion of the generation of Gaussian random numbers. A portion of the output is shown in Table IX-3. See Wang (2003 [163234], SN-LBNL-SCI-236-V1, p. 76) and DTN: LB0307FMRADTRN.001 for the complete output.

The sequence of calculations is as follows:

Column A: Uniform random numbers generated by the Excel spreadsheet function RAND() and saved. These are the cumulative probabilities, p.

Column B: The normalized Gaussian random number corresponding to the cumulative probability in Column A.

Column C: The corresponding random value of Y is derived from the normalized Gaussian random variable through the normalization definition:

$$f = x_p\sigma_Y + \mu_Y \tag{Eq. IX-12}$$

In Excel, this is

Crn=Brn*$I$2+$H$2

where μ_Y and σ_Y are defined as discussed below.

Column D: This column calculates the fracture frequency through the inverse of (Eq. IX-11)

$$X = \exp(Y) \qquad \text{(Eq. IX-13)}$$

In Excel, this is

Drn=exp(Crn)

Column E: The matrix diffusion coefficient is obtained from a known value of X using Equation IX-8. In Excel, this is

Ern=10^(-Drn-9) (Eq. IX-14)

Column F: The cumulative probability based on rank. In Excel, this is

Frn=F(rn-1)+$F$2

and

F1=1/1001

Column G: The values from Column E in ascending order.

Column H: Contains the value of μ_Y (see below).

Column I: Contains the value of σ_Y (see below).

The mean value for the case shown in Figure 6.4-13 is equal to the log(D_m), which is equal to the logarithm of the square root of the product of the mean values from Table 4.1-2f. The standard deviation is then adjusted to provide a distribution with a spread representative of the anion and cation curves shown in Figure 6.4-13. The mean value for Y is then computed from Equations IX-9 and IX-11. The "high" and "low" cases shown in Figure 6.4-14 are computed using mean values for log(D_m) computed from Equation IX-7, using the 5th and 95th percentile matrix water content and matrix effective permeability computed in the mean infiltration scenario from Attachment VI and converting to m^2/s. The data shown in Figure 6.4-15 are from DTN: LA0003JC831362.001 [149557] and from Reimus et al. (2002 [163008]). Both data sets contain values of D_m for pertechnetate (technetium) and tritium. Data for bicarbonate diffusion come from Reimus et al. (2002 [163008]). These data are combined and ordered to generate a cumulate probability distribution, where the cumulative probability is defined by the order number of the sequence divided by the number of samples plus 1.

Table IX-3. Matrix Diffusion Coefficient Distribution using Reimus et al. (2002 [163008]) Correlation

	A	B	C	D	E	F	G	H	I
1	**Fixed Uniform Random Number (P)**	**x_P - normalized Gaussian random number**	**x - Gaussian random number**	**Transformation to -9-logDm**	**Transformation to Dm**	**Cumulative Probability**	**Ordered Dm for Reimus mean high**	**Transformed mean**	**standard deviation**
2	5.3281E-01	8.2139E-02	2.79E-01	1.32E+00	4.76E-11	9.99E-04	7.89E-13	2.54E-01	3.00E-01
3	4.6699E-01	-8.2631E-02	2.30E-01	1.26E+00	5.52E-11	2.00E-03	1.04E-12		
4	3.3136E-01	-4.3574E-01	1.24E-01	1.13E+00	7.38E-11	3.00E-03	1.34E-12		
5	9.3271E-01	1.4966E+00	7.03E-01	2.02E+00	9.53E-12	4.00E-03	1.42E-12		
6	6.3809E-01	3.5292E-01	3.60E-01	1.43E+00	3.68E-11	5.00E-03	1.61E-12		
7	8.6930E-01	1.1232E+00	5.91E-01	1.81E+00	1.56E-11	5.99E-03	1.63E-12		
8	4.5888E-01	-1.0301E-01	2.24E-01	1.25E+00	5.62E-11	6.99E-03	2.00E-12		
9	2.0184E-01	-8.3491E-01	4.02E-03	1.00E+00	9.91E-11	7.99E-03	2.09E-12		
10	8.4635E-01	1.0209E+00	5.61E-01	1.75E+00	1.77E-11	8.99E-03	2.42E-12		
11	5.7322E-01	1.8423E-01	3.10E-01	1.36E+00	4.33E-11	9.99E-03	2.43E-12		
12	3.3340E-01	-4.3010E-01	1.25E-01	1.13E+00	7.35E-11	1.10E-02	2.66E-12		
13	1.2658E-01	-1.1428E+00	-8.84E-02	9.15E-01	1.21E-10	1.20E-02	2.76E-12		
14	9.0245E-01	1.2958E+00	6.43E-01	1.90E+00	1.25E-11	1.30E-02	2.76E-12		
15	6.4196E-01	3.6326E-01	3.63E-01	1.44E+00	3.64E-11	1.40E-02	3.14E-12		
16	9.9078E-01	2.3570E+00	9.62E-01	2.62E+00	2.42E-12	1.50E-02	3.23E-12		
17	5.1764E-01	4.4122E-02	2.68E-01	1.31E+00	4.93E-11	1.60E-02	4.08E-12		
18	9.3863E-01	1.5437E+00	7.18E-01	2.05E+00	8.92E-12	1.70E-02	4.20E-12		
19	7.0570E-01	5.4049E-01	4.17E-01	1.52E+00	3.04E-11	1.80E-02	4.33E-12		
20	6.8929E-01	4.9342E-01	4.03E-01	1.50E+00	3.19E-11	1.90E-02	4.88E-12		
21	2.9941E-01	-5.2571E-01	9.68E-02	1.10E+00	7.91E-11	2.00E-02	4.97E-12		
22	4.4436E-01	-1.3961E-01	2.13E-01	1.24E+00	5.80E-11	2.10E-02	5.04E-12		
23	7.3649E-04	-3.1802E+00	-7.00E-01	4.97E-01	3.19E-10	2.20E-02	5.11E-12		
24	8.9592E-01	1.2588E+00	6.32E-01	1.88E+00	1.31E-11	2.30E-02	5.11E-12		
25	3.2285E-01	-4.5932E-01	1.17E-01	1.12E+00	7.52E-11	2.40E-02	5.20E-12		
26	7.2163E-01	5.8732E-01	4.31E-01	1.54E+00	2.90E-11	2.50E-02	5.45E-12		
27	9.9740E-01	2.7953E+00	1.09E+00	2.98E+00	1.04E-12	2.60E-02	5.50E-12		
28	6.8463E-01	4.8028E-01	3.99E-01	1.49E+00	3.24E-11	2.70E-02	5.52E-12		
29	7.1169E-01	5.5794E-01	4.22E-01	1.52E+00	2.99E-11	2.80E-02	5.89E-12		
30	7.9956E-01	8.3989E-01	5.06E-01	1.66E+00	2.19E-11	2.90E-02	6.01E-12		

Output-DTN: LB0307FMRADTRN.001

INTENTIONALLY LEFT BLANK

ATTACHMENT X – EXAMPLE OF CALCULATION FOR FRACTURE-MATRIX PARTITIONING

This attachment provides additional information pertaining to Section 6.4.4 of the main text. The calculation tool used to solve Equations 40 through 44 is Mathcad V11. The implementation of Mathcad for nominal cases 1 with 1,024 points is given on the following pages.

NOMINAL CASE 1 - 1024

Values used for calculation

$Pe_{fe} := -1$ **Pe_{fe} is the fracture Peclet number**

$Pe_m := -0.004$ **Pe_m is the matrix Peclet number**

$\theta_f := 0.0001$ **θ_f is the fracture water content**

$y_{dm} := 4.00$ **y_{dm} is the dimensionless invert thickness**

$b_d := \theta_f$ **b_d is the dimensionless fracture water thickness**

$j_{max} := 1023$ **j_{max}+1 is the number of Fourier coefficients**

Distance coordinate along drift wall

$i := 0 .. j_{max}$ **i is reference number for the coordinates along the drift wall**

$j := 0 .. j_{max}$ **j is the reference number for the Fourier coefficients**

$x_{d_i} := \frac{i}{j_{max}}$ **x_{di} is the dimensionless distance along the drift wall**

Sample values for verification of x_{di}

$x_{d_0} = 0$ $x_{d_1} = 9.775 \times 10^{-4}$ $x_{d_2} = 1.955 \times 10^{-3}$ .... $x_{d_{1022}} = 0.999$ $x_{d_{1023}} = 1$

Solution for Fourier coefficients

$$q_{d_i} := Pe_{fe} + 0.5\cdot\left(Pe_m - Pe_{fe}\right)\cdot\left(\Phi\left(x_{d_i} - b_d\right) - \Phi\left(b_d - x_{d_i}\right) + 1\right)$$

Eq. (29), (30), (31) from main text

q_{di} is the dimensionless water flux profile at the invert-rock interface

Note that the heaviside step function (Φ) is defined to be 1 at x=0. Therefore, the combination of step functions, 0.5(Φ(x)-Φ(−x)+1), is needed to make $q_{di} = 0.5*(Pe_{fe}+Pe_m)$ at $x_{di}=b_d$

Sample values for verification of q_d

$q_{d_0} = -1$ $q_{d_1} = -4\times 10^{-3}$ $q_{d_2} = -4\times 10^{-3}$ .... $q_{d_{1022}} = -4\times 10^{-3}$ $q_{d_{1023}} = -4\times 10^{-3}$

$$M_{i,j} := \Phi(-j)\cdot\left(1 - y_{md}\cdot q_{d_i}\right) + \Phi(j-1)\cdot\cos\left(j\cdot\pi\cdot x_{d_i}\right)\cdot\left(j\cdot\pi - q_{d_i}\cdot\tanh\left(y_{md}\cdot j\cdot\pi\right)\right)$$

Eq. (36) from main

$M_{i,j}$ is the coefficient matrix for A

Sample values for verification of $M_{i,j}$

$M_{0,0} = 5$ $M_{0,1} = 4.142$ .... $M_{0,1022} = 3.212\times 10^3$ $M_{0,1023} = 3.215\times 10^3$

$M_{1,0} = 1.016$ $M_{1,1} = 3.146$ .... $M_{1,1022} = -3.211\times 10^3$ $M_{1,1023} = -3.214\times 10^3$

$M_{2,0} = 1.016$ $M_{2,1} = 3.146$ .... $M_{2,1022} = 3.211\times 10^3$ $M_{2,1023} = 3.214\times 10^3$

. .
. $M_{511,511} = -1.134\times 10^3$.
. .

$M_{1022,0} = 1.016$ $M_{1022,1} = -3.146$ .... $M_{1022,1022} = -3.211\times 10^3$ $M_{1022,1023} = 3.214\times 10^3$

$M_{1023,0} = 1.016$ $M_{1023,1} = -3.146$ .... $M_{1023,1022} = 3.211\times 10^3$ $M_{1023,1023} = -3.214\times 10^3$

$A := M^{-1} \cdot q_d$ From Eq. (35) in main text

A is the vector of Fourier coefficients

Verification of matrix solution for Fourier coefficients, A. CheckA is a vector of the residuals for M*A-q_d

$\text{CheckA} := M \cdot A - q_d$

Plot of residuals for M*A-q_d

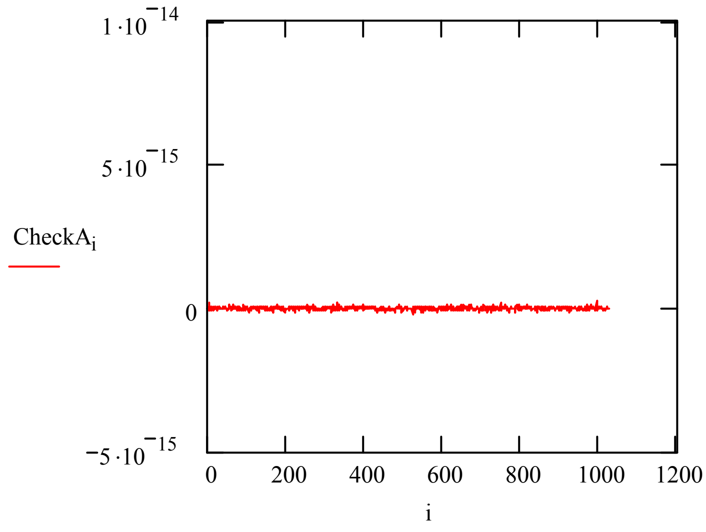

Calculations for cumulative dimensionless flux and flux ratio in fractures and matrix

$$F_{dfA} := Pe_{fe} \cdot \left[\theta_f \left(1 + A_0 \cdot y_{md}\right) + \sum_{j=1}^{j_{max}} \frac{A_j}{j \cdot \pi} \cdot \tanh\left(j \cdot \pi \cdot y_{md}\right) \cdot \sin\left(j \cdot \pi \cdot b_d\right) \right]$$

Eq. (43) from main text

$F_{dfA} = -9.801 \times 10^{-5}$

F_{dfA} is the total dimensionless mass flux into the fracture at the drift wall on rock side of boundary

Partial sum for verification of F_{dfA}

$$CheckF_{dfA} := Pe_{fe} \cdot \left[\theta_f \left(1 + A_0 \cdot y_{md}\right) + \sum_{j=1}^{8} \frac{A_j}{j \cdot \pi} \cdot \tanh\left(j \cdot \pi \cdot y_{md}\right) \cdot \sin\left(j \cdot \pi \cdot b_d\right) \right]$$

$A_0 = -4.407 \times 10^{-3}$ $A_1 = -3.034 \times 10^{-4}$ $A_2 = -1.518 \times 10^{-4}$

$A_3 = -1.012 \times 10^{-4}$ $A_4 = -7.591 \times 10^{-5}$ $A_5 = -6.073 \times 10^{-5}$

$A_6 = -5.061 \times 10^{-5}$ $A_7 = -4.338 \times 10^{-5}$ $A_8 = -3.796 \times 10^{-5}$

$CheckF_{dfA} = -9.815 \times 10^{-5}$

$$F_{dmA} := Pe_m \cdot \left[\left(1 - b_d\right) \cdot \left(1 + A_0 \cdot y_{md}\right) - \sum_{j=1}^{j_{max}} \frac{A_j}{j \cdot \pi} \cdot \tanh\left(j \cdot \pi \cdot y_{md}\right) \cdot \sin\left(j \cdot \pi \cdot b_d\right) \right]$$

Eq. (44) from main text

F_{dmA} is the total dimensionless mass flux into the matrix at the drift wall on rock side of boundary

$F_{dmA} = -3.929 \times 10^{-3}$

Partial sum for verification of F_{dfA}

$$CheckF_{dmA} := Pe_m \cdot \left[\left(1 - b_d\right) \cdot \left(1 + A_0 \cdot y_{md}\right) - \sum_{j=1}^{8} \frac{A_j}{j \cdot \pi} \cdot \tanh\left(j \cdot \pi \cdot y_{md}\right) \cdot \sin\left(j \cdot \pi \cdot b_d\right) \right]$$

$CheckF_{dmA} = -3.929 \times 10^{-3}$

$$\frac{F_{dfA}}{F_{dmA} + F_{dfA}} = 0.02434$$

Dimensionless flux ratio on rock side of boundary

Eq. (41) from main text

$$F_{dfD} := \theta_f A_0 + \sum_{j=1}^{j_{max}} A_j \cdot \sin\left(j \cdot \pi \cdot b_d\right)$$

F_{dfD} is the total dimensionless mass flux into the fracture at the drift wall on invert side of boundary

$$F_{dfD} = -9.745 \times 10^{-5}$$

Partial sum for verification of F_{dfD}

$$CheckF_{dfD} := \theta_f A_0 + \sum_{j=1}^{8} A_j \cdot \sin\left(j \cdot \pi \cdot b_d\right)$$

$$CheckF_{dfD} = -1.204 \times 10^{-6}$$

$$F_{dmD} := \left(1 - b_d\right) \cdot A_0 - \sum_{j=1}^{j_{max}} A_j \cdot \sin\left(j \cdot \pi \cdot b_d\right)$$

Eq. (42) from main text

$$F_{dmD} = -4.309 \times 10^{-3}$$

F_{dmD} is the total dimensionless mass flux into the matrix at the drift wall on invert side of boundary

Partial sum for verification of F_{dmD}

$$CheckF_{dmD} := \left(1 - b_d\right) \cdot A_0 - \sum_{j=1}^{8} A_j \cdot \sin\left(j \cdot \pi \cdot b_d\right)$$

$$CheckF_{dmD} = -4.405 \times 10^{-3}$$

$$\frac{F_{dfD}}{F_{dmD} + F_{dfD}} = 0.02211$$

Dimensionless flux ratio on invert side of boundary

NOTE: The output of the calculation, which is the dimensionless flux ratio given above, is not affected by the evaluations from this point forward; these are presented to provide background information on the character of the solution.

Eq. (40) from main text

$$C_{d_i} := A_0 \cdot y_{md} + \sum_{j=1}^{j_{max}} A_j \cdot \cos\left(j \cdot \pi \cdot x_{d_i}\right) \cdot \tanh\left(j \cdot \pi \cdot y_{md}\right)$$

C_{di} are the dimensionless concentrations at the invert-rock interface

$$CP(i) := 1 + C_{d_i}$$

CP(i) is the plotting variable for the unnormalized dimensionless concentration

$$XP(i) := x_{d_i}$$

XP(i) is the plotting variable for the dimensionless distance

Plot of the unnormalized dimensionless concentration (C/C_m) at the solution points for the Fourier coefficients

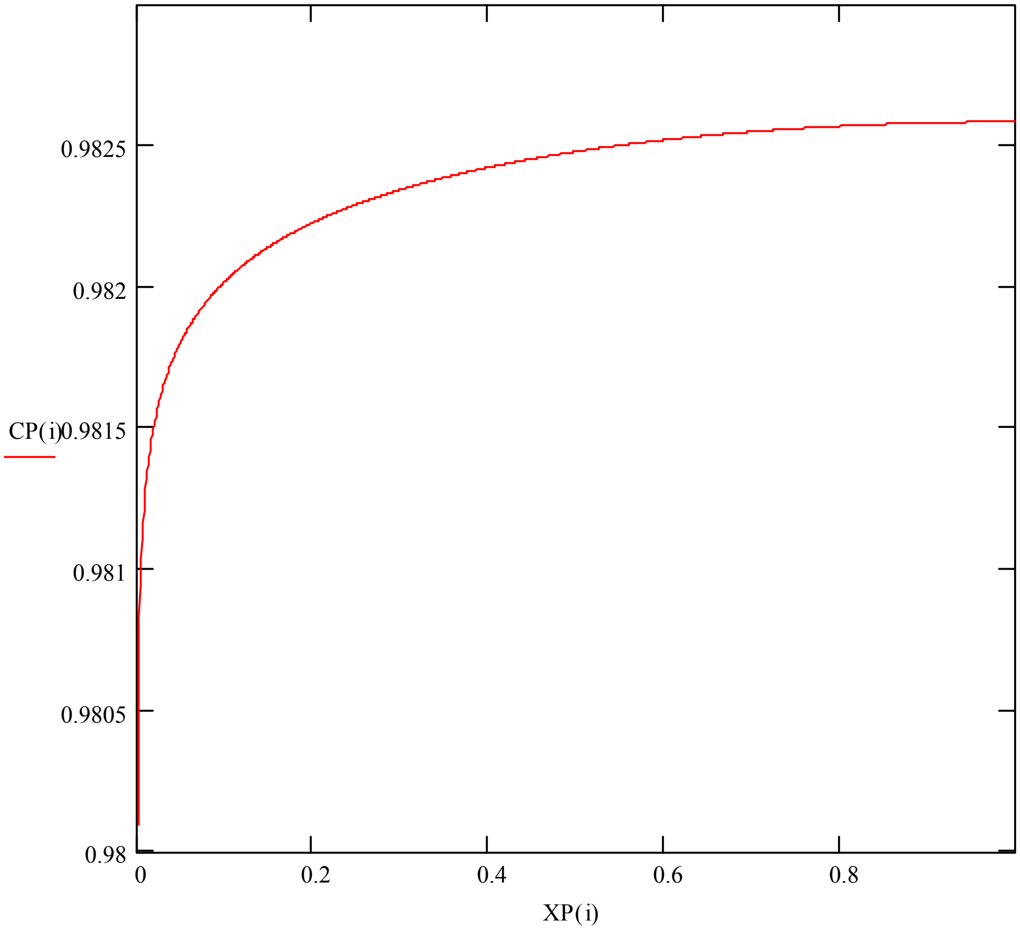

Output-DTN: LB0307FMRADTRN.001

Behavior of local dimensionless mass flux at drift wall

$qC_i := q_{d_i} \cdot \left(C_{d_i} + 1\right)$

Local dimensionless mass flux in rock at drift wall

$qCP(i) := -qC_i$

qCP(i) is the plotting variable for the negative of the local dimensionless advective mass flux in the rock at drift wall

$XP(i) := x_{d_i}$

XP(i) is the plotting variable for the dimensionless distance along the drift wall

Plot of negative of local dimensionless flux at the solution points for the Fourier coefficients

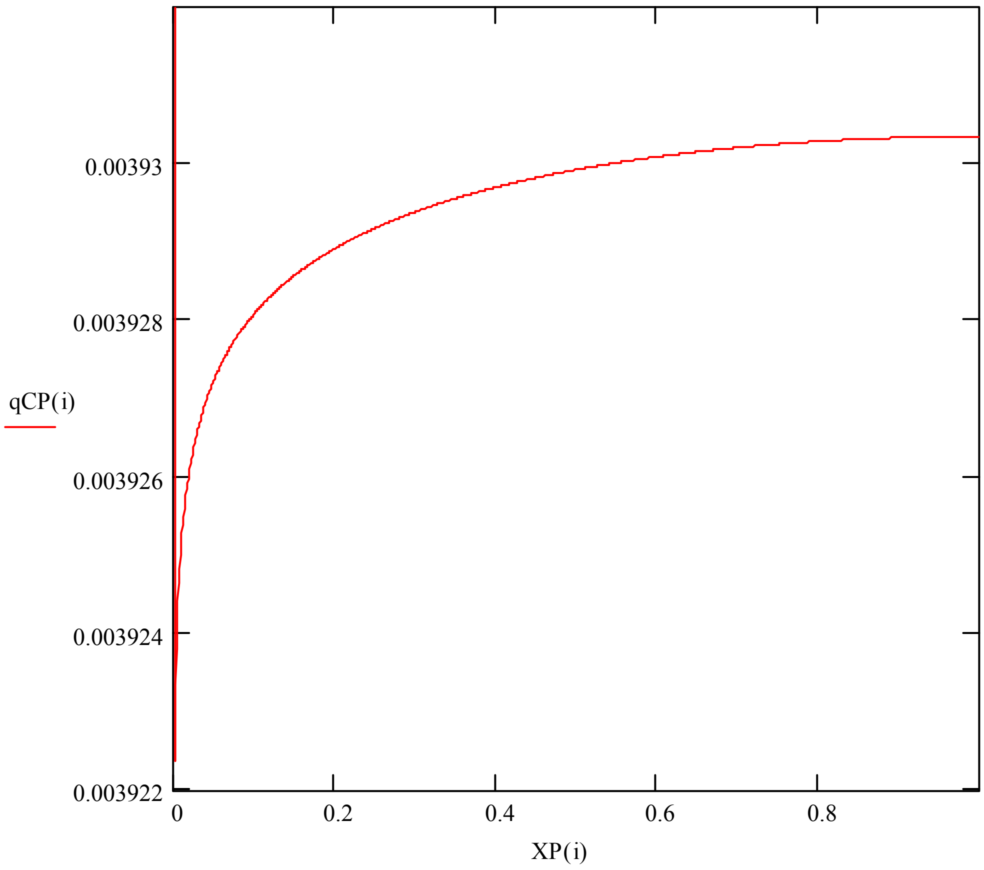

Output-DTN: LB0307FMRADTRN.001

Comparison of radionuclide flux in invert and rock at the drift wall at points not fixed in solution for the Fourier coefficients

$k_{max} := 40000$

$k := 0 .. k_{max}$

k is the reference number for coordinates along the drift wall not fixed in the solution for the Fourier coefficients

$$x_{d_k} := \frac{k}{k_{max}}$$

x_{dk} are the coordinates along the drift wall not fixed in the solution for the Fourier coefficients

$$q_{d_k} := Pe_{fe} + 0.5 \cdot \left(Pe_m - Pe_{fe}\right) \cdot \left(\Phi\left(x_{d_k} - b_d\right) - \Phi\left(b_d - x_{d_k}\right) + 1\right)$$

$$C_{d_k} := A_0 \cdot y_{md} + \sum_{j=1}^{j_{max}} A_j \cdot \cos\left(j \cdot \pi \cdot x_{d_k}\right) \cdot \tanh\left(j \cdot \pi \cdot y_{md}\right)$$

Dimensionless local flux in rock at drift wall

$$qC_k := q_{d_k} \cdot \left(C_{d_k} + 1\right)$$

$$dC_{d_k} := A_0 + \sum_{j=1}^{j_{max}} j \cdot \pi \cdot A_j \cdot \cos\left(j \cdot \pi \cdot x_{d_k}\right)$$

Dimensionless local flux in invert at drift wall

$qCP(k) := -qC_k$

qCP(k) is a plotting variable for the negative of the local dimensionless advective flux in the rock matrix plus the diffusive flux in the fracture at drift wall

$dCP(k) := -dC_{d_k}$

dCP(k) is a plotting variables for the negative of the local dimensionless diffusive flux in the invert at drift wall

$XP(k) := x_{d_k}$

XP(k) is a plotting variable for dimensionless distance

Comparison plot of flux in the invert and rock at the drift wall over the entire domain

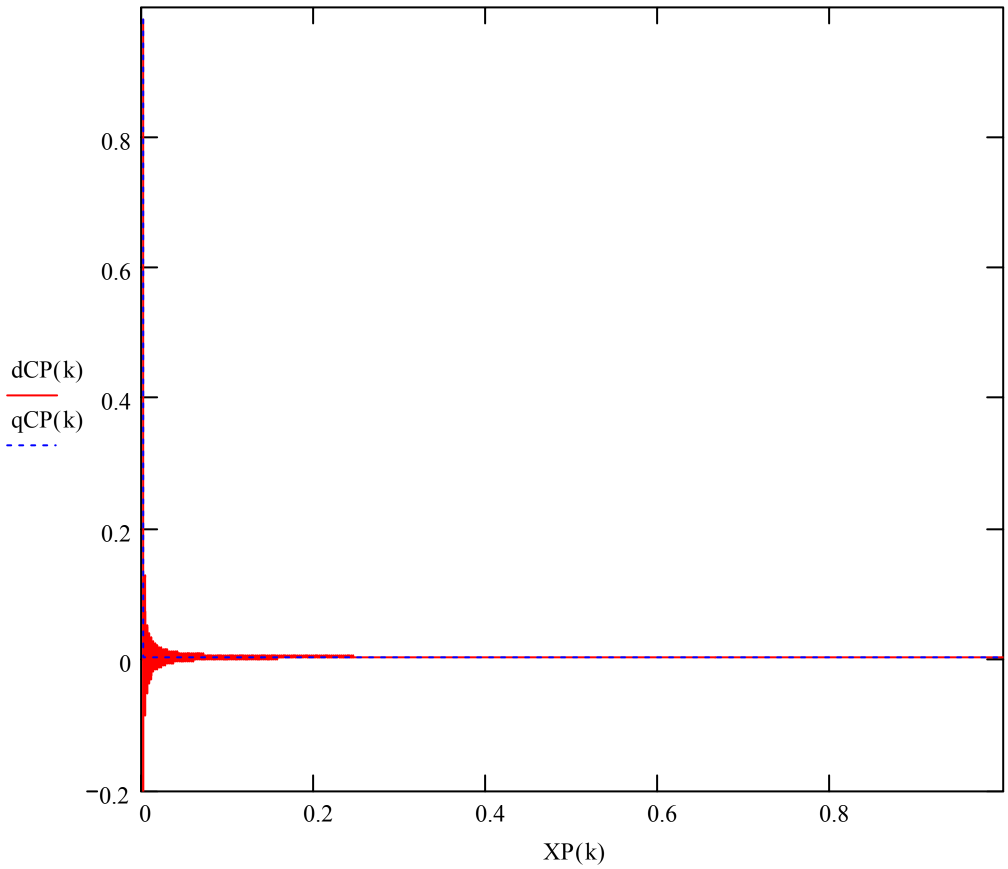

Output-DTN: LB0307FMRADTRN.001

Comparison plot of flux in the invert and rock at the drift wall over region near fracture

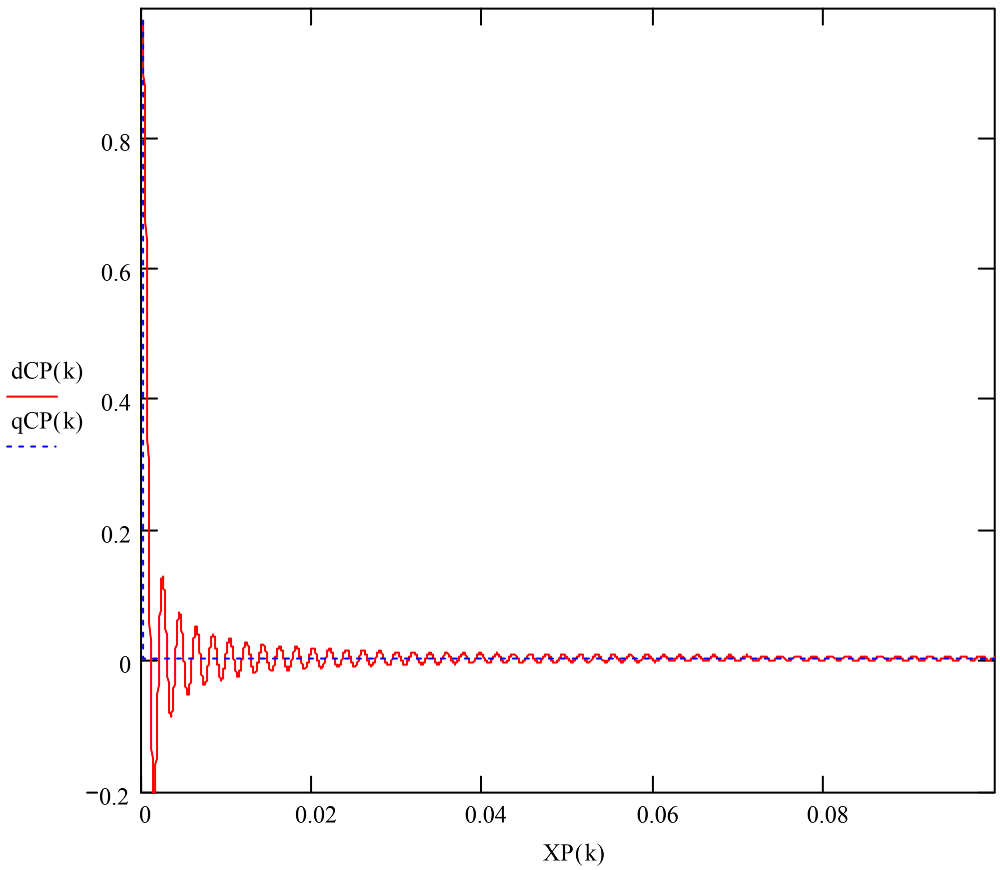

Output-DTN: LB0307FMRADTRN.001

Comparison plot of flux in the invert and rock at the drift wall - fracture close-up

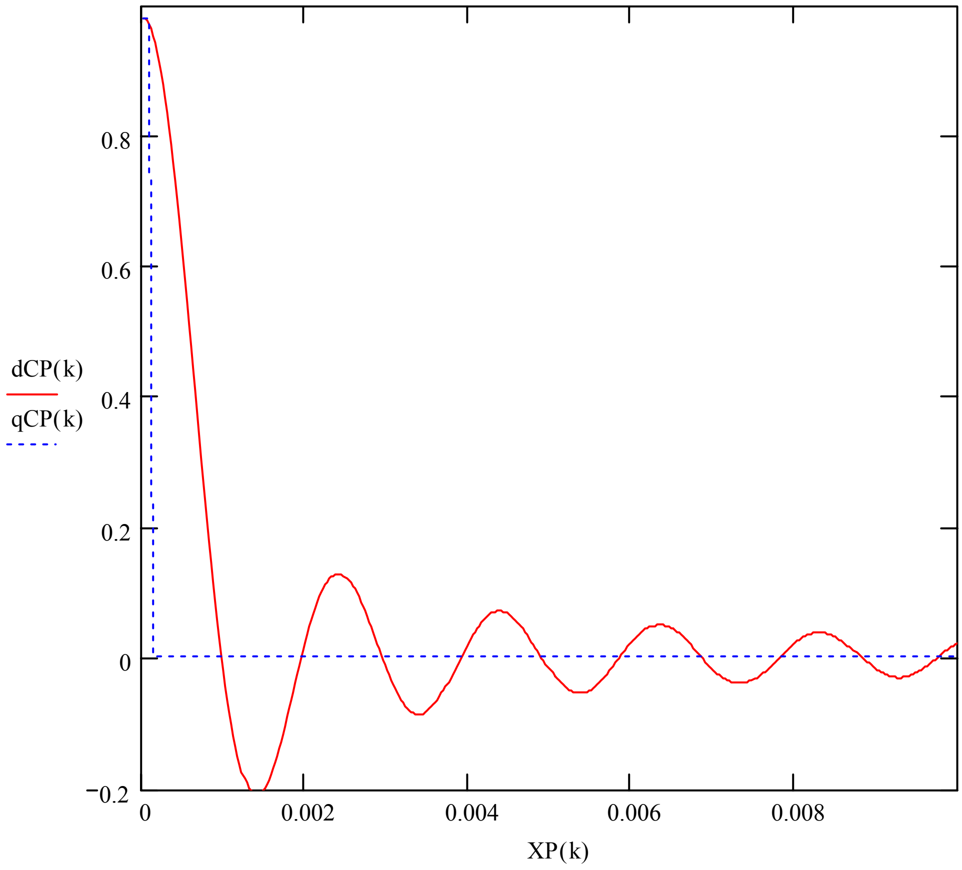

Output-DTN: LB0307FMRADTRN.001

Comparison of boundary condition results (drift wall) at intermediate x-coordinates to those used in the solution for the discrete transform coefficients

$$q_{d_k} := Pe_{fe} + 0.5 \cdot \left(Pe_m - Pe_{fe}\right) \cdot \left(\Phi\left(x_{d_k} - b_d\right) - \Phi\left(b_d - x_{d_k}\right) + 1\right)$$

q_{dk} is the flux function

$$fa_k := \left[\sum_j \left[A_j \cdot \Phi(-j) \cdot \left(1 - y_{md} \cdot q_{d_k}\right) + A_j \cdot \Phi(j-1) \cdot \cos\left(j \cdot \pi \cdot x_{d_k}\right) \cdot \left(j \cdot \pi - q_{d_k} \cdot \tanh\left(j \cdot \pi \cdot y_{md}\right)\right)\right]\right]$$

fa_k is the series expansion of the flux function

Eq. (34) of main text

$$q_{d_1} = -1$$

$XP(k) := x_{d_k}$ **XP(k) is a plotting variable for the dimensionless distance**

$QP(k) := q_{d_k}$ **QP(k) is a plotting variable for the flux function**

$FAP(k) := fa_k$ **FAP(k) is a plotting variable for series representation of the flux function**

Comparison of boundary condition results (drift wall) at intermediate x-coordinates to those used in the solution for the discrete transform coefficients over the entire domain.

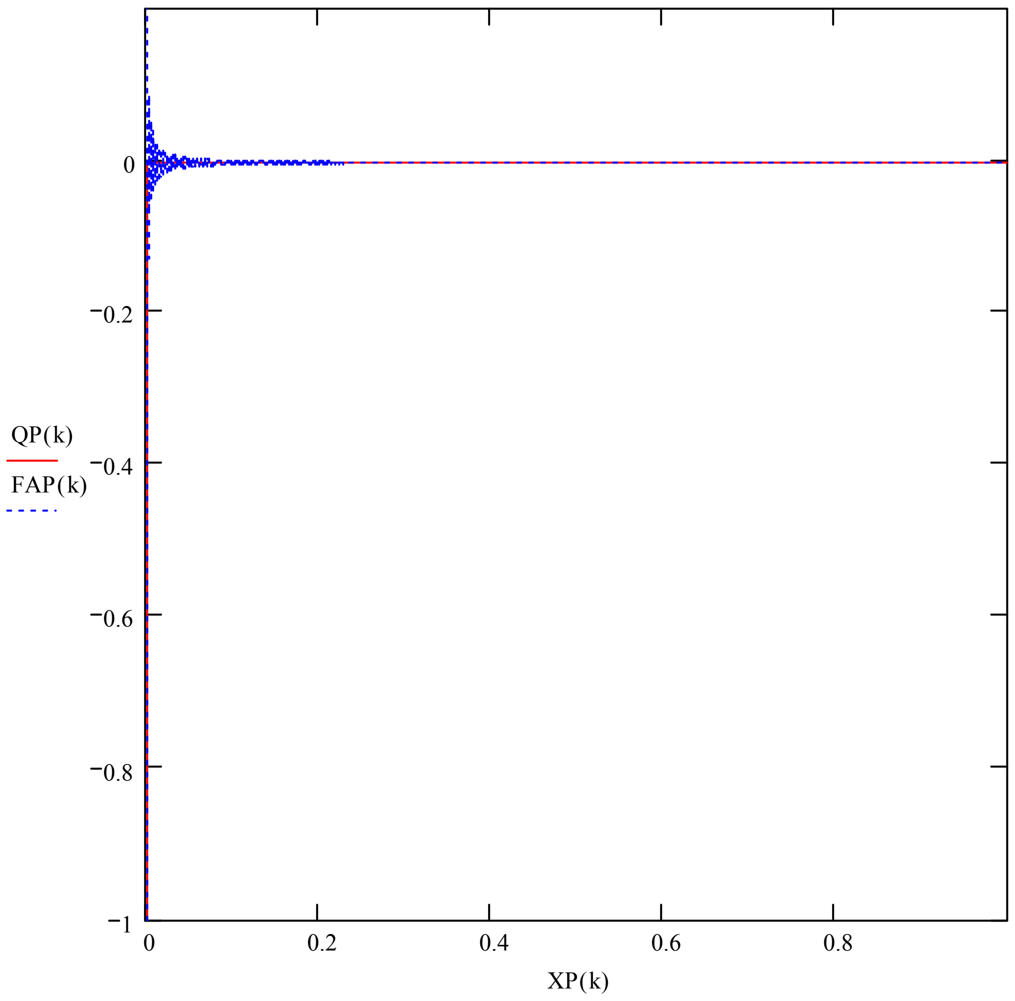

Output-DTN: LB0307FMRADTRN.001

Comparison of boundary condition results (drift wall) at intermediate x-coordinates to those used in the solution for the discrete transform coefficients over a region near the fracture.

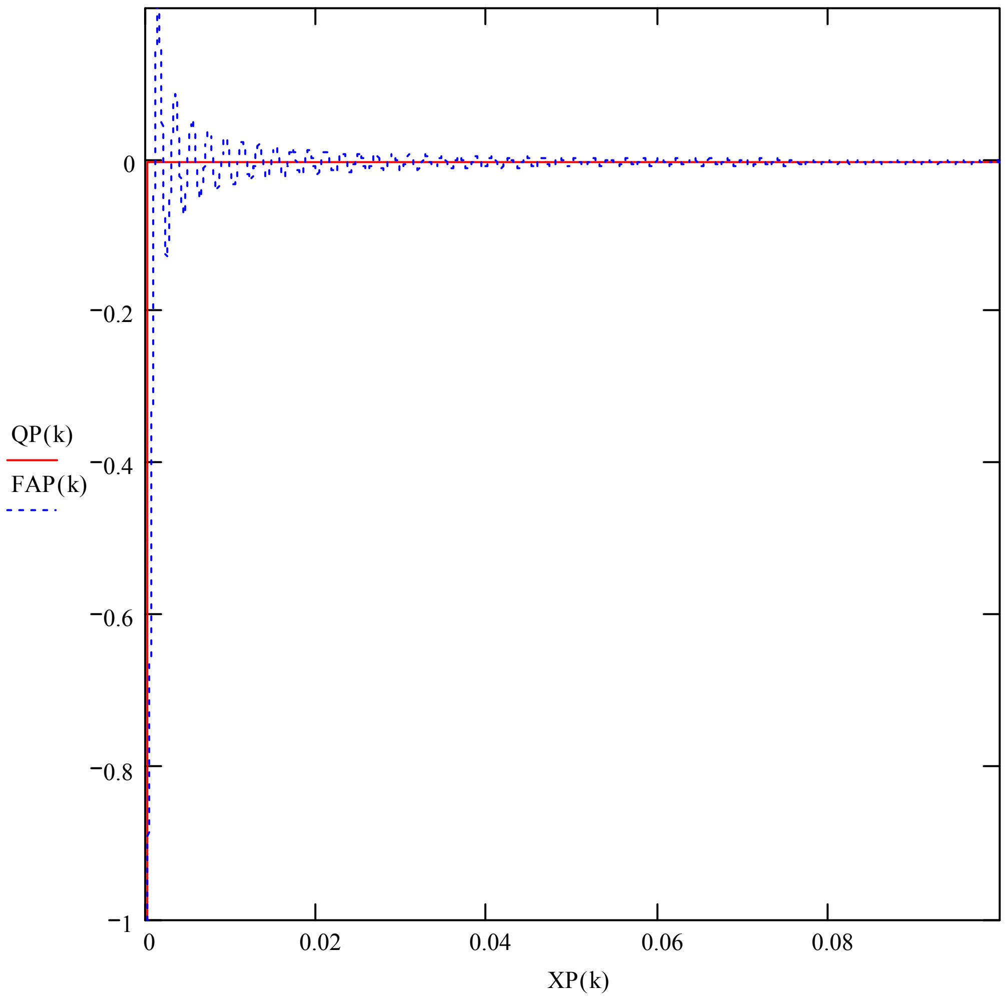

Output-DTN: LB0307FMRADTRN.001

Comparison of boundary condition results (drift wall) at intermediate x-coordinates to those used in the solution for the discrete transform coefficients - fracture close-up.

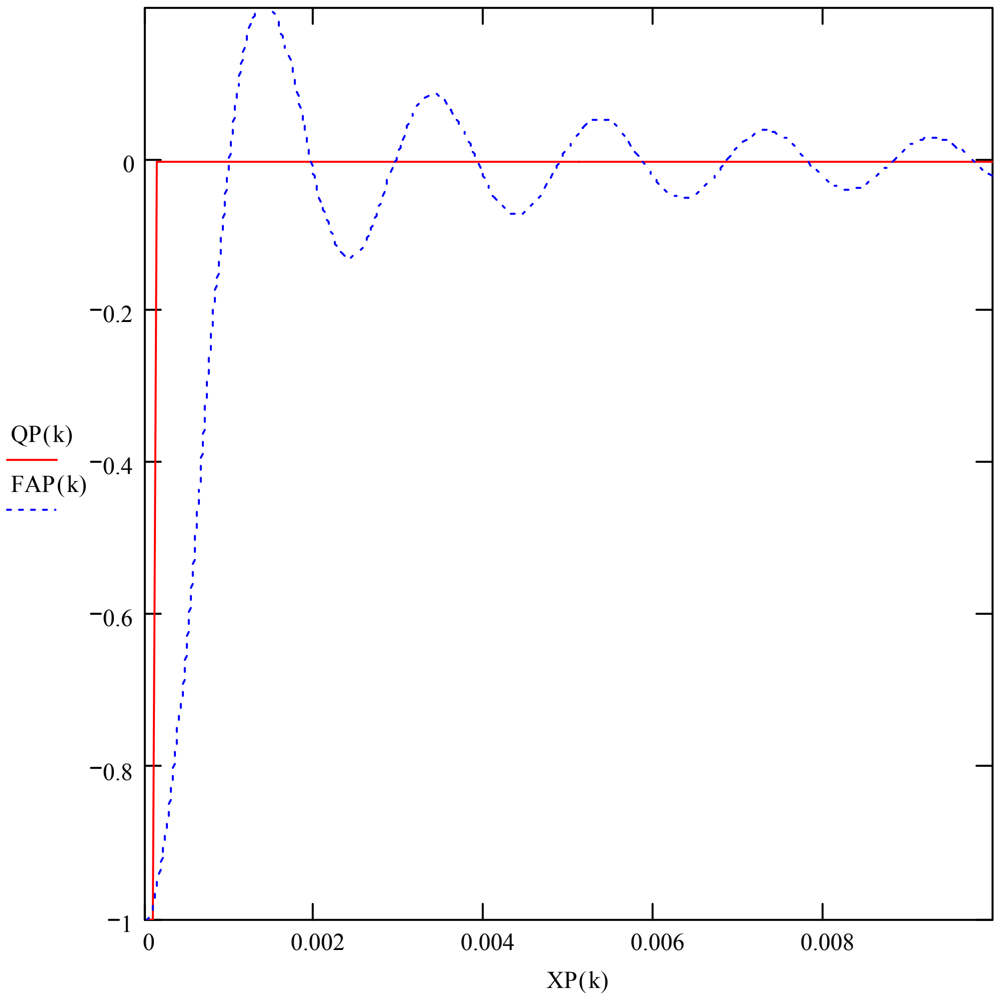

Output-DTN: LB0307FMRADTRN.001

ATTACHMENT XI – SUPPLEMENTARY DERIVATIONS

This attachment provides additional information pertaining to Section 6.4.5 of the main text and Attachments I and IV.

The derivation of Equation (50) in the main text, starting from Equation (49),

$$F = \frac{S_{fna}^{\frac{1}{2}}\left[1-\left(1-S_{fna}^{\frac{1}{m}}\right)^{m}\right]^{2}}{S_{fn}^{\frac{1}{2}}\left[1-\left(1-S_{fn}^{\frac{1}{m}}\right)^{m}\right]^{2}} \qquad \text{(Eq. 49)}$$

and expanding the numerator for small $S_{fma}^{\frac{1}{m}}$ using the following first-order Taylor series expansion:

$(1-x)^{m} \approx 1-mx$ where $x = S_{fma}^{\frac{1}{m}}$

Substitute this into the numerator of Equation 49 gives,

$$F = \frac{S_{fna}^{\frac{1}{2}}\left[1-\left(1-mS_{fma}^{\frac{1}{m}}\right)\right]^{2}}{S_{fn}^{\frac{1}{2}}\left[1-\left(1-S_{fn}^{\frac{1}{m}}\right)^{m}\right]^{2}} \qquad \text{(Eq. XI-1)}$$

Reducing the numerator gives,

$$F = \frac{m^{2}S_{fna}^{\frac{1}{2}+\frac{2}{m}}}{S_{fn}^{\frac{1}{2}}\left[1-\left(1-S_{fn}^{\frac{1}{m}}\right)^{m}\right]^{2}} \qquad \text{(Eq. XI-2)}$$

Rearranging to solve for S_{fma} gives,

$$S_{fna}^{\frac{4+m}{2m}} = \frac{F}{m^{2}}S_{fn}^{\frac{1}{2}}\left[1-\left(1-S_{fn}^{\frac{1}{m}}\right)^{m}\right]^{2} \qquad \text{(Eq. XI-3)}$$

or

$$S_{fna} = \left[\left(\frac{F}{m^2} \right) S_{fn}^{\frac{1}{2}} \left\{ 1 - \left(1 - S_{fn}^{\frac{1}{m}} \right)^m \right\}^2 \right]^{\frac{2m}{4+m}} \qquad \text{(Eq. 50)}$$

Equations (I-1) and (I-2) in Attachment I are derived as follows:

Let Y be log-normal with mean μ_Y and standard deviation σ_Y and X is normal with mean μ_X and standard deviation σ_X; also $X = \ln(Y)$ or $Y = e^X$.

First, find $\overline{e^X}$ and $\overline{e^{2X}}$, or equivalently, $\overline{Y}$ and $\overline{Y^2}$.

$$\overline{e^X} = \int_{-\infty}^{\infty} \frac{e^X}{\sqrt{2\pi}\sigma_X} e^{-\frac{(X-\mu_X)^2}{2\sigma_X^2}} dX = e^{\mu_X + \frac{\sigma_X^2}{2}} \qquad \text{(Eq. XI-4)}$$

or $\mu_Y = e^{\mu_X + \frac{\sigma_X^2}{2}}$ (Eq. XI-5)

and

$$\overline{e^{2X}} = \int_{-\infty}^{\infty} \frac{e^{2X}}{\sqrt{2\pi}\sigma_X} e^{-\frac{(X-\mu_X)^2}{2\sigma_X^2}} dX = e^{2\mu_X + 2\sigma_X^2} \qquad \text{(Eq XI-6)}$$

and because $\sigma_Y^2 = \overline{e^{2X}} - \overline{e^X}^2$, then,

$$\sigma_Y^2 = e^{2\mu_X + \sigma_X^2} \left(e^{\sigma_X^2} - 1 \right) = \mu_Y^2 \left(e^{\sigma_X^2} - 1 \right) \qquad \text{(Eq. XI-7)}$$

Rearranging Equation (XI-7) and solving for σ_X gives,

$$\sigma_X = \sqrt{\ln\left(1 + \frac{\sigma_Y^2}{\mu_Y^2} \right)} \qquad \text{(Eq. I-2)}$$

Rearranging Equation (XI-5) and using Equation (I-2) to solve for μ_X gives,

$$\mu_X = \ln(\mu_Y) - \frac{1}{2} \ln\left(1 + \frac{\sigma_Y^2}{\mu_Y^2} \right) \qquad \text{(Eq. I-1)}$$

The derivation of equations (IV-3) and (IV-4) from Abramowitz and Stegun (1972 [103280], Equation 26.1.33) is shown here:

$$\text{mean} \equiv \mu = \frac{a}{a+b} \qquad \text{(Eq. XI-8)}$$

$$\text{variance} \equiv \sigma^2 = \frac{ab}{(a+b)^2(a+b+1)} \qquad \text{(Eq. XI-9)}$$

Solve equation (XI-8) for *b*

$$b = a\left(\frac{1-\mu}{\mu}\right) \qquad \text{(Eq. XI-10)}$$

Also note from equation (XI-8) that

$$a+b = \frac{a}{\mu} \qquad \text{(Eq. XI-11)}$$

Substitute equations (XI-10) and (XI-11) into equation (XI-9) to give

$$\sigma^2 = \frac{a^2\left(\frac{1-\mu}{\mu}\right)}{\left(\frac{a}{\mu}\right)^2\left(\frac{a}{\mu}+1\right)} \qquad \text{(Eq. XI-12)}$$

Simplifying equation (XI-12) gives

$$\sigma^2 = \frac{\mu(1-\mu)}{\left(\frac{a}{\mu}+1\right)} \qquad \text{(Eq. XI-13)}$$

Solving equation (XI-13) for *a* gives

$$a = \mu\left[\frac{\mu(1-\mu)}{\sigma^2}-1\right] \qquad \text{(Eq. VI-3)}$$

and substituting equation (VI-3) for *a* in equation (XI-10) gives

$$b = (1-\mu)\left[\frac{\mu(1-\mu)}{\sigma^2}-1\right] \qquad \text{(Eq. VI-4)}$$

INTENTIONALLY LEFT BLANK

ATTACHMENT XII – DEMONSTRATION OF EQUIVALENCE OF THE DISCRETE TRANSFORM SOLUTION AND FOURIER SERIES SOLUTION

This attachment provides additional information pertaining to Section 6.4.3 of the main text.

Summary from Sections 6.4.2 and 6.4.3

The steady-state diffusion equation and four boundary conditions to be solved are given by equations (24) through (28) of the main text:

$$\nabla_d^2 C_d(x_d, y_d) = 0 \qquad \text{(Eq. 24)}$$

$$C_d(x_d, 0) = 0 \qquad \text{(Eq. 25)}$$

$$\frac{\partial C_d}{\partial x_d}(0, y_d) = 0 \qquad \text{(Eq. 26)}$$

$$\frac{\partial C_d}{\partial x_d}(1, y_d) = 0 \qquad \text{(Eq. 27)}$$

$$\frac{\partial C_d}{\partial y_d}(x_d, y_{md}) = q_d(x_d)\left(C_d(x_d, y_{md}) + 1\right) \qquad \text{(Eq. 28)}$$

A solution that satisfies Equation 24 and the boundary conditions, Equations 25–27 is

$$C_d(x_d, y_d) = B_0 y_d + \sum_{j=1}^{\infty} B_j \cos(j\pi x_d)\sinh(j\pi y_d) \qquad \text{(Eq. 33)}$$

which may be verified by direct substitution.

Substituting Equation 33 into Equation 28 gives

$$A_0\left(1 - q_d(x_d)y_{md}\right) + \sum_{j=1}^{\infty} A_j \cos(j\pi x_d)\left[j\pi - q_d(x_d)\tanh(j\pi y_{md})\right] = q_d(x_d) \qquad \text{(Eq. 34)}$$

or

$$\sum_{j=0}^{\infty} M_{ij} A_j = q_{di} \qquad \text{(Eq. 35)}$$

where

$$M_{i0} = \left(1 - q_d(x_{di})y_{md}\right) \qquad \text{(Eq. 36)}$$

$$M_{ij} = \cos(j\pi x_{di})\left[j\pi - q_d(x_{di})\tanh(j\pi y_{md})\right] \quad \text{for} \quad i > 0 \qquad \text{(Eq. 37)}$$

$$q_{di} = q_d\left(x_{di}\right) \qquad \text{(Eq. 38)}$$

$$A_j = B_j \cosh\left(j\pi y_{md}\right) \qquad \text{(Eq. 39)}$$

The transformation from B_j to A_j is introduced to eliminate numerical difficulties in the evaluation of $\cosh\left(j\,\pi\,y_{md}\right)$ and $\sinh\left(j\,\pi\,y_{md}\right)$ for large *j*.

Explanation of Discrete Transform Solution Method

If a solution for A_j can be found that satisfies equation (35) at all points in the domain of the problem, then, in combination with equation (39) and equation (33) we have the exact solution to equations (24) through (28). Therefore, equation (35) represents a linear system of equations for A_j that can produce the exact solution in the limit as $j \to \infty$. An approximate solution may be derived by solving for A_j at a finite number of points and this solution converges as *j* increases.

Demonstration of Equivalence with Fourier Series

A test of the discrete transform solution method is given here for a problem in which the standard Fourier solution is also available. In this test, an analytical form for the concentration at the invert-rock boundary was assumed. That is, starting with equations (24) through (27), we then specify the concentration at the invert-rock interface, replacing the flux boundary condition in equation (28) with a concentration boundary condition. With this type of boundary condition, the solution may be obtained using standard Fourier methods. This solution was then substituted into equation (28) to derive a form for $q_d\left(x_d\right)$ that is consistent with the assumed concentration boundary condition. Therefore, we now have the identical problem with a flux-type boundary condition as given in equation (28). A series of values for $q_d\left(x_d\right)$ were then generated from the standard Fourier solution and used as input to the discrete transform solution method to solve equations (24) through (28). The resulting Fourier coefficients may be compared with those generated from the standard Fourier solution, and the concentration distribution at the invert-rock boundary may be compared with the assumed concentration distribution. The following presents the details of this comparison.

Given equations (33) and (39), we have,

$$C_d\left(x_d, y_{dm}\right) = A_0 y_{dm} + \sum_{j=1}^{\infty} A_j \cos\left(j\pi x_d\right)\tanh\left(j\pi y_{dm}\right) \qquad \text{(Eq. 40)}$$

Assume the following form for the concentration distribution at the invert-rock interface:

$$C_d\left(x_d, y_{dm}\right) = K_1 + K_2\left[1 - \exp\left(-K_3 x_d\right)\right] \qquad \text{(Eq. XII-1)}$$

where K_1, K_2, and K_3 are constants.

For the Fourier cosine series,

$$C_d(x_d, y_{dm}) = \frac{a_0}{2} + \sum_{j=1}^{\infty} a_j \cos(jx) \qquad \text{(Eq. XII-2)}$$

where $x = \pi x_d$.

Fourier coefficients are obtained using the orthogonality properties of the cosine function,

$$a_0 = \frac{2}{\pi}\int_0^{\pi}\left\{K_1 + K_2\left[1 - \exp\left(\frac{-K_3}{\pi}x\right)\right]\right\}dx \qquad \text{(Eq. XII-3)}$$

$$a_j = \frac{2}{\pi}\int_0^{\pi}\left\{K_1 + K_2\left[1 - \exp\left(\frac{-K_3}{\pi}x\right)\right]\right\}\cos(jx)\,dx \qquad \text{(Eq. XII-4)}$$

giving the following results for the Fourier Coefficients:

$$a_0 = 2K_1 + 2K_2 - \frac{2K_2}{K_3}\left[1 - \exp(-K_3)\right] \qquad \text{(Eq. XII-5)}$$

$$a_j = \frac{-2K_2K_3}{K_3^2 + j^2\pi^2}\left[1 - \exp(-K_3)\cos(j\pi)\right] \qquad \text{(Eq. XII-6)}$$

Comparing Equations 40 and XII-2 we find,

$$\frac{a_0}{2} = A_0 y_{dm} \qquad \text{(Eq. XII-7)}$$

$$a_j = A_j \tanh(j\pi y_{dm}) \qquad \text{(Eq. XII-8)}$$

Therefore,

$$A_0 = \frac{K_1}{y_{dm}} + \frac{K_2}{y_{dm}} - \frac{K_2}{K_3 y_{dm}}\left[1 - \exp(-K_3)\right] \qquad \text{(Eq. XII-9)}$$

$$A_j = \frac{-2K_2K_3}{K_3^2 + j^2\pi^2}\frac{\left[1 - \exp(-K_3)\cos(j\pi)\right]}{\tanh(j\pi y_{dm})} \qquad \text{(Eq. XII-10)}$$

and expressions for B_j are derived using Equation 39 in combination with XII-9 and XII-10.

Substituting for B_j into equation (33) gives,

$$\begin{aligned} C_d(x_d, y_d) &= \frac{K_1 y_d}{y_{dm}} + \frac{K_2 y_d}{y_{dm}} - \frac{K_2 y_d}{K_3 y_{dm}}\left[1 - \exp(-K_3)\right] \\ &- \sum_{j=1}^{\infty} \frac{2K_2K_3}{K_3^2 + j^2\pi^2} \frac{\left[1 - \exp(-K_3)\cos(j\pi)\right]}{\sinh(j\pi y_{dm})} \cos(j\pi x_d)\sinh(j\pi y_d) \end{aligned} \qquad \text{(Eq. XII-11)}$$

and

$$\begin{aligned} \frac{\partial C(x_d, y_d)}{\partial y_d} &= \frac{K_1}{y_{dm}} + \frac{K_2}{y_{dm}} - \frac{K_2}{K_3 y_{dm}}\left[1 - \exp(-K_3)\right] \\ &- \sum_{j=1}^{\infty} \frac{2K_2K_3(j\pi)}{K_3^2 + j^2\pi^2} \frac{\left[1 - \exp(-K_3)\cos(j\pi)\right]}{\sinh(j\pi y_{dm})} \cos(j\pi x_d)\cosh(j\pi y_d) \end{aligned} \qquad \text{(Eq. XII-12)}$$

Evaluating Equations XII-11 and XII-12 at $y_d = y_{dm}$ gives

$$\begin{aligned} C_d(x_d, y_{dm}) &= K_1 + K_2 - \frac{K_2}{K_3}\left[1 - \exp(-K_3)\right] \\ &- \sum_{j=1}^{\infty} \frac{2K_2K_3}{K_3^2 + j^2\pi^2} \left[1 - \exp(-K_3)\cos(j\pi)\right]\cos(j\pi x_d) \end{aligned} \qquad \text{(Eq. XII-13)}$$

and

$$\begin{aligned} \frac{\partial C(x_d, y_{dm})}{\partial y_d} &= \frac{K_1}{y_{dm}} + \frac{K_2}{y_{dm}} - \frac{K_2}{K_3 y_{dm}}\left[1 - \exp(-K_3)\right] \\ &- \sum_{j=1}^{\infty} \frac{2K_2K_3(j\pi)}{K_3^2 + j^2\pi^2} \frac{\left[1 - \exp(-K_3)\cos(j\pi)\right]}{\tanh(j\pi y_{dm})} \cos(j\pi x_d) \end{aligned} \qquad \text{(Eq. XII-14)}$$

From equation (28)

$$q_d(x_d) = \frac{\dfrac{\partial C(x_d, y_{dm})}{\partial y_d}}{C_d(x_d, y_{dm}) + 1} \qquad \text{(Eq. XII-15)}$$

Substituting Equations XII-13 and XII-14 into Equation XII-15 allows for the evaluation of $q_d(x_d)$.

Letting $K_1 = -0.02$, $K_2 = 0.0025$, and $K_3 = 10$, the concentration profile (equation XII-1) and Fourier representation of that concentration profile (Equation XII-13) using 101 Fourier coefficients is plotted in Figure XII-1 (note that C_d ranges from –1 to 0 and $C_d + 1$ is plotted):

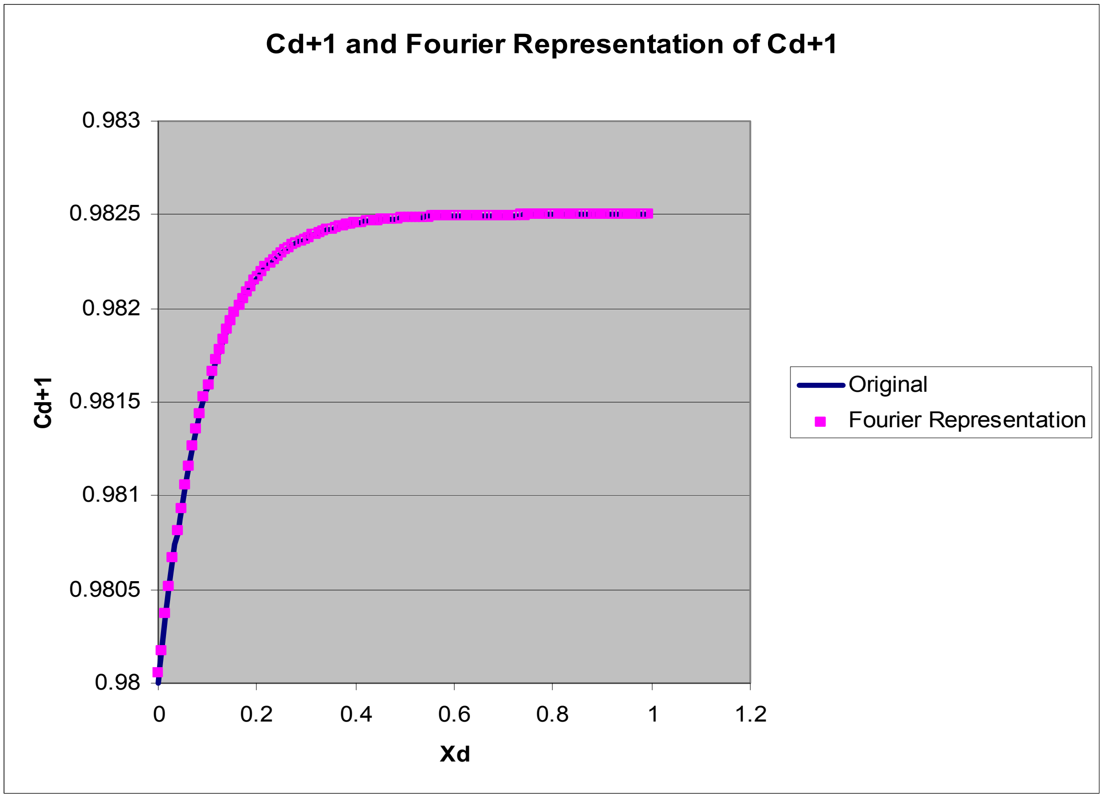

Output-DTN: LB0307FMRADTRN.001

Figure XII-1. Assumed Concentration Profile and its Fourier Representation

As expected, the Fourier decomposition may be used to reconstruct the function.

Using Equation XII-15 to generate values of q_d, the discrete transform solution method was used to solve Equations 24 through 28. For this test case, 128 discrete transform coefficients were used in solution of Equation 35 for A_j. Fourier coefficients determined in Equations XII-9 and XII-10 are compared with the coefficients determined from the discrete transform solution method concentration as shown in Figure XII-2.

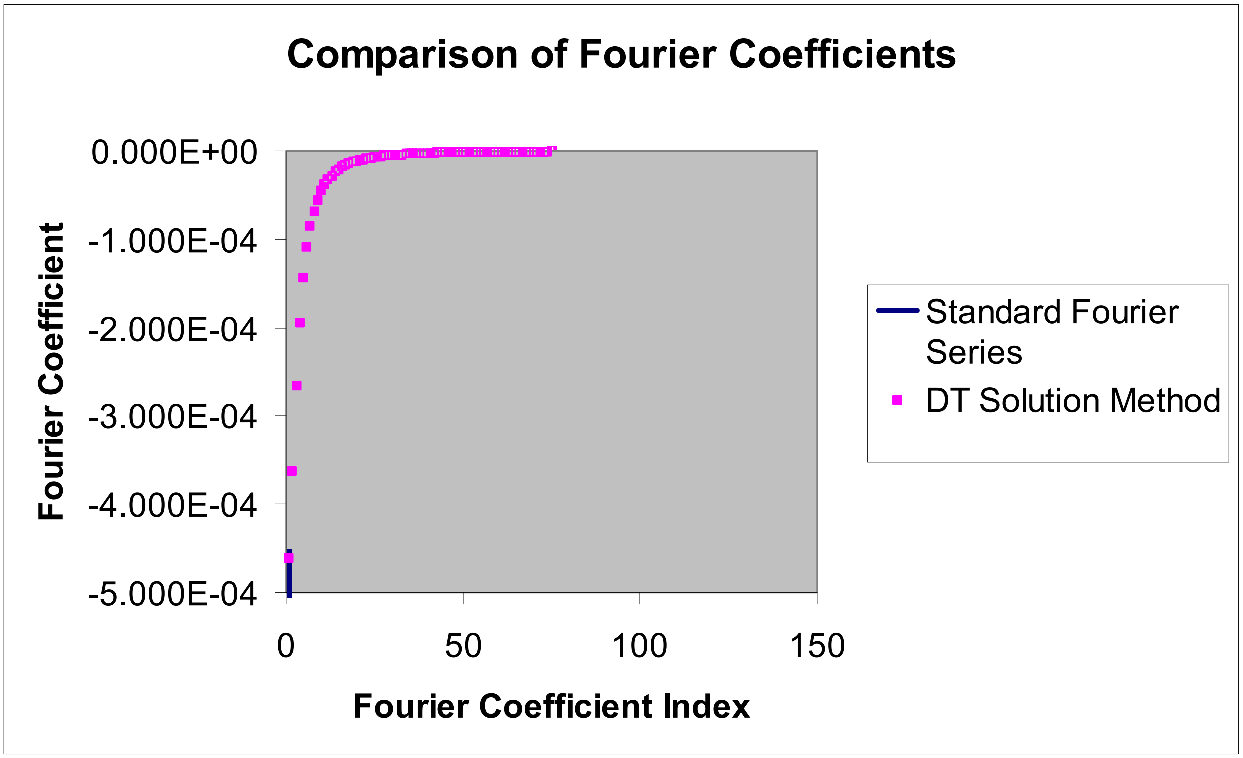

Output-DTN: LB0307FMRADTRN.001

Figure XII-2. Assumed Concentration Profile and its Fourier Representation

This shows that the original Fourier coefficients are closely approximated by the coefficients determined using the discrete transform solution method for the same problem. The coefficient for A_0 is not shown in this figure so that the scale of the figure may more clearly show the comparison for the remaining coefficients. For the original Fourier coefficients, A_0 = -0.004437 as compared with –0.004441 for the discrete transform solution method.

The discrete transform solution method was also used to determine the concentration at the invert-rock interface. The comparison between this concentration and the original concentration shown above is shown in Figure XII-3.

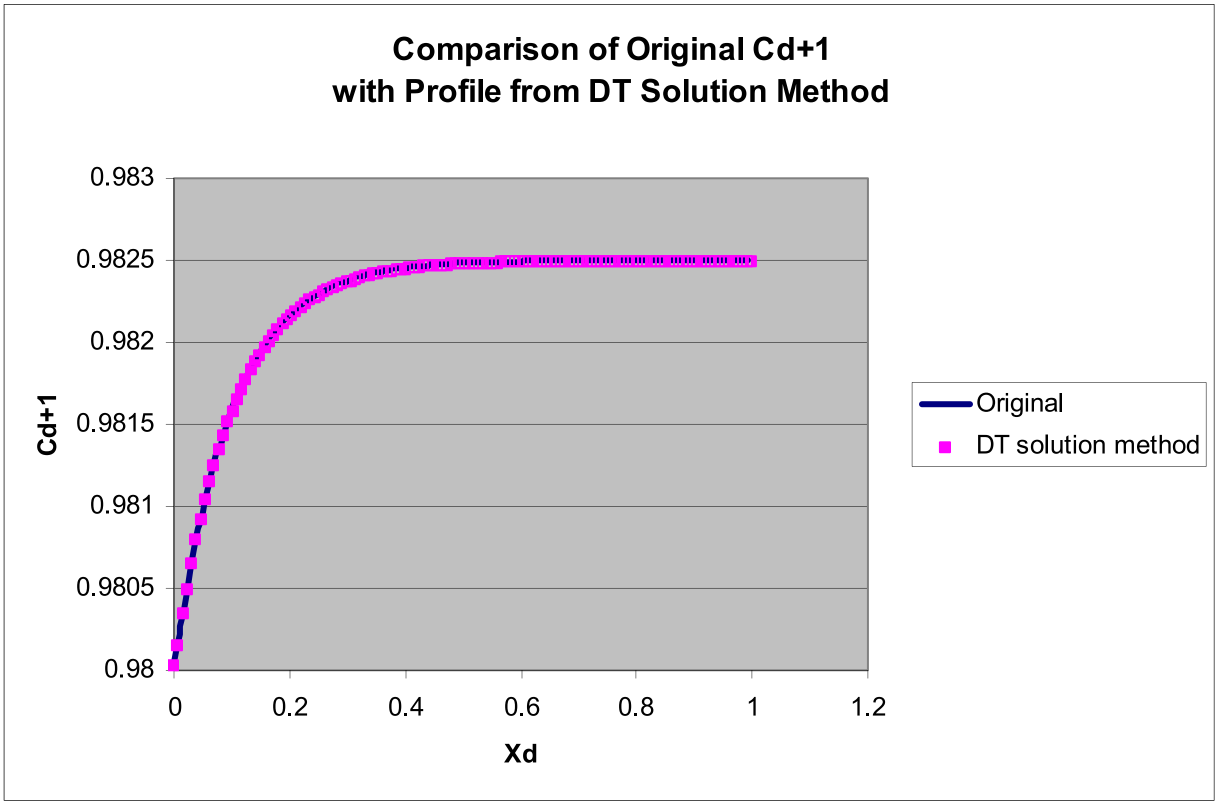

Output-DTN: LB0307FMRADTRN.001

Figure XII-3. Comparison of Assumed Profile and Computed Profile using DT Method

The root-mean-square relative error between the concentration curves is 1.3 x 10^{-5}. Therefore, the discrete transform solution method for Equations 24 through 28 results in a concentration distribution that is essentially identical with the original concentration distribution.

Excel Calculations for Fourier Solution

Equation XII-13 is computed in excel using the following:

For the first Fourier coefficient (evaluated in cell B2), Equation XII-9 in Excel is:

B2=0.25*($CY$1+$CZ$1-($CZ$1/$DA$1)*(1-EXP(-$DA$1)))

Where K1, K2, and K3 (see equation XII-1) are constants in cells CY1, CZ1, and DA1, respectively.

The remaining Fourier coefficients, in cells C2 through CX2, are computed from Equation XII-10, which in Excel is:

COL2=(-2*$CZ$1*$DA$1/($DA$1^2+COL$1^2*PI()^2))*(1-EXP(-$DA$1)*COS(COL$1*PI()))/TANH(COL$1*PI()*4)

where COL is a generic designation for the column label.

The concentration at a given location is computed using Equation XII-13. The cells B3 through B130 contain the dimensionless coordinate, x_d. Cells Crn through CXrn (where rn lies between 3 and 130) are the elements of the summation in Equation XII-13 for each location, x_d, not including the common factor in the summation that is independent of the summation index. The Excel formula for the series elements is:

COLrn=(1-EXP(-$DA$1)*COS(COL$1*PI()))*COS(COL$1*PI()*$Brn)/($DA1^2+COL1^2*PI()^2)

where rn is a generic designation for row number. A portion of the results using these formulas is shown in Table XII-1. See Wang (2003 [163234], SN-LBNL-SCI-236-V1, p. 75) and DTN: LB0307FMRADTRN.001 for the complete output.

Table XII-1. Fourier Coefficients and Calculation of Concentration Profile

	A	B	C	D	E	F	G
1	**j**	0	1	2	3	4	5
2	**Fourier Coefficients**	-0.004437497	-0.00046	-0.000358462	-0.00026	-0.00019	-0.00014
3	**Dimensionless coordinate, Xd**	0	0.009102	0.007169243	0.005296	0.003877	0.002884
4		0.0078125	0.009099	0.007160607	0.005282	0.003858	0.002862
5		0.015625	0.009091	0.007134721	0.005239	0.003803	0.002798
6		0.0234375	0.009077	0.007091646	0.005167	0.00371	0.002691
7		0.03125	0.009058	0.007031488	0.005068	0.003582	0.002544

Output-DTN: LB0307FMRADTRN.001

The summation is carried out in cells CY3 thorugh CY130 using the following formula:

CYrn=SUM(Crn:CXrn)

The common factor is multiplied by the summation results in cells CYrn and the constant in Equation XII-13 is added. This is performed in CZ3 through CZ130 using the following formula:

CZrn=$CY$1+$CZ$1-($CZ$1/$DA$1)*(1-EXP(-$DA$1))-2*$CZ$1*$DA$1*Cyrn

The value of Cd+1 is given by the values in CZrn plus 1 in column DB.

The calculation of Equation XII-14 is also performed in Excel. This is done using a similar structure as for the series expression for Equation XII-13 discussed above. Cells B135 through B262 contain the values of the dimensionless coordinate, x_d. Cells Crn through CXrn (where rn lies between 135 and 262) are the elements of the summation in Equation XII-14 for each location, x_d, not including the common factor in the summation that is independent of the summation index. The Excel formula for the series elements is:

COLrn=(COL$134*PI())*(1-EXP(-$DA$1)*COS(COL$134*PI()))*COS(COL$134*PI()*$Brn)/(($DA$1^2+COL$134^2*PI()^2)*TANH(COL$134*PI()*4))

A portion of the results using these formulas is shown in Table XII-2. See Wang (2003 [163234], SN-LBNL-SCI-236-V1, p. 75) and DTN: LB0307FMRADTRN.001 for the complete output.

Table XII-2. Calculation of Concentration Derivative with Respect to y_d

134	**j**		1	2	3	4	5
135	**Dimensionless coordinate, Xd**	0	0.028595	0.045045679	0.049915	0.048721	0.045304
136		0.0078125	0.028587	0.04499142	0.049779	0.048486	0.044963
137		0.015625	0.028561	0.044828772	0.049374	0.047785	0.043946
138		0.0234375	0.028518	0.044558128	0.048702	0.046623	0.042268
139		0.03125	0.028457	0.044180139	0.047765	0.045012	0.039954

Output-DTN: LB0307FMRADTRN.001

The summation is carried out in cells CY135 thorugh CY262 using the following formula:

CYrn=SUM(Drn:CYrn)

The common factor is multiplied by the summation results in cells CYrn and the constant in Equation XII-14 is added. This is performed in CZ135 through CZ262 using the following formula:

CZrn=0.25*$CY$1+0.25*$CZ$1-(0.25*$CZ$1/$DA$1)*(1-EXP(-$DA$1))-2*$CZ$1*$DA$1*Cyrn

The dimensionless flux (q_d) profile is then computed from Equation XII-15 using the following Excel formula:

DBrn=CZrn/DB(rn-132)

which gives the dimensionless flux at each coordinate x_d.

Mathcad Calculations for the Discrete Transform Method.

The discrete transform calculation discussed above was performed using Mathcad and is given on the following pages:

Solution Method Test Case

Values used for calculation

$y_{dm} := 4.00$ **y_{dm} is the dimensionless invert thickness**

$j_{max} := 127$ **j_{max}+1 is the number of Fourier coefficients**

Distance coordinate along drift wall

$i := 0..\, j_{max}$ **i is reference number for the coordinates along the drift wall**

$j := 0..\, j_{max}$ **j is the reference number for the Fourier coefficients**

$x_{d_i} := \frac{i}{j_{max}}$ **x_{di} is the dimensionless distance along the drift wall**

Sample values for verification of x_{di}

$x_{d_0} = 0$ $x_{d_1} = 7.874 \times 10^{-3}$ $x_{d_2} = 0.016$ .... $x_{d_{126}} = 0.992$ $x_{d_{127}} = 1$

Solution for Fourier coefficients

$q_d :=$ 💾

qd is input from the Fourier solution, Equation XII-15.

DTN: LB0307FMRADTRN.001

q_{di} is the dimensionless water flux profile at the invert-rock interface

Sample values for verification of q_d

$q_{d_0} = -0.06$ $q_{d_1} = -0.041$ $q_{d_2} = -0.023$ .... $q_{d_{126}} = -4.107 \times 10^{-3}$ $q_{d_{127}} = -4.026 \times 10^{-3}$

$$M_{i,j} := \Phi(-j)\cdot\left(1 - y_{md}\cdot q_{d_i}\right) + \Phi(j-1)\cdot\cos\left(j\cdot\pi\cdot x_{d_i}\right)\cdot\left(j\cdot\pi - q_{d_i}\cdot\tanh\left(y_{md}\cdot j\cdot\pi\right)\right)$$

$M_{i,j}$ is the coefficient matrix for A

Sample values for verification of $M_{i,j}$

$M_{0,0} = 1.242$ $M_{0,1} = 3.202$ .... $M_{0,126} = 395.901$ $M_{0,127} = 399.043$

$M_{1,0} = 1.166$ $M_{1,1} = 3.182$ .... $M_{1,126} = -395.761$ $M_{1,127} = -399.024$

$M_{2,0} = 1.09$ $M_{2,1} = 3.16$ .... $M_{2,126} = 395.379$ $M_{2,127} = 399.005$

.
.
.

$M_{64,64} = 141.293$

.
.
.

$M_{126,0} = 1.016$ $M_{126,1} = -3.145$ .... $M_{126,126} = -395.724$ $M_{126,127} = 398.986$

$M_{127,0} = 1.016$ $M_{127,1} = -3.146$ .... $M_{127,126} = 395.845$ $M_{127,127} = -398.986$

$A := M^{-1}\cdot q_d$

A is the vector of Fourier coefficients

Verification of matrix solution for Fourier coefficients, A.
CheckA is a vector of the residuals for $M*A-q_d$

$\text{CheckA} := M\cdot A - q_d$

Plot of residuals for M*A-q_d

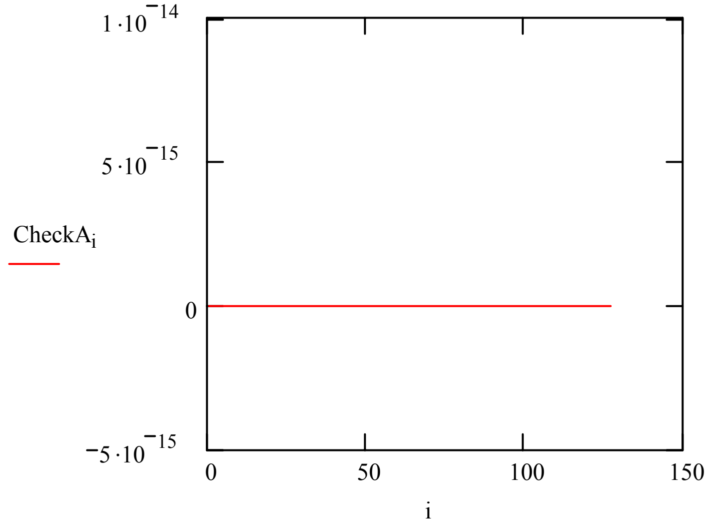

$$C_{d_i} := A_0 \cdot y_{md} + \sum_{j=1}^{j_{max}} A_j \cdot \cos\left(j \cdot \pi \cdot x_{d_i}\right) \cdot \tanh\left(j \cdot \pi \cdot y_{md}\right)$$

C_{di} are the dimensionless concentrations at the invert-rock interface

$$CP(i) := 1 + C_{d_i}$$

CP(i) is the plotting variable for the unnormalized dimensionless concentration

$$XP(i) := x_{d_i}$$

XP(i) is the plotting variable for the dimensionless distance

Plot of the unnormalized dimensionless concentration (C/C_m) at the solution points for the Fourier coefficients

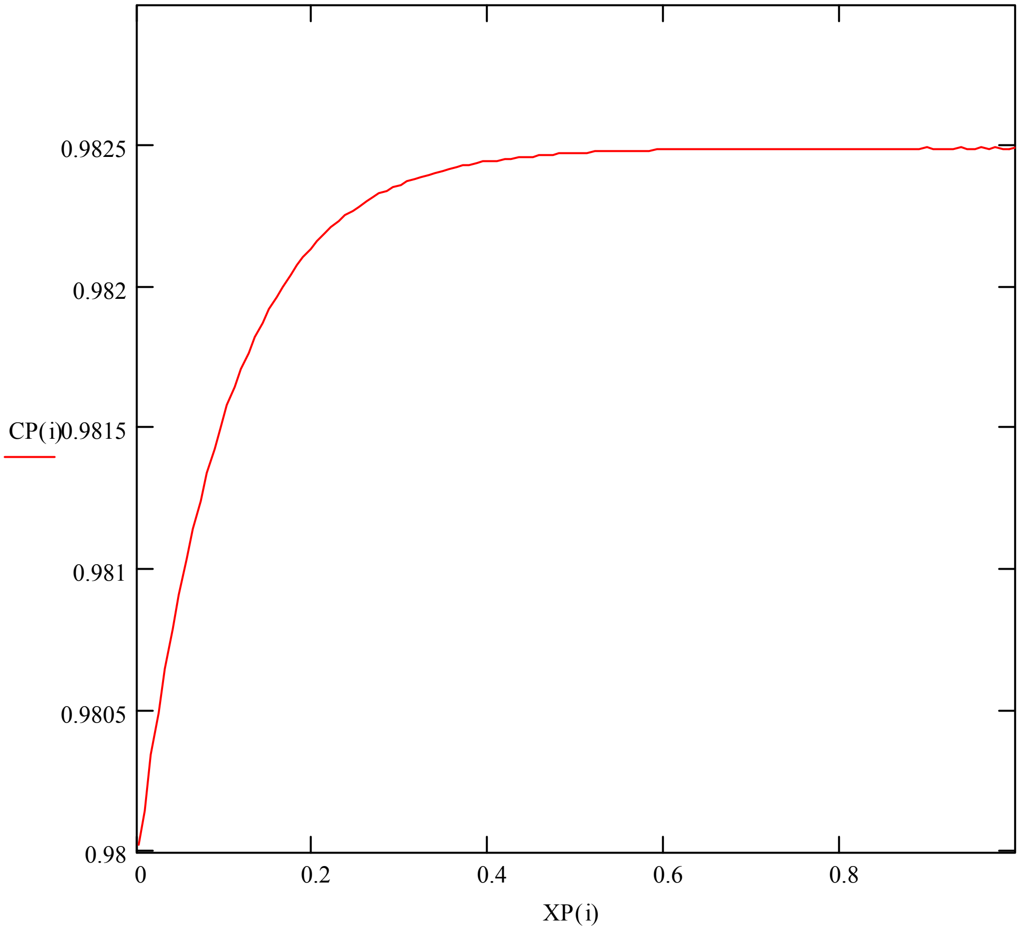

Output-DTN: LB0307FMRADTRN.001

Behavior of local dimensionless mass flux at drift wall

$qC_i := q_{d_i} \cdot \left(C_{d_i} + 1\right)$

Local dimensionless mass flux in rock at drift wall

$qCP(i) := -qC_i$

qCP(i) is the plotting variable for the negative of the local dimensionless advective mass flux in the rock at drift wall

$XP(i) := x_{d_i}$

XP(i) is the plotting variable for the dimensionless distance along the drift wall

Plot of negative of local dimensionless flux at the solution points for the Fourier coefficients

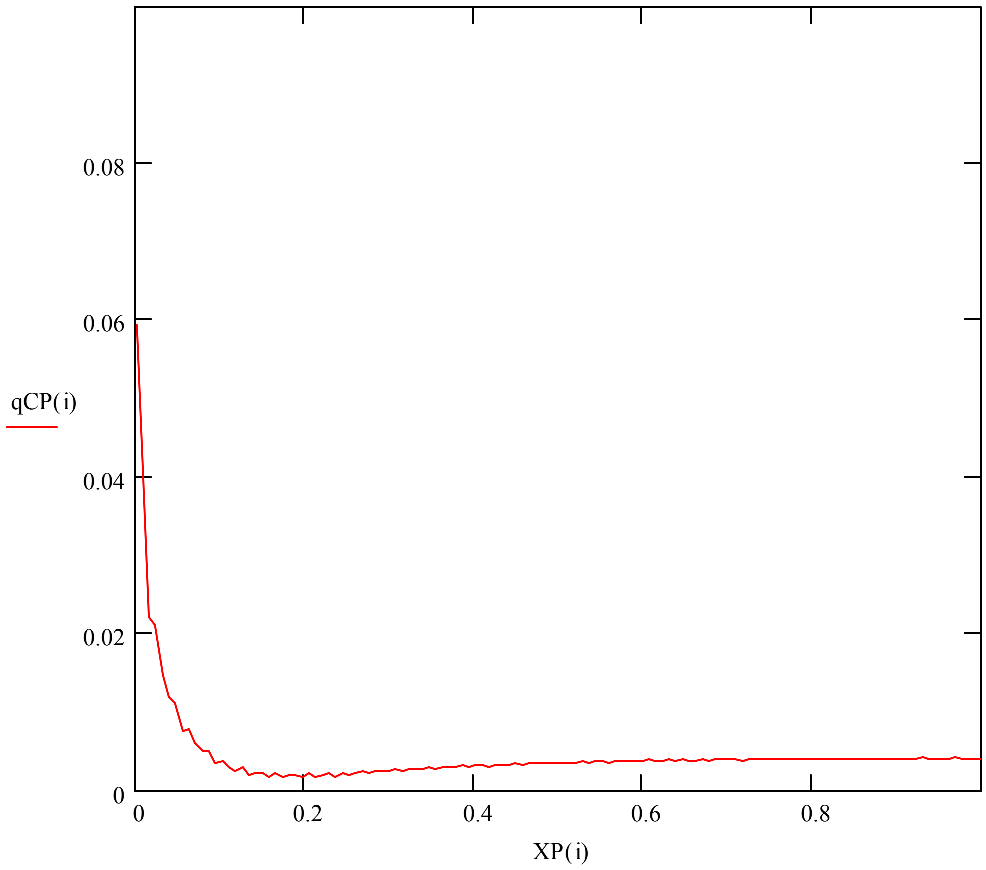

Output-DTN: LB0307FMRADTRN.001